

**THE EFFECTS OF SiC PARTICLE ADDITION ON
THE FOAMING AND MECHANICAL BEHAVIOR
OF ALUMINUM CLOSED-CELL FOAMS
PRODUCED BY FOAMING OF POWDER
COMPACTS**

**A Thesis Submitted to
the Graduate School of Engineering and Sciences of
İzmir Institute of Technology
in Partial Fulfillment of the Requirements for the Degree of**

DOCTOR OF PHILOSOPHY

in Mechanical Engineering

**by
Sinan YÜKSEL**

**July 2010
İZMİR**

We approve the thesis of **Sinan YÜKSEL**

Prof. Dr. Mustafa GÜDEN
Supervisor

Prof. Dr. Muhsin ÇİFTÇİOĞLU
Committee Member

Assoc. Prof. Dr. Alper TAŞDEMİRCİ
Committee Member

Assist. Prof. Dr. Seçil ARTEM
Committee Member

Assist. Prof. Dr. Uğur MALAYOĞLU
Committee Member

08 July 2010

Prof. Dr. Metin TANOĞLU
Head of the Department of Mechanical
Engineering

Assoc. Prof. Dr. Talat YALÇIN
Dean of the Graduate School of
Engineering and Sciences

ACKNOWLEDGEMENTS

I would like to thank to my advisor, Prof. Dr. Mustafa Güden, for his constant support throughout dissertation. His continuous guidance is greatly appreciated. I am also grateful to the other committee members for the guidance.

I would like to thank to the team of IZTECH Materials Research Center (IYTE-MAM) for their helps in the microscopic analysis of specimens. Also, I would like to acknowledge the financial support of TUBITAK project number 106M186, for giving chance to this experimental study.

I would like to appreciate deeply my colleagues N.Deniz KARSU, A.Kaan TOKSOY for their support during the experimental studies and reports of the project. I would like to thank to my family for their constant encouragement and support. And finally, I would like to express my special thanks to my friends Onur, Çe and Zeynep for their encouragement, support and patience during this graduate work.

ABSTRACT

THE EFFECTS OF SiC PARTICLE ADDITION ON THE FOAMING AND MECHANICAL BEHAVIOR OF ALUMINUM CLOSED-CELL FOAMS PRODUCED BY FOAMING OF POWDER COMPACTS

The maximum and linear expansions of a large number of SiC particle/Al powder compacts of varying average SiC particle size (0.03-67 μm), weight percentage (wt%) and size distribution and Al compacts without particle addition were experimentally determined. The powder compacts showed varying expansion values depending on the size, wt% and size distribution of the particles. The linear and maximum expansions for small size SiC particle additions were found to be relatively high at relatively low wt%'s (5 wt%) and decreased with increasing wt% of the particles from 5 wt% to 10 and 15 wt%. The compacts with small average particle size but wider particle size distribution showed higher expansions than the compacts with the similar average particle size but narrower particle size distribution, showing the importance of the particle size distribution on the expansions of Al compacts. The foam expansions were further shown to increase with SiC particle addition until about a critical cumulative particle surface area; however, the expansions decreased significantly at increasingly high cumulative particle surface areas due to the excessive increase in the compact viscosity. For the investigated powder compacts, the optimum wt% of SiC addition was determined, as a function particle size, based on the critical cumulative particle surface area. Compression tests showed that the density of the foam was the most effective parameter in increasing the plateau stresses. Microscopic analysis showed that the main deformation mechanism in Al and SiC/Al foams was the cell wall bending, i.e. cell edges buckled over cell walls. This resembled the deformation characteristics of the open cell foams. It was finally shown that SiC particle addition increased the foam plateau stresses over those of Al foam without particle addition, which was mainly attributed to the reduced fraction of the metal on the cell edges.

ÖZET

TOZ TABLETLERİN KÖPÜKLEŞTİRİLMESİ İLE ÜRETİLEN ALÜMİNYUM KAPALI HÜCRELİ KÖPÜKLERDE SiC PARÇACIK KATKISININ KÖPÜKLEŞME VE MEKANİK ÖZELLİKLERE ETKİLERİ

Farklı SiC parçacık boyutu (0.03-67 μm), ağırlıkça parçacık yüzdesi ve parçacık boyut dağılımına sahip ve katkısız Al köpüklerdeki maksimum ve doğrusal genleşme değerleri, çok sayıda numune ile deneysel olarak saptanmıştır. Basılmış tozlar eklenen parçacığın boyutu, ağırlıkça oranı ve boyut dağılımına göre değişen genleşme davranışları sergilemişlerdir. Küçük tane boyutlu SiC parçacık eklenen numunelerde maksimum ve doğrusal genleşme değerleri düşük parçacık katkılarında (%5) daha yüksek saptanmıştır. Bu değerler parçacık yüzdeleri %5 ten %10 ve %15 çıktıkça azalmışlardır. Daha geniş parçacık boyutu aralığına sahip toz eklenen köpüklerde, aynı ortalama parçacık boyutuna sahip fakat daha dar bir boyut aralığındaki parçacık katkısından daha yüksek genleşme değerlerine ulaşıldığı gözlenmiştir. Bu bize parçacık boyut aralığının önemini göstermiştir. Köpük genleşmeleri SiC parçacık katılması ile belirli bir parçacık toplam yüzey alanı değerine kadar artmıştır. Bu değerden daha yüksek toplam parçacık yüzey alanına sahip katkılarda ise eriyik viskositesindeki artış nedeni ile genleşme değerlerinde belirli düşüşler gözlenmiştir. Kritik toplam parçacık yüzey alanına dayanarak, çalışılan parçacık boyutları için optimum SiC katkı oranları belirlenmiştir. Köpüklere uygulanan ezilme deneyleri, köpük yoğunluğunun plato gerilme değeri için en etkili değişken olduğu bulunmuştur. Mikroskobik çalışmalar sonrasında, Al ve SiC/Al köpüklerde asıl deformasyon mekanizmasının hücre duvarı bükülmesi olduğu görülmüştür. Bu açık hücreli köpüklerin deformasyon mekanizmalarıyla benzetilmektedir. Son olarak da SiC parçacık katkısının köpük plato gerilme değerlerini katkısız köpüklere göre artırdığı görülmüştür. Bu hücre köşelerindeki metal oranının azalmasına bağlanmıştır.

TABLE OF CONTENTS

LIST OF FIGURES	viii
LIST OF TABLES	xvi
CHAPTER 1. INTRODUCTION	1
CHAPTER 2. MANUFACTURING METHODS AND APPLICATION	
AREAS OF CLOSED CELL ALUMINIM FOAMS	4
2.1. Manufacturing Methods of Closed Cell Aluminum Foams.....	4
2.1.1. Foaming of Melts by Gas Injection	5
2.1.2. Foaming of Melts with Blowing Agents	8
2.1.3. Foaming from Powder Compacts	9
2.1.4. Accumulative Roll-Bonding Technique (ARB)	13
2.1.5. Laser Assisted Aluminum Foaming	14
2.2. Applications of Closed-Cell Aluminum Foam	15
CHAPTER 3. MECHANICAL PROPERTIES OF CLOSED-CELL	
ALUMINUM FOAMS.....	19
3.1. Crash Energy Absorption.....	26
3.2. Sound Absorption	34
3.3. High Strain Rate Mechanical Properties.....	36
CHAPTER 4. FOAM STABILITY OF CLOSED-CELL ALUMINUM	
FOAMS	38
CHAPTER 5. MATERIALS AND EXPERIMENTAL METHODS.....	58
5.1. SiC Powder and Whisker	58
5.2. Compact Preperation.....	61
5.3. Foaming Set-Up and Foaming Experiments.....	65
5.4. Compression and Hardness Testing.....	69
5.4. Microstructure Analysis.....	70

CHAPTER 6. FOAM EXPANSION	71
6.1. The Effect of TiH ₂ wt% on the Foam Expansion	71
6.2. Expansion of Al compacts	75
6.3. Expansion of Unsieved P6 and P7 SiC/Al Compacts.....	79
6.4. Expansion of Nano SiC (P10)/Al Compacts.....	84
6.5. Expansion of Whisker SiC (P9)/Al Compacts.....	89
6.6. Expansion of 2 micron SiC (P8)/Al Compacts.....	94
6.7. Expansion of the Sieved SiC (P1-P5)/Al Compacts.....	96
6.8. Expansion of Layered Compacts	99
CHAPTER 7. MICROSTRUCTURAL ANALYSIS FOR EXPANSION TESTS.....	101
7.1. Foamed 30 nm SiC/Al Compacts	101
7.2. Foamed SiC whisker/Al Compacts.....	104
7.2. Foamed SiC particle/Al Compacts.....	105
CHAPTER 8. COMPRESSION BEHAVIOR OF SiC ADDED FOAMS.....	111
CHAPTER 9. DISCUSSIONS	122
9.1. The Effect of Particle Addition on the Compact Expansions.....	122
9.2. The Characteristics of the Compact Expansions	128
9.2. The Effect of Cumulative Surface Area.....	131
9.2. The Effect of Compact Relative Density	133
9.2. The Reaction Between SiC and Liquid Al.....	135
9.2. Mechanical Behavior	135
CHAPTER 10. CONCLUSIONS	141
10.1. Recommendations for Future Studies.....	142
REFERENCES	144
APPENDIX A. HARDNESS TEST RESULTS.....	154

LIST OF FIGURES

<u>Figure</u>		<u>Page</u>
Figure 1.1.	Pore structure of (a) an open cell and (b) a closed cell metal foam.....	2
Figure 2.1.	Effect of metal foam manufacturing process on cell size and relative density	5
Figure 2.2.	Schematic representation of producing aluminum foams by gas injection to the melt	7
Figure 2.3.	Effect of particle volume fraction and particle size on the viscosity of Al melt	7
Figure 2.4.	The process steps used in the manufacture of aluminum foams by gas-releasing particle decomposition in the melt (Alporas process)	9
Figure 2.5.	Schematic representation of foaming from powder compacts.....	10
Figure 2.6.	Views of (a) complicated shaped foam parts, and (b) sandwich foam panel.....	11
Figure 2.7.	a) Schematic of the manufacturing process of a perform sheet through ARB process (b) prediction of gradual distribution of added blowing agent particles.....	13
Figure 2.8.	The block diagram of laser assisted AlSi7 foaming for three processing speeds, in decreasing	15
Figure 2.9.	(a) Prototypes of foam filled tubes designed as energy absorbers, (b) Prototype of a part of an engine mount consisting of foam core and cast shell.....	17
Figure 2.10.	Foam layer used under an elevated viaduct as a noise insulator.....	17
Figure 2.11.	View of (a) aluminum foam sandwich panel, (b) assembled cone of a space craft made from sandwich panels, and (c) cone segment with detailed flange and upper edge.....	18
Figure 3.1.	Compression stress-strain curves of ideal and real Al foam and mechanical property parameters	20
Figure 3.2.	Compression localized deformation sequence of aluminum closed cell foam (0.27 g.cm^{-3}) at various strain and deformed foam cell structure in the localized deformed region.	20

Figure 3.3.	(a) Relative modulus vs. relative density of open and (b) relative compressive strength vs. relative density of open and closed cell foams; comparison with experimentally determined values.....	22
Figure 3.4.	Deformed cross-sections of Al foams using (a) spherical and (b) flat-end indenters	25
Figure 3.5.	Schematic of foams (a) stress-strain curve of various relative densities and (b) corresponding normalized specific absorbed energy vs. normalized stress curves.....	26
Figure 3.6.	(a) Load-displacement, (b) energy-displacement and (c) crush force and total efficiency -displacement curves of a crush element	28
Figure 3.7.	Interaction effect in Al foam (0.27 g cm^{-3}) filled tube.....	29
Figure 3.8.	View of (a) three deformation region in an aluminum foam filler: undeformed, densified and extremely densified regions and (b) deformation of aluminum foam filled vs. empty tube	30
Figure 3.9.	(a) The use of crash-boxes in an automobile and (b) ideal deceleration curve of a medium class car	32
Figure 3.10.	Bending deformation patten of (a) empty and (b) aluminum foam-filled stainless steel beams	33
Figure 3.11.	Comparison of bending deflection of aluminum foam panels and sandwiches with the same weight aluminum sheets	34
Figure 3.12.	Sound absorption coefficient of Alporas foam of relative density ~ 0.09	35
Figure 4.1.	Cross-section of aluminum foam showing thin cell walls, thick cell edges and dense metal layer at the bottom section	39
Figure 4.2.	Schematic view of (a) non-wetted particle, (b) partially wetted particle and (c) fully-wetted particle.....	41
Figure 4.3.	Critical thickness of cell features of various aluminum alloys made by foaming a precursor.....	43
Figure 4.4.	Relationship between mean pore diameter and the density of the foams expanded under different conditions.....	43
Figure 4.5.	Influence of oxide content of Al powder on the expansion behavior of the foam	44

Figure 4.6.	Schematic of the different arrangement of the stabilizing particles on the cell walls.	45
Figure 4.7.	Effect of Mg and Al ₂ O ₃ additions on the expansion of Al foams	46
Figure 4.8.	SEM micrographs showing the attachment of Al ₂ O ₃ particles at the cell wall surfaces for (a) and (c) Al–6 wt% Al ₂ O ₃ and (b) and (d) Al–6 wt% Al ₂ O ₃ –0.6 wt% Mg foams	46
Figure 4.9.	Cross sections of Al foams made using different Al powders: (a) as-received, (b) powder heat treated at 500 °C for 60 min, (c) powder heat treated at 500 °C for 180 min, and (d) powder heat treated at 550 °C for 60 min.....	47
Figure 4.10.	(a) Liquid film in a foam (R is the radius of curved films, Δp is the pressure difference within a film), (b) adsorbed particles with film bridges, (c) modulated interfaces, (d) particle layers on interfaces connected by particle bridges, (e) drainage reduction by particles and (f) model for particles.	49
Figure 4.11.	Stability diagram for metal foams relating particle volume fraction and particle size.	51
Figure 4.12.	Schematic presentation of the foaming experiments with blowing gas into a melt filling a mold	52
Figure 4.13.	Criterion to obtain stable Al foams (alloy A356, T = 727 °C)	53
Figure 4.14.	Relation of stirring time and Ca content with apparent viscosity of Al melt	54
Figure 4.15.	Effect of (a) particle shape and (b) total particle surface area of SiC particles on the fluidity of the melt	56
Figure 4.16.	Effect of volume percentage of SiC particles on the fluidity of Al alloys.....	57
Figure 5.1.	SEM micrograph of (a) P1, (b) P2, (c) P3, (d) P4, (e) P5 (f) P6, (g) P7 and (h) P8 SiC powders	59
Figure 5.2.	SEM micrograph of (a) P9 whisker and (b) P10 nano powder.....	61
Figure 5.3.	Schematic representation of foaming process	62
Figure 5.4.	Dies used for the compact preparation	62
Figure 5.5.	Microstructure of compacts having 5-10 % SiC from (a) P1 (b) P2 (c) P3 (d) P4 (e) P5 powder.	63

Figure 5.6.	Picture of (a) a cold pressed compact and (b) density measurement set-up	64
Figure 5.7.	Schematic of foam expansion measurement set-up	66
Figure 5.8.	(a) Foaming mold and sliding top and bottom rods, (b) low friction pulley and (c) pulley mechanism of the foaming set-up	66
Figure 5.9.	(a) Foaming mold and (b) LVDT and Data logger	67
Figure 5.10.	Typical expansion-time and temperature time graph of foaming experiments	68
Figure 5.11.	(a) Microhardness measuring device and (b) view of the indentation part on the cell wall after force applied.	69
Figure 6.1.	Typical linear expansion and temperature vs. time graph of foaming Al compact	72
Figure 6.2.	The expansion-time and temperature-time graphs of Al compacts with varying wt% of TiH ₂	72
Figure 6.3.	Pictures of the foams with 0.6 wt% TiH ₂ blowing agent addition (at maximum expansion); (a) uncut and (b) crosssection	73
Figure 6.4.	Pictures of the foams with 0.8 wt% TiH ₂ blowing agent addition (at maximum expansion); (a) uncut and (b) crosssection	73
Figure 6.5.	Pictures of the foams with 1 wt% TiH ₂ blowing agent addition (at maximum expansion); (a) uncut and (b) cross-section	74
Figure 6.6.	The number of cells and cell sizes as function of wt% of TiH ₂ addition	74
Figure 6.7.	Expansion-time graph for (a) pure Al foams (700s) and (b) interrupted foaming experiments	76
Figure 6.8.	(a) Pictures of foamed pure Al compacts at various furnace holding time and (b) corresponding cross sections	77
Figure 6.9.	The number of cells and cell sizes of foamed Al compacts as function foaming time	78
Figure 6.10.	Linear expansion-time graphs of the compacts with P6 SiC addition of (a) 5 wt%, (b) 10 wt% and (c) 15 wt% and (d) comparison of particle percentage	79

Figure 6.11.	(a) Linear expansion-time graphs of the compacts with 5 wt% P7 SiC addition and (b) linear expansion-time graphs of the compacts with 5wt% P6 and P7 SiC addition and Al compact	79
Figure 6.12.	(a) Foamed 5 wt% P6 SiC/Al compact (interrupted foaming) and (b) the corresponding cross-sections.....	81
Figure 6.13.	(a) The pictures of foamed P6 SiC/Al compacts with 5, 10 and 15 wt% SiC addition and (b) their cross sections after 900 s furnace holding time	82
Figure 6.14.	(a) The effect of furnace holding time (5 wt% SiC) and (b) wt% of SiC addition on the number of cells and cell sizes (900 s) of foamed P6 SiC/Al compacts	83
Figure 6.15.	(a) The pictures of foamed P7 SiC/Al compacts and (b) their cross sections after 900 s furnace holding time	84
Figure 6.16.	Expansion-time graph of foamed 30 nm SiC/Al compacts (P10).	85
Figure 6.17.	(a) Expansion-time-temperature graphs of 0.15 wt% nano SiC/Al compacts (b) effect of heating rate (c) foam structure at different furnace holding times.....	86
Figure 6.18.	Expansion behavior of nano size SiC added foams with (a) 0.0133 wt%, (b) 0.05 wt%, (c) 0.10 wt% and (d) 0.15 wt% particle additions.....	87
Figure 6.19.	Pictures of the nano size SiC added P10 foams and their sections at maximum expansion and after 900 s furnace holding time.	88
Figure 6.20.	Number of cells and cell sizes of foamed nano SiC/Al compacts at the maximum expansion	89
Figure 6.21.	Linear expansion-time graphs of SiC whisker/Al compacts (P9).....	90
Figure 6.22.	The cross sections of foamed SiC whisker/Al compacts (numbers show wt% of SiC whisker after 900 s holding time).	91
Figure 6.23.	Linear expansion-temperature-time graphs of SiC whisker/Al compacts (a) 0.5 wt% and (b) 1 wt% whisker addition.	92
Figure 6.24.	Linear expansion- temperature-time graphs of 1 wt% SiC whisker/Al compacts of different heating rate	93
Figure 6.25.	The structure of foamed 1 and 0.5 wt% SiC whisker/Al and Al compacts after 900 s furnace holding time	93

Figure 6.26.	Number of cells and cell sizes of foamed whisker shaped SiC/Al compacts at the maximum expansion	94
Figure 6.27.	Linear expansion-time graphs of P8 SiC/Al compacts of varying particle wt%'s	95
Figure 6.28.	The structure of foamed 0.1, 0.5 and 1 wt% P8 SiC/Al compacts after 900 s furnace holding time	96
Figure 6.29.	The linear expansion-time graphs of 5 and 10 wt% P1-P5 SiC/Al compacts (a) P1, (b) P2, (c) P3, (d) P4 and (e) P5.....	96
Figure 6.30.	The cell structures of foamed P1-P5 SiC/Al compacts after 900s furnace holding time (a) 5 and (b) 10 wt% addition.....	97
Figure 6.31.	Schematic presentations of the layered compacts.....	99
Figure 6.32.	Views of the expanded foams from the both groups of layers	100
Figure 6.33.	Picture of (a) group 1 layered foamed compact and (b) crosssection and structure of group 2 foamed compacts	100
Figure 7.1.	EDAX analysis of a (a) TiH ₂ particle and (b) the reaction zone around the TiH ₂ particle in a foamed 30 nm 0.15 wt% SiC/Al compact (P10) after 900 s furnace folding time.....	102
Figure 7.2.	SEM micrographs showing (a) and (b) a cell wall in foamed 0.15 wt% nano SiC/Al compact and (c) EDAX analysis of the precipitates in the cell wall	103
Figure 7.3.	Elemental mapping of the cell wall in a foamed 0.15 wt% nano SiC/Al compact: (a)Al, (b) Si, (c) C and for (d) O	104
Figure 7.4.	SEM pictures of a foamed 1 wt% whisker/Al compact (a) cell wall and surface, (b) cell wall surface, (c) cell wall (d) suspended whiskers on the cell wall surfaces.....	105
Figure 7.5.	SEM pictures of cell wall surfaces of foamed (a) P1, (b) P2, (c) P3, (d) P4, (e) P5 SiC/Al compacts after 900 s furnace holding time.	106
Figure 7.6.	SEM pictures of cell wall surfaces of foamed P10 1wt% SiC/Al compacts after 900 s furnace holding time	107
Figure 7.7.	EDAX analysis of the cell wall surface of a foamed 1 wt% P10 SiC/Al compact after 900 s furnace holding time.....	108

Figure 7.8.	SEM pictures of cell walls of the foams with (a) and (b) 5 wt% P2 SiC/Al, (c) 5 wt% P5 and (d) 10 wt% P5 SiC/Al foam	108
Figure 7.9.	Particles at cell wall surfaces (c) 5 wt% P5 SiC/Al foamed compact and (d) 5 wt% P7 SiC/Al foamed compact after 900 s	109
Figure 7.10.	Average hardness values of the cell walls vs. SiC particle size	110
Figure 8.1.	View from (a) dense shell of the cut foam and (b) prepared compression test specimens from expanded 5 wt% P5 SiC/Al foams.....	111
Figure 8.2.	Stress-Strain curves of the foams with; (a) P0, (b) %5 P1 SiC, (c) %10 P1 SiC, (d) %5 P2 SiC, (e) %10 P2 SiC, (f) %5 P3 SiC , (g) %10 P3 SiC , (h) %5 P4 SiC, (i) %10 P4 SiC, (j) %5 P5 SiC, (k) %10 P5 SiC, and (l) %1 SiC whisker additions.....	112
Figure 8.3.	The stress-strain curves of the similar density foams: (a) 5 wt% P1-P5 SiC/Al and SiC whisker/Al and (b) 10 wt% P1-P5 SiC/Al foam	115
Figure 8.4.	The variation of SAE values of foams with relative density; (a) 5 wt% P1-P5 SiC and 1 w% SiC whisker and (b) 10 wt% P1-P5 SiC/Al foams.....	118
Figure 8.5.	The deforming Al foam sample at various percent strains	119
Figure 8.6.	The deforming 10 wt% P6 SiC/Al foam sample at various percent strains	120
Figure 8.7.	The deformed cell micrographs of (a) Al foam and (b) 10 wt% P6 SiC/Al foam samples showing cell wall bending and tearing	120
Figure 8.8.	Development of cracks around the SiC particles (a) near to a cell edge and (b) on the bent cell walls of 10 wt% P6 SiC/Al foam tested until about 50% strains	120
Figure 8.9.	The pictures of the deformed (0.40 strain) cell walls of (a) Al (P0), (b) 5 wt% P1, (c) 5 wt% P3 and (d) 5 wt% P5 SiC/Al foams	121
Figure 9.1.	Typical linear expansion and temperature vs. time graph of an Al compact.....	123
Figure 9.2.	The variation of (a) number of cells and (b) average cell wall thickness with furnace folding time in foamed compacts.....	125

Figure 9.3.	Cell wall thickness variation along the foam cylinder; (a) P0 after 100 and 200 s, (b) P0 and P6 after 100 s and (c) P0 and P6 after 200 s	125
Figure 9.4.	Linear and maximum expansion as function of particle size; (a) 5 and (b) 10 wt% particle added compacts	127
Figure 9.5.	The characteristic behavior of the compact foaming (0.5 wt% P9).....	129
Figure 9.6.	The effect of heating rate on the (a) expansion time (t_3) and (b) expansion rate of the foamed compacts	130
Figure 9.7.	Effect of heating rate on (a) maximum and (b) average linear expansion for different foams	130
Figure 9.8.	Relation between maximum and average linear expansion.....	131
Figure 9.9.	Variation of linear and maximum expansion with cumulative particle surface area of SiC particles	132
Figure 9.10.	Optimum wt% of SiC particle addition as a function of particle size	133
Figure 9.11.	The effect of relative density on (a) LE and (b) LE_{max} values of Al and P1-P5 SiC/Al foamed compacts.....	134
Figure 9.12.	Stress vs. relative density of foamed Al and SiC/Al compacts based on the open cell foam structure (a) 5% P1, (b) 5% P2, (c) 10% P1 and (d) 10% P2	137
Figure 9.13.	Stress vs. relative density of foamed Al and SiC/Al compacts based on ϕ value (a) 5% P1, (b) 5% P2, (c) 10% P1 and (d) 10% P2	137
Figure 9.14.	Stress-behavior of Al foams according to both experimental and analytical results	139
Figure 9.15.	. Stress-strain behavior comparison of experimental and calculated results for (a) 10 wt% and (b) 5 wt% SiC added Al foams	139

LIST OF TABLES

<u>Table</u>	<u>Page</u>
Table 2.1. Foaming routes and current manufacturers for aluminum based metal foams.....	5
Table 5.1. Powders used for the compact preparation.....	58
Table 5.2. Mean particle diameter values of the powders measured from SEM images.....	59
Table 5.3. Percentages of SiC in SiC/Al compacts.....	62
Table 6.1. The coding, dimensions and density of the compacts with various TiH ₂ addition.....	73
Table 6.2. The coding, weight, thickness, density and expansions of Al compacts without SiC addition (P0).....	77
Table 6.3. The coding, weight, thickness, density and expansions of P6 and P7 SiC/Al compacts.....	80
Table 6.4. The coding, weight, thickness, density and expansions of SiC(P10)/Al compacts.....	85
Table 6.5. The coding, weight, thickness, density and expansions of SiC (P10.st)/Al compacts.....	87
Table 6.6. The coding, weight, thickness, density and expansions of P9 SiC whisker/Al compacts.....	91
Table 6.7. The coding, weight, thickness, density and expansions of P8 SiC/Al compacts.....	95
Table 6.8. The coding, weight, thickness, density and expansions P1-P5/Al compacts.....	99
Table 6.9. The coding, weight, thickness, density and expansions of layered compacts.....	99
Table 7.1. Hardness Vickers values of foamed Al and P1-P5 SiC/Al compacts.....	110
Table 8.1. Foam compression test samples and mechanical properties of foamed Al and 5 wt% SiC/Al compacts.....	116
Table 8.2. Foam compression test samples and mechanical properties of foamed 10 wt% SiC/Al compacts.....	117

CHAPTER 1

INTRODUCTION

Foam is a substance characterized by regularly distributed arrays of cells, formed by trapping gas bubbles in a liquid or solid. It is an extremely complex system consisting of poly-sized gas bubbles separated by films. The cells are formed by the liquid phase while the gas phase fills the space in between the cells. This way of structuring of liquid and gas phases is also referred as to cellular and often observed in natural materials such as bone and wood. If the cell material is replaced with a solid metal, the resultant structure is usually referred to as “metal foam” or “foamed metal”. The solid foams can be categorized into two groups according to their pore structure: open cell and closed cell. The pores in open cell foam are connected to each other, whereas the pores in closed cell foam are separated by a cell wall (Figure 1.1).

Metal foams have unique mechanical and physical properties, which make them attractive materials in structural and functional applications. They are very light, possessing densities as low as one tenth of the density of the metal of which they are made. They crush under compressive loads almost at a constant load until about very large strains, allowing the absorption of a great deal of deformation energy. The energy absorbing capabilities of metal foams make them attractive materials to be potentially used in crash and blast protections. Application of the foams includes such as the core materials in between the metal plates in sandwich structures for blast protection of buildings and military vehicles and filler for the bumpers and empty spaces in the car body to prevent shock wave passage through the passenger compartment in accidents involving collisions.

The mechanical properties of the metal foams are mainly dictated by the distribution of the cell material in the cell walls (surface), edges and nodes. In open cell foams, the metal phase is distributed at the cell edges and vortex, where 3 and 4 cells meet, respectively. While in the closed cell foams, additional metal phase forms the cell walls, where two cells meet. The final foam structure including the relative distribution of the metal phase in the cell walls, edges and nodes is formed by the foaming process, which is usually conducted in liquid state at relatively elevated temperatures. The

structure of liquid foams changes constantly over time by various types of events including drainage, cell wall rupture and coarsening. If the change in the foam structure is relatively slow, the foam is said to be kinetically stable. In other words, stable foam shows negligible changes in the structure with time. The foam stabilization plays a key role in forming of controllable homogeneous foam structures. In aqueous foams, the stabilization is achieved by means of (a) surfactants and (b) small particles, which act as elastic separator between the cells. It is noted that only the later can be used for the metal foam stabilization.

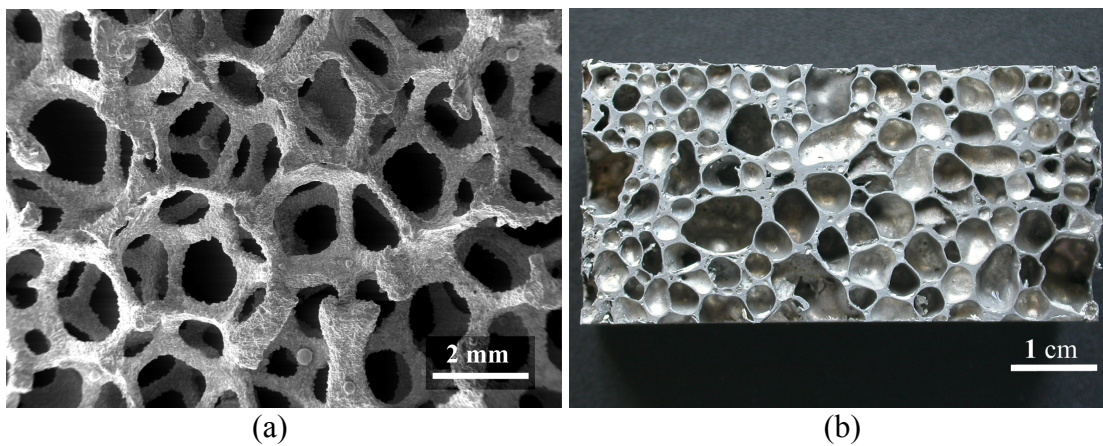


Figure 1.1. Pore structure of (a) an open cell and (b) a closed cell metal foam.

Al closed-cell foams are currently manufactured by several different processes, in which the liquid foam is stabilized by the addition of ceramic particles to the liquid metal either in-situ or ex-situ. In Alcan foaming process, in which the liquid metal is foamed by gas injection, the liquid foam stabilization is achieved by adding SiC particles (Banhart 2000a). In the Alporas foaming process, the viscosity of the liquid metal is adjusted by Ca-addition into the melt, which results in the formation of oxide particles by internal oxidation (Miyoshi, et al. 2000).

The ceramic particle addition in the foaming of powder compact process was subjected to several studies. TiB_2 addition, although, increased the plateau stresses of Al foams, it was not effective in long-term foam stabilization (Kennedy and Asavavisitchai 2004). Contrary to TiB_2 -addition, SiC_p -addition of 3 wt% was shown to improve the foam stability of Al powder compacts (Kennedy and Asavavisithchai 2004). The compact expansion is expected to vary with the size and wt% of the particle addition, along with some other important process parameters, while a comprehensive study of

the effect of particle size on the expansion of the powder compacts is still absent in the literature. The present thesis is therefore conducted as a further, but a more comprehensive investigation of the effect of SiC-particle addition on the foaming behavior of Al powder compacts in the foaming powder compact process. For that purpose, a large number of SiC/Al composite and Al powder compacts having the similar relative densities were prepared and foamed. SiC powder average particle size investigated ranged between 30 nm and ~67 μm with the particle additions of 0.05-15 wt%. The effect of SiC particle addition on the foaming behavior was determined by comparing the expansions of SiC/Al and Al compacts without particle addition processed under the same condition. The effect of SiC particle addition on the mechanical properties was further assessed by the compression testing of the foams with the similar densities. The experimental study presented in this thesis was part of a TÜBİTAK project, which was aimed to optimize foam structures with respect to the particle addition in order to increase the foam energy absorption in certain applications such as foam filled crash boxes for the automobiles.

CHAPTER 2

MANUFACTURING METHODS AND APPLICATION AREAS OF CLOSED CELL ALUMINUM FOAMS

2.1. Manufacturing Methods of Closed Cell Aluminum Foams

There are essentially nine distinct process-routes for the production of the cellular metals (Ashby, et al. 2000). Each of these processes is applicable to certain type of metals and they result in different foam structures and properties mainly dictated by the nature of the process (Figure 2.1). Closed cell Al foams are manufactured by five different methods. These are 1) foaming of melts by gas injection, 2) foaming of melts with blowing agents, 3) foaming from powder compacts, 4) accumulative roll-bonding technique and 5) laser assisted foaming. The first three methods are currently used to produce commercial closed cell Al foams, while the others are still in the development stage. The process technique used to produce foam is noted to be very effective on the final structure of the foam including cell size and the density of the foam (Figure 2.1). Therefore every process technique results in different foams that are suitable for different applications.

The production methods of closed cell Al foams can also be basically divided into two main groups according to their processing strategies as direct and indirect foaming (Table 2.1). Direct foaming method starts from molten metal containing uniformly dispersed non-metallic particles with either gas is injected into the melt or a blowing agent is used to lead to the foam structure (Banhart 2001). On the other hand, indirect foaming methods start from the solid precursors which consist of an aluminium matrix containing uniformly dispersed blowing agent particles. These are mostly titanium or zirconium hydride. Upon melting, this precursor expands and forms cellular structure of the foam.

Table 2.1. Foaming routes and current manufacturers for aluminum based metal foams
(Source: Banhart 2007).

Direct foaming	Melt alloy Make alloy foamable Create gas bubbles Collect foam Solidify foam	Indirect foaming	Prepare foamable precursor Remelt precursor Create foam Solidify foam
Manufacturers (products)	Cymat, Canada (<i>SAF</i>) Foamtech, Korea (<i>Lasom</i>) Hütte Kleinreichenbach (<i>HKB</i>), Austria (<i>Metcomb</i>) Shinko-Wire, Japan (<i>Alporas</i>) (Distributor: Gleich, Germany)	Manufacturers (products)	alm, Germany (<i>AFS</i>) Alulight, Austria Gleich-IWE, Germany Schunk, Germany

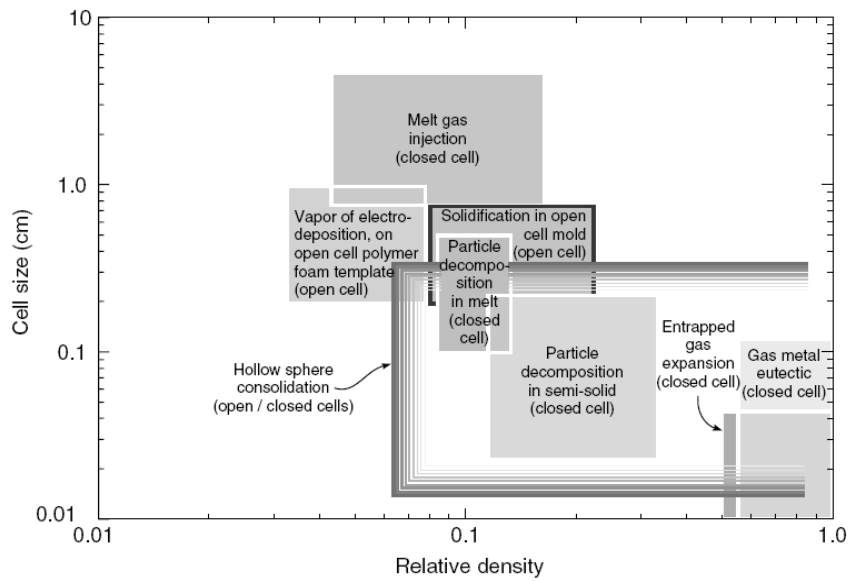


Figure 2.1. Effect of metal foam manufacturing process on cell size and relative density
(Source: Ashby, et al.2000)

2.1.1. Foaming of Melts by Gas Injection

Foaming of melts by gas injection is a continuous foam production technique that was developed by ALCAN International Limited and is currently being used by Alcan N. Hydro (Norway) and Cymat Aluminum Corporation (Canada) (Banhart 2000a, Banhart and Baumeister 1998). Ceramic particles like SiC, Al₂O₃, or MgO are

added in order to enhance the viscosity of the liquid metal to be foamed. In the second step, the melt is foamed by injecting gas (air or nitrogen) using rotating air injection shaft which generates fine gas bubbles and distributes them homogeneously in the melt (Banhart and Baumeister 1998). The schematic representation of the process is shown in Figure 2.2. Since the bubbles are stabilized by the ceramic particles, they can be pulled off melt surface using a conveyor belt. Finally, the foam is cooled down below the melting point of metal matrix resulting in continuous aluminum foam panels with various width and thickness values.

Drainage is usually observed in the foamed slabs, which causes density and pore size gradients. The conveyor belt further induces shearing forces, leading to the formation of elongated cells (Beals and Thompson 1997). Solidified foams with dense outer surface layers can be directly used or machined into any desired shape. However, machining of these foams may be difficult due to the presence of hard ceramic particles in the metal matrix. The process has the capability for continuous production of large volumes of low-density metal matrix composite foams at a relatively lower cost. The main disadvantage of this direct foaming method is the necessity for the secondary processes such as cutting and machining. The size of the ceramic particles added to the melt ranges between 5 and 20 micrometers, while the weight percentages of the particles vary between 10 % and 20 % (Raj and Daniel 2007). Typical density, average cell size and cell wall thickness are $0.069\text{-}0.54\text{ g.cm}^{-3}$, 3-25 mm, and 50-85 μm , respectively (Kenny 1996). Average cell size, average cell wall thickness and density can be adjusted by varying processing parameters including gas injection rate and rotating shaft speed.

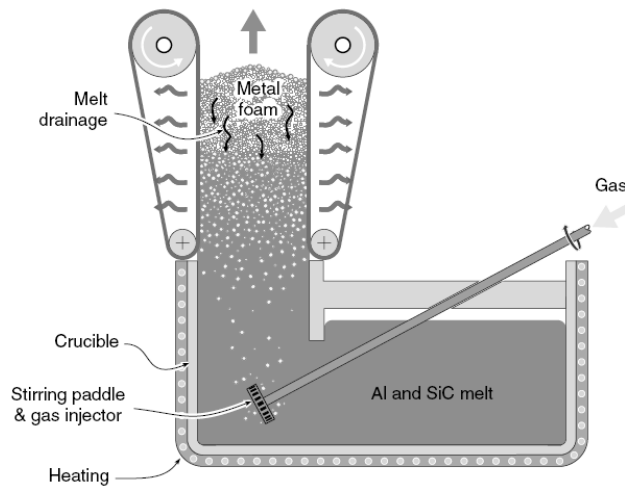


Figure 2.2. Schematic representation of producing aluminum foams by gas injection to the melt (Source: Ashby, et al. 2000).

The effects of particle volume fraction and particle size on the viscosity of an Al melt are shown in Figure 2.3. The viscosity of the molten Al can also be adjusted by injecting oxygen, air and other gas mixtures through the melt which causes the formation of Al_2O_3 particles. Complicated temperature cycles, difficulty in the adjustment of variables and the possible need for secondary processing (machining) are the disadvantages of the process.

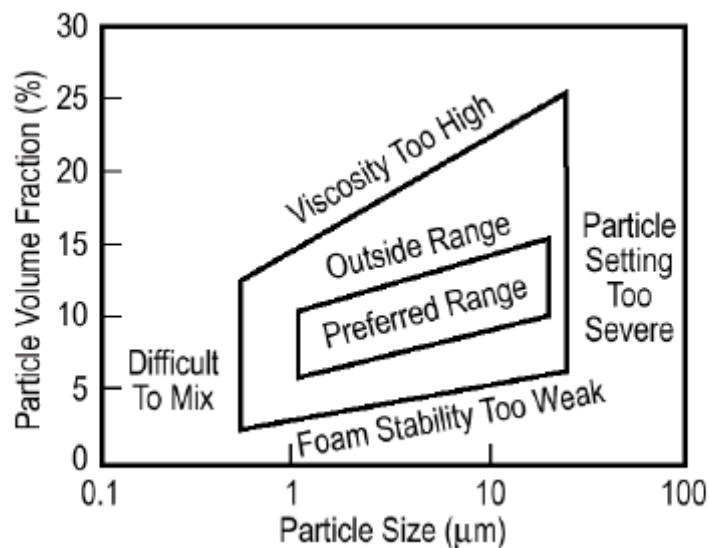


Figure 2.3. Effect of particle volume fraction and particle size on the viscosity of Al melt (Source: Banhart 2006).

2.1.2. Foaming of Melts with Blowing Agents

The second method of Al closed-cell foam production is to add a foaming or blowing agent (0.5-2% TiH_2 by weight) into liquid metal. As the foaming agent decomposes, the released gas drives the foaming process (Figure 2.4). This method is also known as ALPORAS foaming process and has been used since 1986 by Shinko Wire Co (Japan) for the production of closed-cell Al foams. Before foaming, 1.5 wt% calcium is added into Al melt and then the melt is stirred quickly. The viscosity of the melt increases with increasing stirring time because of the formation of oxide and/or metallic compounds (calcium oxide, calcium-aluminum oxide, or Al_4Ca intermetallic) that thickens the metallic melt (Miyoshi, et al. 2000). In a later stage of the process, after adjusting the viscosity of the liquid metal, TiH_2 with an amount of 1.6 wt% is added into the melt, which releases hydrogen gas in the hot viscous liquid according to the following reaction



Above reaction results in the expansion of the liquid metal and fills the foaming vessel with liquid foam at a constant pressure. Finally, the liquid foam is cooled down below the melting point of the foamed alloy quickly and the solidified Al foam is further processed for specific applications. Al foams produced by the process, *Alporas*TM, is the most homogeneous foams produced currently (Banhart 2000b). Typical densities of the cast foams are between 0.18 g/cm^3 and 0.24 g/cm^3 with an average pore size ranging from 2 mm to 10 mm (Banhart 2000b, Miyoshi, et al. 2000).

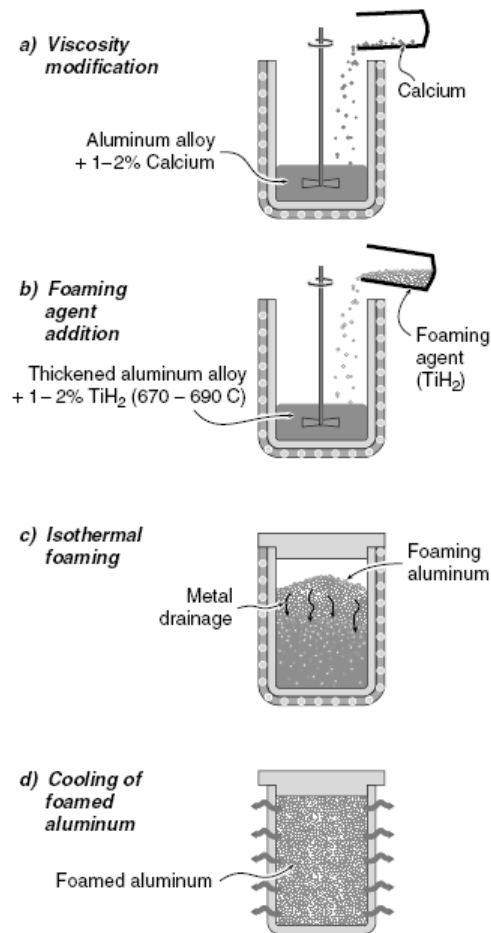


Figure 2.4. The process steps used in the manufacture of aluminum foams by gas-releasing particle decomposition in the melt (Alporas process) (Source: Ashby, et al. 2000).

2.1.3. Foaming from Powder Compacts

Foaming from powder compacts is a technique developed by Fraunhofer-Institute (Germany). The method is based on the foaming of the pressed dense Al/ TiH₂ compacts (0.6 % by weight) by increasing the temperature over the melting temperature (Baumeister and Schrader 1992). Some companies like FOAMINAL (Schunk GmbH) and ALULIGHT (Alulight International GmbH) are producing closed cell foams using this technique. The process starts with mixing metal powders with a blowing agent which upon heating releases a foaming gas (Figure 2.5). Metal powder-blowing agent mixture is then compressed to a dense, semi-finished foamable product via metal forming processes such as hot compaction, extrusion and rolling. In a final step, the semi-finished product is heated to a temperature near to the melting point of the metal.

During heating, the blowing agent decomposes and subsequently releases gas, leading to the expansion of the molten or mushy metal and the formation of a highly porous structure.

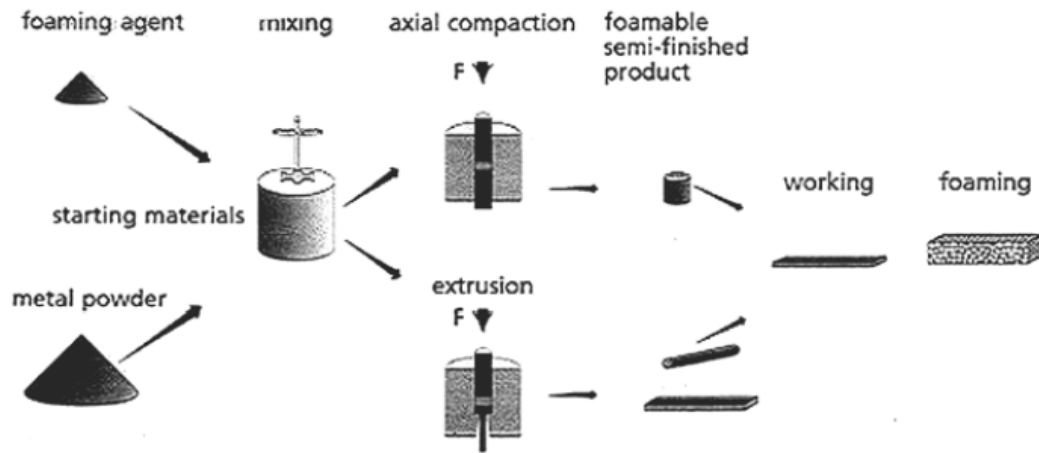


Figure 2.5. Schematic representation of foaming from powder compacts (Source: Baumgartner, et al. 2000).

Besides metal hydrides (e.g., TiH_2), carbonates (e.g., calcium carbonate, potassium carbonate, sodium carbonate and sodium bicarbonate), hydrates (e.g., aluminum sulphate hydrate and aluminum hydroxide) or substances that evaporate quickly (e.g., mercury compounds or pulverized organic substances) can also be used as blowing agent.

For efficient foaming, it is very critical to form a gas-tight semi finished product in which the blowing agent is fully entrapped in the metallic matrix. Therefore the temperature and the pressure of hot compaction must be high enough to bond the individual metal powder particles and form a gas-tight seal around the blowing agent particles so that early decomposition of the blowing agent and the escape of H_2 gas before the melting of semi-finished product is avoided. In compaction by rolling, a temperature range between 350°C and 400°C is sufficient for the diffusion between the particles (Baumeister and Schrader 1992). The weight ratio of blowing agent for forming of aluminum foam and its alloys has been found to be small. Calculations have shown that a foamable Al compact which contains 0.6 wt% TiH_2 would give an expansion factor of 17; a value almost 4 times higher than the expansion factor (4-5) experimentally found (Baumeister and Schrader 1992, Baumgartner, et al. 2000). This

presents that, only 25% of the released hydrogen is effective in forming pores, and the rest is lost during foaming. The time needed for full expansion of the semi-finished product depends on the temperature and size of the precursor and ranges from a few seconds to several minutes. The process is not only restricted to Al and its alloys, but also tin, zinc, brass, lead, gold, and some other metals and alloys can also be foamed using appropriate blowing agents and process parameters (Yu, et al. 1998).

If a piece of foamable precursor is foamed in a furnace, the result will be a lump of metal foam with an undefined shape unless the expansion is limited. This is done by inserting the semi-finished foamable precursor into a mold having the desired shape of product and allowing expansion by heating. This process results in near-net shaped parts with a closed and dense outer skin and a highly porous cellular core. Complicated parts can be manufactured by pouring the expanding liquid foam into a mold (Figure 2.6 (a)). Sandwich panels consisting of a foamed metal core and two metal face sheets can be manufactured by bonding the face sheets to a piece of foam with adhesives. Another way is to roll clad Al or steel sheets onto a sheet of foamable material and allow the foamable core to expand while the face sheets remain dense (Figure 2.6 (b)). By this method, Al foam structures can be combined with steel or titanium face sheets as well as with Al face sheets. In the latter case, Al sheets with melting points that are higher than the core material must be used to avoid melting of the face sheets during foaming.

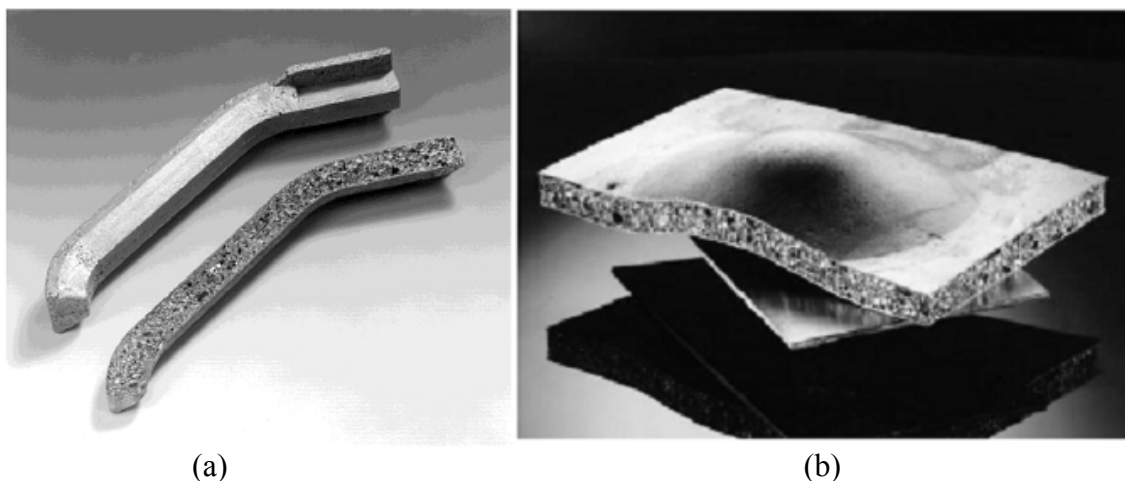


Figure 2.6. Views of (a) complicated shaped foam parts (Source: Baumgartner, et al. 2000), and (b) sandwich foam panel (Source: Yu, et al. 1998).

It is also possible, with this process by applying suitable heating, to produce bodies that have continuously or discontinuously changing densities over the cross

section. If the foaming process is interrupted after a certain time at a constant temperature, a certain density will be obtained and if the foaming process is continued further, a higher density value will result. For example, structures having higher foam densities on the locations exposed to higher external loads could be manufactured by this method. If the hot compaction process is performed inside a mold, the powder mixture will be surrounded completely or partially by a blowing agent free metal powder. Upon foaming, this forms a dense or less porous cover layer and a highly porous foam core. This offers advantages for joining of similar or different structures and for the production of foam core structures that require a dense cover such as car doors and frames.

Foaming from powder compact process has been recently modified by incorporating TiH_2 particles directly into an Al melt instead of using powders to prepare a foamable precursor material. To avoid premature H_2 evolution, the melt should be quickly cooled down below its melting point after mixing or the blowing agent has to be passivated to prevent it from releasing gas before solidification. The former technique, called *Foamcast* is carried out in a die-casting machine and the TiH_2 is injected into the die simultaneously with the melt (Banhart 2000a, Yu, et al. 1998). The resulting cast part is virtually dense and could be foamed by re-melting in analogy to foaming from powder compacts; however, achieving a homogeneous distribution of TiH_2 powders in the die is difficult. The latter route requires that TiH_2 powders be subjected to a heat treatment cycle that forms an oxide layer on each particle, which delays the decomposition of TiH_2 . TiH_2 is then added to the melt and the melt can be cooled at comparatively slow rates after stirring. Melts containing SiC particles are used to obtain stable foams. The name *Formgrip* has been given to this process which is an acronym of foaming of reinforced metals by gas release in precursors (Gergely and Clyne 2000).

2.1.4. Accumulative Roll-Bonding Technique (ARB)

This process is recently proposed by Kitazono *et al.* (Kitazono, et al. 2004) and based on the dispersion of foaming agent into bulk metal sheets through sequential rolling. The stages of process are schematically illustrated in Figure 2.7 (a). Two metal strips are stacked together with blowing agent powder (TiH_2) in between them. The stacked strips are then roll-bonded by the reduction of thickness. The bonded strips are then cut and after surface treatment, they are stacked again and roll-bonded. After several roll-bonding cycles, rolled foamable precursor composite in which the blowing agent particles dispersed in a metal matrix is obtained (Figure 2.7 (b)). The composite is used as the starting material for the following high temperature foaming process.

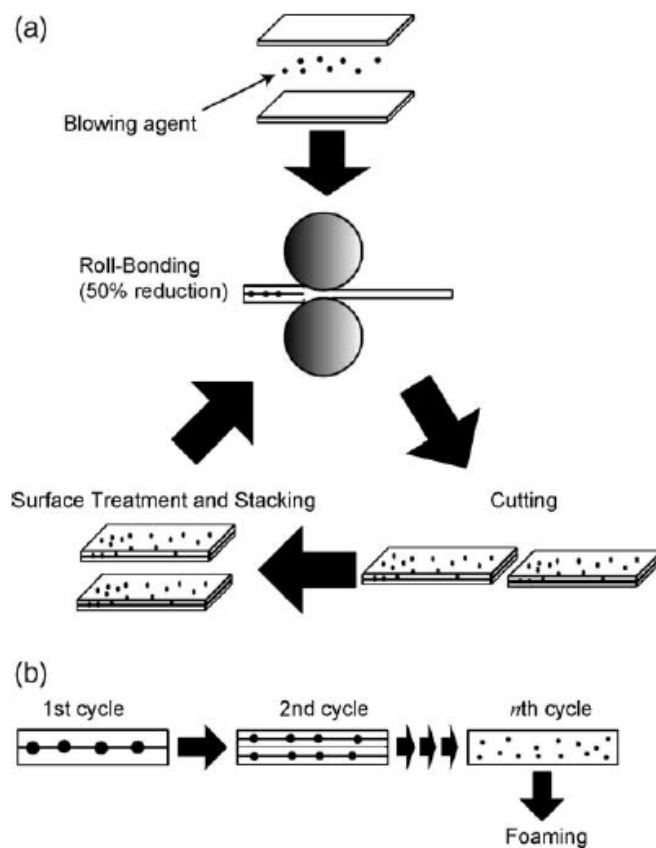


Figure 2.7. a) Schematic of the manufacturing process of a perform sheet through ARB process (b) prediction of gradual distribution of added blowing agent particles (Source: Kitazono, et al. 2004).

The microstructure of the manufactured preform using ARB method is the same as the precursor produced by powder metallurgy process. Closed-cell aluminum foams with about 40% porosity were successfully produced through the ARB process. This process has the potential to produce a large scale sandwich structure comprising a foam core and skin plates using conventional cladding techniques.

2.1.5. Laser Assisted Aluminum Foaming

Laser Assisted Foaming of Aluminum was proposed by Kathuria (Kathuria 2001b). The basic principle of laser assisted foaming is shown schematically in Figure 2.8. The precursor material with blowing agent, prepared by P/M process, is foamed by heating it up to its melting point by a high power laser beam irradiation. The uni-directional expansion of the foamable precursor material can be observed during the entire foaming process in the irradiation direction. The expansion in the other directions is relatively negligibly small.

Besides H_2 evolution and foaming, the shield gas Ar is an additional help for the formation of the porosity and may also become trapped inside the solidified foam. In the conventional thermal melting process, the average temperature gradient of the interface varies as the bulk temperature is lower. This is accompanied by a slow cooling rate and hence a long time for the stabilization of the pores to occur. However, in the case of laser process the average temperature gradient of the interface is much higher; thus, a faster cooling rate results in the pore stabilization. Figure 2.8 also illustrates how the processing speed could affect the cell morphology and the expansion ratio of the buildup foam. Increasing the processing speed changes the structure of the foam from 3 to 1 as seen presented in Figure 2.8.

The foamable Al-alloy sandwich samples fabricated according to the P/M procedure are used in this technique. Porous structures with relative densities of 0.33-0.39 and porosity of (61-67%) can be fabricated by using this method.

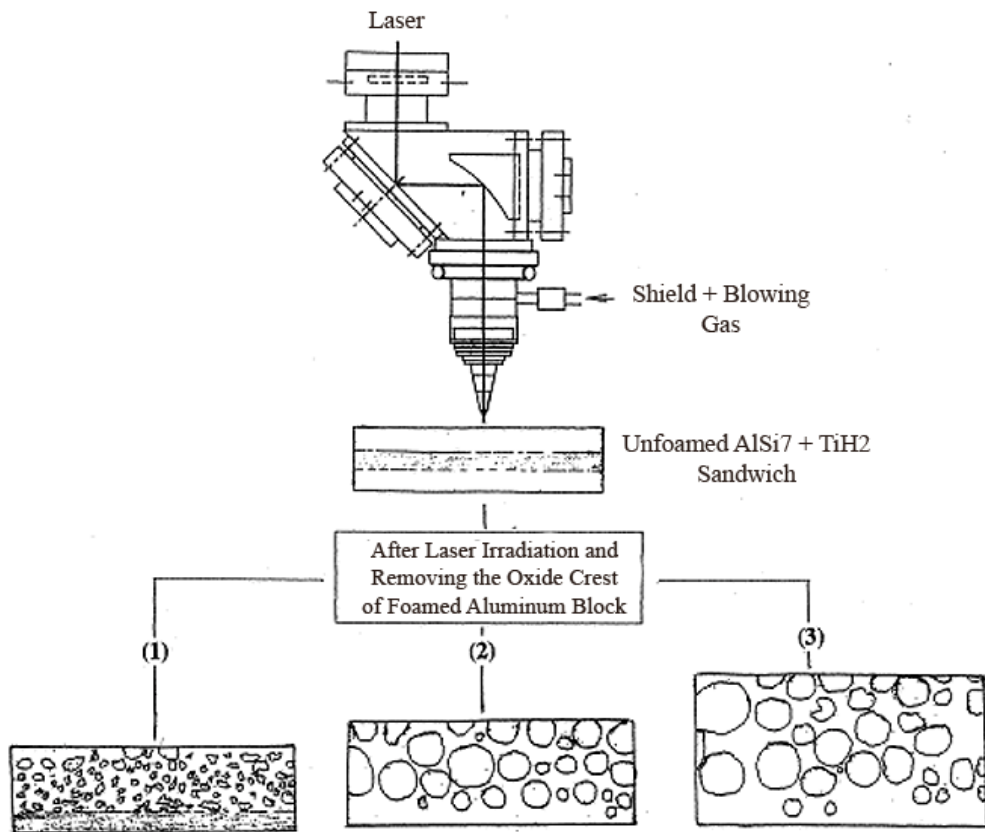


Figure 2.8. The block diagram of laser assisted AlSi7 foaming for three processing speeds, in decreasing order (1)>(2)>(3) (Source: Kathuria 2001b).

2.2. Applications of Closed-Cell Aluminum Foam

Properties of aluminum foams including high mechanical energy absorption per unit volume, high stress and stiffness to weight ratio, constancy over time, temperature and moisture range, good acoustic, vibration and electromagnetic insulation, recyclability make them usable materials in various applications. These application areas are also presented briefly in the product datasheets of the companies which commercially manufacture aluminum foam, like Alulight (Appendix B). Properties and the applications of the commercially available foams were also investigated deeply in academic researches like Alporas foam (Miyoshi, et al. 2000). Aluminum foams have become popular with the potential applications that can be listed as follows:

- Lightweight machine castings with improved sound and vibration damping
- Impact energy absorption components for cars, lifting and conveyor systems
- Stiff machine parts with significantly reduced weight

- Housings for electronic devices providing electromagnet and thermal shielding
- Permanent cores for castings, replacing sand cores
- Isotropic cores for sandwich panels and shells
- Fillings in hollow shapes to inhibit buckling
- Heat shields and encapsulates
- Floating structures at elevated temperatures and pressures
- Sound absorbers for difficult conditions

Aluminum Foams have relatively high collapse strength compared to polymeric foams and very long plateau stress and therefore they are identified as very efficient energy absorbers. The dynamic deformation of aluminum foam (high strain rate) starts at the impact face and continues through the foam until the densification strain (Gama, et al. 2001).

They are very suitable materials to be used in cashboxes of automobiles (Fig. 2.9 (a)) and in composite armor as the intermediate layer which increase the stress wave passage to backing composite plate (Gama, et al. 2001). The other important properties of metallic foams such as non-inflammability and good sound absorbability are the advantages for their use in transport industry. Other application areas of these materials include railway and ship constructions and space vehicle landing pads. The shape ability of the metallic foams is a key factor for replacing the honeycomb components in existing helicopter designs (Banhart 2001).

Because of the porous structure metal foams have higher loss factor than the ordinary bulk material for sound absorbing properties. This situation makes the sound wave partially entering and damped out while the other part is reflected back. Figure 2.10 shows the foam panel use under an elevated viaduct. These panels absorb the noise and therefore reduce the amount of noise produced in viaducts. Properties as fire resistance and no dangerous gas existence in case of a fire can further make the metal foams preferred but the sound insulating properties of metal foams are noted to be worse than existing polymer based foams or glass wool.

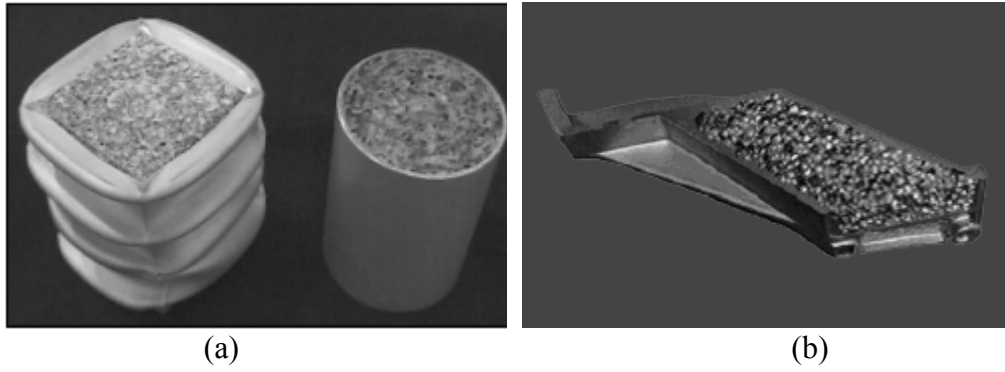


Figure 2.9. (a) Prototypes of foam filled tubes designed as energy absorbers, (b) Prototype of a part of an engine mount consisting of foam core and cast shell (Source: Banhart 2003).

Aluminum foam may be used in aerospace vehicles and all the other mechanisms where light-weight is an important factor. Aluminum foam cores are currently used in the tail booms of helicopters (Banhart 2001). They are also used in elevator systems where reduction of weight can make a significant effect while absorbing more energy than the ordinary bulk material in case of an impact. Naturally, aluminum foam can be used in sporting equipments such as helmet or bicycle frame with some composite materials. Balconies in buildings made of metal foam can be safer in case of an earthquake.



Figure 2.10. Foam layer used under an elevated viaduct as a noise insulator (Source: Miyoshi, et al. 2000).

Aluminum foam in sandwich structures (similar to one shown in Figure 2.11) are also used in lots of applications due to its high mechanical properties. Aluminum foam sandwiches were also tested for space applications (Schwingel, et al. 2007). Same material has also high potential to be used in construction of sea vehicles as it has lower density than the water besides it is a high strength metal panel.

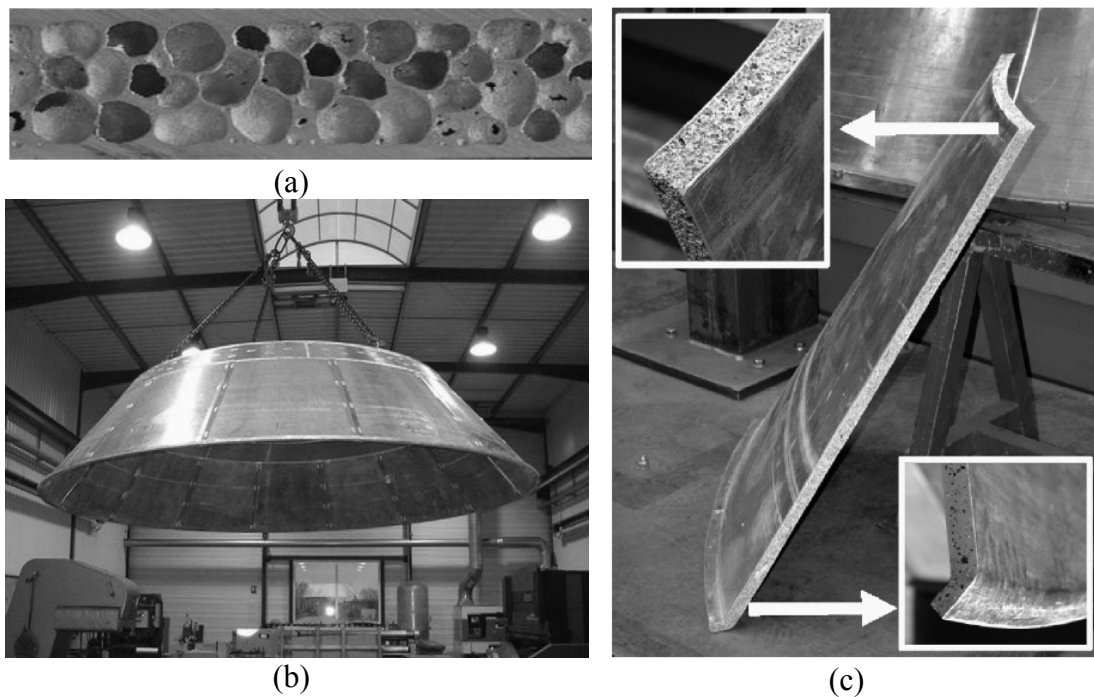


Figure 2.11. View of (a) aluminum foam sandwich panel, (b) assembled cone of a space craft made from sandwich panels, and (c) cone segment with detailed flange and upper edge (Source: Schwingel, et al. 2007).

CHAPTER 3

MECHANICAL PROPERTIES OF CLOSED-CELL ALUMINUM FOAMS

Closed-cell foam metals show characteristic compressive stress-strain curves; comprising three distinct deformation regions: linear elastic, collapse and densification as marked in Figure 3.1. In linear elastic region deformation is controlled by cell wall bending and/or stretching. The elastic region is followed by a highly localized collapse region occurring by cell edge buckling, crushing and tearing (Figure 3.2). The repetitive nature of the process of cell collapse and densification may lead to oscillations in stress values. The collapse region is characterized by a *collapse stress* and/or a *plateau stress* either with a constant value or increasing slightly with strain, as shown in Figure 3.1. At a critical strain, ϵ_d , cell walls start to touch each other and, as a result of this, the material densifies (densification region). The stress in this region increases sharply and approaches to the strength of the bulk aluminum metal. The high energy absorption behavior of aluminum foams under compressive loads is associated with low plateau stresses and long collapse regions, which makes them ideal materials for crash and blast protections where the kinetic energy is absorbed by the plastic collapse.

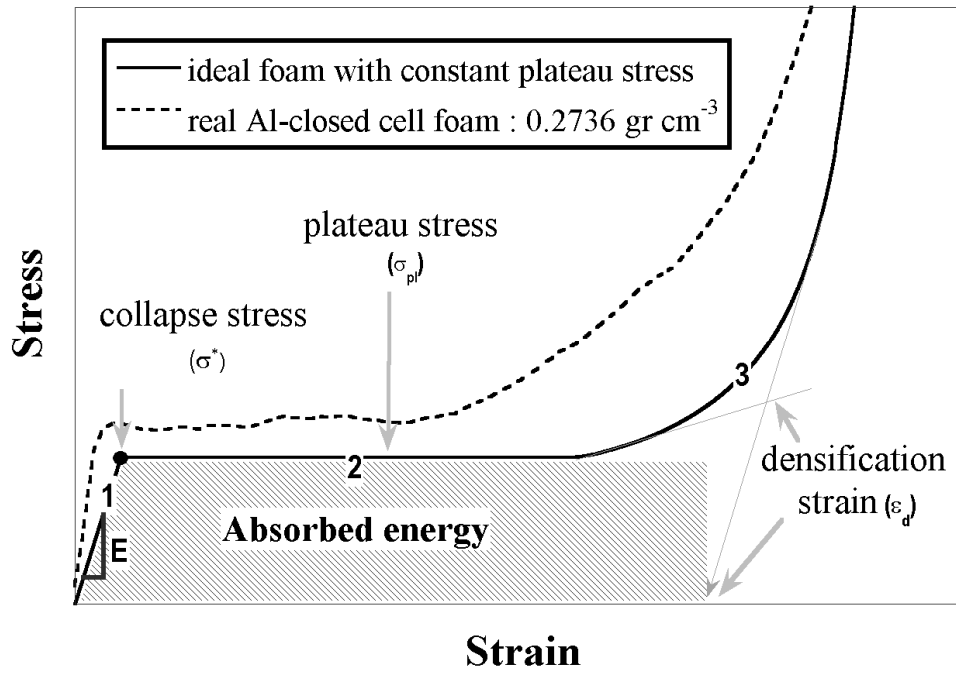


Figure 3.1. Compression stress-strain curves of ideal and real Al foam and mechanical property parameters.

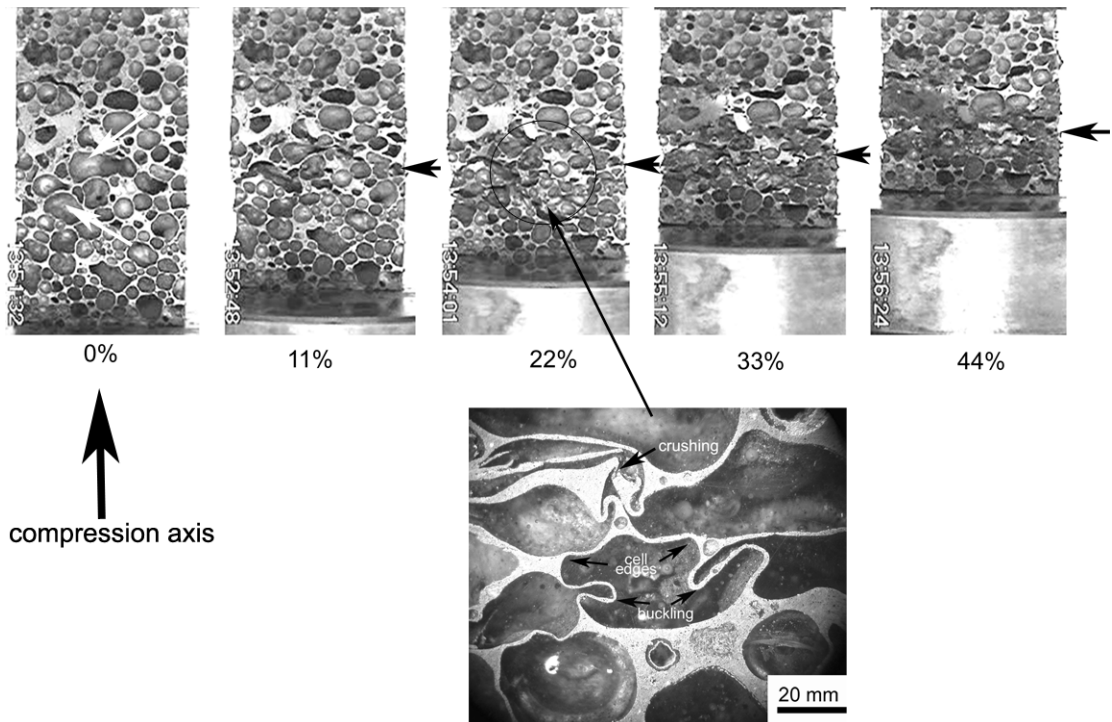


Figure 3.2. Compression localized deformation sequence of aluminum closed cell foam ($0.27 \text{ g}\cdot\text{cm}^{-3}$) at various strain and deformed foam cell structure in the localized deformed region.

The elastic moduli of ideal open and closed cell foams can be calculated from the cell edge bending deflection and the stretching of the planar cell faces and are given sequentially by the following relations (Gibson 2000)

$$\frac{E^*}{E_s} = c_1 \rho^2 \quad (3.1)$$

and

$$\frac{E^*}{E_s} = c_2 \rho^2 + c_3 \rho \approx c_4 \rho \quad (3.2)$$

where E^* and E_s are the elastic modulus of the foam and the cell wall material, respectively; c_1 , c_2 , c_3 and c_4 are the constants and ρ is the relative density which is,

$$\rho = \frac{\rho^*}{\rho_s} \quad (3.3)$$

where ρ^* and ρ_s are the densities of foam and cell wall material, respectively. For tetrakaidecahedral: $c_1 \sim 1$, $c_2 = c_3 \sim 0.32$. For low density foams, the value of c_4 is ~ 0.32 (Gibson 2000). Experimentally measured moduli values of commercial Al closed-cell foams were found lower than those predicted by Equation 3.2 particularly at relatively low foam densities (Figure 3.3 (a)). The moduli degradation is partly due to the thicker cell edges as compared to cell walls since the surface tension draws the liquid metal to the intersections during the foaming process. Including material distribution between cell walls and edges, Gibson and Ashby proposed the following equation for the modulus of the imperfect closed-cell foams (Gibson and Ashby 1997);

$$\frac{E^*}{E_s} \approx \phi^2 \rho^2 + (1 - \phi) \rho \quad (3.4)$$

where ϕ is the volume fraction of the solids contained on the plateau borders. The first term in Equation 3.4 is due to bending and the second membrane stretching. Equation 3.4 predicts elastic modulus of an open-cell foam, when $\phi = 1$, and closed cell foam,

when $\phi=0$. The values of ϕ can be approximated using the following relation developed for tetrakaidecahedral foam (Simone and Gibson 1998):

$$\phi = 1 - \frac{3t(l - 2w_p)^2 + 6t\sqrt{3}(l - (2/\sqrt{3})w_p)^2}{11.31 l^3 \rho} \quad (3.5)$$

where l , w_p , and t are the cell wall length, plateau border thickness and cell wall thickness, respectively.

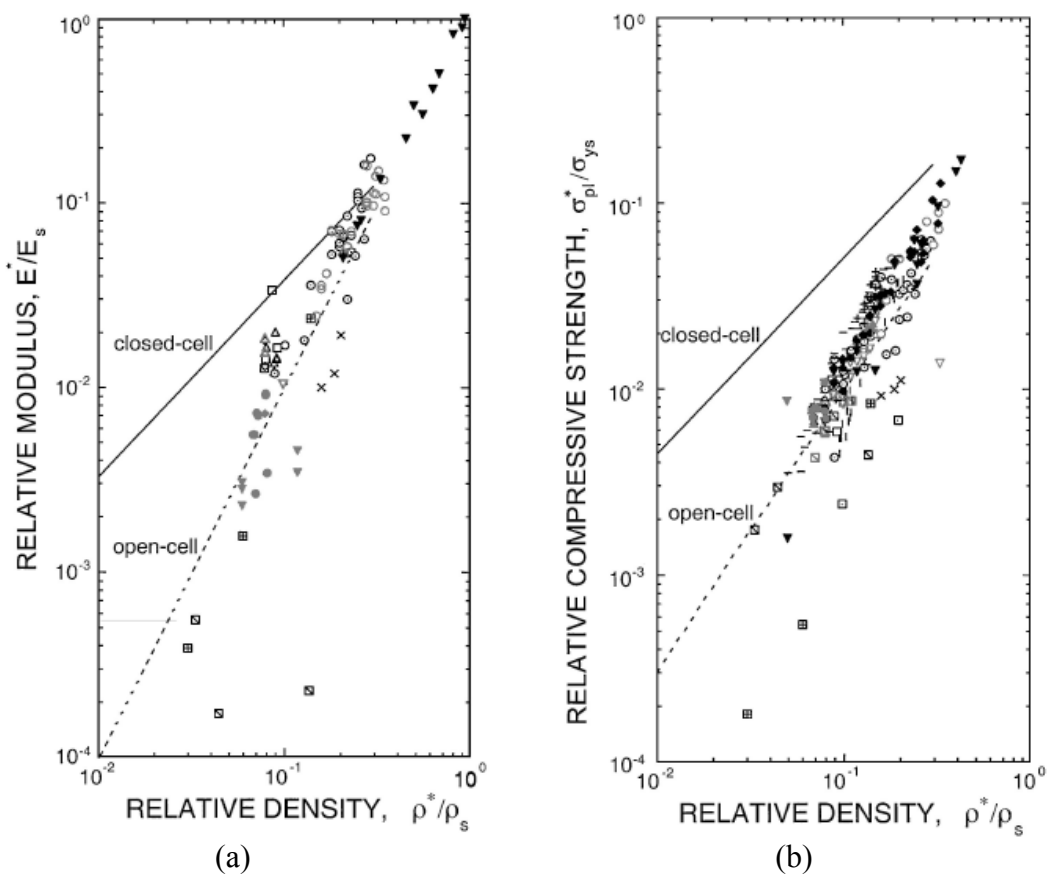


Figure 3.3. (a) Relative modulus vs. relative density of open and (b) relative compressive strength vs. relative density of open and closed cell foams; comparison with experimentally determined values (Source: Gibson 2000).

The collapse stress or plateau stress is an indication for the progression of the inelastic and inhomogeneous deformation and determines the amount and the efficiency of plastic energy absorption. For ideal open and closed-cell foams, the plastic collapse is expected to occur by the plastic hinges at the bent cell edges and cell wall stretching

in a direction perpendicular to compression axis. The plateau stresses for ideal open-cell and tetrakaidecahedra closed-cell foams (Simone and Gibson 1998) are given sequentially by the following relations,

$$\frac{\sigma_{pl}}{\sigma_{ys}} = 0.3\rho^{3/2} \quad (3.6)$$

and

$$\frac{\sigma_{pl}}{\sigma_{ys}} = 0.33\rho^2 + 0.44\rho \quad (3.7)$$

where σ_{pl} and σ_{ys} are the plateau stress and yield strength of the cell wall material respectively. By including material distribution between cell edges and cell walls following relation is proposed for a closed-cell foam plateau stress (Gibson and Ashby 1997),

$$\frac{\sigma_{pl}}{\sigma_{ys}} = 0.3(\phi\rho)^{3/2} + (1-\phi)\rho \quad (3.8)$$

The first term in Equation 3.8 correspond to plastic hinge formation and the second to the membrane stretching of the cell walls. Again, $\phi=1$ and $\phi=0$ represent the collapse stresses of open-cell and closed-cell foam, respectively.

A high value of ϕ is generally found in commercially available Al closed-cell foams. The values of ϕ changes with density and were reported 0.65 and 0.85 for Alcan foams of 0.15 and 0.32 g.cm⁻³, respectively (Valente, et al. 2000) and 0.57, 0.7 and 0.6 for Alulight, Alporas and Alcan foams of 0.37 g.cm⁻³, respectively (Elmoutaouakkil, et al. 2002). High values of ϕ , together with imperfections such as curved, wrinkled and missing cell walls, voids on the cell edges and cell walls and non-uniform density degrades the plateau stresses of commercial Al closed-cell foams to the levels of those of open-cell foams (Figure 3.3(b)). Alporas foams show monomodal cell size distribution and hence exhibit the most homogeneous cell size distribution; whereas, Alulight and Alcan foams show bimodal cell size distribution (Elmoutaouakkil, et al. 2002). Although Alulight and Alporas foams' cells are nearly spherical, the cells are mostly elongated in Alcan foams due to shear forces acted during the transporting of the

liquid foam on the conveyer belt. The minimum cell wall thicknesses that basically support the cell edges and cell walls depend on the size and content of the ceramic particles and alloying elements and found to range between 40 and 100 μm in Alulight foams (Banhart 2006).

The densification strain (Figure 3.1) is generally defined as the strain at which the slope of the tangent of stress-strain curve in densification region is equal to that of the elastic regime, while some reserachers considered the intersection of the tangents to the stress plateau regime and densification regime as the densification strain (Chan and Xie 2003, Paul and Ramamurty 2000). The densification strain determines the extent of energy absorption behaviour and is given as,

$$\varepsilon_d = 1 - 1.4 \rho \quad (3.9)$$

The densification strains of commercial Al closed cell foams range between 0.4 and 0.9 with the density range of 0.07-0.3 g/cm^3 (Ashby, et al. 2000).

The foam section under the indenter crushes as in the compression and the indenter tears the foam around the perimeter (Figures 3.4 (a) and (b)). Considering the indentation crushing load is the sum of the compression crushing load and the shearing load at the perimeter, the following relation is given for the indentation strength of Al closed cell foams (Andrews, et al. 2001),

$$\frac{\sigma_{\text{ind}}}{\sigma_{\text{pl}}} = 1 + k \left(\frac{\tau_{\text{pl}}}{\sigma_{\text{pl}}} \right) \frac{d}{D} \quad (3.10)$$

where τ_{pl} , k , d and D are the shear plateau stress, a constant (~ 4), cell diameter of the foam and diameter of the indenter, respectively. As the indenter size increases, the indentation strength decreases until indentation strength reaches the plateau stress and therefore metal foams show indentation strengths slightly higher than uniaxial collapse strength (Andrews, et al. 2001, Kumar, et al. 2003).

The foam mechanical properties are also size dependent: the bulk modulus, plateau stresses-reached above the specimen size/cell size aspect ratios of 5-6 (Andrews, et al. 2001, Onck, et al. 2001, Rakow and Waas 2005).

Aluminum foams absorb relatively high amount of deformation energy associated with the low plateau stresses and large densification strains. The energy-absorption-diagrams are widely used to optimize the foam density choice for the energy absorption applications (Maiti, et al. 1984). The area under the stress-strain curves gives the absorbed energy per unit volume,

$$SAE_v = \int_0^{\varepsilon} \sigma(\varepsilon) d\varepsilon \quad (3.11)$$

The maximum useful energy absorption normalized with the modulus of foamed metal up to densification is given for closed-cell foam as

$$\frac{SAE_{max,v}}{E_s} \approx \frac{\sigma_D}{E_s} [1 - (3.1(\frac{\sigma_D}{E_s})^{2/3})] \quad (3.12)$$

where σ_D is the stress corresponding to the shoulder in stress-energy absorption curve constructed from stress-strain curve (Figures 3.5 (a) and (b)).

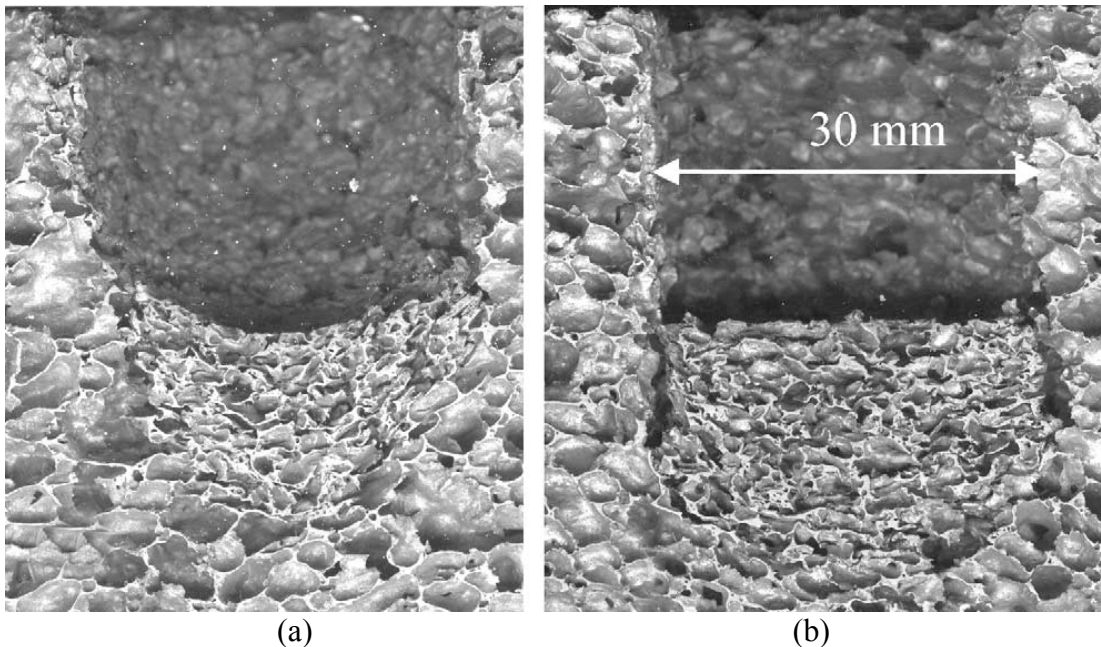


Figure 3.4. Deformed cross-sections of Al foams using (a) spherical and (b) flat-end indenters (Source: Kumar, et al. 2003).

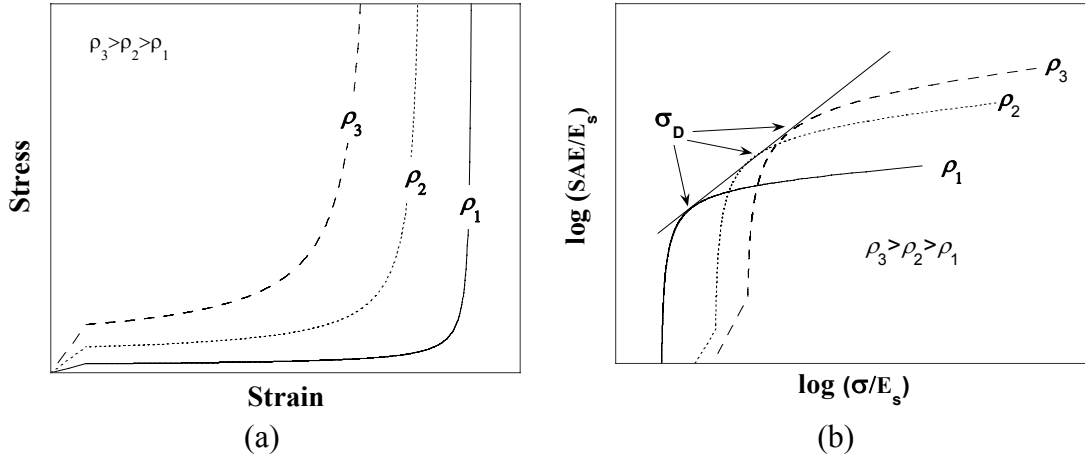


Figure 3.5. Schematic of foams (a) stress-strain curve of various relative densities and (b) corresponding normalized specific absorbed energy vs. normalized stress curves.

3.1. Crash Energy Absorption

The crash energy absorbing structures have been generally constructed in tubular/columnar forms of materials that absorb the deformation energy nearly at a constant load. The constant load energy absorption results from the progressive folding mechanism of thin walls, which was first analytically formulated by Alexander in 1960 (Alexander 1960). The area under the load-displacement curve of a crushable element of tubular structure with a total length of l is shown in Figure 3.6 (a) gives the total absorbed energy (E) until about a displacement of δ . The mean crushing load (P_m) and the specific absorbed energy per unit mass (SAE_m) the capability of a structure to absorb the deformation energy is formulated per unit mass and volume as,

$$P_m = \frac{\int_0^{\delta} P d\delta}{\delta} \quad (3.13)$$

and

$$SAE_m = \frac{\int_0^{\delta} P d\delta}{m_t} \quad (3.14)$$

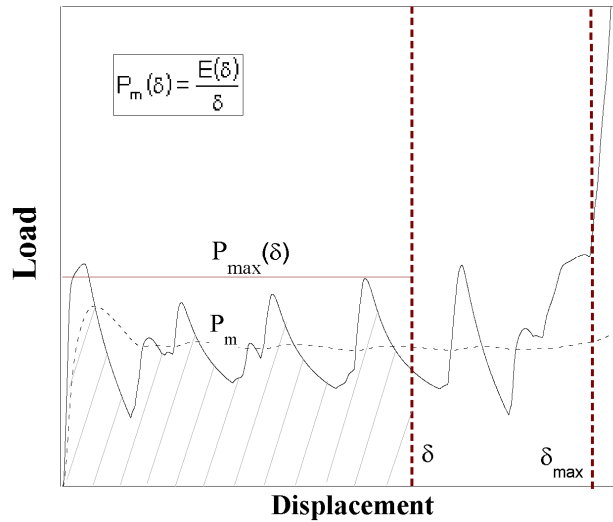
where P , δ and m_t are the load, displacement and the total mass of the deformation element. The efficiency of energy absorption is checked by the total efficiency (T_E) and crush force efficiency (A_E). The stroke efficiency is defined as the ratio between the point at which the total efficiency has its maximum value (δ_{max}) and total length (l) of the crushing element,

$$S_E = \frac{\delta_{max}}{l} \quad (3.15)$$

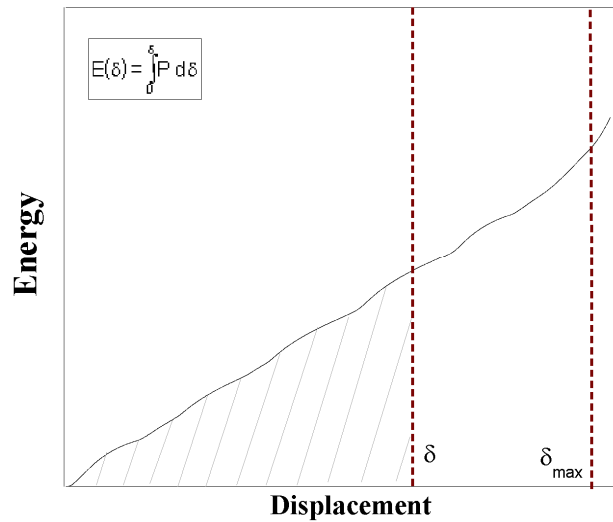
The efficiency terms are directly related to the deformation capacity (D_C), which is the displacement divided by the initial length of the element:

$$D_C = \frac{\delta}{l} \quad (3.16)$$

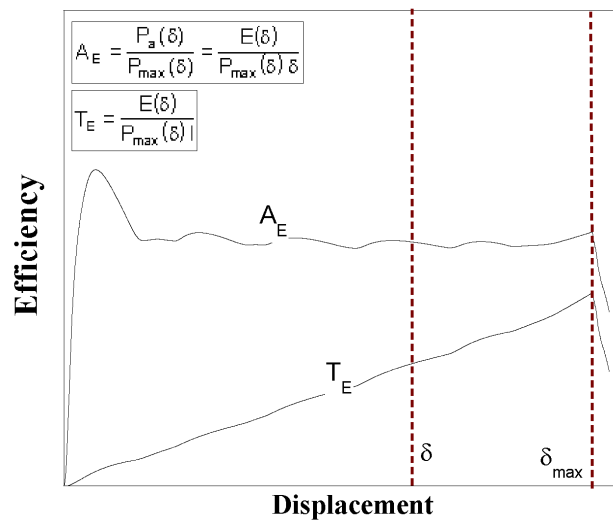
Comparison of SAEs of tubes with those of foams on volume and mass basis gives a ratio of about 3 between tube and foam, showing that tubes are energetically more efficient than foams. When aluminum and steel metal tubes are filled with light weight core materials such as Al closed cell foams, there exists an *interaction effect* between tube wall and foam filler (Guden, et al. 2006, Hanssen, et al. 2000, Santosa and Wierzbicki 1998, Seitzberger, et al. 1997). The crushing loads of foam filled tubes are therefore found to be higher than the sum of the crushing loads of foam (alone) and tube (alone) mainly due to this effect as shown in Figure 3.7. The interaction may be partly due to the resistance of filler to the inward and/or outward folding of tube wall and partly due to the interfacial friction stress between foam and tube wall. The use of adhesive can contribute to the specific energy absorption of tube by two mechanisms, namely, increased load transfer from tube wall to the foam core and peeling of the adhesive. The latter mechanism occurs mainly due to the outward folding of the tube.



(a)



(b)



(c)

Figure 3.6. (a) Load-displacement, (b) energy-displacement and (c) crush force and total efficiency -displacement curves of a crush element (Source: Fuganti, et al. 2000).

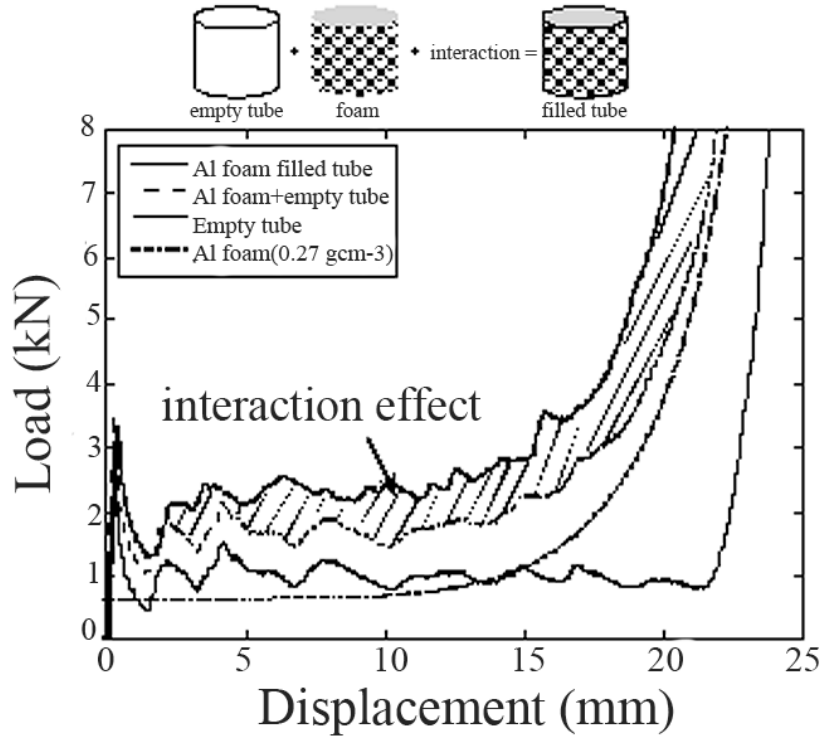


Figure 3.7. Interaction effect in Al foam (0.27 g cm-3) filled tube.

The filler deformation was divided in two parts: a densified region at mid sections of the tube and extremely densified region next to the tube folds. The extremely deformed region (above the densification strain of the foam filler) shown in Figure 3.8 (a) was proposed to be the main factor leading to interaction effect in filled tubes (Song, et al. 2005). The foam filling generally increases the number of folds formed and decreases the fold lengths in the metal tubes as depicted in Figure 3.8 (b). Further, the tendency for the axisymmetric (concertina) mode of deformation increased with foam filling due to the thickening effect of foam filling. Hanssen *et al.* (Hanssen, et al. 1999, Hanssen, et al. 2000) developed an equation for the average crushing load of foam filled (P_{af}) columns by including contributions of the average crushing load of empty tube (P_{ae}), foam plateau stress (σ_{pl}) and interaction effect. The equation was found to be well agreed with experimental results and is given as

$$P_{af} = P_{ae} + \sigma_{pl} b^2 + C_{avg} \sqrt{\sigma_{pl} \sigma_y} bt \quad (3.17)$$

where C_{avg} , σ_y , b and t are the dimensionless constant which is directly related to the interaction effect, yield strength of the tube material and tube width and thickness,

respectively. The second term of the right hand side of the Equation 3.17 accounts for the axial compression of the foam and the last term for the interaction effect. Santosa *et al.* (Santosa, et al. 2000b) noted that the bonding between filler and tube wall increased the average crushing load of filled tube over the unbounded filled tube when appropriate tube geometry and foam density were chosen. Based on finite element modeling results the same authors proposed the following equation for the average crushing load of foam-filled square tubes of length b ,

$$P_{af} = P_{ae} + C \sigma_{pl} b^2 \quad (3.18)$$

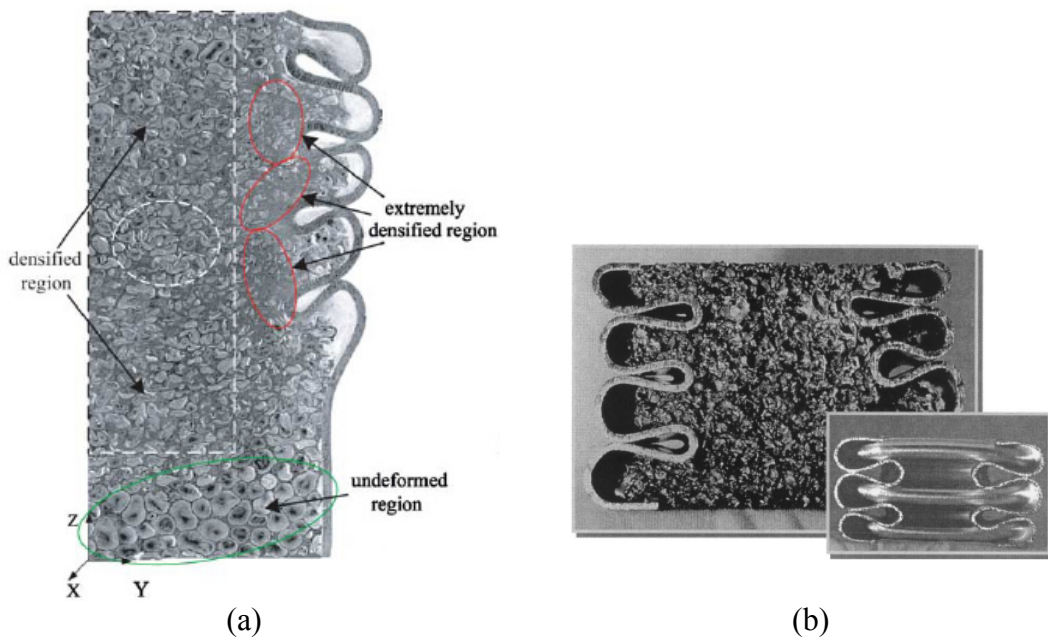


Figure 3.8. View of (a) three deformation region in an aluminum foam filler: undeformed, densified and extremely densified regions (Source: Song, et al. 2005), and (b) deformation of aluminum foam filled vs. empty tube (Source: Hanssen, et al. 2001).

The constant C in Equation 3.18 is considered *strengthening coefficient* of foam filling. The values of C for foam-filled single tubes were shown to be 1.8 and 2.8 for the unbounded and bounded cases, respectively (Santosa, et al. 2000b). The partially foam filling of length of $L-H$ (where L is the length of the steel section and H is half of the fold length) showed higher SAE values than full foam filling in single and double hat sections (Wang, et al. 2005). Bitubal arrangements comprising an outer and an inner

profile and foam filler might be preferable to monotubal arrangements (Seitzberger, et al. 2000).

Al foams have potentials to be used in automobiles as crash energy-absorbing filling materials in various places. There are two main groups of energy absorbers used in automobiles: (a) for relatively low impact energies such as bumpers for frontal collision and for relatively large impact energies such as side beams (B-pillars) to avoid severe intrusion in the passenger compartment. The foam-filled sections may also be used in the A-pillar and roof frame structures to reduce the roof crushing in roll-over accident. Bumpers avoid the chassis plastic deformation up to 3-5km/h and the introduction of crash boxes placed between bumper and chassis (Figure 3.9(a)) increase this limit up to 15 km/h (Fuganti, et al. 2000). The function of crash boxes is to absorb the crash energy in controllable manner to reduce the damage to the passenger cell. Brain damage can easily occur above the decelerations of 20g, therefore in designing with crash boxes the resultant force should be below 20g (Ramakrishna and Hamada 1998). The deceleration curve of a medium class car colliding with a concrete wall at a speed of 35 mph is shown in Figure 3.9 (b). In region A the deformation of bumper and front panel, in region B the deformation of front section of the car with very large displacements and in region 3 the deformation of passenger cell occur. The function of crash boxes is to reduce the damage at low speeds and protect the passenger cell at high speed collisions. The crash boxes are usually made from square aluminum extrusions (Figure 3.10) or welded steel sections. The foam filling increases the energy absorbing capability of the crash boxes and therefore (a) provides weight savings, (b) reduce the length of the crash box and (c) volume of the crash boxes (Fuganti, et al. 2000). However, in the filling tubes and boxes with Al foam there exist a critical total filled tube mass and the corresponding critical foam density above which the use of foam filling became more efficient than thickening of empty tube (Guden, et al. 2006, Santosa and Wierzbicki 1998). The foam filling is more efficient if the following equation is satisfied:

$$\frac{SAE_{ft}}{SAE_e} \geq 1 \quad (3.19)$$

where subscripts f_t and e refer to the filled-tube and empty tube. The critical foam filler density decreases with increasing tube inner radius or decreasing thickness of the tube, increasing tube metal density and strength and increasing with interaction effect.

Foam filling may also result in chance deformation mode from progressive folding to the lower energy absorbing deformation model of global buckling at high foam density fillers (Seitzberger, et al. 1997).

Foam filling changes the crushing mode of empty beams from localized folding (Figure 3.10(a)) to multiple propagating folds (Fig. 3.10 (b)) (Chen 2001, Santosa, et al. 2000a, Santosa, et al. 2001). It provides higher bending resistance and momentum by retarding the inward fold formation and hence increases the crush energy absorption. Partial foam filling of beams provides significant weight savings without reducing the energy absorption. Effective foam length (L_{eff}) which would give foam strengthening effect in beam was predicted using following equation (Santosa, et al. 2000a):

$$L_{eff} = L\left(\frac{1 - \eta}{\eta}\right) - 4H \quad (3.20)$$

where, L , η and H are the beam length, strengthening ratio of the maximum bending of the fully foam filled top empty beam and the fold length, respectively.

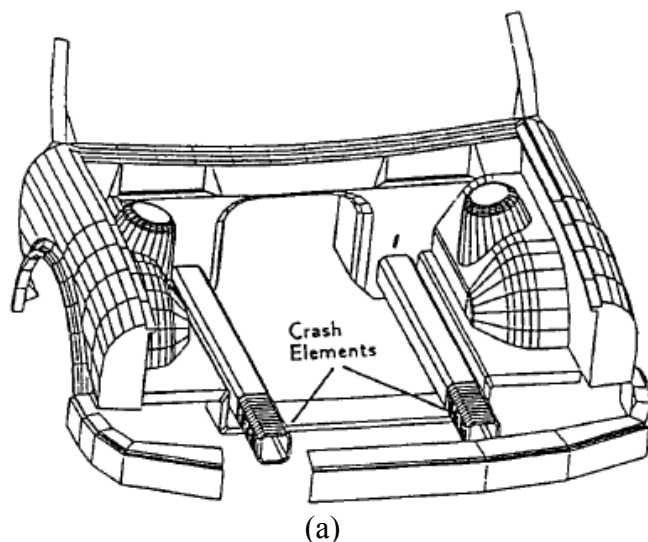
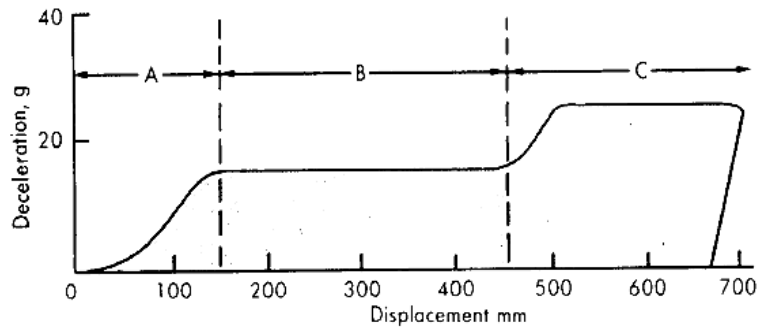


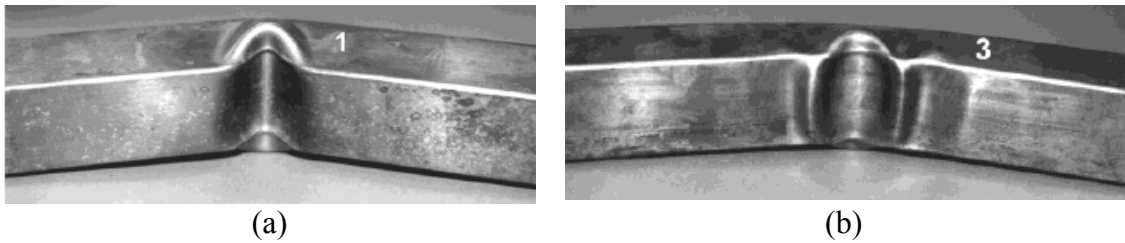
Figure 3.9. (a) The use of crash-boxes in an automobile and (b) ideal deceleration curve of a medium class car (Source: Ramakrishna and Hamada 1998).

(cont. on next page)



(b)

Figure 3.9. (cont.)



(a)

(b)

Figure 3.10. Bending deformation pattern of (a) empty and (b) aluminum foam-filled stainless steel beams (Source: Santosa, et al. 2000a).

The bending deflections of Al foam plate and Al foam sandwich plate were compared with aluminum sheet material of the same weight. The deflection was shown to decrease by a factor 5 for Al foam plate and more for Al sandwich structures as compared with Al sheets (Figure 3.11). Aluminum foam sandwich (AFS) parts may be used in the construction of body panels, bonnets, boot lids and sliding roofs. The German manufacturer Karmann, introduced the concept of AFS parts, produces shaped sandwich panels which replaced the stamped steel sheets. The application reduced the weight by 25% and increased the stiffness by 700% (Banhart 2001).

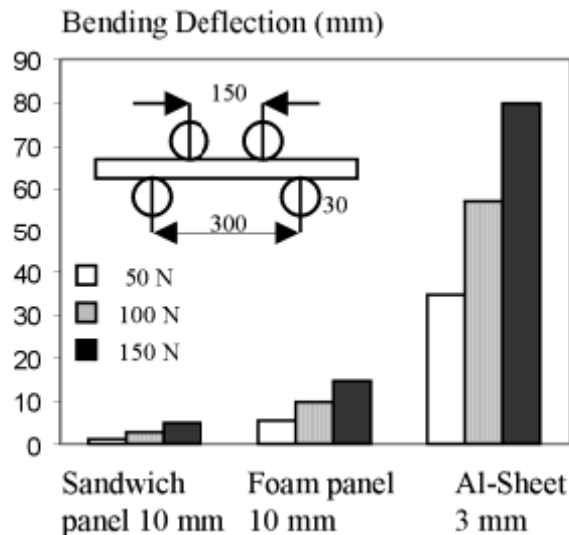


Figure 3.11. Comparison of bending deflection of aluminum foam panels and sandwiches with the same weight aluminum sheets (Source: Korner and Singer 2000).

3.2. Sound Absorption

The sound absorption of closed-cell Al alloy foams increases with decreasing foam relative density. And the hole-drilling and rolling/compression of the foams with an appropriate air-gap backing improve the sound absorption coefficients by increasing peak sound absorption coefficients and decreasing the corresponding peak frequencies (Han, et al. 1998, Lu, et al. 1999). Hole-drilling is more effective in improving the sound absorption than rolling and compression. The rolled foam samples showed sound absorption coefficients and peak sound absorption frequencies comparable with that of glass wool as shown in Figure 3.12 (Miyoshi, et al. 2000). The improved foam sound absorption behavior was attributed to the viscous flow across the small cracks, which resulted in passage ways for the in-and-out movement of air. The open-cell Al foams show higher sound absorption coefficients than closed-cell Al foam within 100-5000 Hz frequency range.

Sound absorption in metallic foams is mainly due to (a) viscous losses as the pressure wave pumps air in and out of cavities in the absorber, (b) thermal losses due to heat transfer to the matrix and (c) Helmholtz-type resonators (Lu, et al. 1999). The Helmholtz-type resonators in rigid frame cellular solids operate at relatively high frequencies (20 KHz). The viscous effect increases with increasing frequency and

decreasing pore size. The viscous effect is comparable with thermal effect for relatively thin samples (1 cm). The small holes connecting the large pores results in considerable sound wave dissipation via friction. The increasing sound absorption capacity of the hole-drilled foam samples are therefore attributed to the viscous flow across the small holes. The effect is likely to be more pronounced in small size hole-drilled foam samples since the smaller drill size results in smaller holes connecting the larger pores (Lu, et al. 1999). While compression and rolling can be easily applied to relatively thin foam plates, hole drilling is more appropriate for relatively thick samples. In applications involving the foam filling of tubular structures, a rigid-wall backing is always present at the back of the foam filler. Therefore, inserting air-gap at the back of the foam plate may have no practical applications when the foam is used as filler. It should also be noted that the sound absorption coefficient is a function of the sample thickness.

Aluminum foams are used to absorb the vehicles sound in elevated viaduct and subway tunnel as sound absorbing lining with a backing plate to reduce the noise for the neighboring residents and to damp the shock waves created by the trains in Japan. It is also used as an impact cushion for railway rolling stock (Miyoshi, et al. 2000).

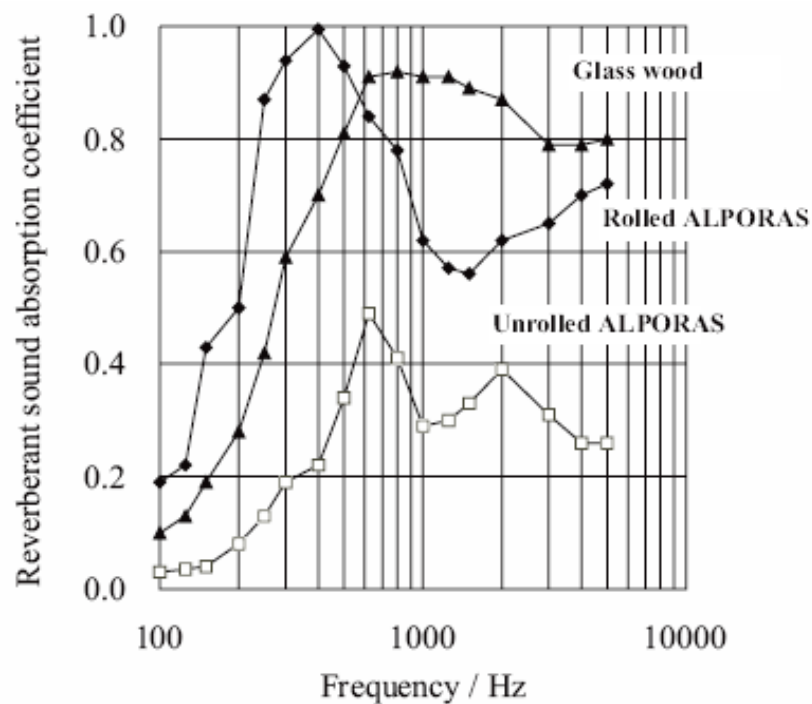


Figure 3.12. Sound absorption coefficient of Alporas foam of relative density ~ 0.09 (Source: Miyoshi, et al. 2000).

3.3. High Strain Rate Mechanical Properties

The effect of strain rate on the collapse behavior of the cellular materials was also previously investigated. Deshpande and Fleck (Deshpande and Fleck 2000) found strain rate insensitive plateau stresses for Alulight closed-cell and Duocell open-cell Al foams up to 5000 s^{-1} . Similar strain rate insensitive plateau stresses were also reported for Alulight closed-cell Al-Si (Peroni, et al. 2008) and 6061-Al foams (Hall, et al. 2000). On the other hand; Mukai *et al.* (Mukai, et al. 1999, Mukai, et al. 2006) and Paul and Ramamurty (Paul and Ramamurty 2000) found apparent strain sensitive plateau stresses of Alporas Al closed-cell foams. The strain rate sensitive crushing stresses of cellular materials may be attributed to the strain rate sensitivity of the material from which the cellular structure is made, the micro-inertial effects, shock wave propagation and the compressed air pressure within the cells (Zhao, et al. 2005). Calculations for adiabatic compression have shown that the compressed air pressure in dynamic loading contributed less than 1.5% of the quasi-static strength of closed-cell aluminum foams (Deshpande and Fleck 2000). The calculation used in (Deshpande and Fleck 2000) was repeated for the tested Metallic Hollow Sphere (MHS) structure with a densification strain of 0.71. Similar contribution of the compressed air was found for the tested MHS structure. At increasing deformation velocities, excess of 50 m s^{-1} , shock wave propagation was shown to have a significant contribution to the strength of the cellular metallic structures (Reid and Peng 1997). Micro-inertial effects arise due to lateral inertia which results in increase of the buckling loads at increasing strain rates (Calladine and English 1984). The columnar structures are mainly classified in two groups depending on their response to micro-inertia: Type I and Type II structures (Calladine and English 1984, Su, et al. 1995a, Su, et al. 1995b). Type I structures are characterized with a flat-topped quasi-static stress strain curves (the stress-strain curve is flat after yielding), showing limited or no strength enhancement at increasing deformation velocities. Type II structures are characterized with a strong softening after yielding at quasi-static strain rates and the lateral inertia forces lead to increased bending forces at increasing deformation velocities. The increased deformation forces at increasing strain rates in the compression of aluminum honeycomb structures through out of plane (Zhao, et al. 2005), metallic columnar structures (Langseth and Hopperstad 1996), aluminum foams (Lee, et al. 2006, Paul and Ramamurty 2000, Zhao, et al. 2005,

Zhao, et al. 2006) and balsa wood in the axial direction (Reid and Peng 1997, Tagarielli, et al. 2008) were reported to result from the micro-inertial effects.

CHAPTER 4

FOAM STABILITY OF CLOSED CELL ALUMINUM FOAMS

In foaming of aluminum the metal should be in the liquid state; otherwise foaming process cannot take place due to the high viscosity. Just after the expansion of the liquid metal starts, several different mechanisms become operative quickly in the molten metal, and change the cell structure of the foam continuously. The expansion is a function of several parameters such as the rate of gas evolution, the viscosity and microstructure of the melt, the stability is a different phenomenon. It emphasizes cell structures of the stable foam, which do not change over time. This means that, for a period of time, the liquid foam is stable. The basic principles of the liquid metal stabilization will be analyzed with the mechanisms of liquid foam stability in different foaming processes in this chapter.

To understand the foam stability, the forces acting on the liquid foam within the foaming process should be known. The forces are categorized in two groups as driving forces and tensile force (Asavavisithchai and Kennedy 2006c, Banhart 2006, Kaptay 2004). Driving forces consist of gravitational forces and capillary forces while the tensile force is formed from atmospheric pressure and the pressure of the blowing gas. These forces are effective on the stability of the liquid foams and lead to several different events to occur in the liquid foam while they change with time.

The flow of liquid metal from cell walls to the cell edges is known as drainage. Drainage leads to thinner cell walls, thicker cell edges and a dense layer at the bottom of the foam (Figure 4.1). It occurs by the action of gravitational force and capillary forces. Another problem in foaming process is made up from the diffusion of the gases from smaller to larger bubbles causing coarsening of the cells in foam structure (Banhart 2006). The rupture (coalescence) is the disappearance of cell walls during the foaming process due to sudden instability of the pressure (Weaire and Hutzler 1999). These events happen simultaneously in liquid foam and interrelated. Under capillary forces,

the liquid metal flows from cell walls to edges and results in cell wall thinning and under tensional forces the cell walls rupture, which overall reduce the stability of foams.



Figure 4.1. Cross-section of aluminum foam showing thin cell walls, thick cell edges and dense metal layer at the bottom section.

Gergely and Clyne (Gergely and Clyne 2004) modeled the drainage in the standing foams of relatively thick cell faces. The model emphasized that the small initial cell size and high initial porosity level inhibited the drainage; the attention should be given to the rapid foaming processes and cell wall stabilization using a foaming agent that would oxidize the cell faces.

X-ray tomography of 2D and 3D characterization of Alulight (IFAM), Alporas and Alcan foams were performed, for the same density of foams, by Elmoutaouakkil et. al. (Elmoutaouakkil, et al. 2002). Results have shown that Alporas foam exhibits more homogeneous cell size distribution with the highest value of fraction of metal accumulated at the cell edges (ϕ). The cell size distribution was further shown to be monomodal for Alporas and bimodal for Alulight and Alcan foams. The values of ϕ changes with the foam density and the typical values were given as 0.57, 0.7 and 0.6 for Alulight, Alporas and Alcan foams of 0.37 g.cm^{-3} densities, respectively. It has been further shown that although the cells in Alulight and Alporas foams are nearby

spherical, in Alcan, they are mostly elongated due to shear forces acting during the transport of the liquid foam on the conveyer belt.

Aluminum closed cell foam production is not a new process: two relating patents of aluminum foam production appeared in 1940's and 1960's. (Allen, et al. 1963, Sosnick 1948). The interest on these materials has recently grown, as the novel structural to functional applications of these material were exploited.

Aqueous liquid foams and liquid metal foams show resemblances. Aqueous liquid foams are primarily stabilized by either surfactants or solid particles or both (Wubben and Odenbach 2004). However, in liquid metal foams only atoms or at most complexes/clusters made of several atoms can be surface active (Kaptay 2004). Therefore, the surfactants cannot be used to stabilize metal foams. However, liquid metal foams can be stabilized with particles. The solid particles accumulate at gas/liquid interface and prevent the bubble-bursting and therefore stabilize the liquid foam (Wubben and Odenbach 2004). Commonly used solid particles include SiC, Al₂O₃, MgO and alloying elements (Babcsan, et al. 2004, Leitmeyer, et al. 2002, Wang and Shi 2003). The particles in liquid can effectively stabilize the foam, if they are partially wetted by the liquid metal (Figure 4.2). The non-wetted particle will be found in the gas phase, while fully wetted particles in the liquid. Partially wetted particles sit at gas/liquid interface increase the surface viscosity of the cell wall, leading to reductions in the amount of liquid metal flow from cell faces to the cell edges.

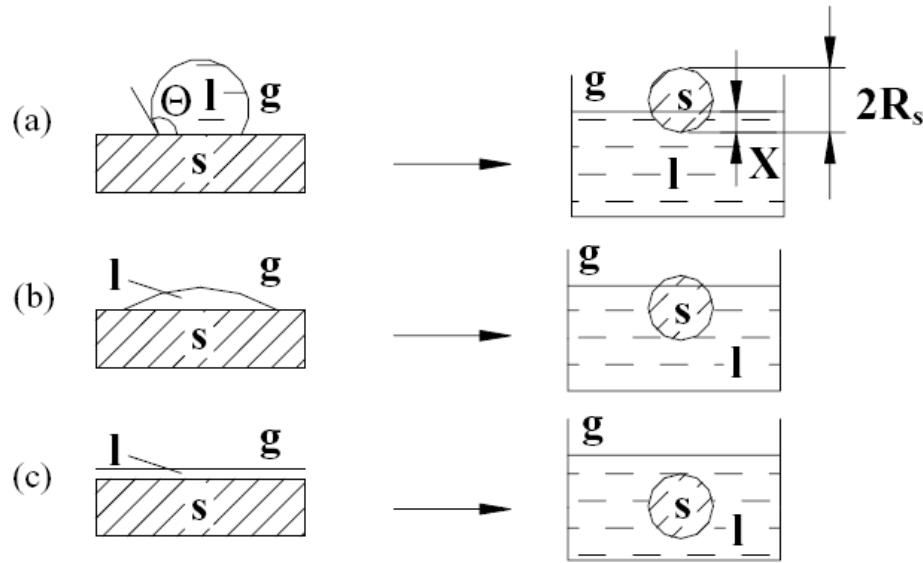


Figure 4.2. Schematic view of (a) non-wetted particle, (b) partially wetted particle and (c) fully-wetted particle (Source: Kaptay 2004).

Deqing and Ziyuan (Wang and Shi 2003) investigated the effect of SiC (1, 7, 14 and 20 μm) and Al_2O_3 (3.5, 5 and 10 μm) particles, foaming temperature and gas flow rate on the cell sizes, cell wall thicknesses of Al foams in Alcan foam processing route. Cell sizes and cell wall thicknesses increased with increasing particle size and particle volume fractions, while the cell wall thicknesses decreased with increasing foaming temperature. The cell wall thicknesses varied between 45 to 80 μm depending on the particle size and volume fraction. The cell size increased, while cell wall thickness decreased with increasing gas flow rates. It was noted in the same study that, the presence of particles in liquid foam increased the bulk viscosity of the composite melt; hence, reduced the liquid flow from cell faces to cell edges. The particles at liquid/gas interface further reduced the capillary pressure difference between cell edge and cell wall. Both were noted to be effective on the stability of the composite foam. Low concentration of large particles could not form an adequate coverage of cell surface hence lead to unstable foam, while high concentration of small particles increase the viscosity of the melt significantly so that the air injection could not foam the composite melt.

Yang and Nakae (Yang and Nakae 2000) investigated the foaming behavior of liquid A356 Alloy with the addition of 0.5 to 4wt% TiH_2 foaming additions and at various temperatures. The liquid viscosity was adjusted by Al powder addition.

Increasing the amount of foaming agent addition increased the porosity until about 1wt% TiH₂, while foaming efficiency decreased with increasing foaming agent. The optimum foaming agent addition was determined as 1wt% by considering cell uniformity and foaming efficiency. At low foaming temperatures, less than 630 °C, sufficient gas release from foaming did not occur while foaming at temperatures above 650 °C, resulted in rapid bubble coalescence. The optimum foaming temperature was given in the range of 630-650 °C for studied melt alloy.

Banhart (Banhart 2006) has recently reviewed stabilization of Al foams in various processes. It was shown by comparison of various Al alloys that the critical cell wall thickness (cell wall thickness just before the rupture of the film or the cell wall thickness that carry the foam structure) was thickest in pure Al foams and reduced with Si and Cu addition. It was further shown using the following equations that the growth was accompanied by film rupture in foaming process.

$$D \propto \sqrt[3]{\rho^{-1} - 1} \quad (\text{for coalescence-free growth}) \quad (4.1)$$

$$D \propto 6d_{\text{crit}}(\rho^{-1} - 1) \quad (\text{growth with rupture ad } d_{\text{crit}}) \quad (4.2)$$

It shows that when bubbles are blown in a fixed volume size D of the fixed number of bubbles increases. If a critical cell wall thickness exists for the foam (Figure 4.3), below which a film ruptures, the number of bubbles will reduce like the mean pore diameter grow more quickly (Figure 4.4). It was concluded that the stabilization of foams was accompanied by viscosity enhancing effects and the surface activity of particles. Effect of the oxide content of the powder used for making precursors on the maximum expansion value of pure Al foams for six different powder sources is shown in Figure 4.5.

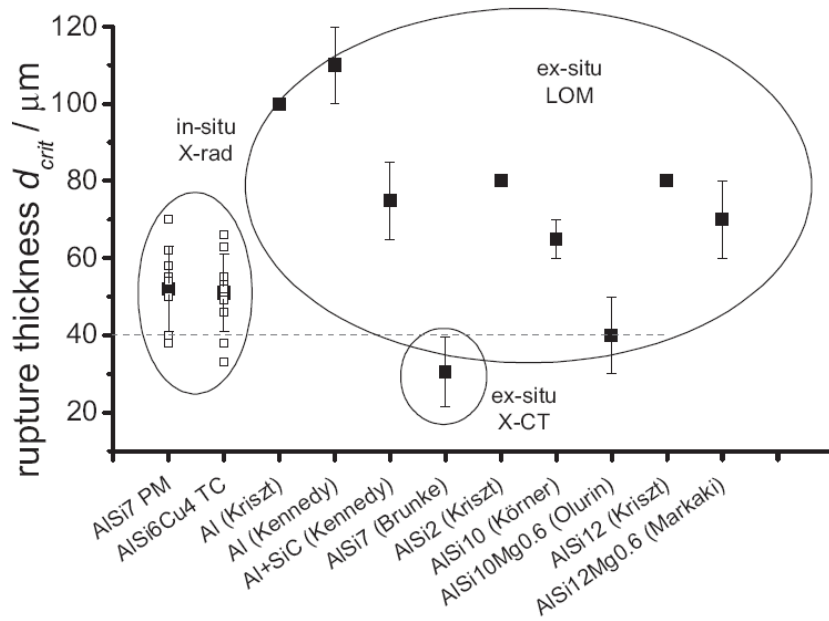


Figure 4.3. Critical thickness of cell features of various aluminum alloys made by foaming a precursor (Source: Banhart 2006).

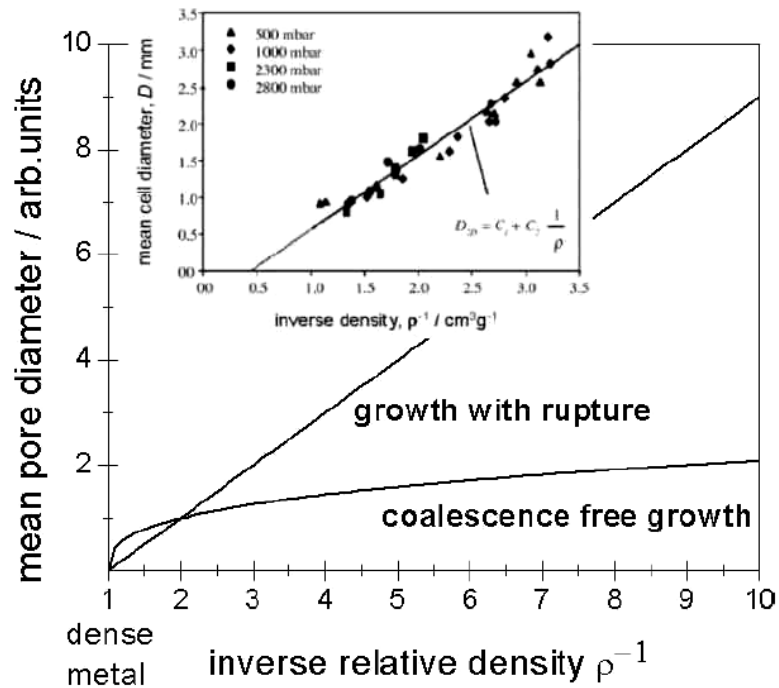


Figure 4.4. Relationship between mean pore diameter and the density of the foams expanded under different conditions (Source: Banhart 2006).

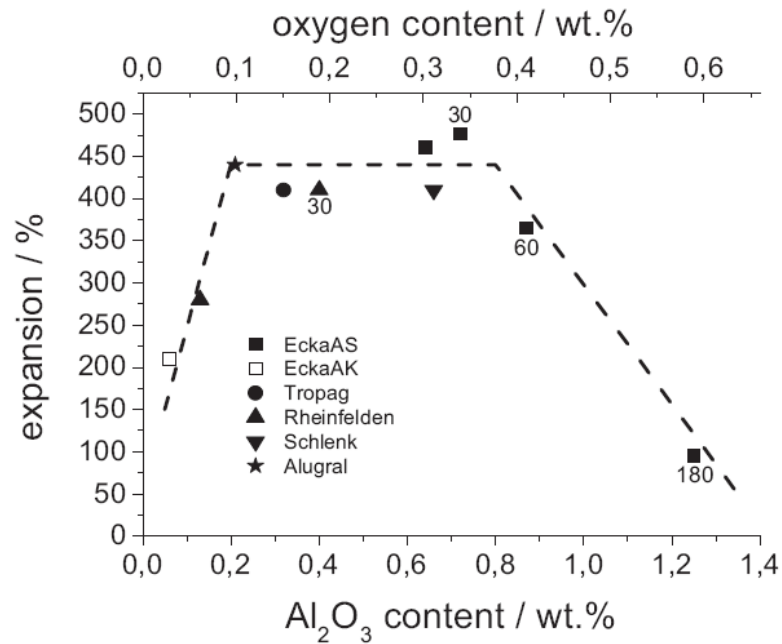


Figure 4.5. Influence of oxide content of Al powder on the expansion behavior of the foam (Source: Banhart 2006).

Kaptay (Kaptay 2004) developed a stabilization criteria for liquid foams based on the separation pressure acting on neighboring bubbles. Various kinds of particle arrangements on the cell wall were considered (Figure 4.6). The stability of foams increased in the following order: loosely packed single layer of particles, closely packed single layer of particles, loosely packed double layer of clustered particles, loosely packed ‘double+’ layer of clustered particles, closely packed double layer of particles and closely packed ‘double+’ layer of particles. The critical wetting angles for various types of particle arrangement were further developed. It was further shown that foam stability was not possible when $\frac{PR_s}{\sigma} > 40$ (where P is the pressure that destabilizes the foam, R_s is the radius of particles and σ is the surface tension of the liquid). It was also estimated that particles smaller than 30 μm stabilized the liquid metal foams.

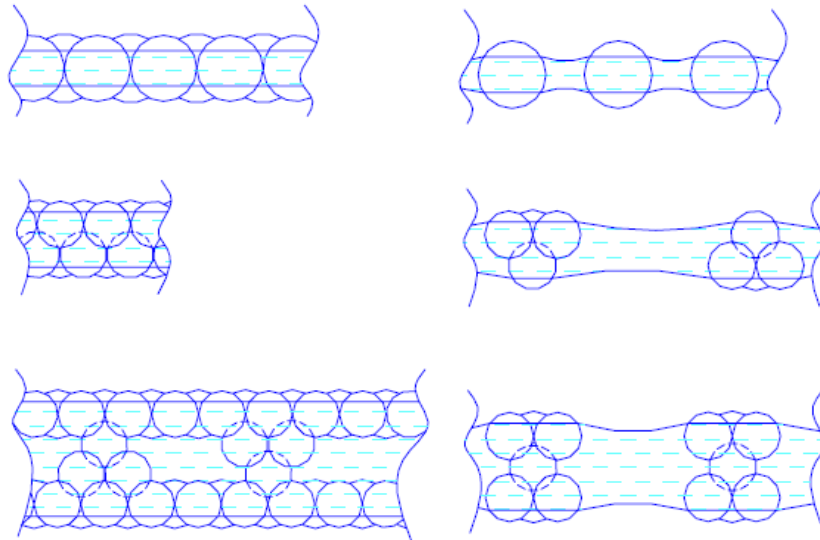


Figure 4.6. Schematic of the different arrangement of the stabilizing particles on the cell walls (Source: Kaptay 2004).

Kennedy (Kennedy 2002) and Kennedy and Lopez (Kennedy and Lopez 2003) studied the effect of TiH_2 heat treatment on the gas release rate foaming of Al powder compacts. The heat treatment process between 400-500 °C retarded the gas evolution starting at about 495 °C in untreated TiH_2 powder to higher temperature. The heat treatment however did not prevent the gas release before the melting of the compact and hence had small effect on foam expansions.

Kennedy and Asavavisithchai (Kennedy and Asavavisithchai 2004) investigated the effect of 10 μm and 3 vol% Al_2O_3 , SiC and TiB_2 addition on the foaming of Al powder compacts. Although particle addition increased the maximum expansion of the powder compact, at longer waiting times TiB_2 and Al_2O_3 contained powder compacts showed reduced expansion compared with Al compact without particle addition. The increased drainage in TiB_2 and Al_2O_3 contained powder compacts were attributing to the non-wetting behavior of the particles, leading increased drainages.

Asavavisithchai and Kennedy (Asavavisithchai and Kennedy 2006b) showed that the Mg-addition improved the stability of Al/ Al_2O_3 powder compacts by improving the wetting behavior of Al_2O_3 particles. With Mg addition particles were found to be embedded at cell wall surface by the cell wall, leading to reduced drainage and hence increased expansion values (Figure 4.7). The addition of relatively small amount (0.6 wt%) of Mg particles in powder compacts was found to enhance the wetting of Al_2O_3 particles (Figure 4.8). It was also shown that there is an optimum oxygen content which

leads to maximum expansion in compact. The foam made of Al powder containing 0.333 wt% oxygen was shown to be the most stable (Figure 4.9).

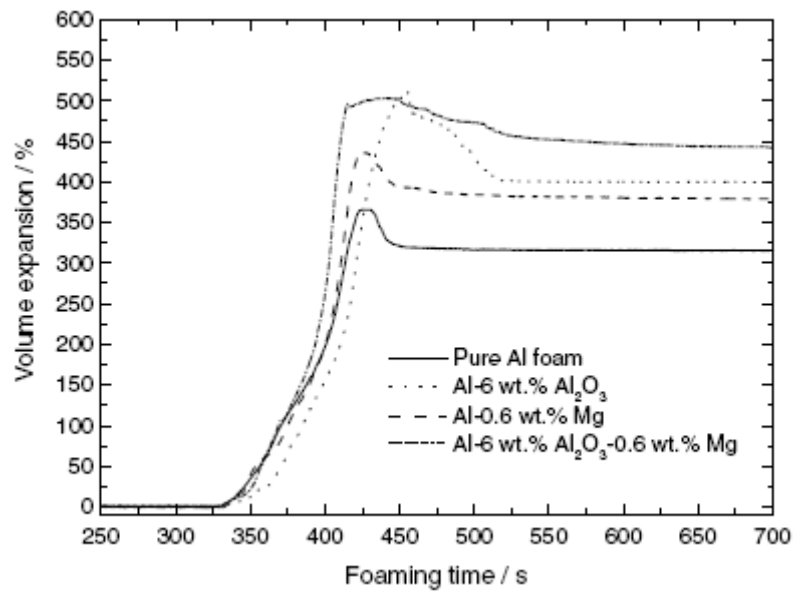


Figure 4.7. Effect of Mg and Al₂O₃ additions on the expansion of Al foams (Source: Asavavisithchai and Kennedy 2006b).

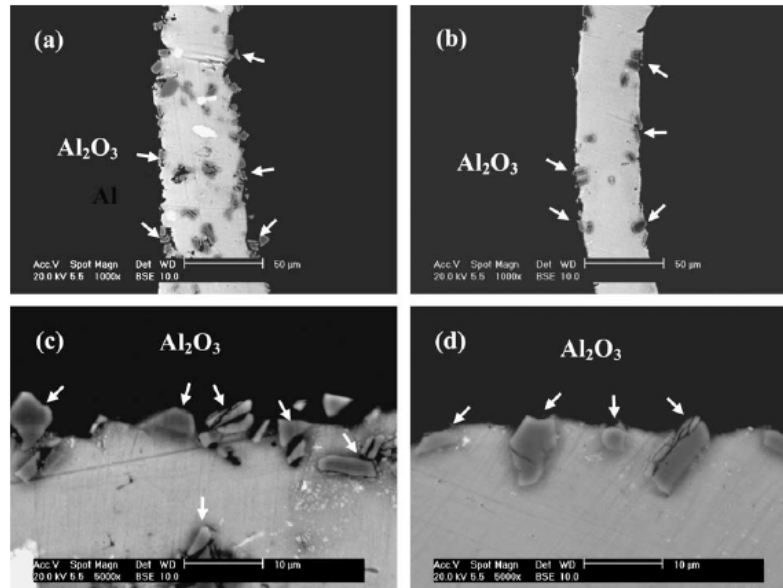


Figure 4.8. SEM micrographs showing the attachment of Al₂O₃ particles at the cell wall surfaces for (a) and (c) Al-6 wt.%Al₂O₃ and (b) and (d) Al-6 wt.%Al₂O₃-0.6wt.% Mg foams (Source: Asavavisithchai and Kennedy 2006b).

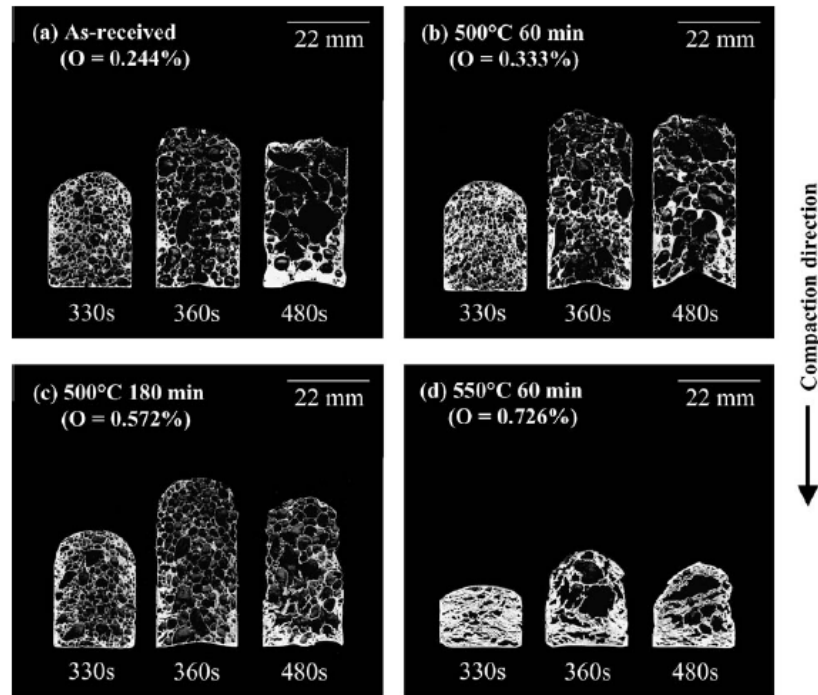


Figure 4.9. Cross sections of Al foams made using different Al powders: (a) as-received, (b) powder heat treated at 500 °C for 60 min, (c) powder heat treated at 500 °C for 180 min, and (d) powder heat treated at 550 °C for 60 min (Source: Asavavisithchai and Kennedy 2006b).

Duarte and Banhart (Duarte and Banhart 2000) and Duarte et. al. (Duarte, et al. 2002) studied effects of hot compaction and the foaming conditions on the foaming behavior and microstructure of AlSi7 and 6061 Al compacts. It was found that increasing foaming temperature increased the foam expansion in both compacts within the temperature range of 600-800 °C. Increasing temperatures reduced the viscosity and promoted gas evolution, leading to increased foam expansions. It was shown in the same study that the volume expansion were saturated at 750 °C for AlSi7 alloy compact, while the viscosity of 6061 Al alloy compact was not sufficient for the efficient foaming until about 800 °C. For the studied Al compacts, the foaming temperature was held between 700-730 °C and the maximum expansion was found to vary between 4.13-4.86.

The early stage pore formation in AA6061 Al and Al-7%Si powder compacts (Alulight) was investigated by synchrotron-radiation tomography (Helfen, et al. 2005). The pores in the former alloy formed dominantly around the blowing agent, while in the later alloy the pores preferentially initiated around Si particles.

Stanzick *et al.* (Stanzick, et al. 2002a) observed the foaming behavior of uniaxially compacted AlSi7 and thixocast AlSi6Cu4 foamable precursors using real

time X-ray radiography. The anisotropy in compacted precursor was observed in the early stage of the foaming; the expansion occurred parallel to the compaction direction and the initial cells formed were crack-like. While the precursor produced by casting showed no directional expansion and cells were round at all times. The cell wall rupture time for both types of precursors were determined around 50 milliseconds and cell rupture occurred at thickness of cell walls below 50 μm . The cell rupture time (T) was further approximated using following relation

$$\tau = \frac{b}{2} \sqrt{\frac{c\rho}{\sigma}} \quad (4.3)$$

where, b, c, ρ and σ are the cell wall length, thickness, liquid metal density and surface tension, respectively. Using the typical values of Al in above equation, a rupture time of 1.2 ms was calculated. Several types of defects included into the precursor were found to be not effective in changing the morphology of the fully expanded foams.

Banhart *et al.* (Banhart, et al. 2001) analyzed the foaming behavior of Al-based sandwich panels using X-ray radiography. The foamable sandwich precursor was prepared by roll-cladding of AA3103 Al alloy sheets to the extruded Al alloy foamable precursor. In the early stages of the foaming, crack-like pores were formed normal to the foaming direction, which was related to the direction of powder consolidation. The foamable sandwich precursor showed strong dependency on the foaming temperature and duration. Low foaming temperatures resulted in low expansion of the precursor, while high foaming temperatures resulted in melting of the face sheet.

Haibel *et al.* (Haibel, et al. 2006) have recently analyzed the possible stabilization mechanisms operative in foaming of powder compact processes. The liquid metal on a film (cell wall) connected to the plateau border (cell edge), under the effect of the pressure difference, flows from the cell wall to the plateau borders. Pressure difference is as follows.

$$\Delta P = 2\sigma \left(\frac{1}{R_{PB}} - \frac{1}{R_F} \right) \approx \frac{2\sigma}{R_{PB}} \quad (4.4)$$

Several different stabilization models were considered. The partially wetted particles on the cell wall form menisci of radius of $R_F \cong R_{PB}$, which reduces the pressure difference and capillary suction (Figure 4.10 (b)). In another model, small particles sit at the liquid/gas interface, which gives rise to local menisci between adjacent particles Figure 4.10(c); hence reduce the melt flow from the film. Another model, which has become popular recently, is based on the mechanical connection of the particles covering the opposite film surface, which provides repulsive mechanical forces Fig 4.10(d). The last model is based on the increased viscosity of the melt by the presence of small particles in the film, which immobilized the liquid metal flow (Figure 4.10 (d)). These models were investigated by the foaming of a metal matrix composite Al-10wt% Si-1 wt%Mg/10 vol%SiC (13 μm) foamable precursor. It was shown microscopically from the solidified foam samples that most of the particles were located at the metal/gas boundaries and only few were found at the interior of the cell walls. X-ray tomography analysis of cell walls further showed no evidences of mechanical bridges between the particles of the opposite cell faces. The global distribution of SiC particles in foaming melt was further determined. The particles were found to be predominately located near the liquid/gas interface (37%), while at a 40 μm distance from the liquid/gas interface the particle concentration dropped to 7%. Finally, a model of foam stabilization comprising the particle covering of the cell faces and increased apparent viscosity of the melt (Fig. 4.10(f)) was proposed.

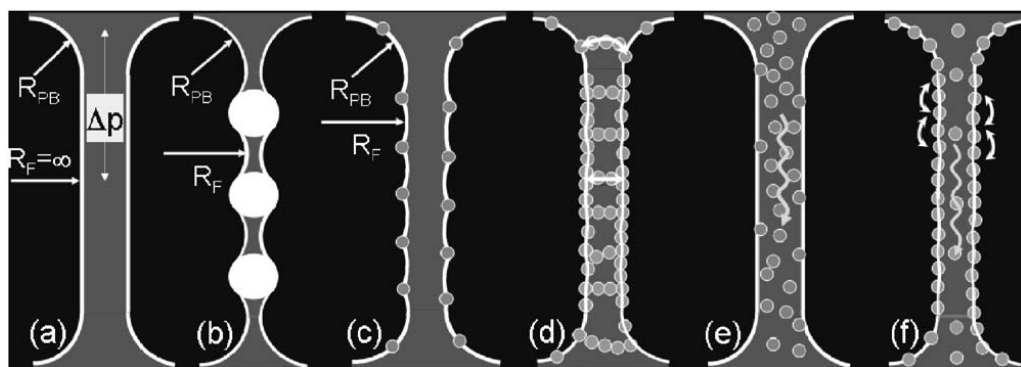


Figure 4.10. (a) Liquid film in a foam (R is the radius of curved films, Δp is the pressure difference within a film), (b) adsorbed particles with film bridges, (c) modulated interfaces, (d) particle layers on interfaces connected by particle bridges, (e) drainage reduction by particles and (f) model for particles (Source: Haibel, et al. 2006).

Babcsan *et al.* (Babcsan, et al. 2005, Babcsan, et al. 2007) analysed ex-situ and in-situ the stability of aluminum metal foaming processes. In foam prepared by Formgrip process with 13 μm sized SiC particles, the particles were observed to segregate to the cell surface, while in foams of 70 μm SiC particles, only small amount of particles were observed on the cell surface. The cell wall thicknesses were also found to be quite different: 85-100 μm in foams of 13 μm SiC particles and up to 300 μm in foams of 70 μm SiC particles. In Alporas foams, the size and volume of the oxide inclusions were predicted as 1 μm and 1%, respectively. A chart showing particle size and particle volume fractions that stabilize the 3 foams, namely CYMAT, ALPORAS and ALULIGHT, was further developed (Fig.4.11). For CYMAT foam, the particle size and volume fraction for foam stabilization were above 1 μm and 1 vol%, while these were less than 1 μm and 1 vol% in Alporas and Alulight foams. In gas injection foaming of Al melts, it was found that TiB_2 particles were not effective in stabilizing the foam and they were considered as non-wettable. It was also shown that the composition of the melt alloy was effective in particle distribution. Foaming of an $\text{AlSi0.8Mg0.8/10vol\% Al}_2\text{O}_3$ melt in Alcan process produced thicker cell walls than the alloy containing lower Si/Mg ratio. In three different foaming processes, Cymat, Alporas and Alulight, the foamed alloy were considered as, by similarity, suspensions (50-100 μm), sols (micrometer size particles) and gels (nano size particles), respectively. These alloys were foamed through external foaming (gas injection) and internal foaming (blowing agent). Results showed that internal foaming of Alporas alloy produced longer standing foams than Alulight metal alloy. In external foaming, Alcan metal showed the highest and Alulight metal shows the lowest foam qualities. In external foaming of 20vol% SiC (10 μm) particle containing melt by argon gas blowing, a rupture time of cell wall of below 33 ms were found. It was also shown that rupture increased with increasing foaming duration but after an incubation time of 106 s.

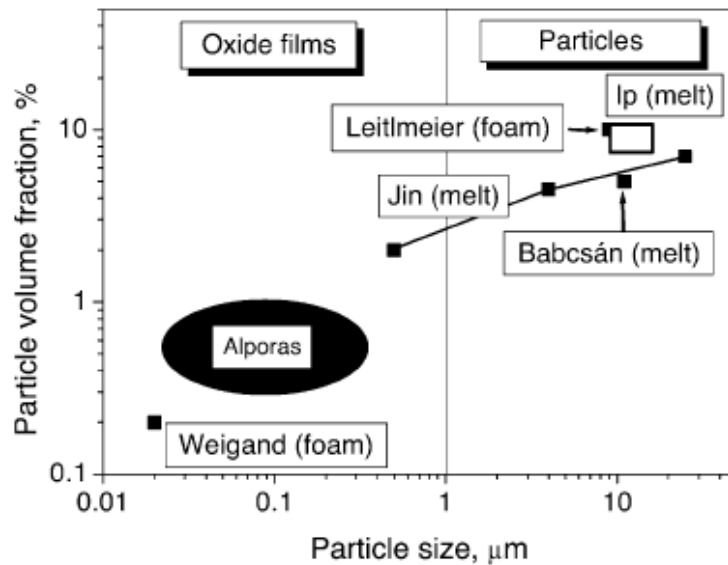


Figure 4.11. Stability diagram for metal foams relating particle volume fraction and particle size (Source: Babscan, et al. 2005).

In laser foaming of the foamable compacts produced by powder metallurgy, the interaction time was found to be effective on the cell size (Kathuria 2001a, Kathuria 2001c, Kathuria 2003a, Kathuria 2003b). Longer laser beam interaction times induced larger cells and shorter beam interaction led to small size but partial foaming in the powder compact.

The effect of foaming time on pore size and pore size distribution in Alporas foam processing method was investigated experimentally and numerically by Song and Nutt (Song and Nutt 2007). Two forces were identified resisting the foam expansion: the frictional forces between liquid foam and foaming mold surface and excess surface pressure arising from the surface tension. The expansion rate was found to increase with increasing mold cross-section and decrease with increasing foam height and melt viscosity and pore size and pore size distribution was shown to be a function of furnace holding time.

The effect of compaction method on the expansion of Al-0.6%TiH₂ powder compacts was investigated by (Asavavisithchai and Kennedy 2006a). It was shown that simple cold compaction of Al powder compacts of >99% dense and containing 0.3-0.4% oxygen produced foam expansions similar to the ones prepared by hot compaction forming processes.

The effect of oxygen content of the starting Al powder on the expansion and stability of Al-0.6%TiH₂ powder compacts was investigated (Asavavisithchai and

Kennedy, 2006c). The oxide content of the powder was increased by the pre-heat treatment. It was shown that the maximum foam expansion increased by increasing the oxygen content to 0.333 wt% while increasing oxygen content above 0.333-0.6wt% level resulted in low expansion but stable foams. The oxide particles formed clusters of crumpled films, restricting drainage.

Leitlmeier *et al.* (Leitlmeier, et al. 2002) have modified gas blowing foaming process by using a new gas bubbling equipment which controls the gas bubble formation and guiding the particle stabilized foam on the surface of the melt into a mold (Figure 4.12). The foam prepared in this modified foaming technique is called Metcomb. It was also shown that smaller depths of immersion gas bubbling equipment lead to unstabilized bubbles and bubbles burst on the surface of the melt. The minimum thickness of depth of immersion of bubbling equipments was shown to increase with decreasing particle content (Al_2O_3 and SiC). The use of nitrogen as blowing gas resulted in more frequent bursting of the bubbles before reaching to the melt surface when compared with air or oxygen blown foams. It was also found that when nitrogen was used for blowing, SiC covered the surface of the walls, while oxygen blown foams the cell wall surfaces and SiC particles were covered with thin oxide layer. Stable foam processing in Cymat method as a function of distance traveled by bubbles and SiC volume fraction is shown in Figure 4.13. At low traveling distances and low SiC volume contents, the bubbles are bursted and the stability was lost as depicted in Figure 4.13, while the stability is achieved at long traveling distances and high volume content of SiC particles.

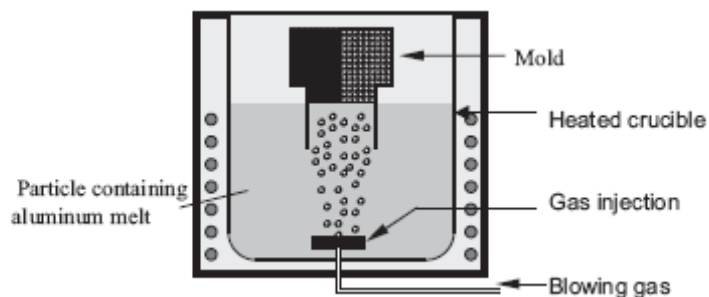


Figure 4.12. Schematic presentation of the foaming experiments with blowing gas into a melt filling a mold (Source: Leitlmeier, et al. 2002).

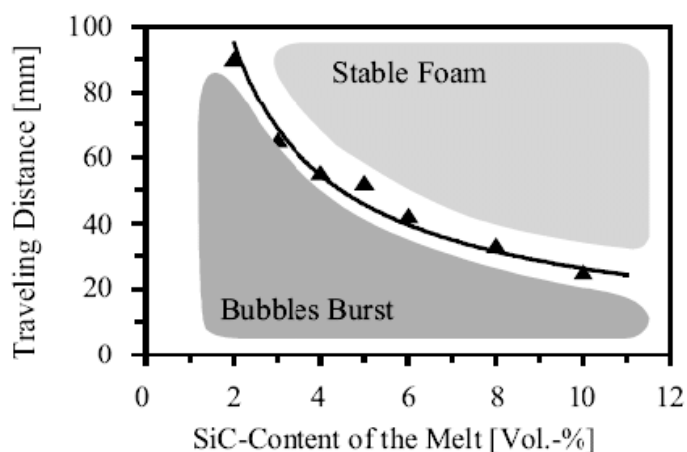


Figure 4.13. Criterion to obtain stable Al foams (alloy A356, $T = 727\text{ }^{\circ}\text{C}$) (Source: Leitmeier, et al. 2002).

Babcsan *et al.* (Babcsan, et al. 2004) investigated the foaming behavior of Al melts containing SiC particles through foaming by gas blowing process. It was noted that Al melts without particle did not form stable bubbles on the surface of the melt. It was concluded that a certain concentration of particles were needed for bubble stabilization formed by blowing and the stabilization is due to the particle segregation at the liquid/gas interface; the surface oxide layer formed in oxygen containing blowing gases, provide additional foam stabilization.

The effects of melt (pure Al) viscosity (adjusted by the Ca-addition and melt stirring time) and holding time on the cell structure of Alporas foams were studied by Song *et al.* (Song, et al. 2000, Song, et al.2001). It was observed that pore structure is affected by the melt viscosity. With increasing melt viscosity, the metal foam stability increased and the cell size decreased. It was further emphasized that too high viscosity might prevent the homogenous dispersion of the foaming agent. For large cell size, holding time increased and the amount of foaming agent decreased. Too low viscosity always leads to rapid floating of bubbles, and too high viscosity suppresses the formation and the growth of bubbles. Therefore, it is important to control the viscosity carefully in the foaming process. Viscosity of aluminum melt was measured by measuring the voltage of paddle motor during the period of stirring. When a liquid is stirred, the resistance from the liquid can be signified as the apparent but not the real concept of viscosity. As the apparent viscosity is high, higher motor power and the winding voltage of stirring motor is needed. As can be seen from Figure 4.14 below addition of calcium into aluminum melt can increase the apparent viscosity.

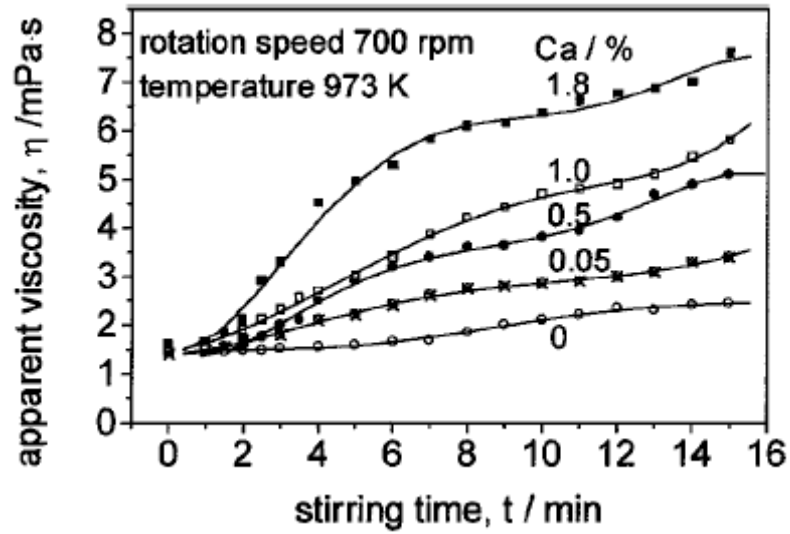


Figure 4.14. Relation of stirring time and Ca content with apparent viscosity of Al melt (Source: Song, et al. 2000).

It was observed by Ravi *et al.* that the effective or apparent viscosity rises markedly above the viscosity of pure (monolithic) melts when the liquid metal contains a dispersion of particles in their study of investigating fluidity of Al alloys and composites (Ravi, et al. 2008). For dilute suspensions with particle volume fraction smaller than 0.1, the effective viscosity, μ_c , of the suspension can be predicted using Einstein equation

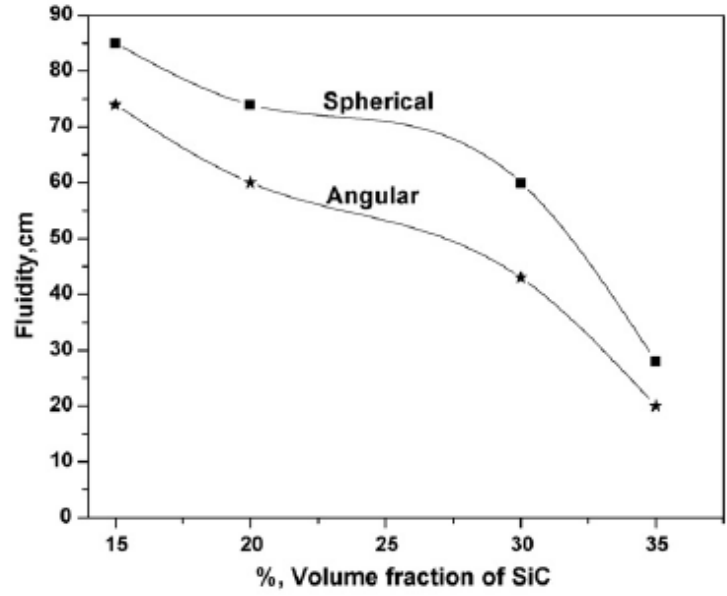
$$\mu_c = \mu_0 (1 + 2.5\phi + 10.25\phi^2) \quad (4.5)$$

where μ_c is the apparent viscosity of composite slurries (g/cm.s), μ_0 the viscosity of fluids without any particle (g/cm.s) and ϕ is the volume fraction of the suspended particles. Literature suggests that the viscosity of aluminum lies between 1.0-1.4 mPa.s (Iida and Guthrie, 1988). In concentrated suspensions, it is necessary to account for the effects such as hydrodynamic interactions, particle rotation, collision between particles and agglomerate formation. At high volume fractions, the relationship between viscosity and concentrations become non-linear. The following equation was developed by Wang *et al.* (Wang, et al. 2003) for viscosity of composite melt considering the influence of particle size, shape as well as volume fraction

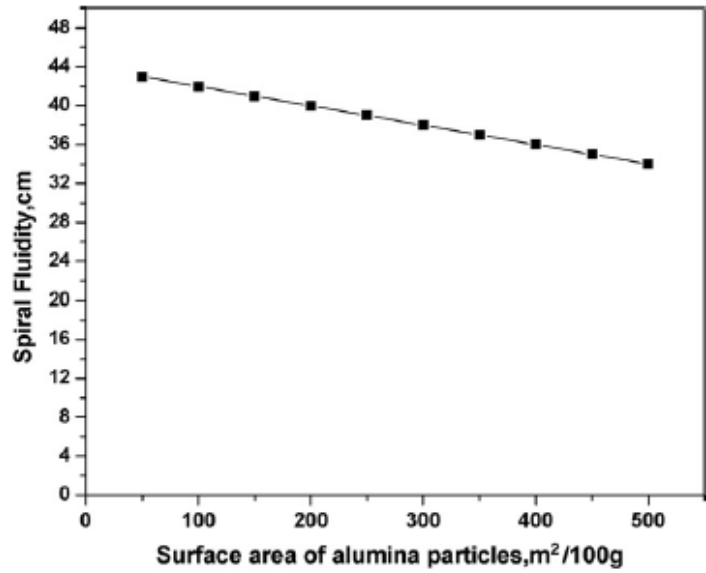
$$\mu_c = \mu_0 \left[\left(\frac{\xi(1+D_p^{0.95})}{(0.01+37.35D_p^{0.95})} \right) \phi \right] \quad (4.6)$$

where D_p is the diameter of spherical particles (cm) and ξ is the factor related to the particle height–diameter ratio. The melt viscosity can significantly increase for reducing particle sizes with constant particle volume.

It was observed by Ravi *et al.* (Ravi, et al. 2008) that increasing angularity of the particle reinforcements leads to a progressively greater decrease in the fluidity at a given temperature and volume fraction of particle (Figure 4.15(a)). Fluidity is measured as the flowing distance of the melt metal in a spiral shaped mold till it solidifies. Fluidity, besides being dependent on many parameters, is inversely dependent to the viscosity of the melt. In this study addition of 15 vol% SiC of 9 μm diameter had the lowest flow ability, lower than that of composite containing 20 vol% SiC of 14 μm diameter, showing that particle size has a strong influence on flow of the melt. The decrease in the SiC particle size has been attributed to an increase in the total surface area of particulates causing more resistance to fluid flow as a result of stagnant boundary layers around the particles (Figure 4.15(b)). It was observed that fluidity decreased linearly with the total surface area per unit weight of the particles. Fine particles are more effective in stopping a flowing stream than an equivalent percentage of coarse particles. Hence, fluidity is expected to decrease with grain refinement. Similarly, as can be seen from Figure 4.16, for a constant particle size, increasing the SiC particle percentage in the melt resulted in decrease in the fluidity of different Al alloys (Ravi, et al. 2008). Generally, fluidity of aluminum alloy increases with increasing melt temperature for a given alloy composition. However, in some cases, raising the temperature has a negative effect on the fluidity of Al MMCs. For instance, the fluidity of AA6061–15 vol% SiCp composites was found to decrease with increasing temperature (Ravi, et al. 2008).



(a)



(b)

Figure 4.15. Effect of (a) particle shape and (b) total particle surface area of SiC particles on the fluidity of the melt (Source: Ravi, et al. 2008).

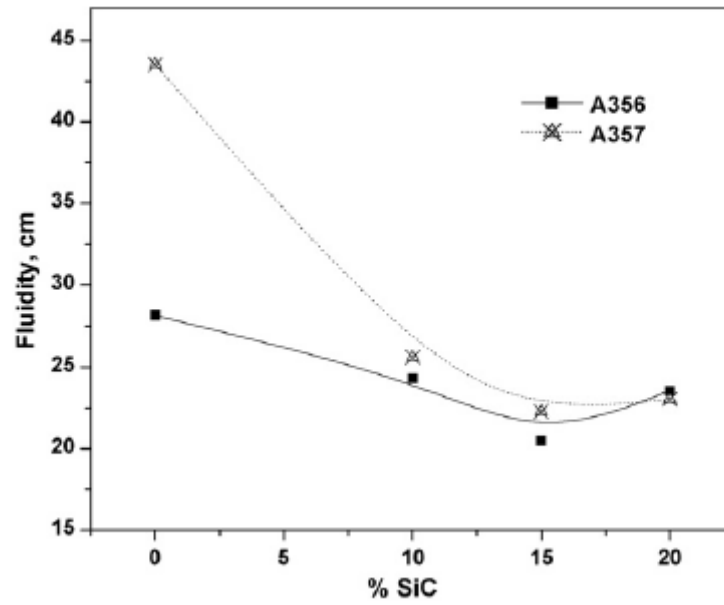


Figure 4.16. Effect of volume percentage of SiC particles on the fluidity of Al alloys.
(Source: Ravi, et al. 2008)

CHAPTER 5

MATERIALS AND EXPERIMENTAL METHODS

5.1. SiC Powder and Whisker

The average particle size of Al powder used to make compacts was 34.64 μm and the size of TiH_2 particles was less than 37 μm as tabulated in Table 5.1. The oxygen content of Al powder was measured as ~0.5% using a LECO oxygen analyzer device. TiH_2 content was kept at 1 wt% in all foamed compacts. SiC-Aldrich 378097 numbered as powder 4 was sieved between 20-30, 30-45, 45-56 and 56-74 μm using a Fritsch Analysette 3 PRO type vibratory sieve shaker, while powders numbered as 5,6,7 and 8 were directly used in compact preparation. 10 different SiC/Al compacts were prepared and foamed.

Table 5.1. Powders used for the compact preparation.

Powder	Particle Size (μm)
1 Aluminum (Aldrich-code 214752)	< 74 μm
2 TiH_2 (Merck-code 1.12384.0100)	< 37 μm
3 SiC particle (Aldrich-code 357391)	< 37 μm
4 SiC particle (Aldrich-code 378097)	30-74 μm
5 SiC particle (Alfa Aesar-code 43884)	30 nm
6 SiC particle (Alfa Aesar-code 40155)	2 μm
7 SiC whisker (Alfa Aesar-code 38787)	1.5 μm in diameter, 18 μm in length
8 SiC particle (Alfa Aesar-code 43332)	< 44 μm

The codes of the compacts foamed are tabulated in Table 5.2 together with the sieved SiC addition sizes. In Table 5.2, P0 refers to the compacts without SiC addition. P1-P8 refers to the compact with SiC particle addition, P9 whisker and P10 nano powder addition. Compacts coded between P1-P5 were prepared using sieved particles. The average sizes of the SiC particles were measured using a Sedigraph device (Micromeritics, Sedigraph 5100). The corresponding SEM micrographs of SiC

additions (particles, whisker and nano powder) are also shown sequentially in Figure 5.1 and Figure 5.2. SiC particles used were generally angular in shape, particularly powders with relatively large particle sizes; therefore, the minor (short) and major (long) axes of the particles were measured from SEM micrographs using an image analyzer program to determine the average particle sizes. At least 100 measurements were taken and the results were averaged and tabulated in Table 5.2. It is noted in Table 5.2 that the sedigraph and SEM measurements show similar average particles sizes. In the analysis of the particle size effect on the foaming behavior of SiC/Al compacts, the particle sizes measured using SEM micrographs were used.

Table 5.2. Mean particle diameter values of the powders measured from SEM images.

Compact Code	Powder interval (μm)	Mean particle size (Sedigraph) (μm)	Mean short axis size (μm)	Mean long Axis size (μm)	Mean particle size (μm)
P0					-
P1	10-20	19	11	17	14
P2	20-30	29	18	29	24
P3	30-45	35	24	43	34
P4	45-56	42	41	73	57
P5	56-74	54	51	82	67
P6	3-40	20	-	-	21
P7	26-74	36	-	-	36
P8	0.2-2	-	-	-	1
P9	1.5-18	-	-	-	-
	(whisker)	-	-	-	-
P10	30 nm	-	-	-	-

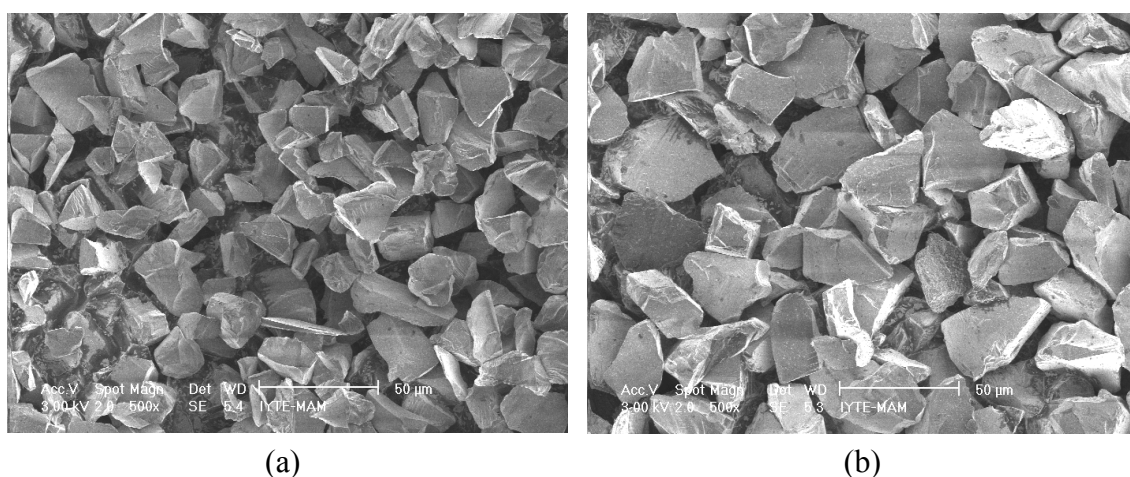
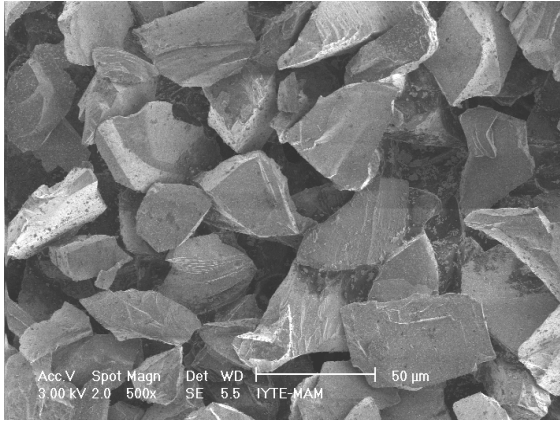
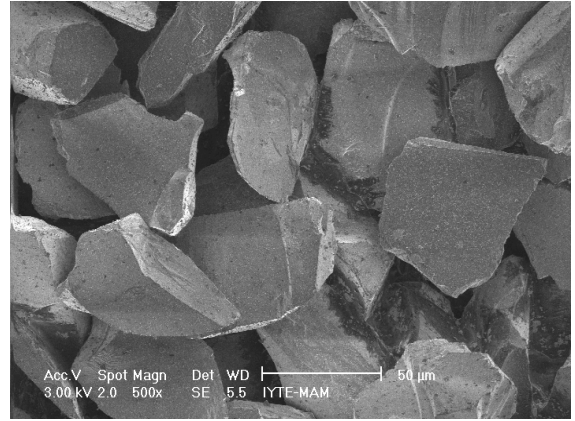


Figure 5.1. SEM micrograph of (a) P1, (b) P2, (c) P3, (d) P4, (e) P5 (f) P6, (g) P7 and (h) P8 SiC powders.

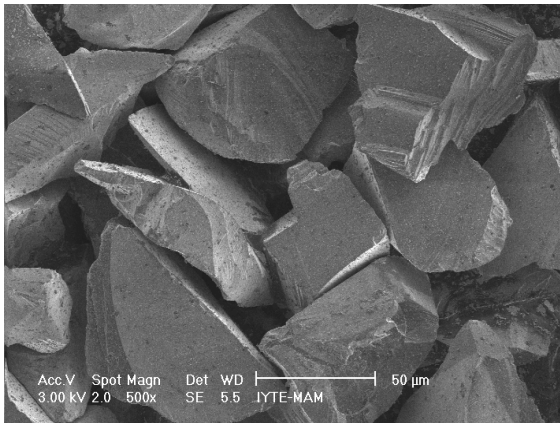
(cont. on next page)



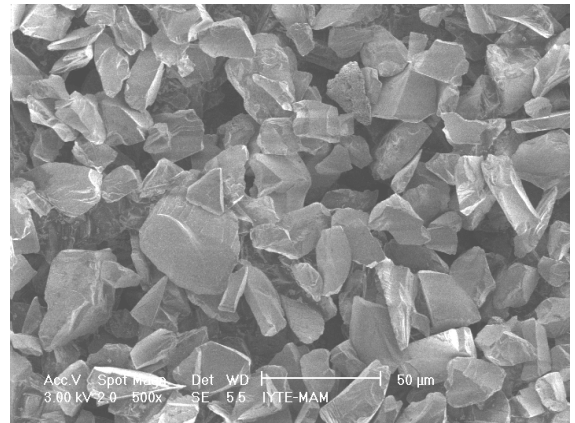
(c)



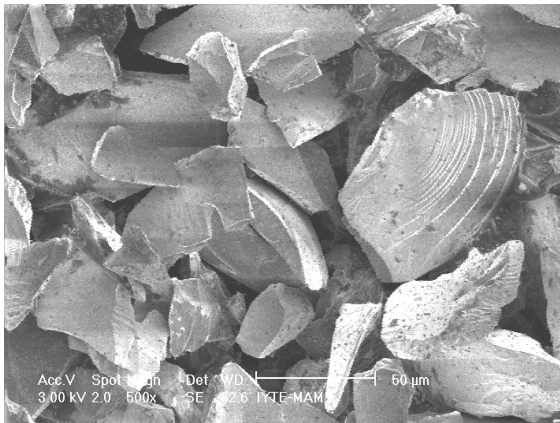
(d)



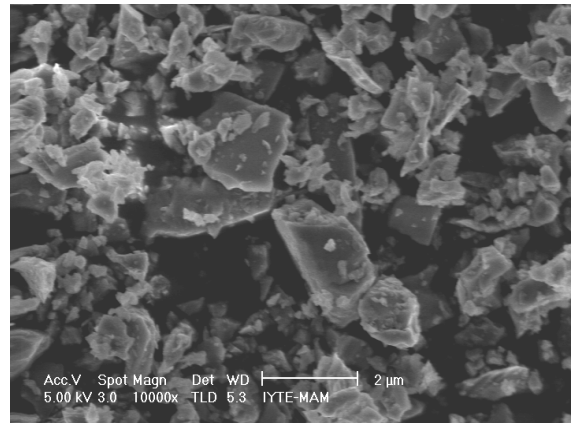
(e)



(f)



(g)



(h)

Figure 5.1. (cont.)

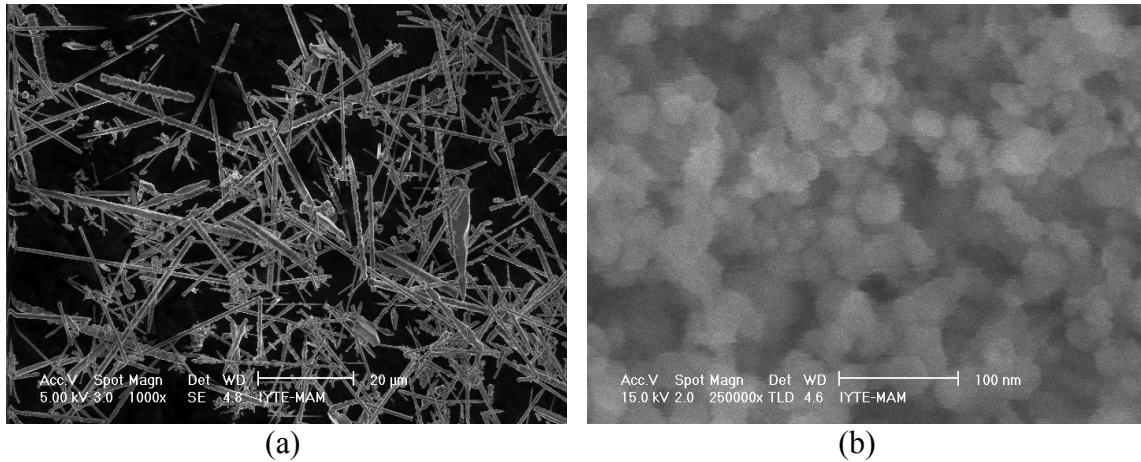


Figure 5.2. SEM micrograph of (a) P9 whisker and (b) P10 nano powder.

5.2. Compact Preparation

The stages of the compact preparation and foaming experiments are schematically shown in Figure 5.3. The process starts with the mixing of appropriate amounts of basic ingredients (Al powder, TiH_2 and SiC) inside a plastic container, which was tightly closed. The powder mixture is then rotated on a rotary mill for $\frac{1}{2}$ h in order to form a homogeneous powder mixture. For the addition of nano and 1 μm size SiC particles, the powder mixture was mixed using a ball milling machine. The mixture was then axially compacted inside a tool steel die (Figure 5.4) with a final compact relative density of ~98-99% using a hydraulic press. The compacts were 30 mm in diameter and ~8 mm in height. The applied pressure to the powder mixture varied between 180 and 260 MPa; higher compaction pressures were applied during the compaction of SiC/Al powder mixtures in order to increase the relative densities to that of Al compact without particle addition. The percentage of SiC particles in the prepared compacts are listed in Table 5.3. The optical micrographs of the polished cross-sections of the prepared P1-P5 compacts with 5 and 10 wt% are shown sequentially in Figure 5.5. As is seen in these figures, no particle agglomeration is seen both for 5 and 10wt% SiC/Al compacts and SiC particles were homogeneously distributed throughout the Al matrix.

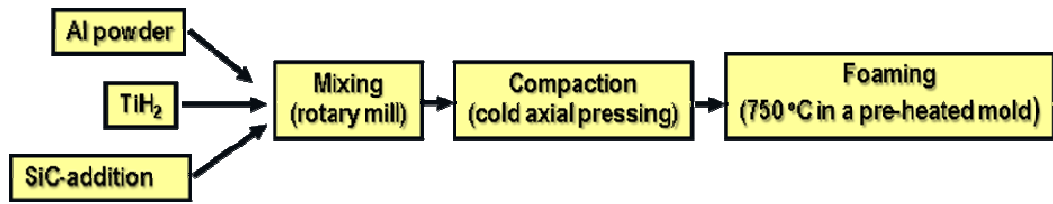


Figure 5.3. Schematic representation of foaming process.



Figure 5.4. Dies used for the compact preparation.

Table 5.3. Percentages of SiC in SiC/Al compacts.

Specimen Code	Mean particle Diameter	Percentage of SiC added (%)
P1	19 μm	5 - 10
P2	29 μm	5 - 10
P3	35 μm	5 - 10
P4	42 μm	5 - 10
P5	54 μm	5 - 10
P6	20 μm	5 - 10 - 15
P7	36 μm	5
P8	1 μm	0.1 - 0.5 - 1 - 3 - 5
P9	1.5-18 μm (whisker)	0.1- 0.5 - 1- 3 - 5
P10	30 nm	0.01- 0.1- 0.15 - 1- 3 - 5

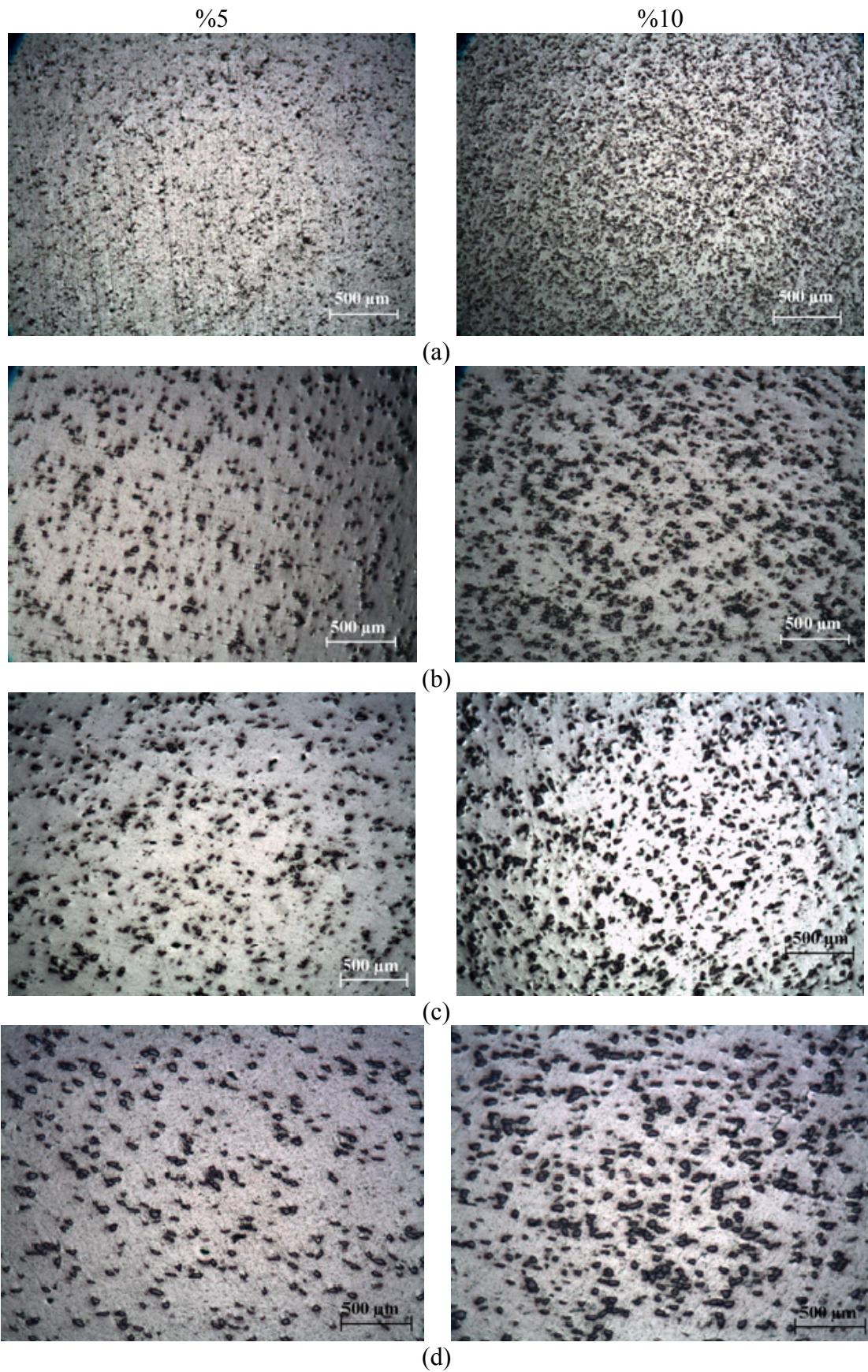
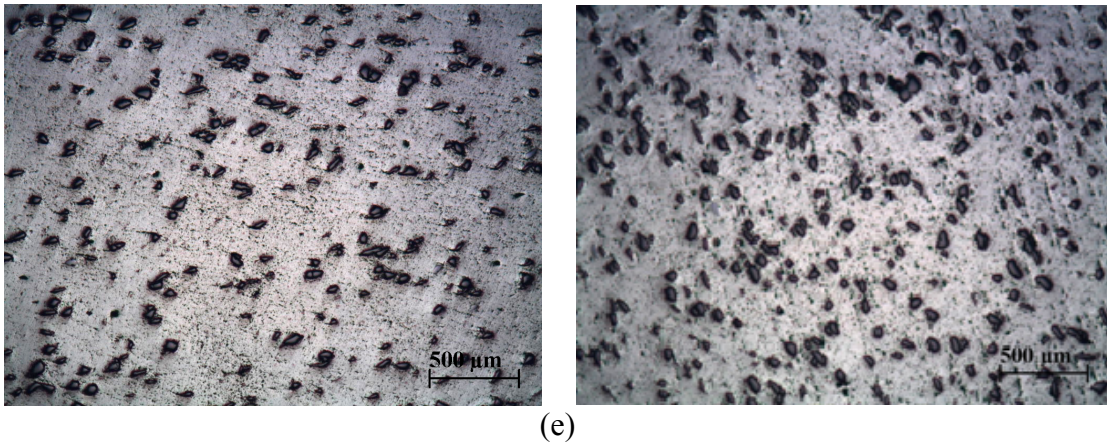


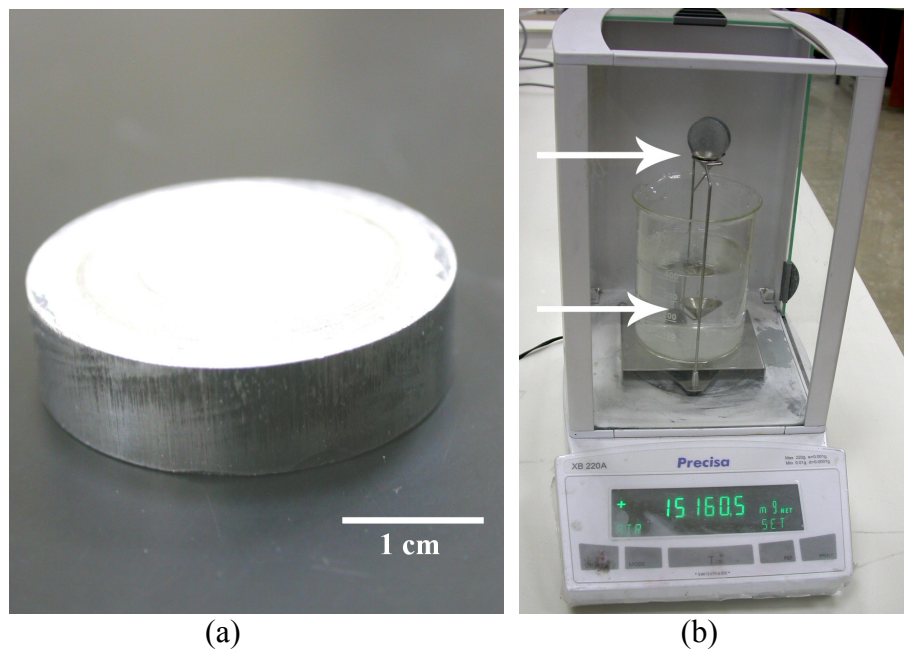
Figure 5.5. Microstructure of compacts having 5-10 % SiC from (a) P1 (b) P2 (c) P3 (d) P4 (e) P5 powder.

(cont. on next page)



(e)
Figure 5.5. (cont.)

The density of the prepared compacts (Figure 5.6(a)) and the dimensions including the diameter and height were measured before the foaming tests. The density of the compacts was measured using the Archimedes' method on precision balance (Figure 5.6(b)). Weight of the compacts was measured in air and in distilled water (shown with white arrows in Figure 5.6 (b)) and density was calculated according to the buoyancy force. Then these measured values were used to compare with the calculated density values of the compacts to understand the relative density of the compacts. Density values used for Al, SiC and TiH₂ powders used in calculation of the density of the compacts are 2.702 g.cm⁻³, 3.217 g.cm⁻³ and 3.910 g.cm⁻³ respectively.



(a) (b)
Figure 5.6. Picture of (a) a cold pressed compact and (b) density measurement set-up.

5.3. Foaming Set-Up and Foaming Experiments

The schematic and front view of the foaming set-up used in the foam expansion experiments are shown in Figure 5.7 and Figure 5.8, respectively. The experimental set-up was composed of a vertical furnace, a linear expansion measurement system and a foaming mold. The bottom of the foaming mold (3 cm in diameter and 8 cm in height) was enclosed tightly and the compact was placed at the bottom of the mold (Figure 5.9(a)). A linear variable displacement transducer (LVDT) was connected to the steel expansion rod through a wire and two pulleys as shown in Figure 5.8. A thermocouple directly contacted to the bottom of the compact was used to measure the compact temperature during foaming. LVDT and thermocouple data were collected using a data logger (Data Taker, DT 80) (Figure 5.9(b)).

The cold compact was inserted inside a stainless steel foaming mold (Fig. 5.9 (a)). The thermocouple is placed inside the lower moving bar that holds the mold and touches the compact from the hole on the center of the bottom part of foaming mold. Expansion rod and the LVDT are connected through very low friction pulleys connected with a metallic thin wire. Both are the components used in some type of electrical discharge machines commercially available. Weight on both sides of these pulleys is balanced using counter weight for the expansion piston to apply minimum force possible on the foam during expansion.

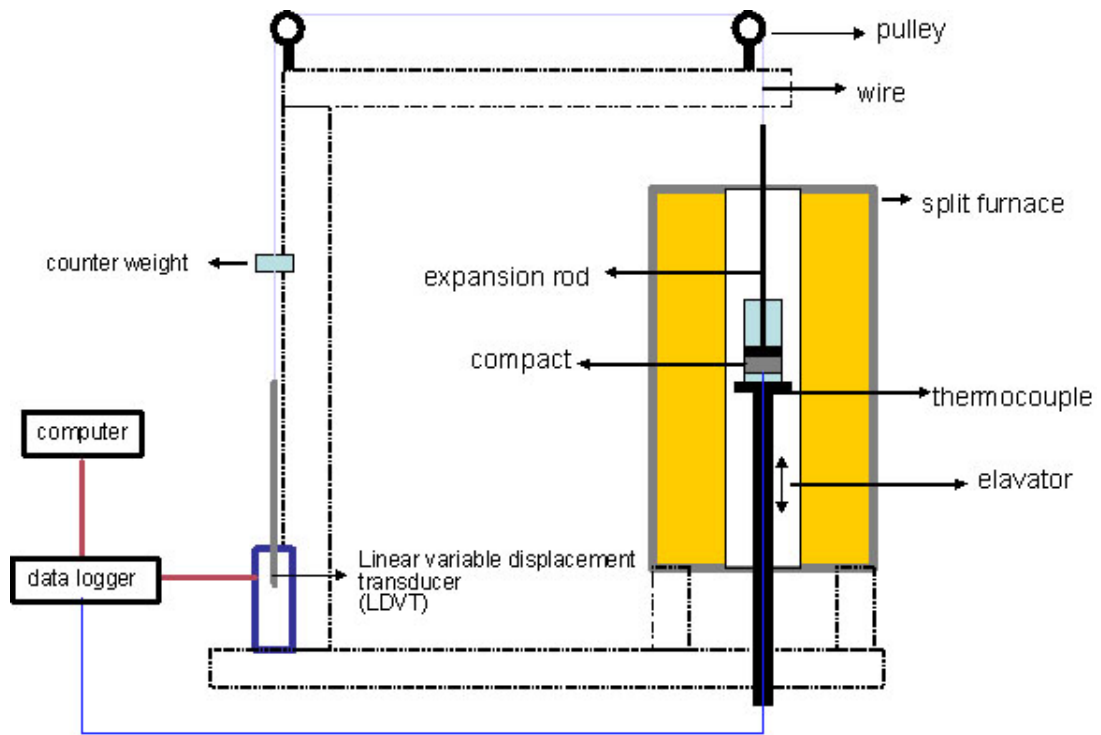


Figure 5.7. Schematic of foam expansion measurement set-up.

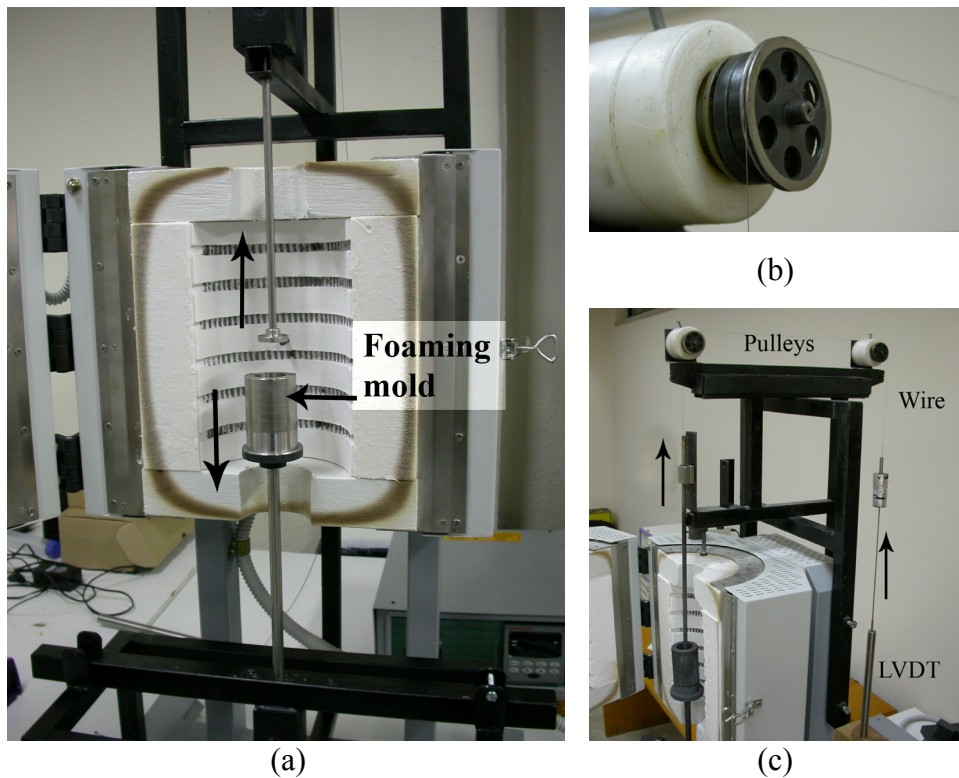


Figure 5.8. (a) Foaming mold and sliding top and bottom rods, (b) low friction pulley and (c) pulley mechanism of the foaming set-up.

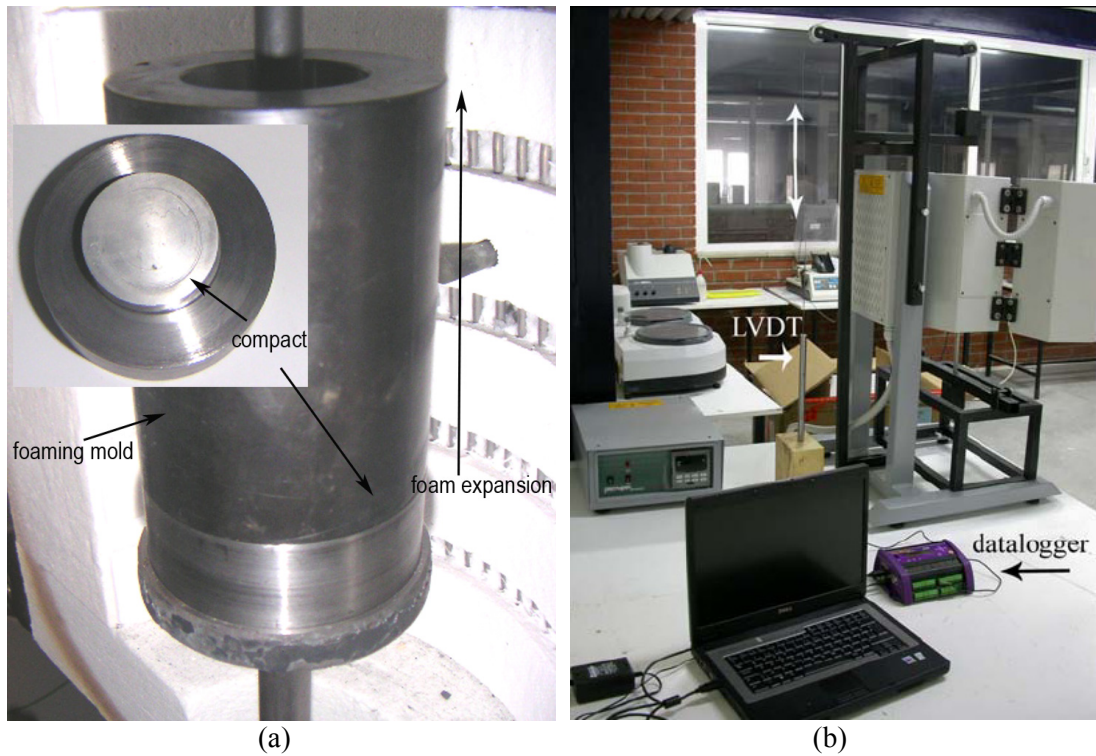


Figure 5.9. (a) Foaming mold and (b) LVDT and Data logger.

In a typical foaming experiment, the furnace is initially heated to 750 °C. Then the compact is inserted into the furnace with the mold by means of an elevator. After the compact insertion into the furnace, the top expansion rod connected to LVDT is lowered until the top mold plate touches the compact surface. A typical expansion-time and temperature-time graph is shown in Figure 5.10. As soon as the mold is inserted, the furnace temperature decreases to ~640 °C and then increases gradually to 750 °C in ~10 min as the mold is heated up. As the compact expanded, the linear expansion measuring wire moves backward and the movement is measured with the help of a data logger which is connected to the LVDT. After foaming, the foaming mold is taken out of the furnace with the help of the elevator and cooled for the foam to solidify. The linear expansion data (mm) is converted to linear expansion (LE) using the following equation:

$$LE = \frac{\text{expansion}}{\text{initial length}} \quad (5.1)$$

The foaming experiments continued until about 900 s. In few experiments, the foamed compacts were taken from the furnace at various furnace holding times and then quenched with water (interrupted foaming tests). The samples recovered from interrupted tests were then sectioned and observed microscopically to evaluate the foam evolution as a function foaming time.

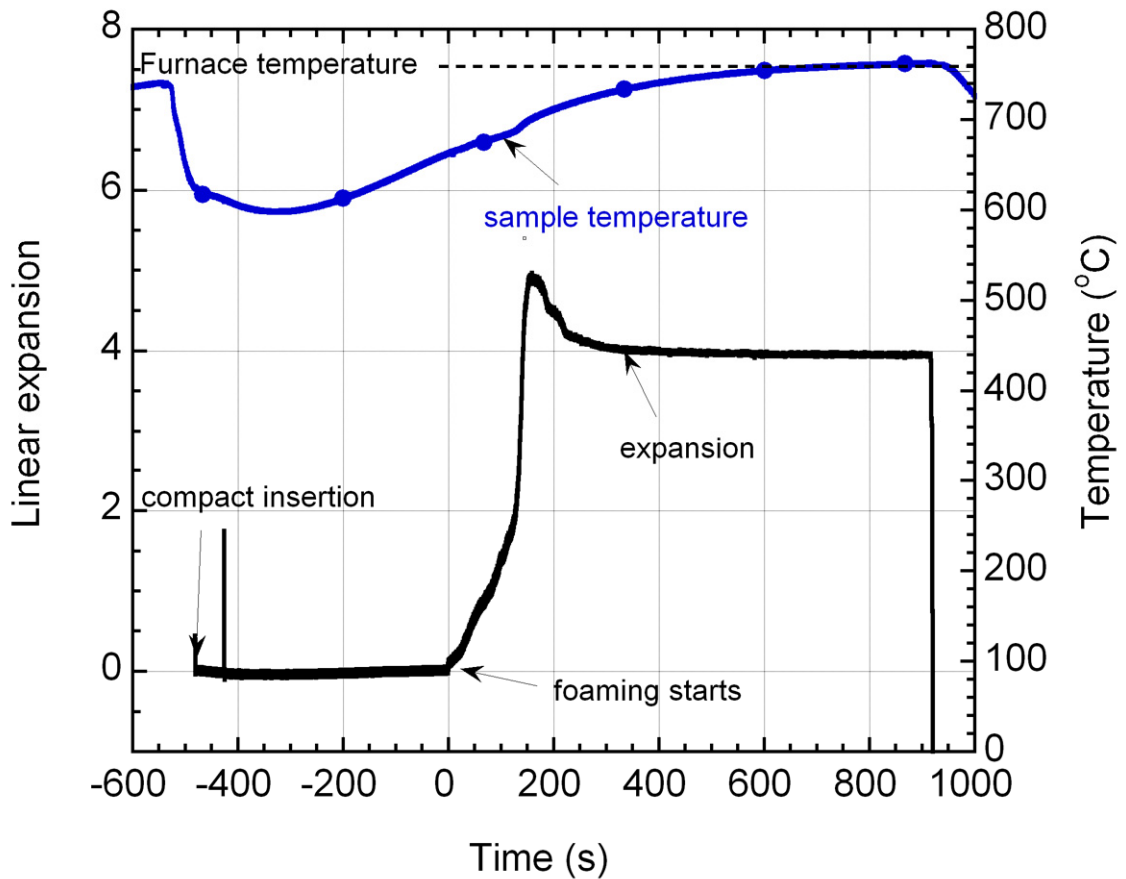


Figure 5.10. Typical expansion-time and temperature time graph of foaming experiments.

5.4. Compression and Hardness Testing

For the compression tests, the foams were taken from the furnace at the maximum expansion. At the maximum expansion, the foam is supposed to have the most homogeneous cell size distribution. The compression test samples were prepared by cutting cylindrical test samples, 25 mm in diameter and 20 mm in length, using an electro discharge machine. Quasi-static compression tests were conducted using a

displacement-controlled SHIMADZU AG-I universal tension-compression test machine with a cross-head speed of 2.5 mm/min, corresponding to a strain rate of $2 \times 10^{-3} \text{ s}^{-1}$. At least three compression tests were performed for each foam sample. The nominal strain (ϵ) and stress (σ) in compression test were calculated using the following relations;

$$\epsilon = \frac{\delta}{L_0} \quad (5.2)$$

and

$$\sigma = \frac{P}{A_0} \quad (5.3)$$

where δ , P , L_0 and A_0 are the displacement, the load and the initial length and cross-sectional area of the tested specimen.

Micro hardness test were performed on epoxy mounted foam samples polished down to $1 \mu\text{m}$ using a Schimadzu Microhardness testing device (HMV-2 Series) (Figure 5.11(a)). Tests were conducted on the locations of the cell walls where there were no ceramic particles in order to prevent the effect of ceramic particles on the hardness (Figure 5.11 (b)). At least 10 hardness tests were performed for each specimen with an applied load of 0.4903N for 10 seconds.

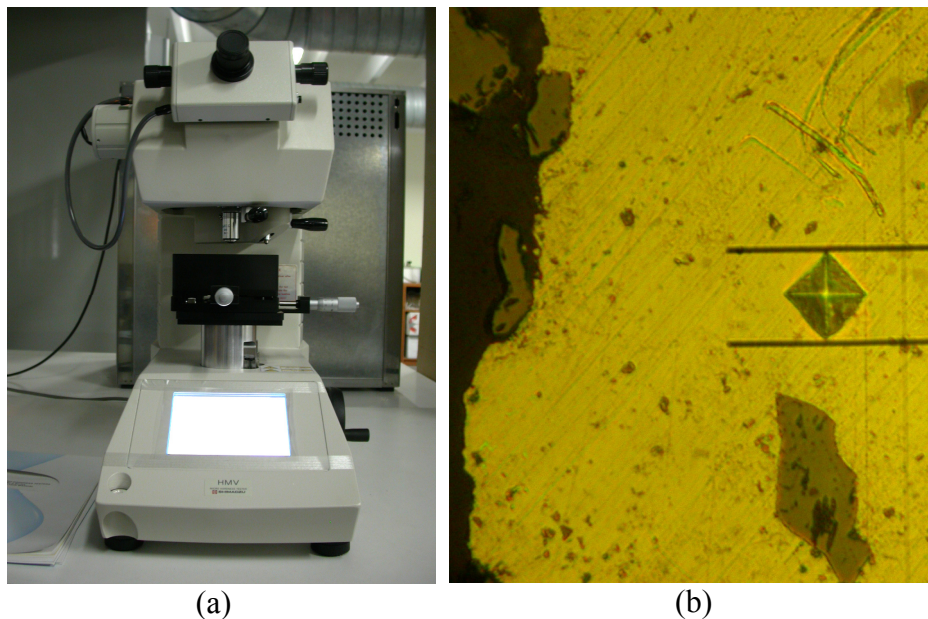


Figure 5.11. (a) Microhardness measuring device and (b) view of the indentation part on the cell wall after force applied.

5.5. Microstructure Analysis

The microscopic analysis was performed using a Nikon Eclipse L150 optical microscope and a Philips XL30-SFEG SEM with an Energy Dispersive X-ray (EDX). The polished cross-sections of epoxy-mounted foam samples were etched with Kroll's reagent (3 cm³ of HF and 6 cm³ of HNO₃ in 100 ml of H₂O).

CHAPTER 6

FOAM EXPANSION

Typical linear expansion-time and temperature-time graph of a foamed Al powder compact is shown in Figure 6.1. The expansion-time curve virtually consists of 4 foaming stages as marked in the same figure with the numbers in the circles (1 through 4). The compact expansion is noted to start at a temperature of 663 °C, below the melting temperature of pure Al (~670 °C) and increases with increasing foaming time in the first and second regions. The transition from Region 1 to Region 2 occurs roughly after about 120 s at about 683 °C (Figure 6.1), just above the melting temperature of pure Al. Owing to the complete melting of the compact, the expansion increases abruptly in the second region until a maximum value (LE_{max}) in about 25 s following the first region (145 s after foaming starts). The expansion then slightly decreases in region 3 and remains almost constant in Region 4, which is taken as LE. During foaming experiments, although the furnace temperature was kept constant at 750 °C, as soon as the cold steel mold accommodating the foamable compact was inserted, the furnace temperature decreased to ~600 °C. After insertion, the furnace was heated up to ~750 °C and the temperature of the compact raised to the furnace temperature after about 600 s.

6.1. The Effect of TiH₂ wt% on the Foam Expansion

The linear expansion-time and temperature-time graphs of Al compacts with 0.6, 0.8 and 1.0 wt% TiH₂ additions are shown in Figure 6.2. Average LE_{max} values for the compacts with 0.6, 0.8 and 1.0 wt% TiH₂ addition are further tabulated in Table 6.1, together with compacts coding, dimensions and density. The maximum linear expansions of the compacts with 0.6, 0.8 and 1.0 wt% of TiH₂ are sequentially 3.525, 4.145 and 4.08. The maximum linear expansion increases slightly with increasing wt% of TiH₂, showing an insignificant effect of TiH₂ wt% on the compact expansion within the investigated wt% of TiH₂. In the thesis, the compacts were foamed using 1.0 wt% TiH₂ addition. Figures 6.3(a) and (b), Figures 6.4(a) and (b) and Figures 6.5(a) and (b)

show the pictures of foamed Al compacts and their cross sections with 0.6, 0.8 and 1.0 wt% of TiH_2 , respectively.

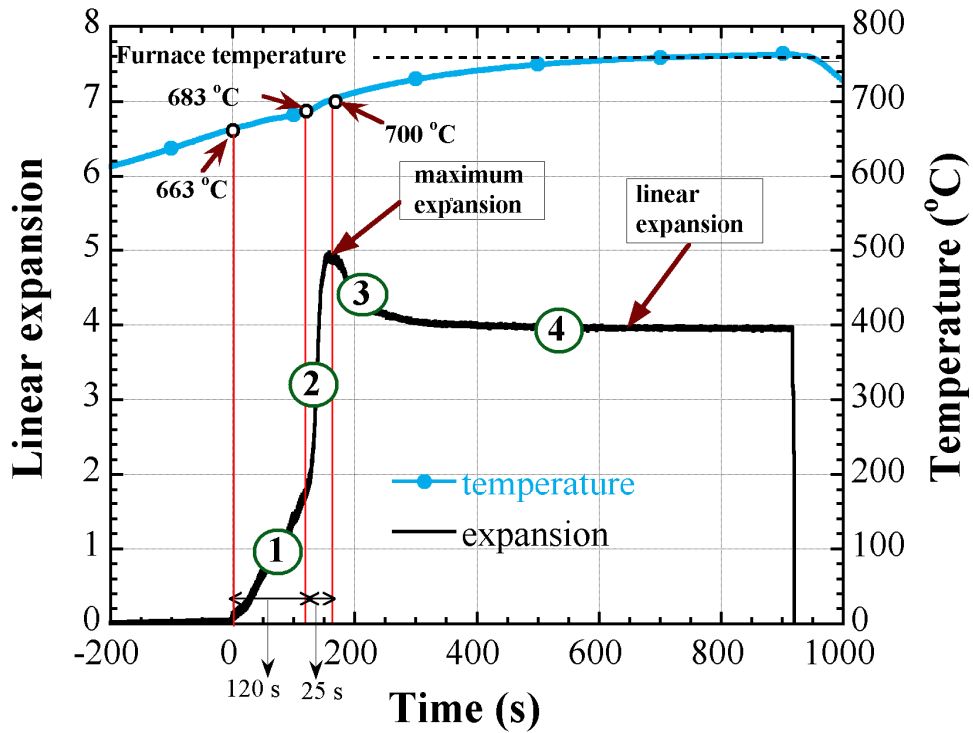


Figure 6.1. Typical linear expansion and temperature vs. time graph of foaming Al compact.

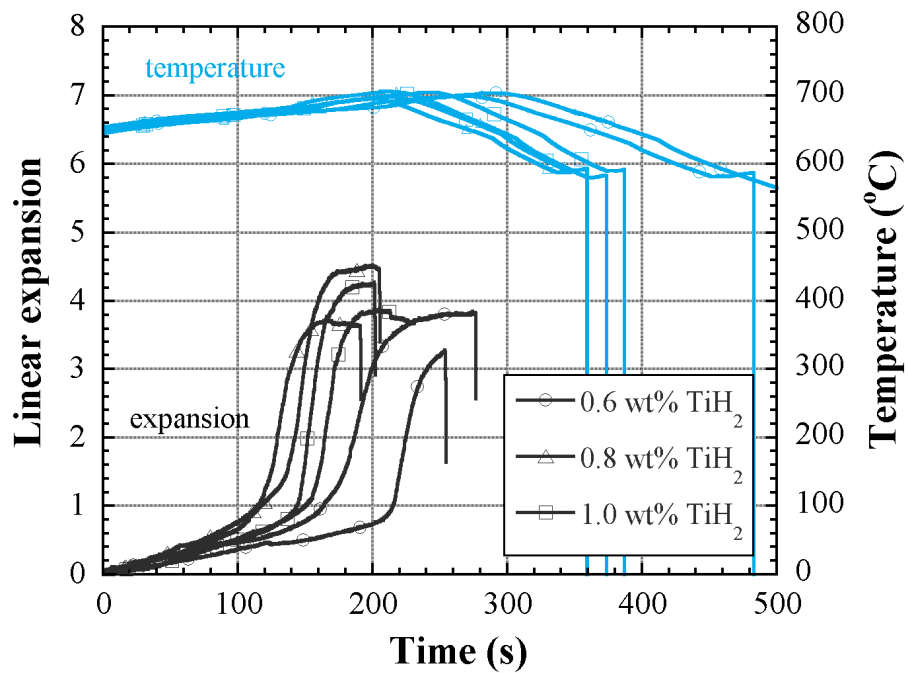


Figure 6.2. The expansion-time and temperature-time graphs of Al compacts with varying wt% of TiH_2 .

Table 6.1. The coding, dimensions and density of the compacts with various TiH₂ addition.

Specimen code	Thickness (mm)	Weight (g)	Density (g cm ⁻³)	Relative density	LE _{max}
P0.TiH2.06%-01	14.9	7.90	2.681	0.990	3.23
P0.TiH2.06%-02	14.8	7.78	2.677	0.988	3.82
P0.TiH2.08%-01	14.7	7.81	2.679	0.988	4.54
P0.TiH2.08%-01	14.9	7.89	2.676	0.987	3.75
P0.TiH2.1%-01	14.8	7.81	2.681	0.988	4.27
P0.TiH2.1%-01	15.0	7.93	2.680	0.987	3.89



Figure 6.3. Pictures of the foams with 0.6 wt% TiH₂ blowing agent addition (at maximum expansion); (a) uncut and (b) cross-section.



Figure 6.4. Pictures of the foams with 0.8 wt% TiH₂ blowing agent addition (at maximum expansion); (a) uncut and (b) cross-section.



Figure 6.5. Pictures of the foams with 1.0 wt% TiH₂ blowing agent addition (at maximum expansion); (a) uncut and (b) cross-section.

In order to verify the effect of TiH₂ wt% on the foam cellular structure, the number of cells and cell sizes of the cross sectional pictures of the foam samples were measured microscopically. The variation of the number of cells and average cell sizes with TiH₂ wt% are shown in Figure 6.6. The lowest TiH₂ wt% contained foam has the highest number of cells and the smallest cell size. The number of cells and the cell sizes of the foams of different TiH₂ content, range between 60 and 100 and 2.8 and 3.4 mm respectively, as depicted in Figure 6.6. The differences between the number of cells and cell size partly result from the small differences between the furnace holding times of the compacts. A small difference in furnace holding time may lead to increased extend of foam cell collapse, which results in the reduction in the number of cells and increase in cell size.

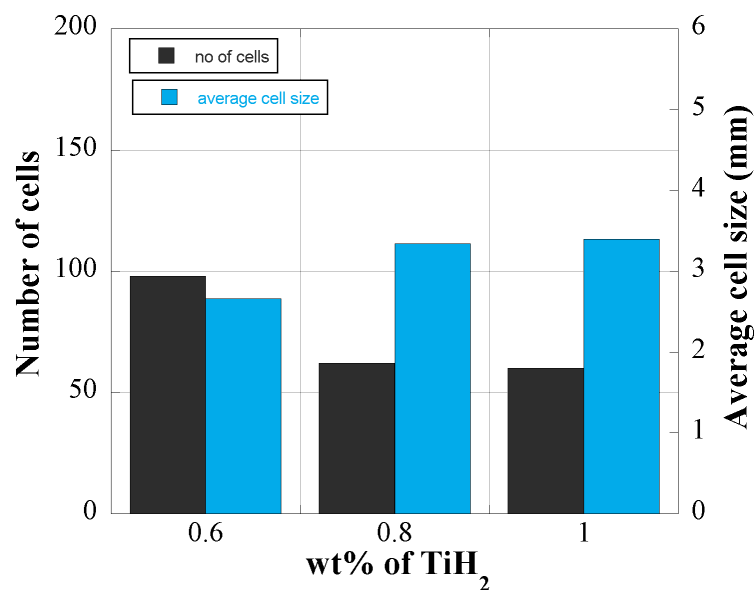
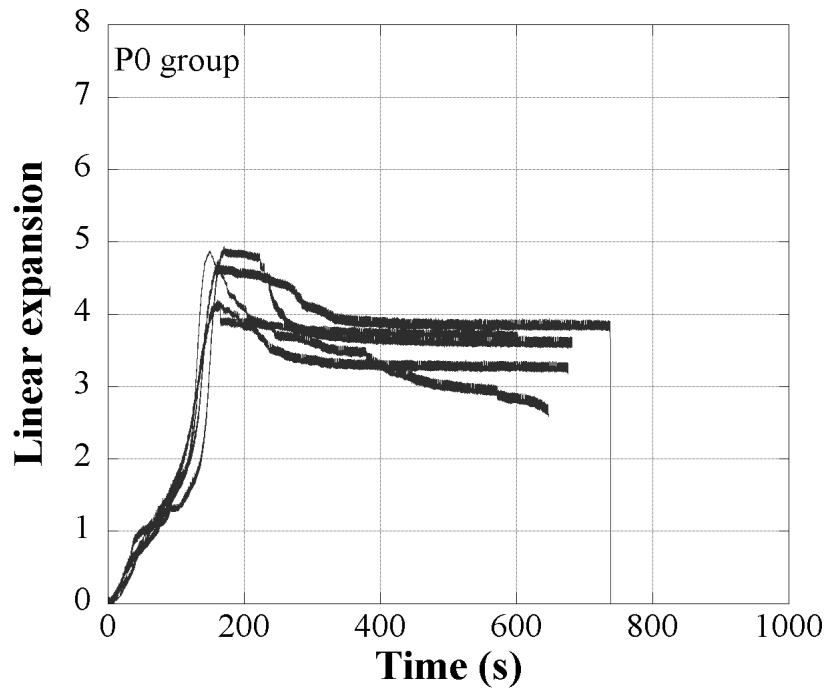


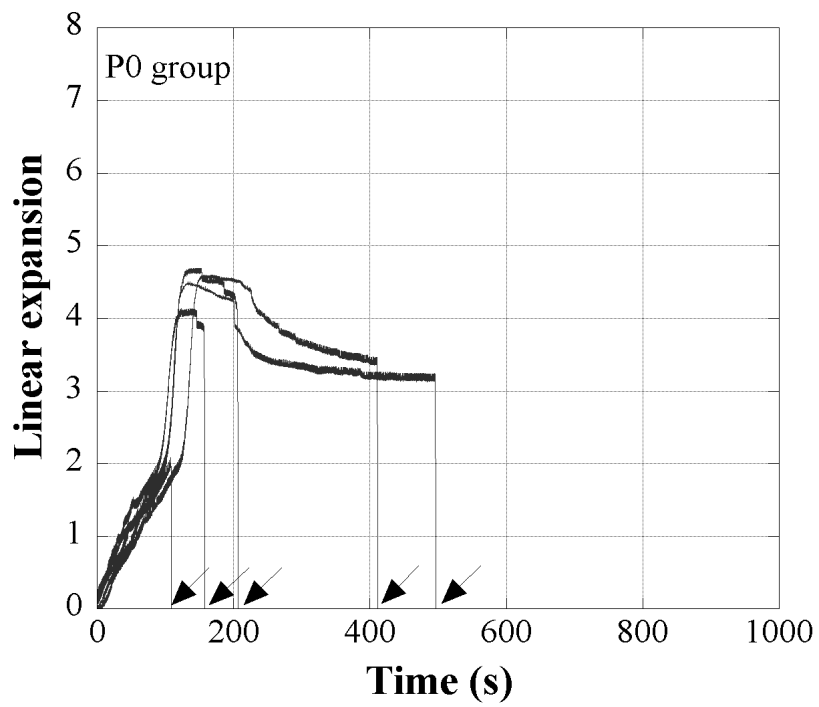
Figure 6.6. The number of cells and cell sizes as function of wt% of TiH₂ addition.

6.2. Expansion of Al Compacts

The expansion-time graphs of Al compacts foamed until about 900 s and prescribed times (interrupted test) are shown in Figures 6.7(a) and (b), respectively. As noted in Figure 6.7(a), the LE_{max} values of the compacts range between 4 and 5, while LE values between 3 and 4. The arrows in Figure 6.7(b) on the time axis show the furnace holding times (100, 150, 200, 400, 500 and 700 s) at which the foams were taken from the furnace. The coding, weight, thickness, density and expansions of Al compacts without SiC addition are further tabulated in Table 6.2. The relative density of Al compacts foamed varies between 0.97 and 0.99. The compacts were prepared at a pressure of 183 MPa. The linear expansion and LE_{max} values vary between 3.25 and 3.87 and 4.06 and 4.84, respectively. Figures 6.8(a) and (b) show the general and cross-sectional pictures of Al foam samples taken from the furnace after a certain furnace holding time, respectively. The final heights of the foam samples in these figures confirm clearly that the linear expansion increases until the maximum expansion (until about 150 s). In addition, the cell size is found to increase as the furnace holding time increases, particular cells become larger at the upper sections of the foam cylinders. The drainage, the accumulation of Al metal at the bottom of foamed compacts, is clearly seen to increase as the furnace holding time increases (Figure 6.8(b)). Another effect of longer furnace holding times is the thickening of the cell walls and cell edges at the bottom and the cell collapse at the upper sections of the foam cylinder. The number of cells and the average cell sizes (diameters) of the foamed compacts taken from the furnace after prescribed furnace holding times are shown in Figure 6.9. The number of cells increases to about 150 until about 150 s furnace holding time; thereafter, decreases below 50 at increasing furnace holding times. Similarly, the average cell size increases above 3 mm at foaming times above 150 s. In accord with the expansion-time graph, the highest number of cells and the smallest cell size are seen when the furnace holding time is about 150 s. It is also found that the cell wall thicknesses at the top sections of the foam are smaller than those at the bottom part of the foam. The difference in cell wall thickness between the top and bottom section increases with increasing foaming time. The mean cell wall thickness values increase from 174 to 277 μm when the foaming time increases from 100 to 500 s.



(a)



(b)

Figure 6.7. Expansion-time graph for (a) pure Al foams (700s) and (b) interrupted foaming experiments.

Table 6.2. The coding, weight, thickness, density and expansions of Al compacts without SiC addition (P0).

Specimen code	Weight (g)	Thickness (mm)	Density (g cm^{-3})	Relative density	LE	LE _{max}
P0.0.1	14.9	7.93	2.648	0.980	3.27	4.13
P0.0.2	15.1	8.01	2.644	0.979	3.62	4.63
P0.0.3	14.9	8.02	2.644	0.979	3.25	4.06
P0.0.4	14.9	7.97	2.644	0.979	3.72	4.84
P0.0.5	14.9	7.97	2.645	0.979	3.87	4.83
P0.0.100	15.1	8.05	2.638	0.976	-	-
P0.0.150	14.9	7.97	2.619	0.969	-	-
P0.0.200	15.0	7.93	2.653	0.982	-	4.58
P0.0.400	15.0	7.93	2.669	0.988	-	4.54
P0.0.500	15.1	7.98	2.669	0.988	3.55	4.83
P0.0.700	14.9	7.90	2.679	0.991	3.62	4.65

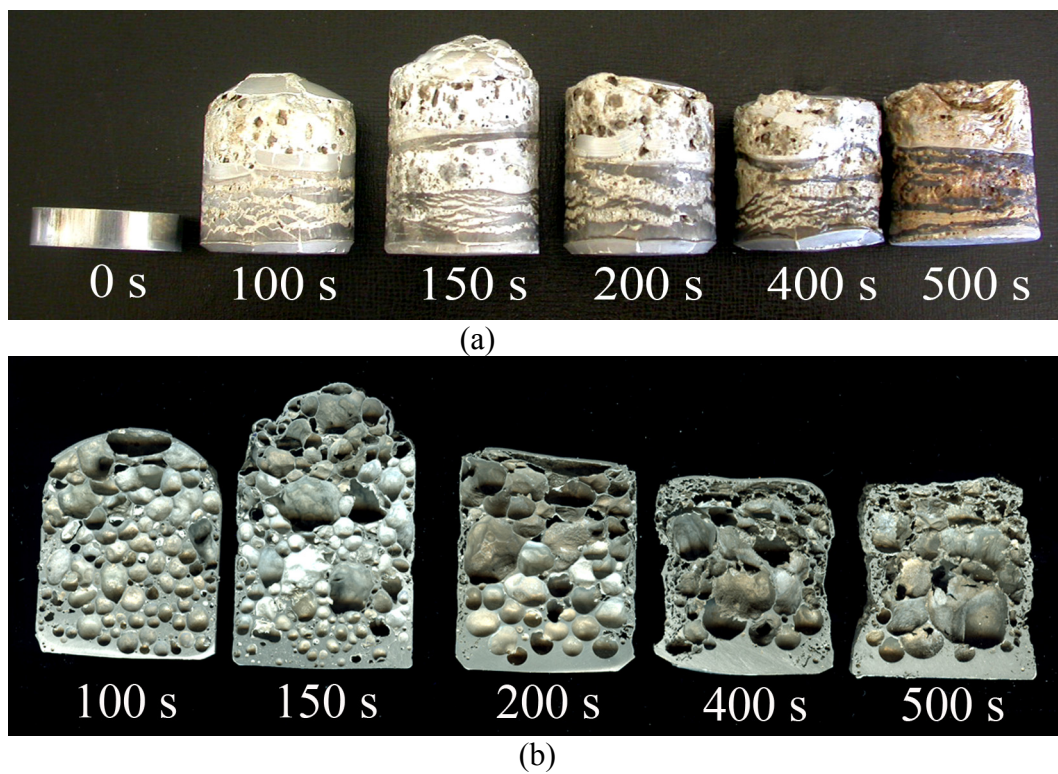


Figure 6.8. (a) Pictures of foamed pure Al compacts at various furnace holding time and (b) corresponding cross sections.

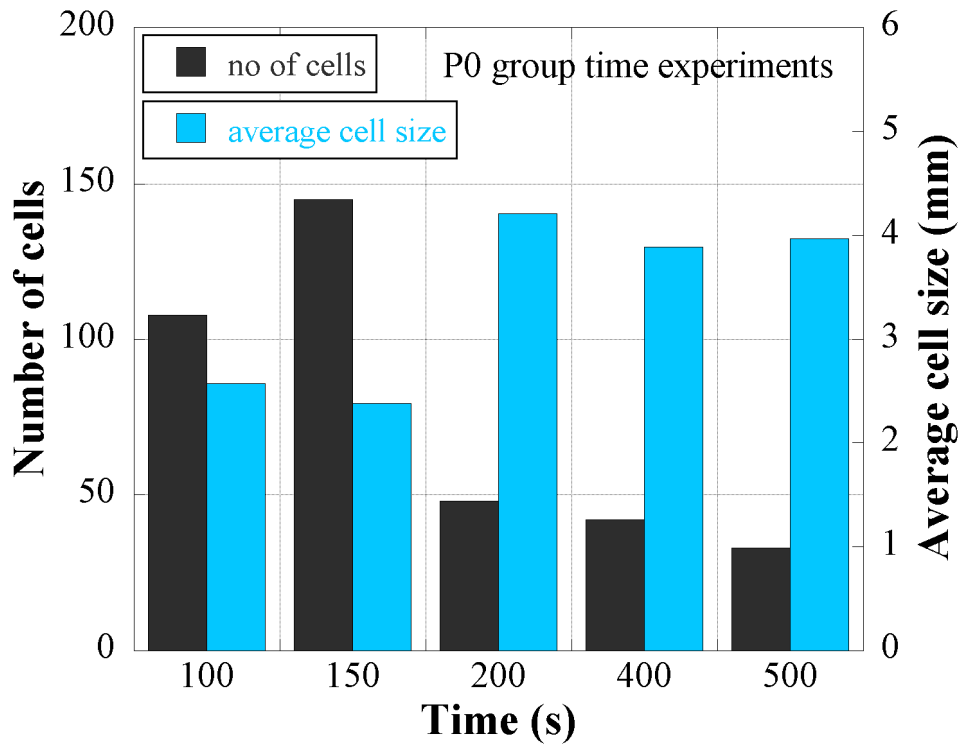


Figure 6.9. The number of cells and cell sizes of foamed Al compacts as function foaming time.

6.3. Expansion of Unsieved P6 and P7 SiC/Al Compacts

The expansion-time graphs of compacts with P6 SiC 5, 10 and 15 wt% addition are shown in Figures 6.10(a), (b) and (c), respectively. The increased wt% of SiC decreases both LE and LE_{max} values. Except 15 wt% SiC addition, the expansion of P6 SiC addition increases the compact expansions over those of Al compacts as shown in Figure 6.10(d). The expansion-time graphs of compacts with 5 wt% P7 SiC addition are further shown in Figure 6.11(a). The expansion values of the compacts with 5 wt% P7 SiC additions are lower than those of the compacts with 5 wt% P6 SiC addition, while higher than those for Al compacts, as shown in Figure 6.11(b).

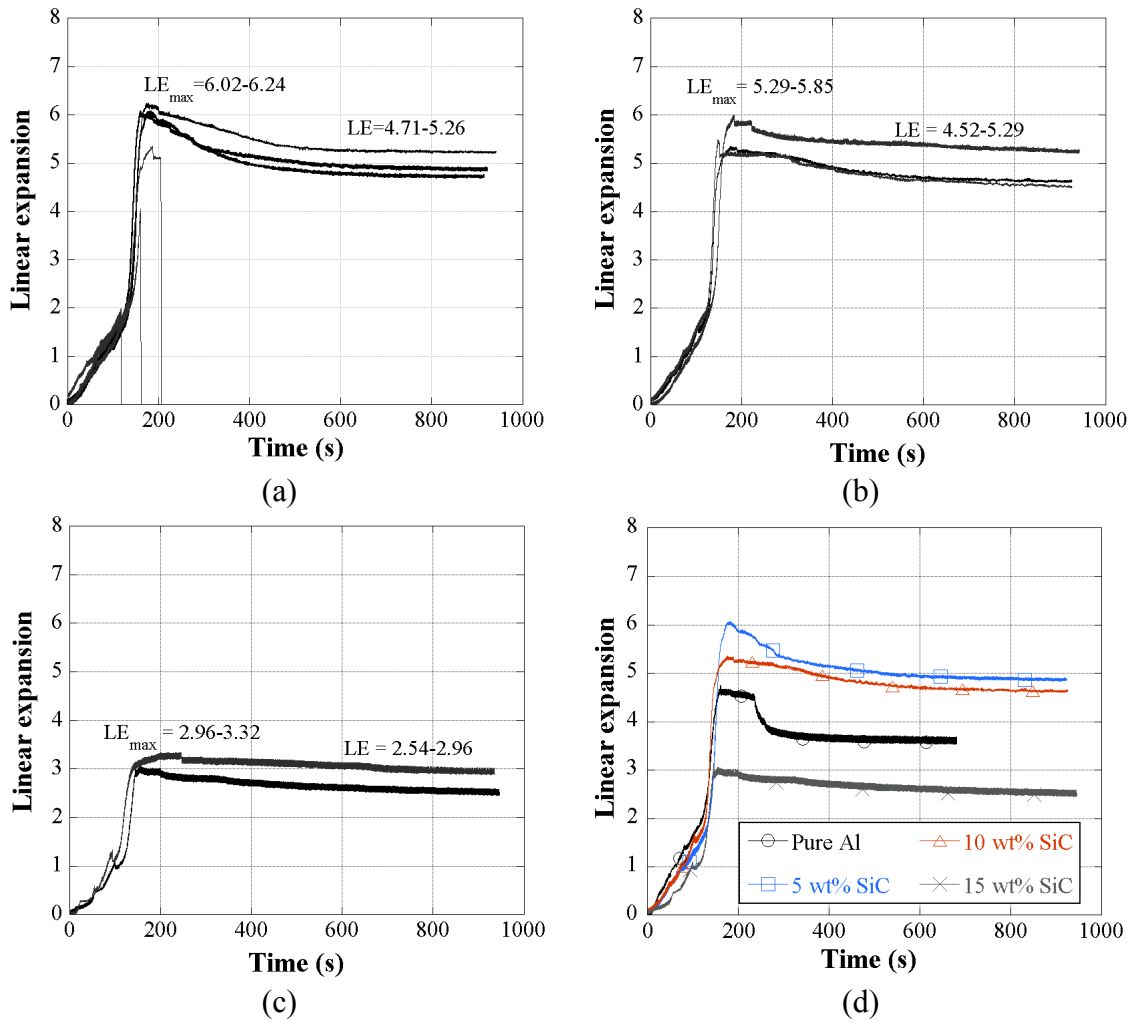


Figure 6.10. Linear expansion-time graphs of the compacts with P6 SiC addition of (a) 5 wt%, (b) 10 wt% and (c) 15 wt% and (d) comparison of particle percentage.

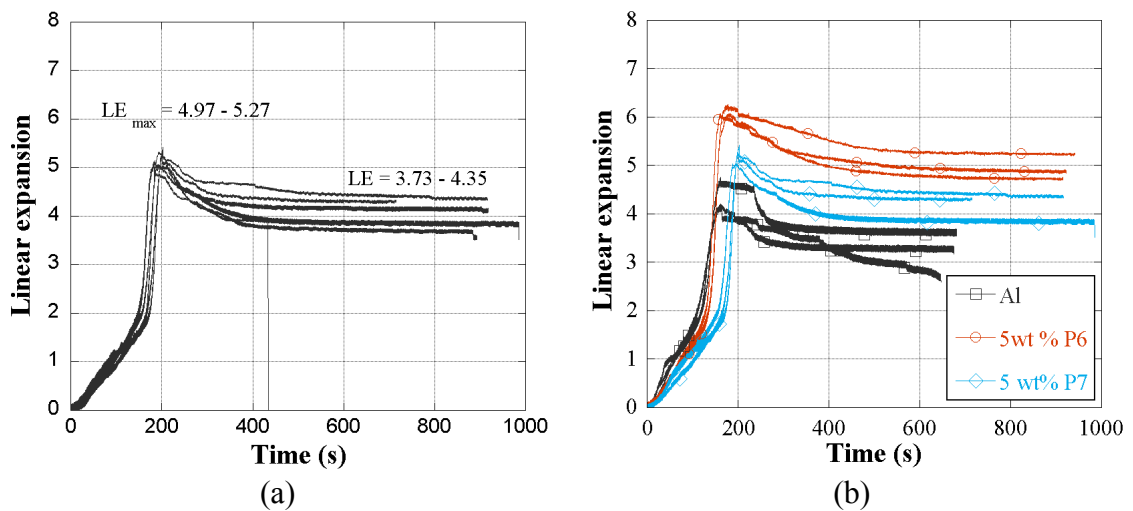


Figure 6.11. (a) Linear expansion-time graphs of the compacts with 5 wt% P7 SiC addition and (b) linear expansion-time graphs of the compacts with 5wt% P6 and P7 SiC addition and Al compact.

The coding, weight, thickness, density and expansions of P6 and P7 SiC/Al compacts are further tabulated in Table 6.3. The compacts were prepared at a pressure of 183 MPa. The linear expansion and LE_{max} values of P6 SiC/Al compacts vary between 4.71 to 5.26 and 6.02 to 6.24 for 5 wt% addition, 4.66 to 5.29 and 5.29 to 5.85 for 10wt% addition and 2.54 to 2.96 and 2.96 to 3.32 for 15wt% addition. The linear expansion and LE_{max} values of P7 SiC/Al compacts vary between 3.73 to 4.35 and 4.97 to 5.27 for 5 wt% addition. The relative density of the compacts varies between 0.957 and 0.983. The smallest relative density is found in 15 wt% P7 SiC/Al compacts, containing relatively high wt% of particles. The compaction pressures used are 210, 240 and 250 MPa for P6 SiC/Al compacts with 5, 10 and 15 wt% SiC addition, respectively, and 260 MPa for P7 SiC/Al compacts. It was noted that increasing compaction pressures over 250 MPa in P6 SiC/Al compacts resulted in cracking of the compact; therefore, the compaction pressure was kept around 250-260 MPa.

Table 6.3. The coding, weight, thickness, density and expansions of P6 and P7 SiC/Al compacts.

Specimen code		Weight (g)	Thickness (mm)	Density (gcm ⁻³)	Relative density	LE	LE_{max}
P6 5wt% SiC	1	15.3	8.00	2.678	0.981	4.91	6.02
	2	15.2	8.05	2.672	0.978	4.71	6.06
	3	15.2	8.04	2.670	0.978	5.26	6.24
P6 5wt% SiC (time group)	100 s	15.2	8.04	2.675	0.980	-	-
	150 s	15.2	8.01	2.684	0.983	-	-
	200 s	14.9	7.92	2.672	0.978	-	-
	400 s	14.8	7.85	2.665	0.976	-	-
	500 s	14.8	7.88	2.644	0.968	-	-
P6 10wt% SiC	1	15.4	8.11	2.679	0.971	4.66	5.29
	2	15.4	8.12	2.678	0.970	4.52	5.37
	3	15.3	8.07	2.694	0.976	5.29	5.85
P6 15wt% SiC	1	15.5	8.14	2.670	0.957	2.54	2.96
	2	15.5	8.15	2.675	0.959	2.96	3.32
P7 5wt% SiC	1	15.2	8.07	2.664	0.976	3.73	5.02
	2	15.2	8.08	2.668	0.977	3.84	4.97
	3	15.2	8.04	2.672	0.978	4.35	5.17
	4	15.3	8.11	2.668	0.977	4.28	5.06
	5	15.3	8.09	2.670	0.978	4.13	5.27
	6	15.2	8.07	2.669	0.977	3.9	5.06

Figure 6.12 (a) and (b) show sequentially the pictures of 5 wt% P6 SiC/Al compacts and their sectioned and polished cross-sections recovered in the interrupted tests after prescribed foaming times. The numbers in these figures correspond to the foaming time at which the foamed compacts were taken from the furnace. In accord with expansion-time graph shown in Figure 6.10, the foam expansion is high until about 150 s, slightly decreases at 200 s and remains almost constant after about 300 s (Figure 6.12(a)). The cells are initially noted to be relatively small and become larger as the foaming time increases (Figure 6.12(b)). The cell collapse/rupture is clearly seen at the upper sections, while a dense metal layer is seen at the bottom sections (Figure 12(b)). This dense bottom layer resulted from liquid metal drainage. The thickness of this layer increases as the foaming time increases as seen in Figure 6.12(b). As compared with Al compacts, the drainage is significantly reduced with SiC particle addition, while the cell collapses are still seen. The collapses of the cells are more obvious for 10 and 15 wt% additions. The increasing wt% of particles in P6 SiC/Al compact is also found to result in irregular cell formation (Figure 6.13(b)).

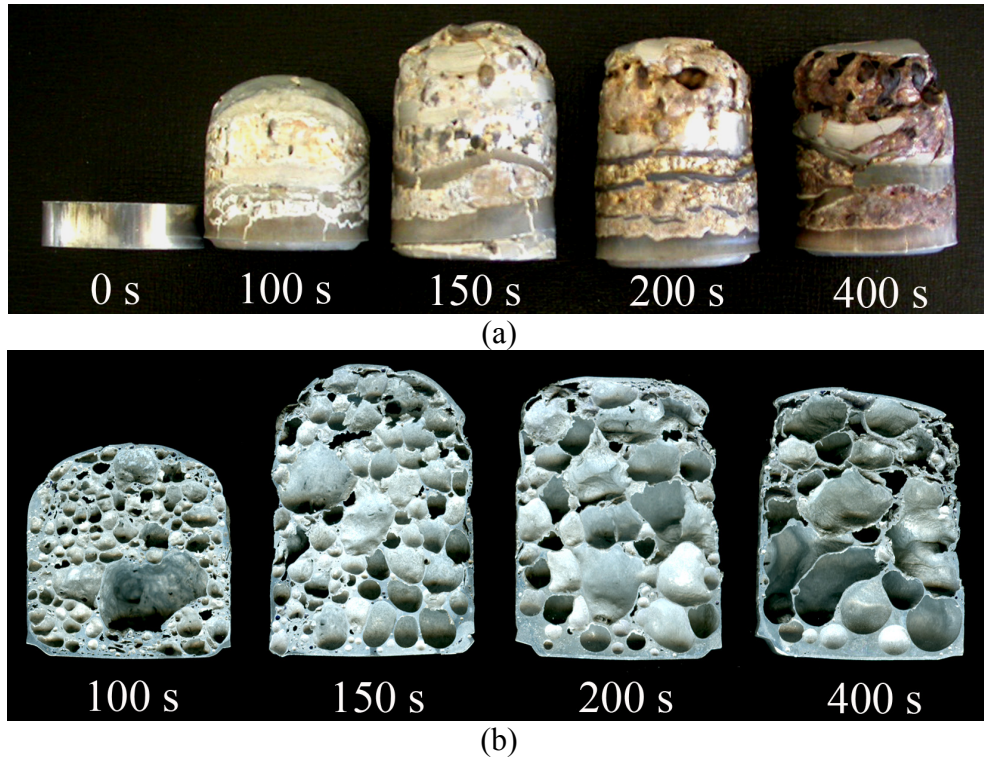


Figure 6.12. (a) Foamed 5 wt% P6 SiC/Al compact (interrupted foaming) and (b) the corresponding cross-sections.

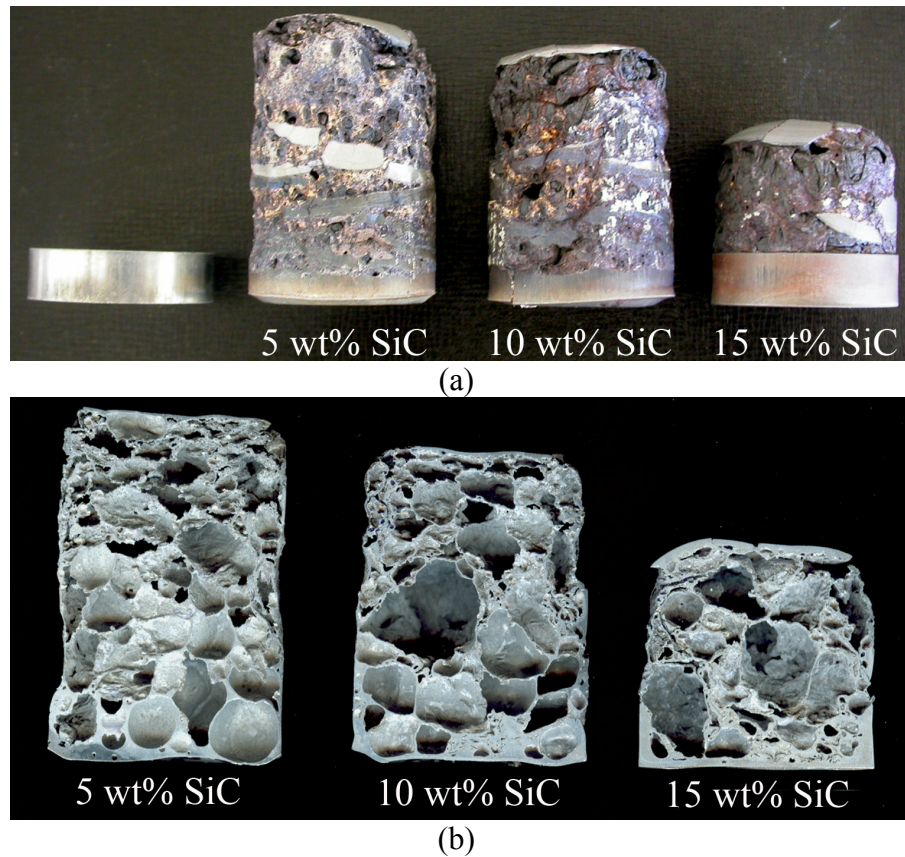


Figure 6.13. (a) The pictures of foamed P6 SiC/Al compacts with 5, 10 and 15 wt% SiC addition and (b) their cross sections after 900 s furnace holding time.

Similar with Al compacts, the number of cells decreases and the cell size increases with the increasing furnace holding times in foamed P6 SiC/Al compacts as shown in Figure 6.14(a). The number of cells decreases from about 100 at 100 s furnace holding time to about 50 at the furnace holding times of 200 and 400 s. Average cell size increases from 2 mm to 4.5 mm within the same range of furnace holding time. Significant increase in cell size and decrease in number of cells occur when wt% of P6 SiC particles increases from 5 and 10 wt% to 15 wt% as shown in Figure 6.14(b). Microscopic observations of the cell walls at the top and bottom sections show that drainage is further not extensive as compared with foamed Al compacts.

The general and cross-sectional pictures of 5 wt% P7 SiC/Al foamed compacts after 400 and 900 s furnace holding time are shown in Figures 6.15 (a) and (b), respectively. After 400 s furnace holding time, the cells of the upper sections of the foam cylinder collapse and the cell walls at the bottom sections become thicker. This shows a significant extent of the drainage. The cell collapse is seen to occur earlier than foamed P6 SiC/Al compacts with same wt% of particle addition.

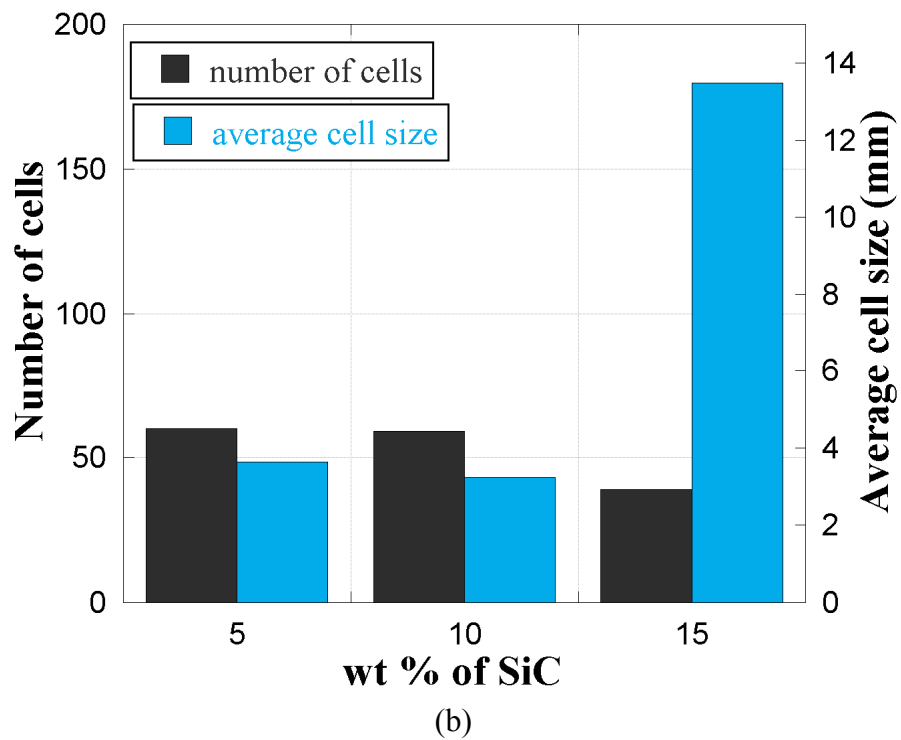
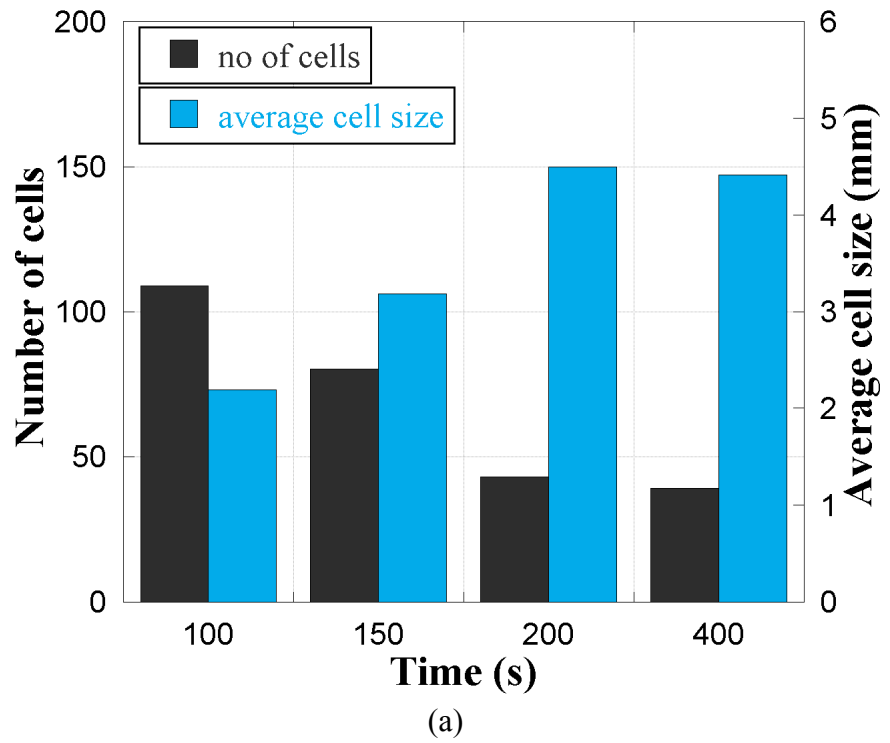
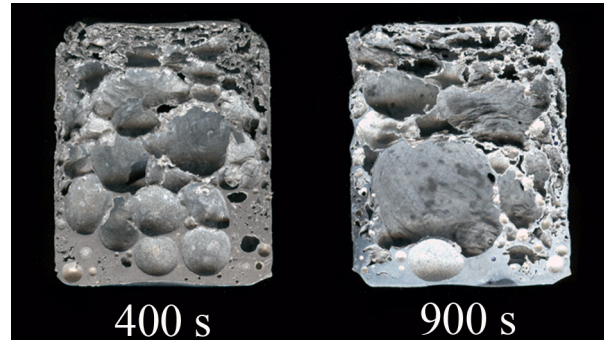


Figure 6.14. (a) The effect of furnace holding time (5 wt% SiC) and (b) wt% of SiC addition on the number of cells and cell sizes (900 s) of foamed P6 SiC/Al compacts.



(a)



(b)

Figure 6.15. (a) The pictures of foamed P7 SiC/Al compacts and (b) their cross sections after 900 s furnace holding time.

6.4. Expansion of Nano SiC/Al Compacts (P10)

The expansion-time graphs of compacts with 0.05, 0.1 and 0.15 wt% of P10 SiC addition are shown in Figure 6.16. The expansions of these compacts first increase to about 3 (Figure 6.16) but, then drops significantly. The coding, weight, thickness, density and expansions of P10 SiC/Al compacts are further tabulated in Table 6.4. The relative density of the compacts varies between 0.975 and 0.985. The compacts with 0.15 wt% ceramic addition were prepared by mixing the Al and SiC powder using a ball milling machine at 500 rpm for 2 h. The compacts were pressed at a pressure of 183 MPa. The linear expansion and LE_{max} values of the compacts vary between 0.83 and 1.41 and 1.2 and 3.63 respectively. In Figure 6.17(a), the temperature-expansion-time graphs of 0.15 wt% SiC/Al compacts are shown. The linear expansion values of these compacts are below 2. In addition, the decrease in heating rate delays the foaming without affecting LE and LE_{max} values as shown in Figure 6.17(b). Figure 6.17(c) shows expansion-time graphs of 0.15 wt% SiC/Al compacts with the pictures of the foam structures at different furnace holding times. Considerably large cells with thicker cell

walls are clearly seen in this figure, proving relatively low foaming property of nano SiC/Al compacts.

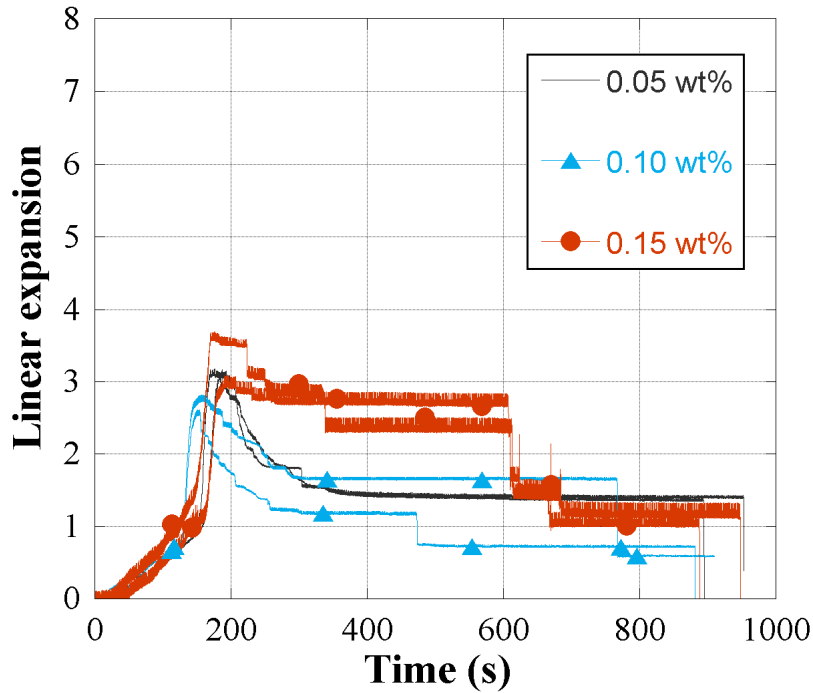


Figure 6.16. Expansion-time graph of foamed 30 nm SiC/Al compacts (P10).

Table 6.4. The coding, weight, thickness, density and expansions of SiC(P10)/Al compacts.

SiC wt%	Specimen code	Weight (g)	Thickness (mm)	Density (g cm^{-3})	Relative density	LE	LE _{max}
0.05	P4.30n.(0.05).I	14.9	7.81	2.662	0.985	1.36	3.15
	P4.30n.(0.05).II	14.7	7.70	2.663	0.985	1.41	3.16
0.1	P4.30n.(0.1).I	14.9	7.81	2.657	0.981	-	2.62
	P4.30n.(0.1).II	14.9	7.80	2.659	0.982	-	2.80
0.15	P4.30n.(0.15).I	14.7	7.68	2.661	0.982	-	3.63
	P4.30n.(0.15).II	14.9	7.85	2.659	0.981	-	3.02
	P10.015-1	15.1	8.30	2.643	0.975	1.23	1.73
	P10.015-2	15.0	8.52	2.648	0.977	1.32	1.79
	P10.015-3	15.1	8.40	2.643	0.975	1.24	1.24
	P10.015-4	15.1	8.20	2.643	0.975	1.1	1.85
	P10.015-5	15.0	8.40	2.638	0.973	0.9	1.63
	P10.015-6	15.0	8.40	2.641	0.974	-	1.2
	P10.015-7	15.2	8.30	2.635	0.972	-	1.26
	P10.015-8	15.2	8.50	2.640	0.974	-	1.76
	P10.015-9	14.2	7.75	2.637	0.973	0.83	1.7
	P10.015-10	14.4	7.80	2.640	0.974	-	-

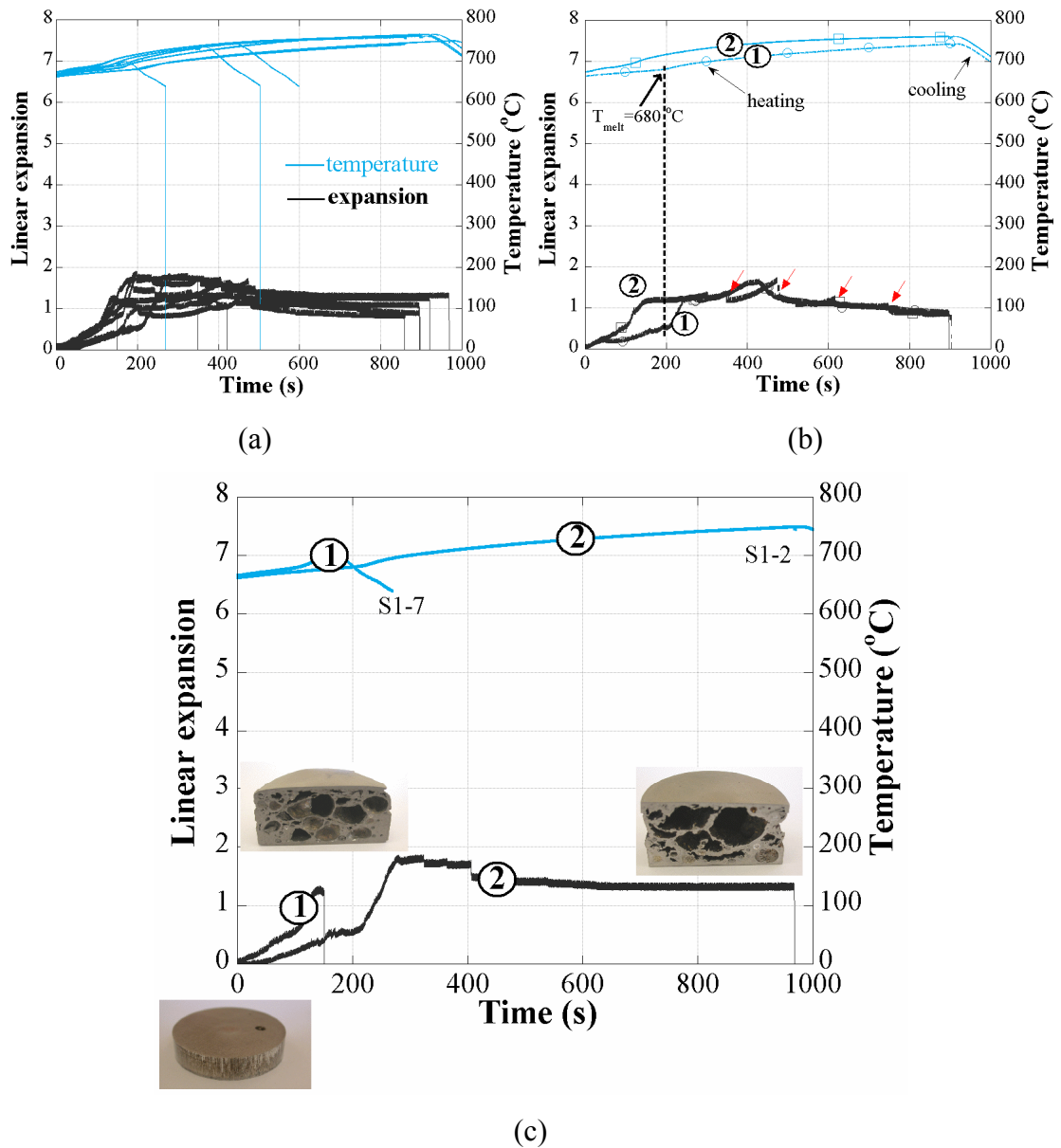


Figure 6.17. (a) Expansion-time-temperature graphs of 0.15 wt% nano SiC/Al compacts (b) effect of heating rate (c) foam structure at different furnace holding times.

In the next group of compacts, the powders were mixed in a low speed mixing device in a closed container with the ceramic balls of 6 mm in diameter. The compacts prepared by using ceramic balls are coded as P10.st. The coding, weight, thickness, density and expansions of these groups of the compacts are further tabulated in Table 6.5. The expansion-time graphs of the compacts with 0.013, 0.05, 0.1 and 0.15 wt% nano SiC addition are sequentially shown in Figures 6.18 (a-d). Nano SiC particle addition of 0.0133 wt% as seen in Figure 6.18 (a) results in very poor expansions with an average LE_{max} value of 0.96. The foam structure is composed of few cells with thick

and non-homogeneous cell wall thickness (Figure 6.19). SiC addition of 0.05 wt% however yields the highest average LE_{max} value, 3.08 (Figure 6.18(b)). The average maximum linear expansion values of 0.10 and 0.15 wt% SiC additions are 2.81 and 2.26, respectively (Figures 6.18(c) and (d)). By considering the cell size, 0.05 wt% addition results in the most homogeneous cell size distribution (Figure 6.19). The foam with 0.05 wt% SiC addition contains 60 cells at the maximum expansion, which is nearly twice as much as the foams with 0.1 and 0.15 wt% addition (Figure 6.20). It is also noted that, at longer furnace holding times (900 s), the collapse of cells is not prevented by the nano particle addition.

Table 6.5. The coding, weight, thickness, density and expansions of SiC (P10.st)/Al compacts.

Specimen code	SiC wt%	Weight (g)	Thickness (mm)	Density ($g\ cm^{-3}$)	Relative density	LE_{max}
P10.st.0133.01	0.0133	14.9	7.90	2.662	0.981	1.18
P10.st.0133.02	0.0133	14.9	7.86	2.669	0.983	0.73
P10.st.05.01	0.05	14.9	7.87	2.663	0.981	3.51
P10.st.05.02	0.05	14.9	7.84	2.664	0.981	2.64
P10.st.10.01	0.10	14.8	7.85	2.659	0.980	2.91
P10.st.10.02	0.10	14.9	7.85	2.660	0.980	2.70
P10.st.15.01	0.15	14.7	7.76	2.657	0.979	2.37
P10.st.15.02	0.15	14.8	7.78	2.660	0.980	2.14

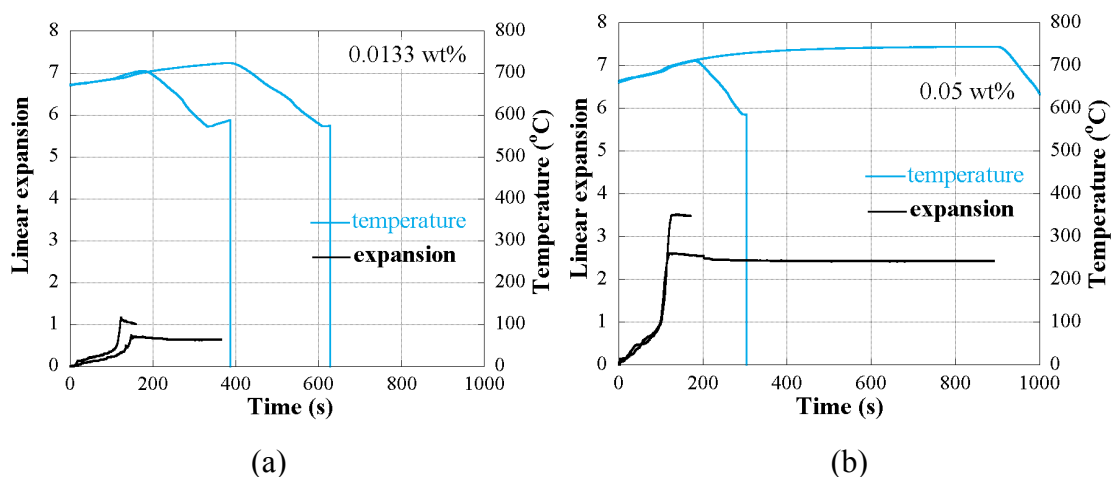


Figure 6.18. Expansion behavior of nano size SiC added foams with (a) 0.0133 wt%, (b) 0.05 wt%, (c) 0.10 wt% and (d) 0.15 wt% particle additions.

(cont. on next page)

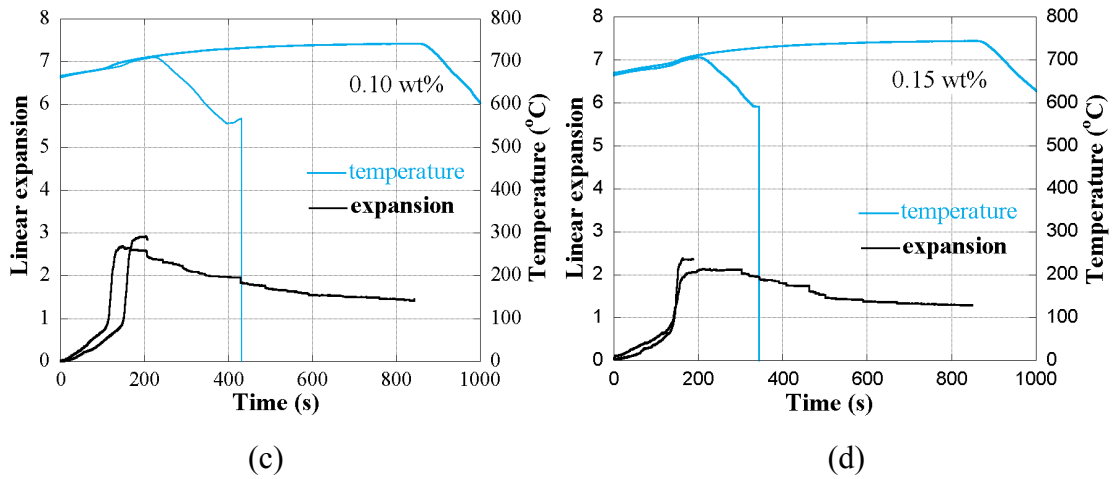
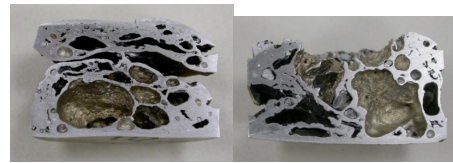


Figure 6.18. (cont.)

Maximum expansion 15 min holding *Maximum expansion 15 min holding*



0.0133 wt% nano SiC



0.05 wt% nano SiC



0.10 wt% nano SiC

Figure 6.19. Pictures of the nano size SiC added P10 foams and their sections at maximum expansion and after 900 s furnace holding time.

(cont. on next page)



0.15 wt% nano SiC

Figure 6.19. (cont.)

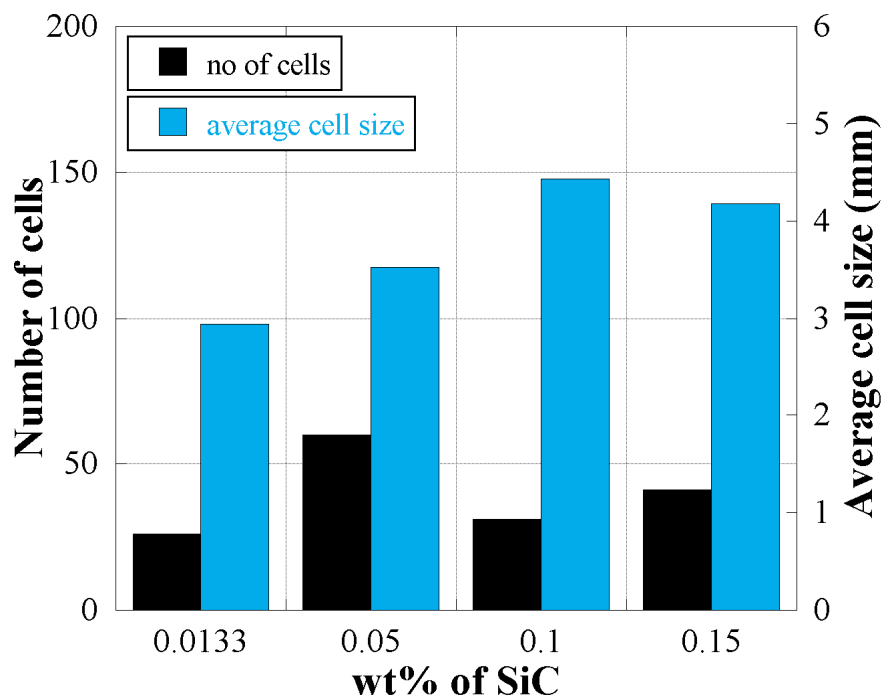


Figure 6.20. Number of cells and cell sizes of foamed nano SiC/Al compacts at the maximum expansion.

6.5. Expansion of Whisker SiC (P9)/Al Compacts

The linear expansion-time graphs of SiC whisker/Al compacts with 0.1-3 wt% addition are shown in Figure 6.21. The expansions are relatively high until about 1wt% addition and above 1 wt% addition the expansions drop sharply. The coding, weight, thickness, density and expansions of these groups of compacts are further tabulated in Table 6.6. The relative density of SiC whisker/Al compacts varies between 0.972 and

0.985. The highest expansion values are found with 0.1 wt% whisker addition as tabulated in Table 6.6. Figure 6.22 show the cell structures of whisker contained foams after 900 s furnace holding time. The dense metal layer at the bottom of 0.1 wt% whisker contained foam is clearly seen in the same figure. The drainage decreases as the wt% increases to 0.5 and 1 wt%. Linear expansion-time-temperature curves for compacts with 0.5 wt% SiC whisker addition is given in Figure 6.23 (a). Linear expansion values tend to increase with the increasing heating rate as seen in the same figure. Similarly the effect of heating rate is also seen in 1 wt% SiC whisker/Al compact (Figure 6.23(b)). The maximum linear expansion is higher for the foamed compact with higher heating rate (Figure 6.24). The cell structures of the 0.5 and 1wt% whisker added foams and Al foams without addition after 900 s furnace holding time are shown in Figure 6.25. The dense metal layer at the bottom section of the foams with whisker addition is seen to decrease considerably as compared with foamed Al compact. It was observed from the cross section of the foams that, number of cells decreased rapidly after reaching the highest number for 0.5 wt% SiC (Figure 6.26). Number of cells formed with the 3 wt% addition is around 30 % of the number of cells with 0.5 wt% addition.

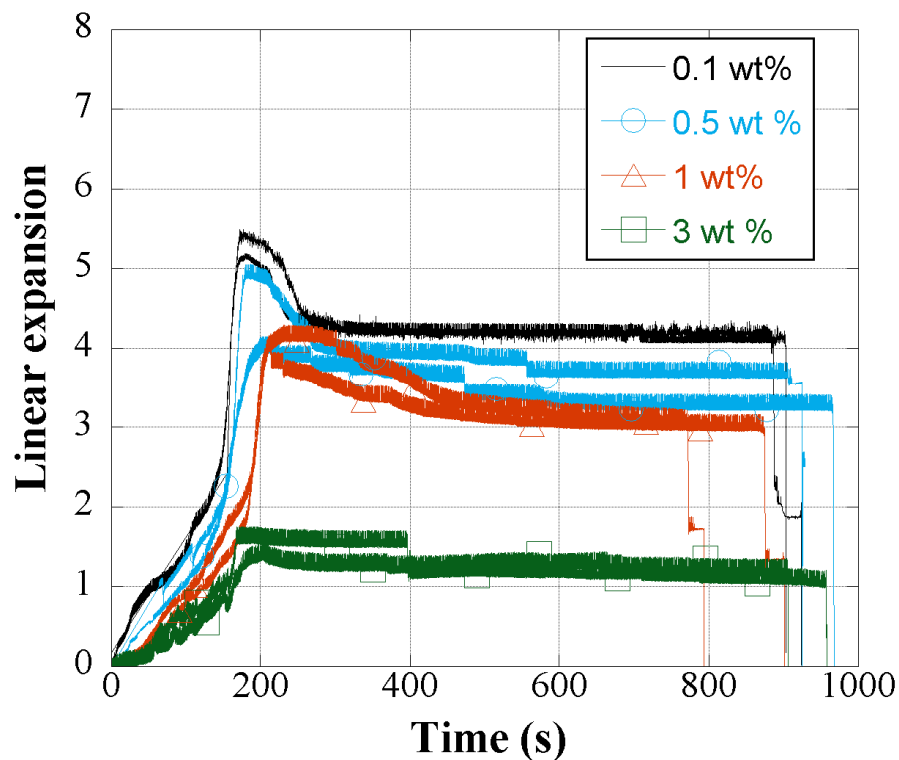


Figure 6.21. Linear expansion-time graphs of SiC whisker/Al compacts (P9).

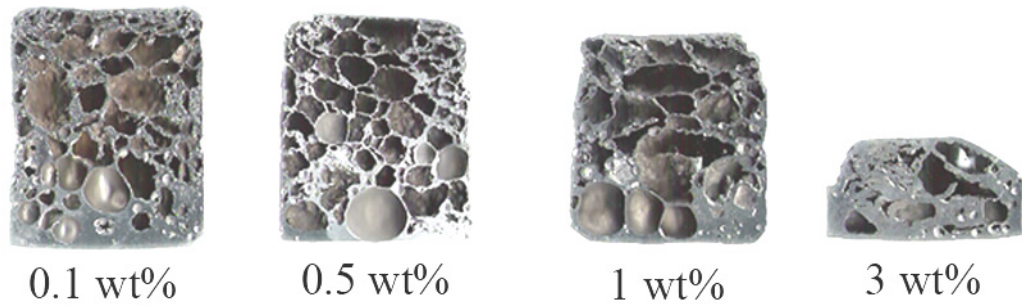
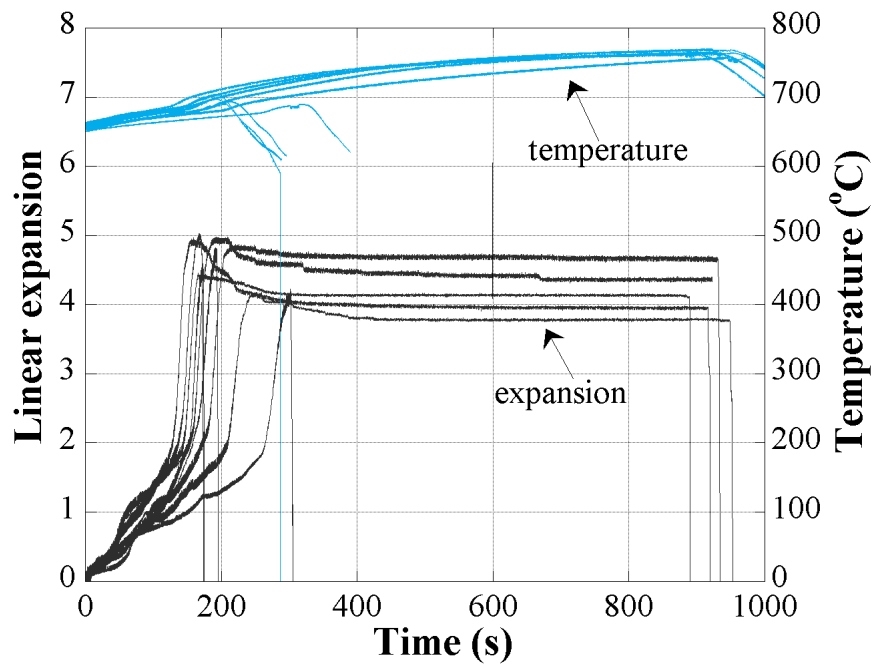


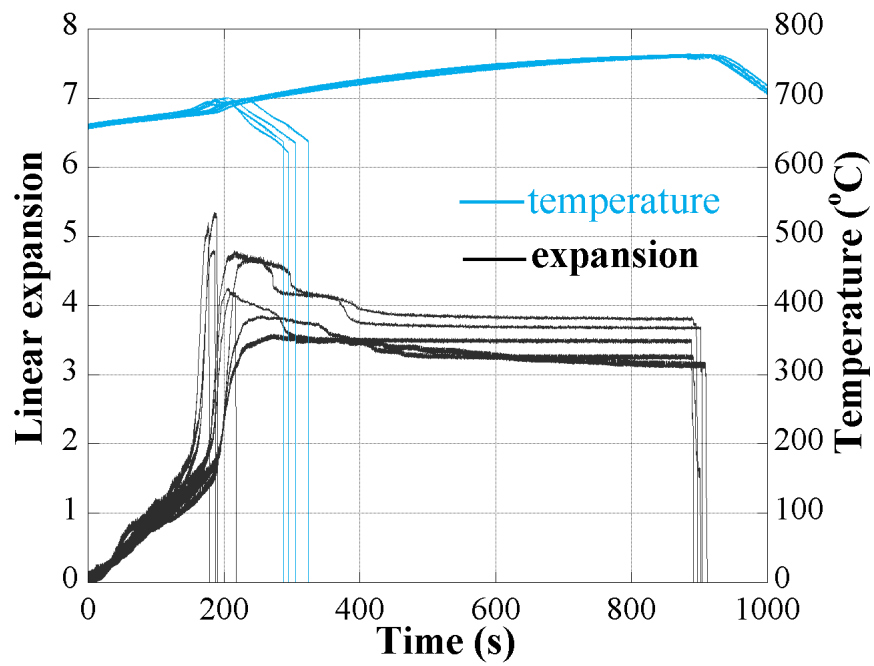
Figure 6.22. The cross sections of foamed SiC whisker/Al compacts (numbers show wt% of SiC whisker after 900 s holding time).

Table 6.6. The coding, weight, thickness, density and expansions of P9 SiC whisker/Al compacts.

Specimen code	SiC wt%	Weight (g)	Thickness (mm)	Density (g cm ⁻³)	Relative density	LE	LE _{max}
P4.w.(0.1).I	0.1	14.9	7.86	2.658	0.983	4.19	5.43
P4.w.(0.1).II		14.4	7.68	2.662	0.985	4.17	5.16
P4.w.(0.5).I	0.5	14.8	7.75	2.665	0.985	3.35	4.08
P4.w.(0.5).II		14.9	7.85	2.663	0.985	3.72	4.96
CBW1-1		15.1	8.03	2.648	0.979	4.68	4.84
CBW1-2		15.1	8.01	2.649	0.979	4.35	4.95
CBW1-3		15.0	7.98	2.648	0.979	3.79	4.14
CBW1-4		14.5	7.68	2.628	0.972	-	-
CBW1-5		15.1	7.98	2.632	0.973	4.15	4.41
CBW1-6		15.1	8.05	2.638	0.975	3.96	4.95
CBW1-7		15.1	8.03	2.642	0.977	-	4.99
CBW1-8		15.0	8.00	2.643	0.977	-	4.56
CBW1-9	15.3	8.14	2.650	0.980	-	4.81	
CBW1-10	15.2	8.08	2.648	0.979	-	4.18	
P4.w.(1).I	1	14.9	7.88	2.654	0.980	3.6	4.2
P4.w.(1).II		14.9	7.88	2.661	0.983	3.08	4.11
CBW2-1		15.1	8.10	2.640	0.975	3.14	3.58
CBW2-2		15.1	8.05	2.642	0.976	3.25	3.85
CBW2-3		14.3	7.65	2.651	0.979	3.8	4.66
CBW2-4		15.1	8.10	2.643	0.976	3.67	4.75
CBW2-5		15.0	8.00	2.649	0.978	3.48	4.25
CBW2-6		14.5	7.70	2.640	0.975	-	4.78
CBW2-7		15.1	8.05	2.648	0.978	-	4.18
CBW2-8	15.2	8.05	2.650	0.979	-	5.34	
CBW2-9	15.1	8.05	2.645	0.977	-	5.16	
P4.w.(3).I	3	14.9	7.84	2.649	0.974	1.26	1.46
P4.w.(3).II		14.9	7.91	2.647	0.973	1.2	1.68



(a)



(b)

Figure 6.23. Linear expansion-temperature-time graphs of SiC whisker/Al compacts (a) 0.5 wt% and (b) 1 wt% whisker addition.

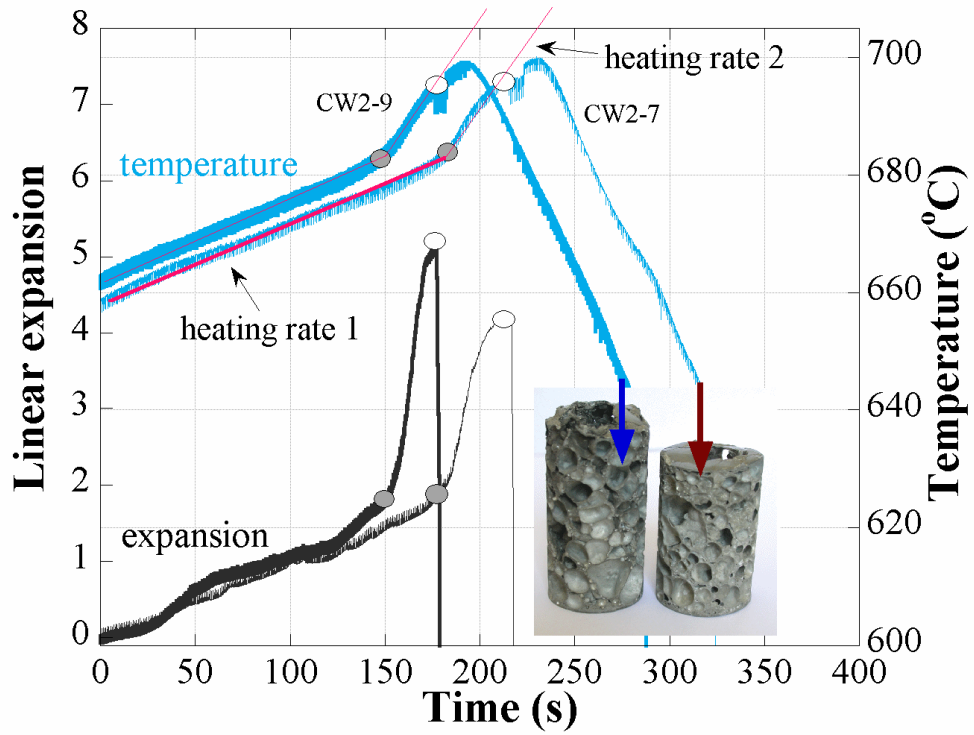


Figure 6.24. Linear expansion- temperature-time graphs of 1 wt% SiC whisker/Al compacts of different heating rate.

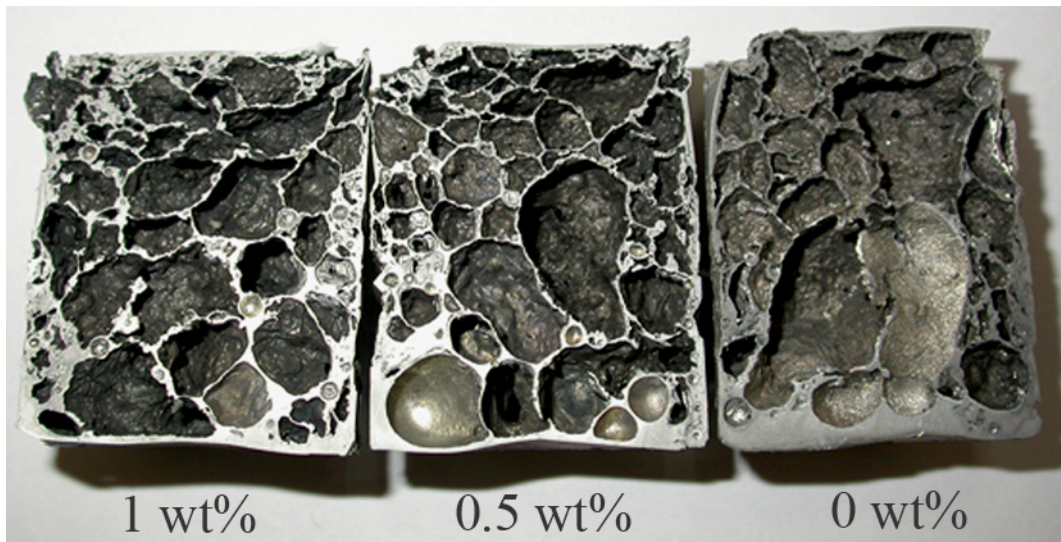


Figure 6.25. The structure of foamed 1 and 0.5 wt% SiC whisker/Al and Al compacts after 900 s furnace holding time.

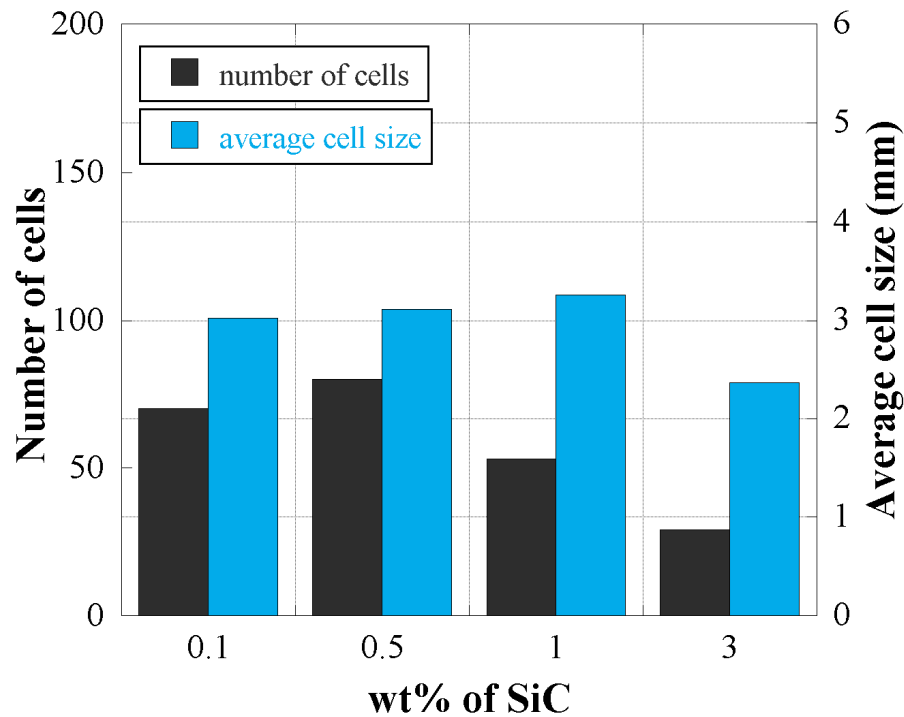


Figure 6.26. Number of cells and cell sizes of foamed whisker shaped SiC/Al compacts at the maximum expansion.

6.6. Expansion of 2 Micron SiC (P8)/Al Compacts

The expansions of P8 SiC/Al compacts vary with the wt% of the particle addition as shown in Figure 6.27. P8 SiC/Al compacts, as seen in the same figure, show almost no expansion after about 1 wt% SiC addition. The coding, weight, thickness, density and expansions of these groups of compacts are further tabulated in Table 6.7. As tabulated in Table 6.7, the expansion values of foamed compact with 3 and 5 wt% addition are relatively low, showing almost no expansion. The cell structures of the foams with 0.1, 0.5 and 1 wt% SiC addition after 900 s furnace holding time are shown in Figure 6.28. At relatively long furnace holding times, the drainage is clearly seen at the bottom sections of the foams.

Table 6.7. The coding, weight, thickness, density and expansions of P8 SiC/Al compacts.

Specimen code	SiC wt%	Weight (g)	Thickness (mm)	Density (g cm ⁻³)	Relative density	LE	LEmax
P4.2.(0.1).I	0.1	14.9	7.77	2.666	0.986	4.12	4.75
P4.2.(0.1).II		14.7	7.67	2.664	0.986	4.23	5.67
P4.2.(0.5).I	0.5	14.3	7.52	2.659	0.983	3.29	4.86
P4.2.(0.5).II		14.9	7.82	2.664	0.985	3.63	4.60
P4.2.(1).I	1	14.9	7.85	2.664	0.984	3.17	4.17
P4.2.(1).II		14.9	7.84	2.665	0.984	3.44	4.87
P4.2.(3).I	3	14.9	7.95	2.642	0.972	0.26	0.26
P4.2.(3).II		14.9	7.96	2.642	0.972	0.17	0.17
P4.2.(5).I	5	15.0	8.03	2.632	0.964	0.105	0.105
P4.2.(5).II		15.0	8.01	2.622	0.960	0.105	0.105

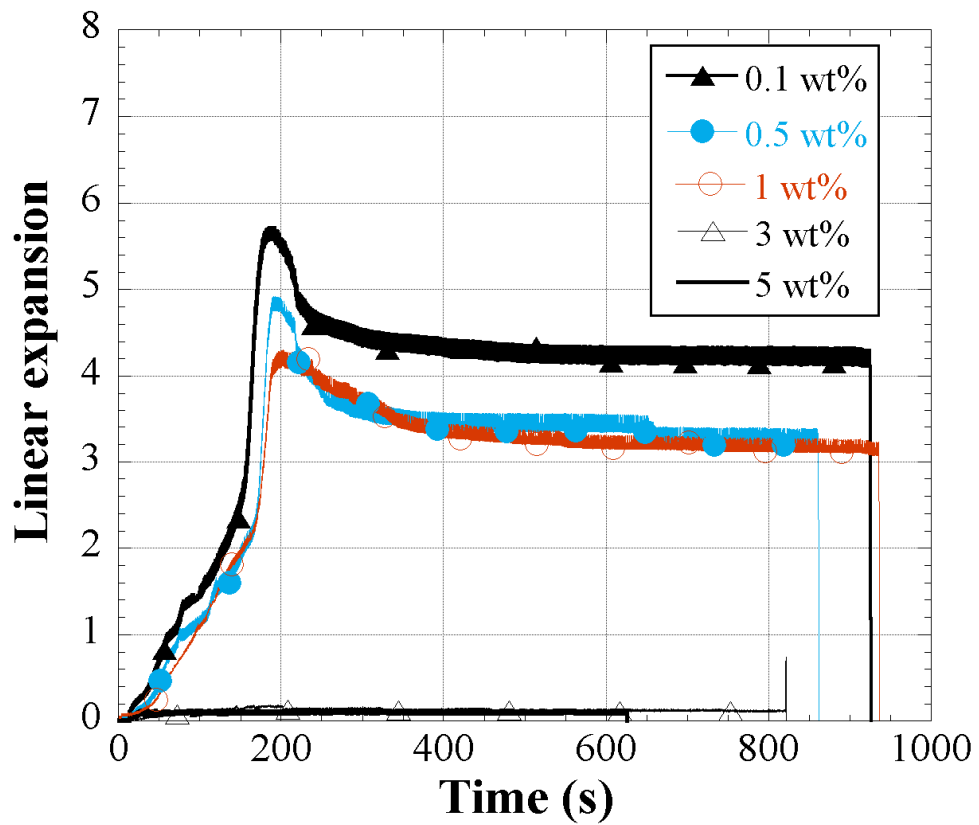


Figure 6.27. Linear expansion-time graphs of P8 SiC/Al compacts of varying particle wt%'s.

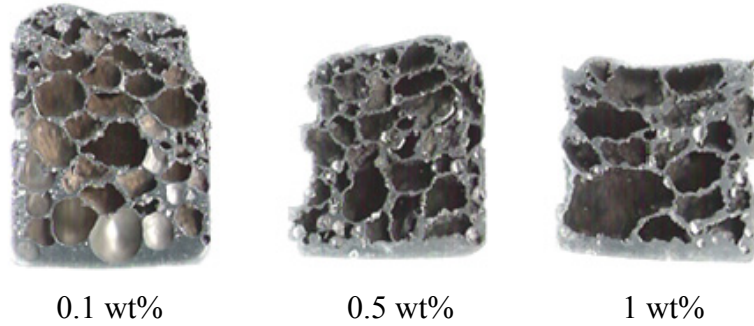


Figure 6.28. The structure of foamed 0.1, 0.5 and 1 wt% P8 SiC/Al compacts after 900 s furnace holding time.

6.7. Expansion of the Sieved SiC (P1-P5)/Al Compacts

The expansion-time graphs of 5 and 10 wt% (P1, P2, P3, P4 and P5) SiC/Al compacts together with those of Al compacts are shown in Figures 6.29 (a) to (e), respectively. At 5 wt% particle addition, the expansions in the largest size SiC (P4 and P5) added compacts are relatively low, while increase with increasing the particle wt% from 5 to 10 wt% (Figure 6.29(d, e)). The coding, weight, thickness, density and expansions of P1-P5 SiC /Al compacts are further tabulated in Table 6.8. The cell structures of foamed 5 and 10 wt% P1-P5 SiC/Al compacts after 900 s furnace holding time are shown in Figures 6.30 (a) and (b), respectively. The dense metal layer at the bottom section of the foams with particle addition is seen to be considerably decreased as compared with foamed Al compacts.

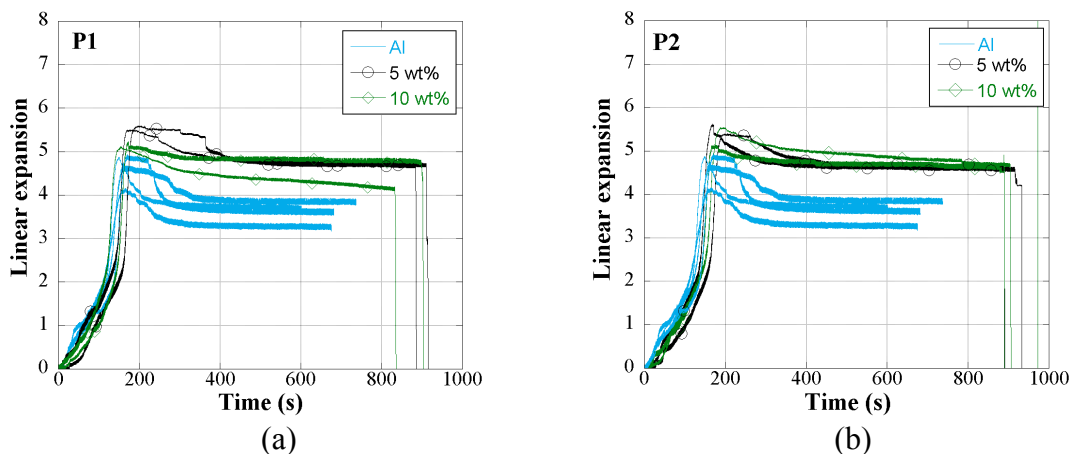


Figure 6.29 The linear expansion-time graphs of 5 and 10 wt% P1-P5 SiC/Al compacts (a) P1, (b) P2, (c) P3, (d) P4 and (e) P5.

(cont. on next page)

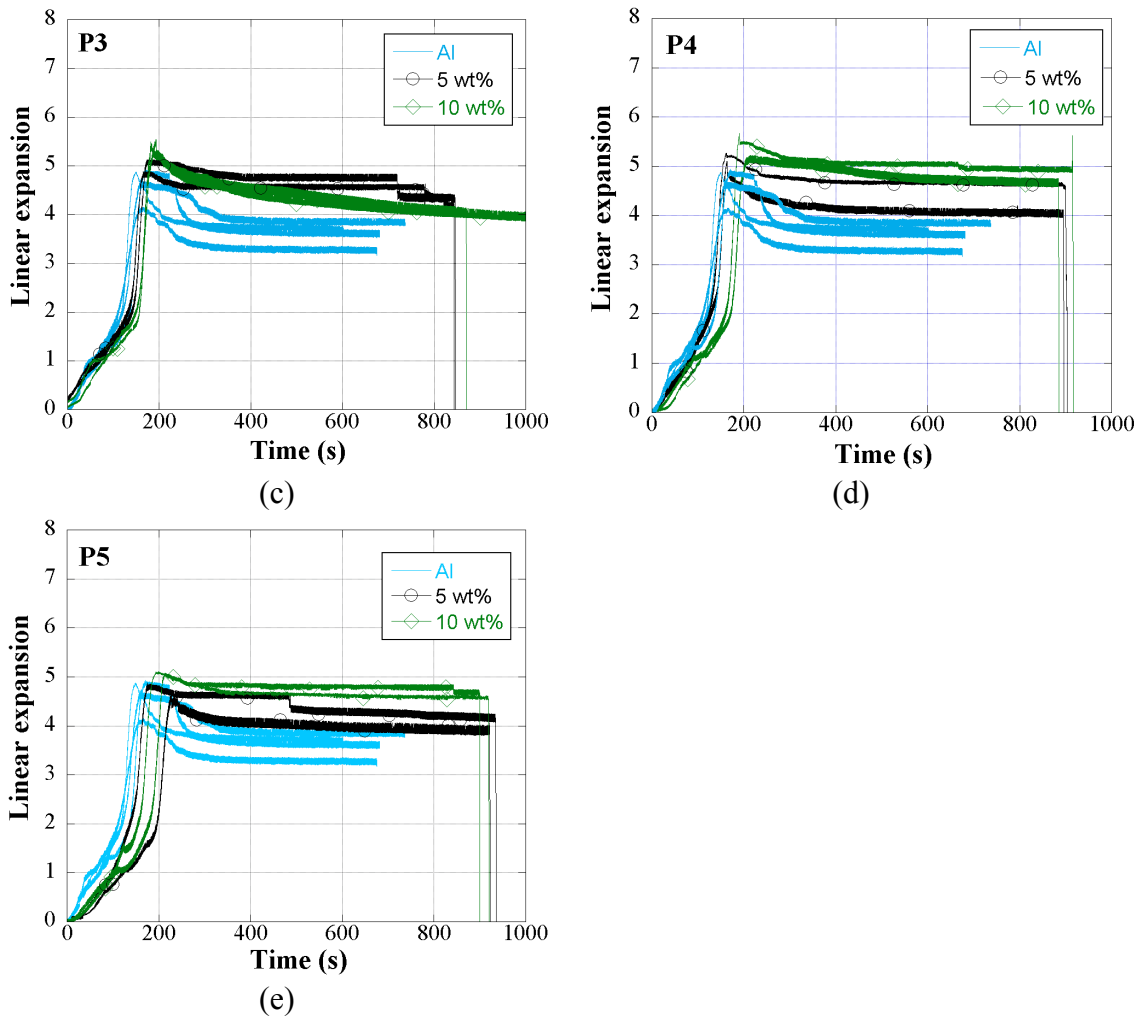


Figure 6.29. (cont.)

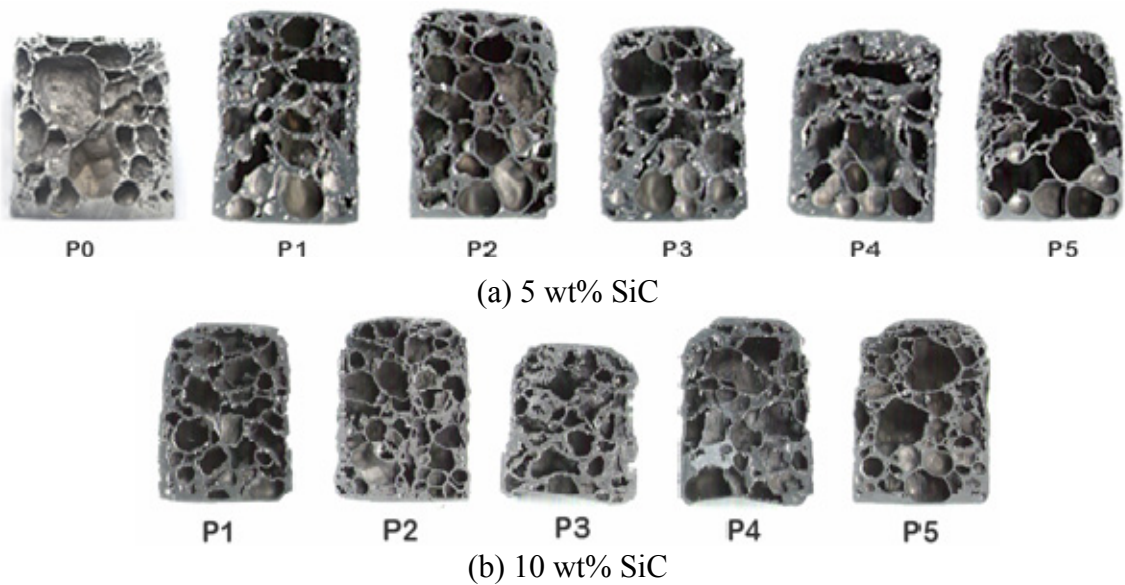


Figure 6.30. The cell structures of foamed P1-P5 SiC/Al compacts after 900 s furnace holding time (a) 5 and (b) 10 wt% addition.

Table 6.8. The coding, weight, thickness, density and expansions P1-P5/Al compacts.

Specimen code		Weight (g)	Thickness (mm)	Density (g cm ⁻³)	Relative density	LE	LE _{max}
P1 group 5 wt%	P1-05-01	14.9	7.85	2.675	0.980	4.29	5.44
	P1-05-02	14.9	7.86	2.686	0.984	3.97	4.84
	P1-05-03	14.9	7.84	2.684	0.983	4.19	5.19
	P1-05-04	14.9	7.84	2.676	0.980	4.23	5.25
	P1-05-05	14.9	7.80	2.683	0.982	4.22	5.25
P1 group 10 wt%	P1-10-01	14.9	7.80	2.684	0.973	3.70	4.09
	P1-10-02	14.9	7.82	2.695	0.977	3.43	4.04
	P1-10-03	14.9	7.78	2.698	0.978	3.44	4.08
	P1-10-04	14.7	7.66	2.699	0.978	3.50	4.16
	P1-10-05	14.9	7.75	2.703	0.979	3.42	4.08
P2 group 5 wt%	P2-05-01	14.9	7.92	2.676	0.980	3.37	4.06
	P2-05-02	14.9	7.92	2.684	0.983	3.50	3.98
	P2-05-03	15.0	7.98	2.682	0.982	3.52	4.29
	P2-05-04	14.7	7.82	2.683	0.982	3.81	4.46
	P2-05-05	14.9	7.90	2.682	0.982	3.84	4.39
P2 group 10 wt%	P2-10-01	14.9	7.92	2.684	0.973	3.25	3.93
	P2-10-02	14.9	7.98	2.682	0.972	3.45	4.33
	P2-10-03	14.7	7.82	2.683	0.972	3.66	4.37
	P2-10-04	14.9	7.90	2.682	0.972	3.70	4.42
	P2-10-05	14.6	7.75	2.682	0.972	3.60	4.66
P3 group 5 wt%	P3-05-01	14.5	7.59	2.686	0.984	4.08	4.70
	P3-05-02	14.7	7.70	2.685	0.983	4.00	4.58
	P3-05-03	14.9	7.81	2.687	0.984	4.13	5.24
	P3-05-04	14.9	7.82	2.683	0.982	3.86	4.82
	P3-05-05	15.0	7.88	2.686	0.984	3.80	4.51
P3 group 10 wt%	P3-10-01	14.9	7.76	2.701	0.979	3.91	4.78
	P3-10-02	14.9	7.75	2.699	0.978	3.16	4.23
	P3-10-03	14.9	7.77	2.704	0.980	3.62	4.78
	P3-10-04	14.9	7.74	2.701	0.979	3.67	4.29
	P3-10-05	14.8	7.70	2.708	0.981	2.94	4.54
P4 group 5 wt%	P4-05-01	14.7	7.65	2.703	0.990	4.49	4.94
	P4-05-02	14.9	7.80	2.709	0.992	4.00	4.41
	P4-05-03	14.8	7.71	2.707	0.991	3.77	4.65
	P4-05-04	14.9	7.82	2.706	0.991	3.51	4.50
	P4-05-05	14.9	7.76	2.712	0.993	3.49	4.44
P4 group 10 wt%	P4-10-01	14.9	7.85	2.692	0.975	3.22	4.21
	P4-10-02	14.9	7.80	2.693	0.976	3.26	4.48
	P4-10-03	14.9	7.79	2.695	0.977	3.32	4.54
	P4-10-04	14.8	7.79	2.692	0.975	3.61	4.40
	P4-10-05	14.9	7.82	2.686	0.973	3.48	4.82
P5 group 5 wt%	P5-05-01	14.9	7.85	2.692	0.986	3.49	4.34
	P5-05-02	14.9	7.80	2.693	0.986	3.56	4.46
	P5-05-03	14.9	7.79	2.695	0.987	3.70	4.26
	P5-05-04	14.8	7.79	2.692	0.986	3.72	4.26
	P5-05-05	14.9	7.82	2.686	0.984	3.35	4.25
P5 group 10 wt%	P5-10-01	14.9	7.77	2.713	0.983	3.13	4.11
	P5-10-03	14.9	7.77	2.701	0.979	2.89	4.44
	P5-10-04	14.9	7.77	2.707	0.981	3.30	4.61
	P5-10-05	14.8	7.66	2.708	0.981	3.11	4.06

6.8. Expansion of Layered Compacts

Two groups of layered compacts were prepared. In the first group, the half of the compact is made of Al and the other half 5 wt% P6 SiC/Al as shown in Figure 6.31. In the other group, the lower part is made of Al and the upper part 5 wt% P6 SiC/Al and vice versa as shown Figure 6.31. In the first group compacts, a thin separator layer was used in the compaction die to separate the powder layers. In the second group, the powder with no SiC particle was first compacted, than the second layer was compacted over the first layer or vice versa. The coding, weight, thickness, density and expansions of layered compacts are further tabulated in Table 6.9. Higher LE_{max} values are found in group 2 foamed compacts as tabulated in Table 6.9.

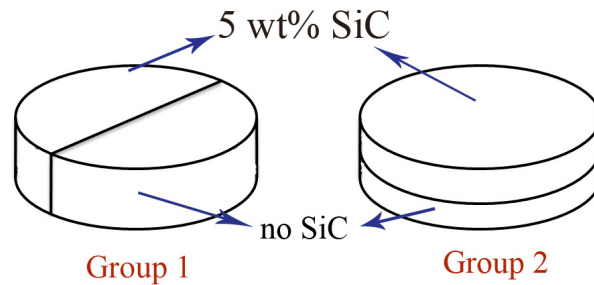


Figure 6.31. Schematic presentations of the layered compacts.

Table 6.9. The coding, weight, thickness, density and expansions of layered compacts.

Specimen code	Thickness (mm)	Weight (g)	Density ($g\ cm^{-3}$)	Relative density	LE_{max}
<i>Group 1</i>					
PL1-01	7.82	14.8	2.674	0.981	4.61
PL1-02	7.78	14.8	2.673	0.980	4.39
PL1-03	7.81	14.8	2.678	0.982	3.82
PL1-04	7.84	14.8	2.669	0.979	4.07
<i>Group 2</i>					
PL2-01	7.73	14.7	2.671	0.979	4.02
PL2-02	7.87	14.9	2.667	0.978	5.19
PL2-03	7.86	14.9	2.664	0.977	4.71
PL2-04	7.77	14.8	2.672	0.980	5.25
PL2-05	7.79	14.8	2.670	0.979	4.02
PL2-06	7.87	14.9	2.674	0.981	4.10

The pictures of group 1 and group 2 foamed layered compacts are shown in Figure 6.32. In group 1 foams, 5 wt% SiC contained section is seen darker in Figure 6.32. The effect of SiC contained layer is visually observable not only on the outer surface of the foam (Figure 6.33 (a)), but also in the cell structure of the foam (Figure 6.33 (b)). The silicon carbide added section has homogeneous cell size distribution, while, the extensive cell wall collapse is seen in Al section. The cell structure of the group 2 layered foams are shown in Figure 6.33 (c). Drainage is observed to decline greatly in these foams.

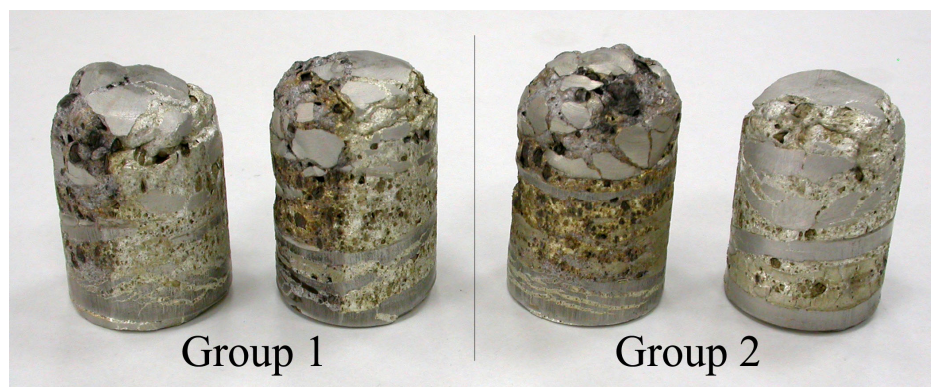


Figure 6.32. Views of the expanded foams from the both groups of layers.

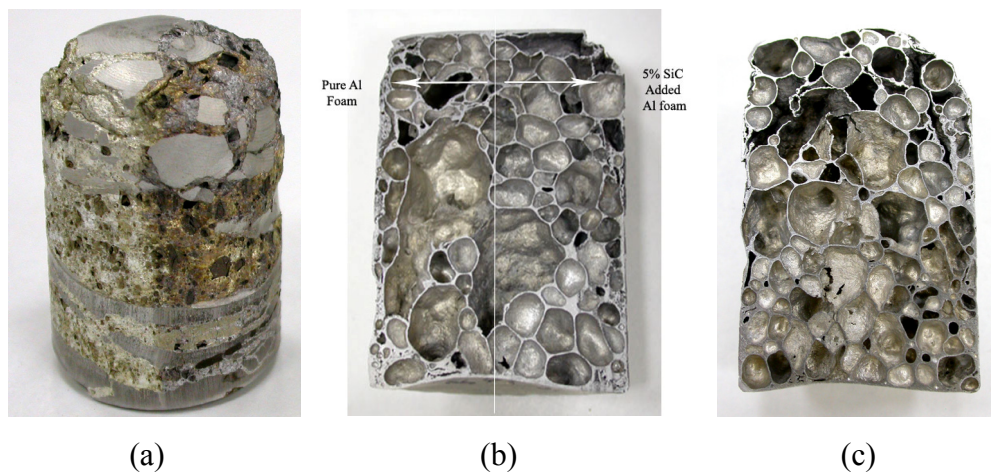


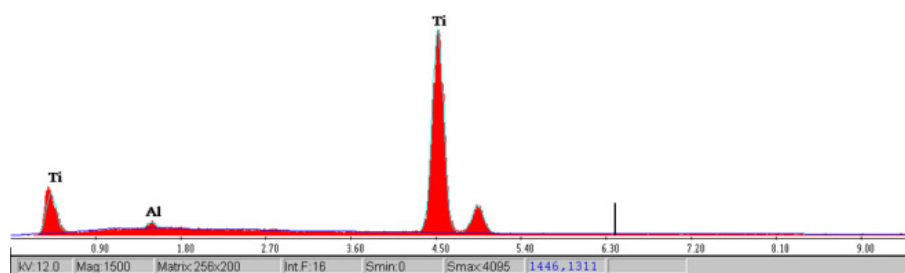
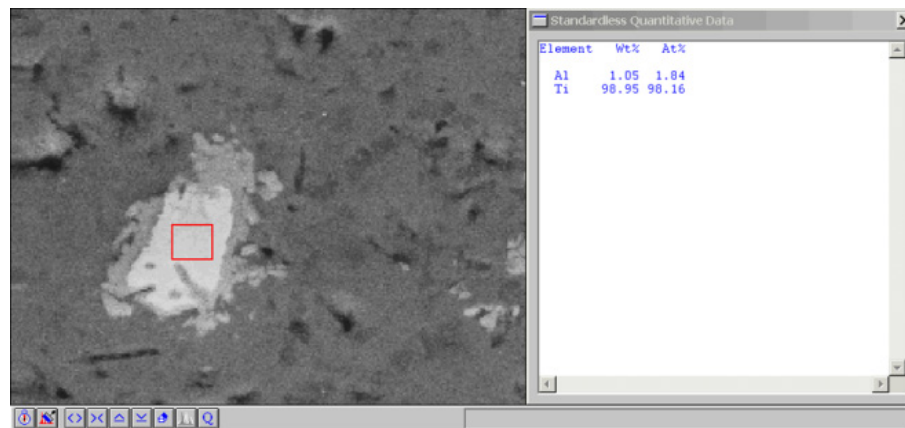
Figure 6.33. Picture of (a) group 1 layered foamed compact and (b) cross-section and structure of group 2 foamed compacts.

CHAPTER 7

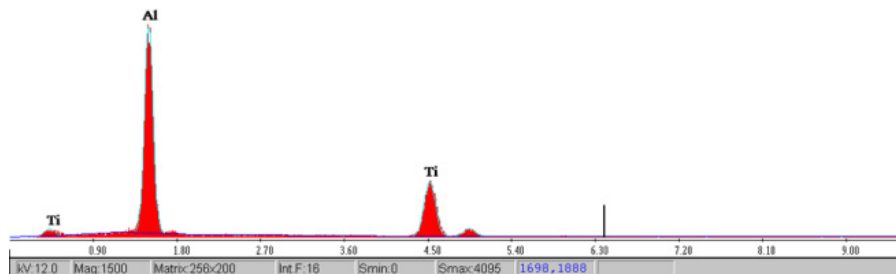
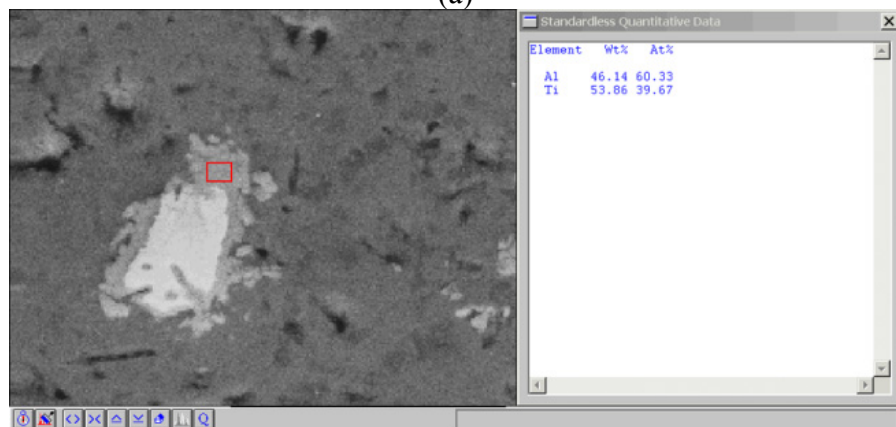
MICROSCOPIC ANALYSIS FOR EXPANSION TESTS

7.1. Foamed 30 nm SiC/Al Compacts

In Figures 7.1 (a) and (b) EDAX analysis of a TiH_2 particle and the reaction zone around the TiH_2 particle in a foamed 30 nm SiC/Al compact (P10) after 900 s furnace folding time is shown respectively. The white part in Figure 7.1(a) is the unreacted TiH_2 and the gray section is Al-Ti intermetallic (Figure 7.1(b)) formed as a result of the reaction between Ti and liquid Al. The cell wall microstructure of the same foam is shown in Figure 7.2(a). A higher magnification view of the same cell wall clearly shows the presence of the secondary phases, precipitates, in 0.5-3 micron size in the cell wall (Figure 7.2(b)). These are Al-Si secondary phases (Figure 7.2(c)), resulting from the reaction between SiC particles and liquid Al. The elemental mapping of the cell wall (Figures 7.3 (a-d)) clearly shows the presence of Si in the cell wall. The lack of C in the selected cell wall in Figure 7.3(c) also confirms Al-C phase formed by the reaction between SiC and liquid Al is removed during grinding and polishing as it is soluble in water.



(a)



(b)

Figure 7.1. EDAX analysis of a (a) TiH_2 particle and (b) the reaction zone around the TiH_2 particle in a foamed 30 nm 0.15 wt% SiC/Al compact (P10) after 900 s furnace folding time.

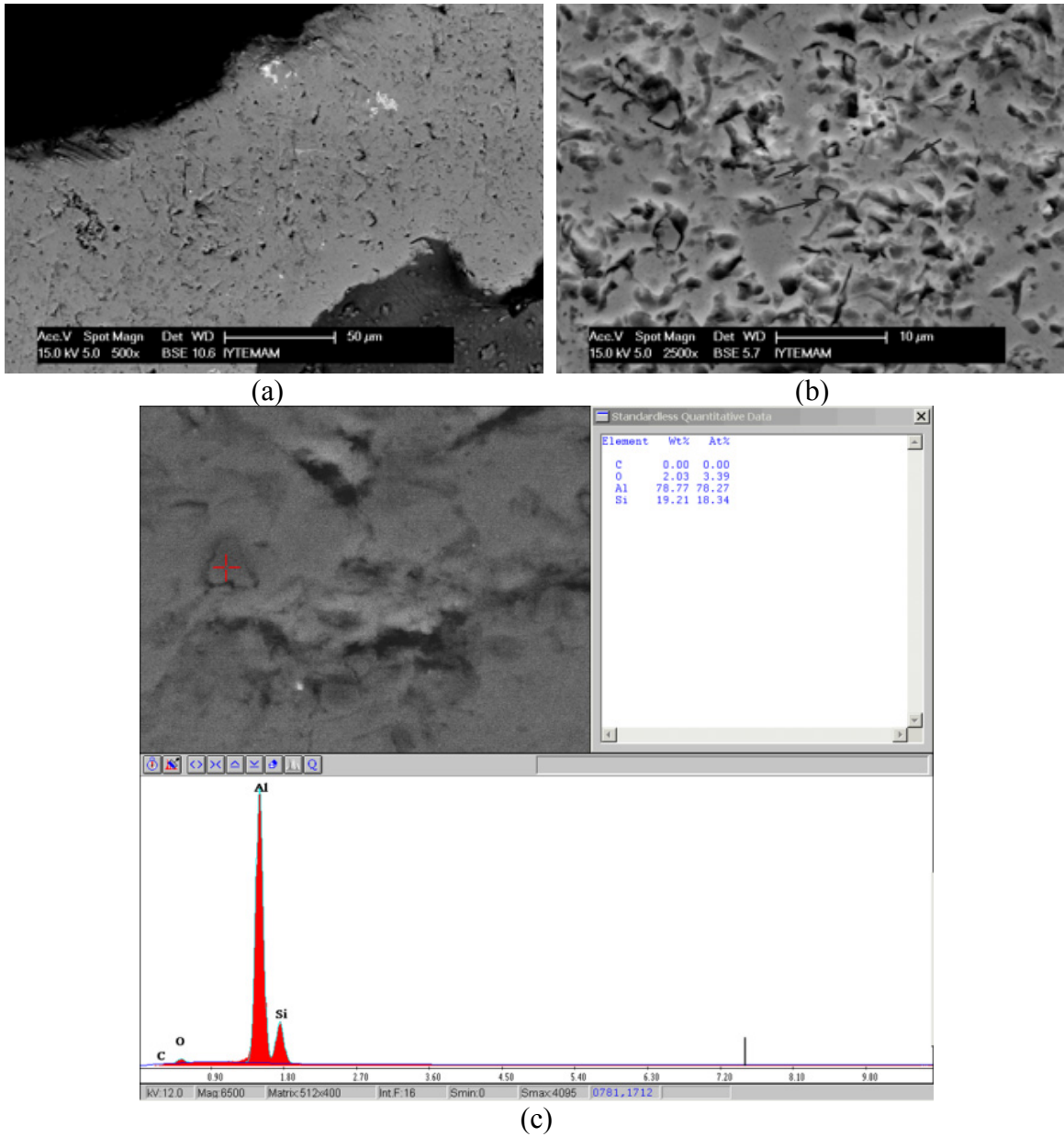


Figure 7.2. SEM micrographs showing (a) and (b) a cell wall in foamed 0.15 wt% nano SiC/Al compact and (c) EDAX analysis of the precipitates in the cell wall.

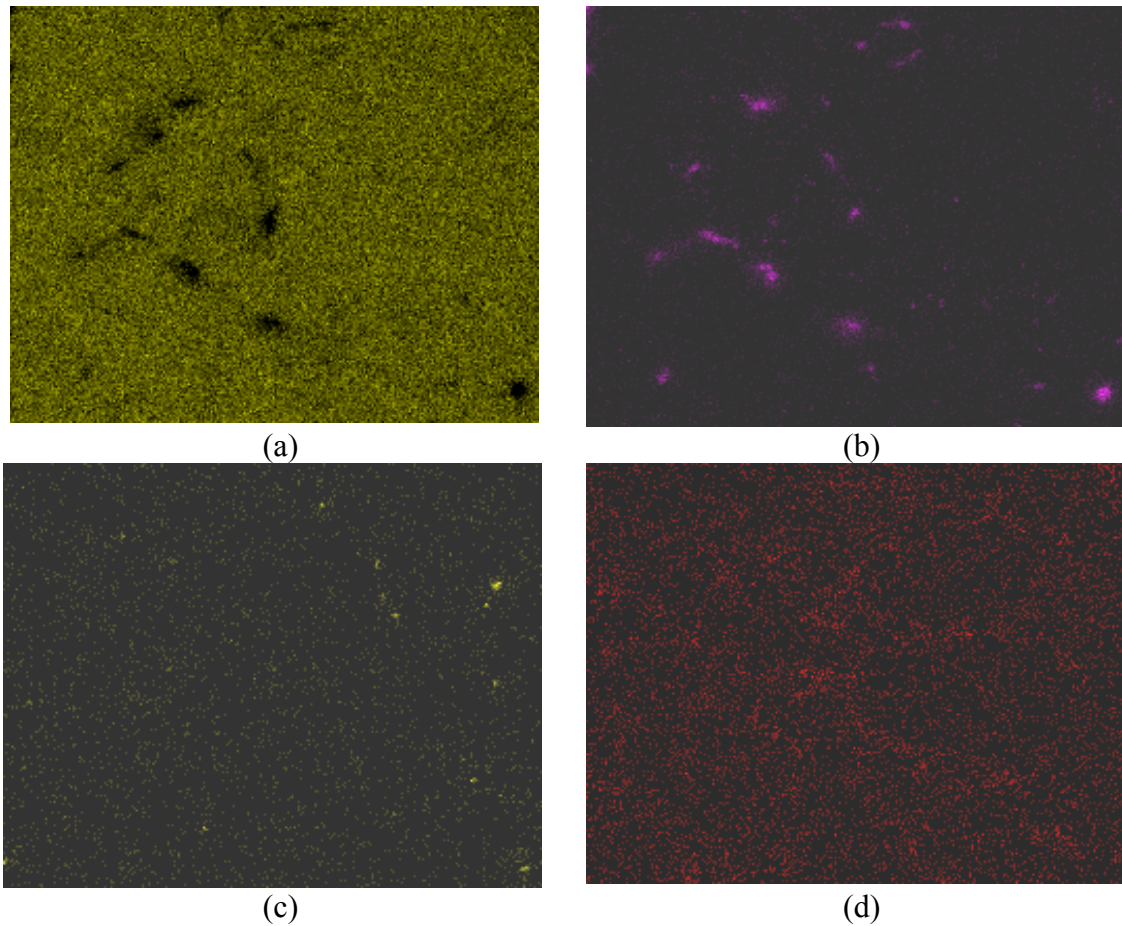


Figure 7.3. Elemental mapping of the cell wall in a foamed 0.15 wt% nano SiC/Al compact: (a)Al, (b) Si, (c) C and for (d) O.

7.2. Foamed SiC Whisker /Al Compacts

The SEM micrographs of the cell wall in a foamed 1 wt% SiC whisker/Al compact is shown in Figure 7.4(a). The whiskers are mostly located on the surface of the cells (Figure 7.4(b)), while few of them are seen interior of the cell wall (Figure 7.4(c)). Figure 7.4(d) further shows that whiskers are partially wetted by the liquid Al as they suspend on the cell surface.

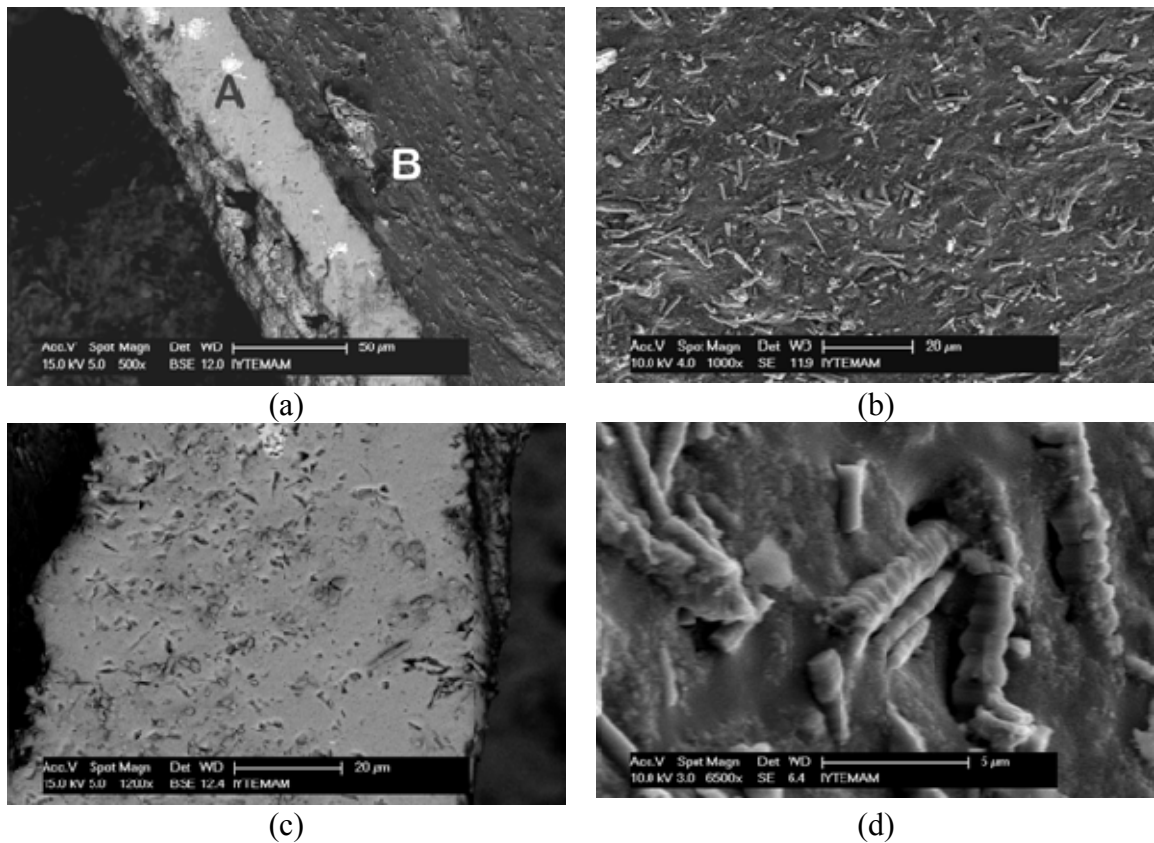


Figure 7.4. SEM pictures of a foamed 1 wt% whisker/Al compact (a) cell wall and surface, (b) cell wall surface, (c) cell wall (d) suspended whiskers on the cell wall surfaces.

7.3. Foamed SiC Particle/Al Compacts

Microscopic observations further show that SiC particles are preferentially located at cell wall surface/gas interface in the foamed 5 and 10 wt% SiC/Al powder compacts as shown in Figures 7.5 (a-f). Increasing wt% of particles is noted to increase the number of particles located at the cell wall surface/gas interface as seen in the same figures. Figures 7.6 (a) and (b) show the cell wall surface SEM pictures of a foamed P10 SiC/Al compact. Since the particle size in foamed P10 1 wt% SiC/Al compacts was relatively small, a relatively high magnification was required to detect the particles on cell wall surfaces. In these foams, SiC particles are also observed to locate at the cell wall surfaces. EDAX analysis of the particle located at the cell surface further show the presence of Al, Si, C and O (Figure 7.7). The high wt% of C in the analysis may also prove the reaction between SiC and liquid Al.

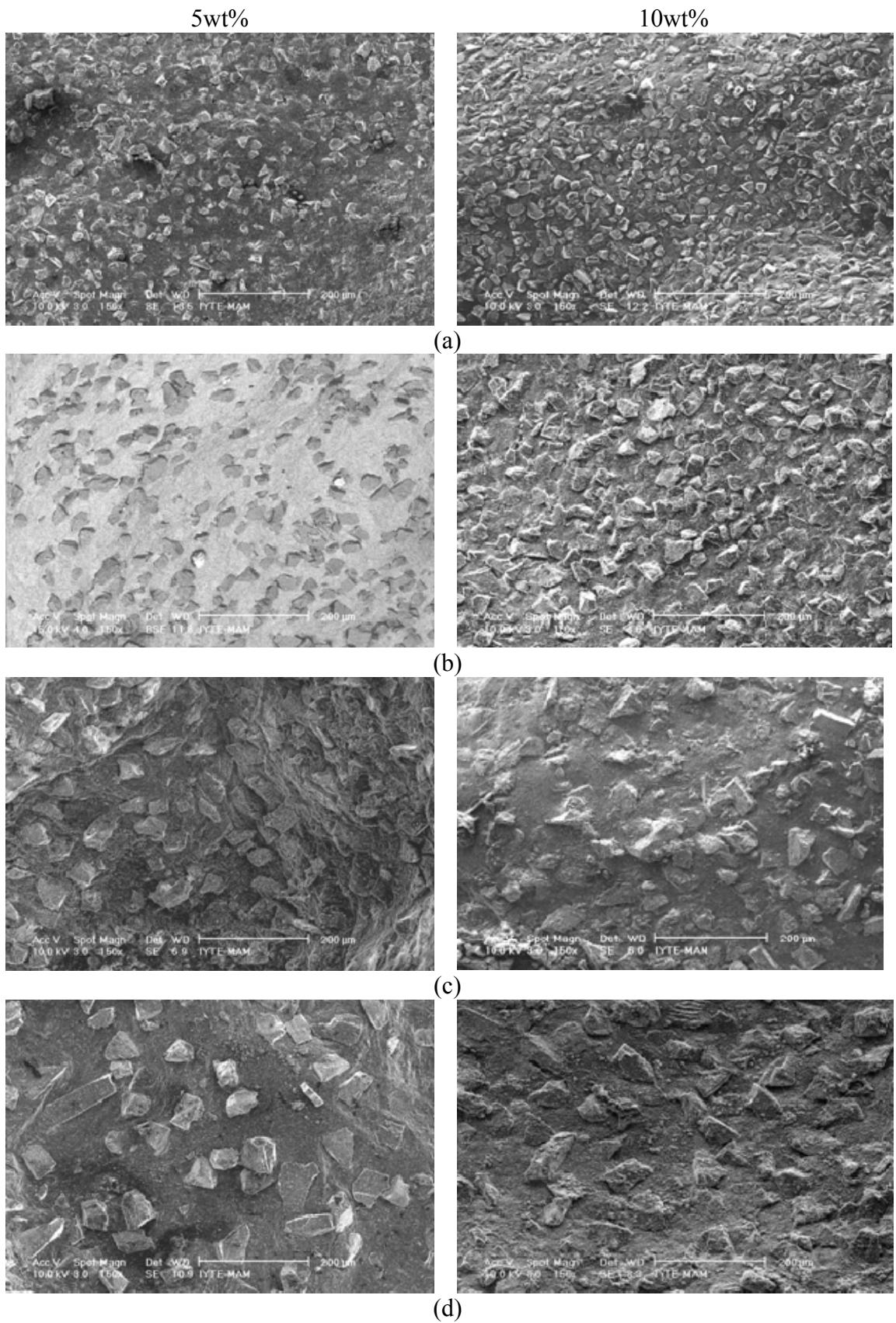
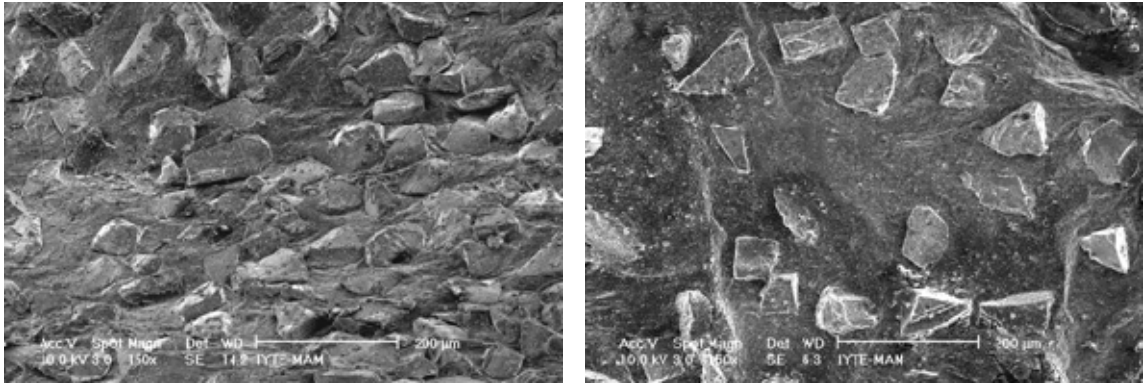


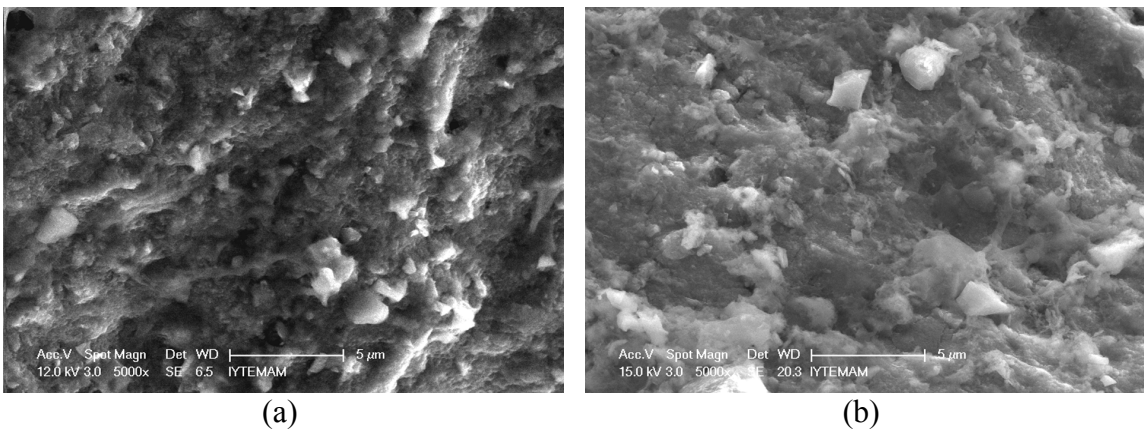
Figure 7.5. SEM pictures of cell wall surfaces of foamed (a) P1, (b) P2, (c) P3, (d) P4, (e) P5 SiC/Al compacts after 900 s furnace holding time.

(cont. on next page)



(e)

Figure 7.5. (cont.)



(a)

(b)

Figure 7.5. SEM pictures of cell wall surfaces of foamed P10 1wt% SiC/Al compacts after 900 s furnace holding time.

A small fraction of the particles are also found interior of the cell walls of small size SiC particle added foams (P2) as shown in Figures 7.8 (a) and (b). Similar observation is also made for the largest size SiC addition (Figures 7.8(c) and (d)). Although nearly equal size particles are observed on the cell wall surfaces of the foamed SiC/Al compact (Figure 7.9(a)) as is expected, small and large particles are collectively seen on the cell wall surfaces of foamed P6 and P7 SiC/Al compacts (Figure 7.9(b)).

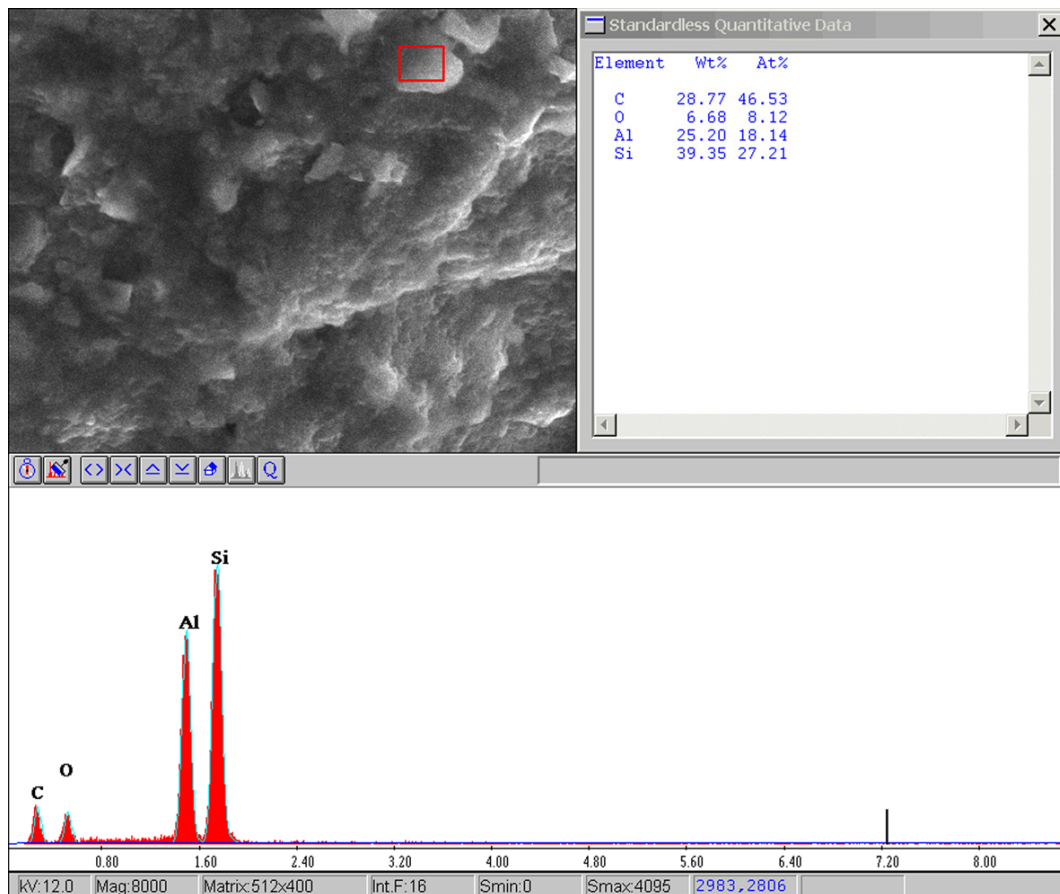


Figure 7.7. EDAX analysis of the cell wall surface of a foamed 1 wt% P10 SiC/Al compact after 900 s furnace holding time.

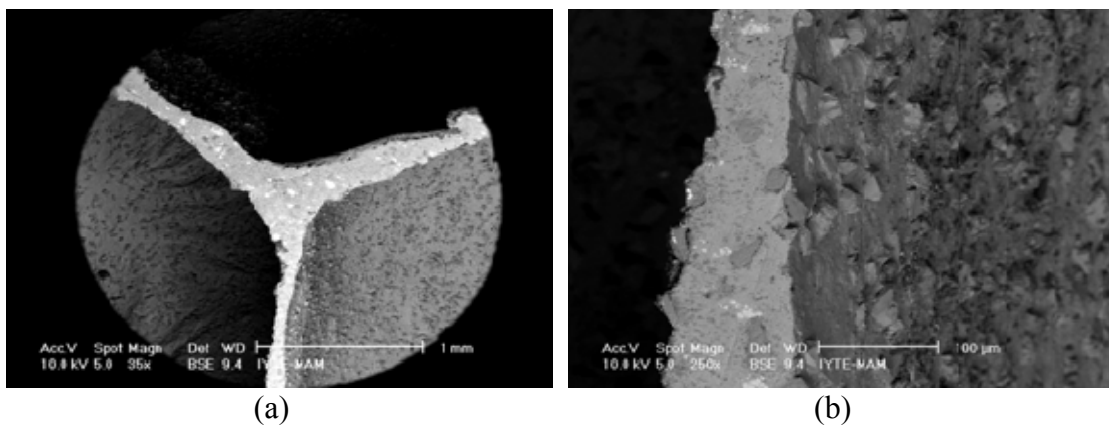


Figure 7.8. SEM pictures of cell walls of the foams with (a) and (b) 5 wt% P2 SiC/Al, (c) 5 wt% P5 and (d) 10 wt% P5 SiC/Al foam.

(cont. on next page)

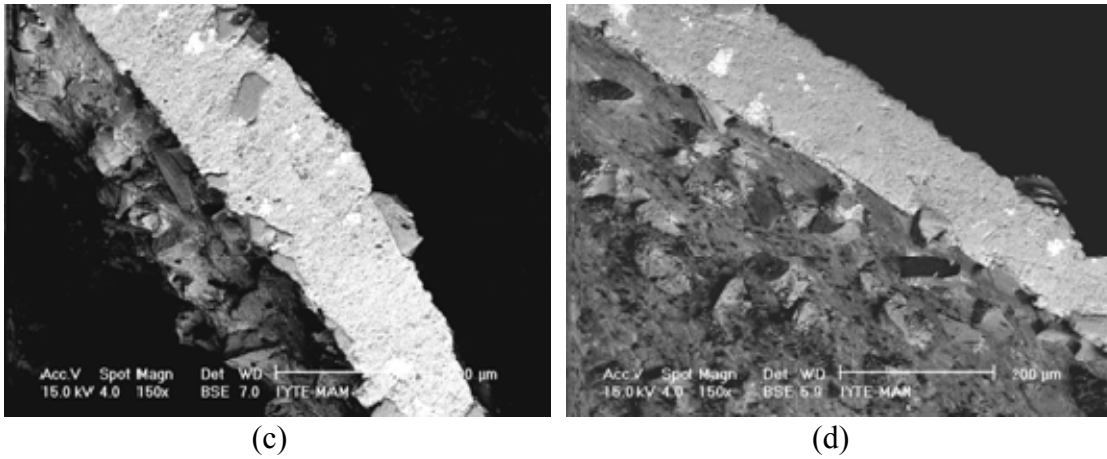


Figure 7.8. (cont.)

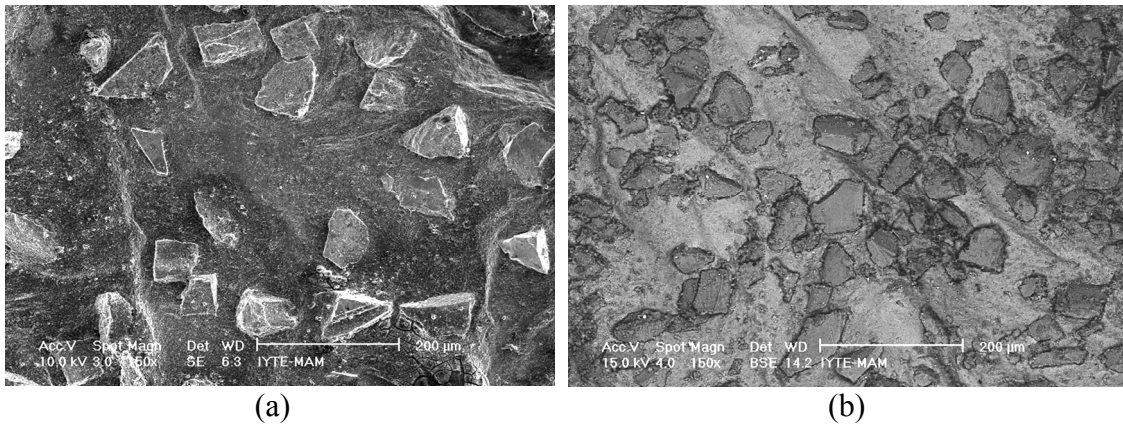


Figure 7.9. Particles at cell wall surfaces (c) 5 wt% P5 SiC/Al foamed compact and (d) 5 wt% P7 SiC/Al foamed compact after 900 s.

The specimen codes and Hardness Vickers (HV) values of foamed Al and P1-P5 SiC/Al compacts cell walls are tabulated in Table 7.1, together with standard deviation values of the test data for each group. For each specimen, 10 hardness tests were made on the surfaces where there is no SiC particle present. Mean value of these tests were taken into consideration. The variation of the hardness values with mean SiC particle size of the foams is shown in Figure 7.10 for 5 and 10 wt% SiC addition. As seen in Figure 7.10, the hardness values of SiC contained foams cell walls are greater than Al foam cell walls and increases with wt% of SiC addition except P5 powder. Besides they have big difference in the percentages added, hardness values for the nano sized 0.1 wt% SiC added foams were observed to be close to the average hardness value with 10 wt% particle added foams (Figure 7.10). This is because of the high surface area of the nano powders compared with the sieved SiC particle addition.

Table 7.1. Hardness Vickers values of foamed Al and P1-P5 SiC/Al compacts.

Specimen group	Mean HV	Standard deviation
P0	33.91	4.86
P10-0.1	46.50	2.09
P1-05	40.60	5.68
P1-10	47.80	3.88
P2-05	42.43	4.54
P2-10	49.50	4.88
P3-05	44.20	3.56
P3-10	48.80	4.66
P4-05	44.50	2.69
P4-10	47.60	2.68
P5-05	53.00	3.84
P5-10	53.30	4.42

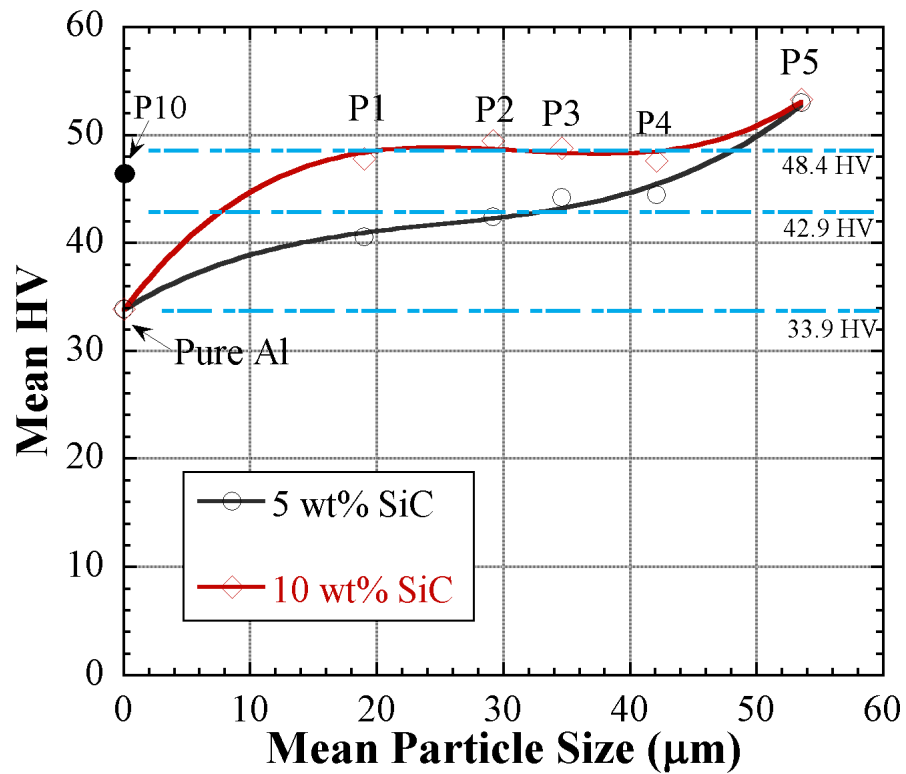


Figure 7.10. Average hardness values of the cell walls vs. SiC particle size.

CHAPTER 8

COMPRESSION BEHAVIOUR OF SiC ADDED FOAMS

The foams expanded until about the maximum expansion were cut into cylindrical compression specimens using an electro discharge machine through the foaming direction with a l/d ratio of ~ 1 (Figure 8.1(a)). These samples were cut from the middle sections of the foam cylinder and therefore contained no dense layer (Figure 8.1(b)). Each foam sample contains more than 5-6 cells. Compression tests were performed until about 10, 40 and 80% strain in order to observe the strain dependent deformation mechanism.



(a)



(b)

Figure 8.1. View from (a) dense shell of the cut foam and (b) prepared compression test specimens from expanded 5 wt% P5 SiC/Al foams.

In Figures 8.2 (a-k), the compression stress-strain behavior tested Al and 5 and 10 wt% P1-P5 SiC/Al foams are shown sequentially. Figure 8.2 (l) shows the compression stress-strain curves of SiC whisker/Al foams of different densities. It is noted in these graphs that, as the foam density increases the stress values increase within the each group of the foam samples. Figures 8.3(a) and (b) show sequentially the compression nominal stress-strain curves of foamed 5 and 10 wt% P1-P5 SiC/Al and Al compacts at the similar densities. The compressive stress of foamed Al compact ($\sim 0.35 \text{ g cm}^{-3}$) at 0.1 strain vary between 1.8 and 1.9 MPa, while the stress in 5 and 10 wt% P1-P4 SiC contained foams increases to 2.5-2.7 MPa, corresponding to a nearly 30% increase in the collapse stress. This proves the stress enhancement of the foam with SiC particle addition under compression loads. Relatively low and no strengthening is found in P5 SiC/Al and SiC whisker/Al foams. Tables 8.1 and 8.2 further tabulates Al and 5 wt% SiC/Al and 5 wt% SiC/Al foam sample densities and corresponding mechanical properties, respectively.

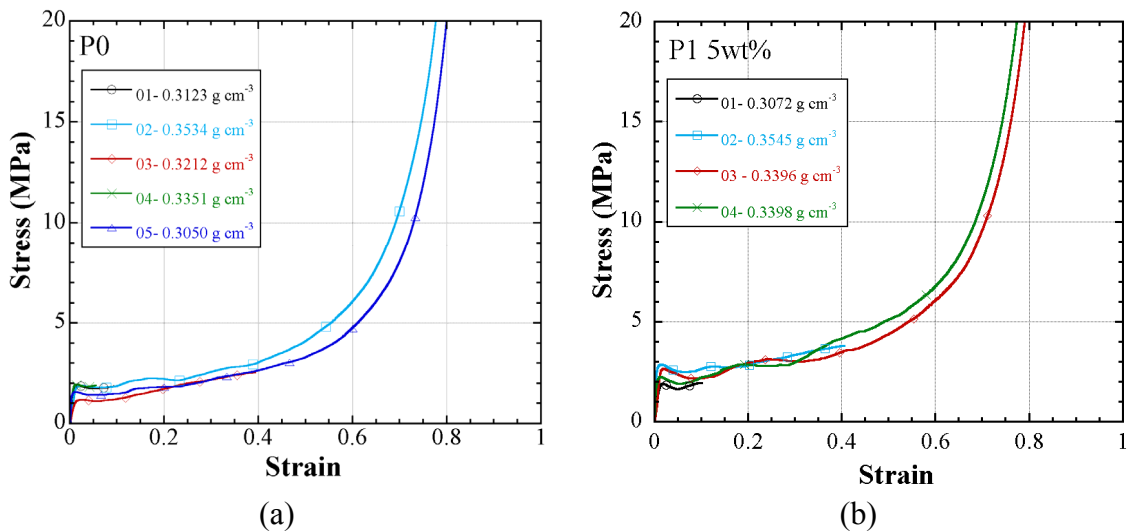
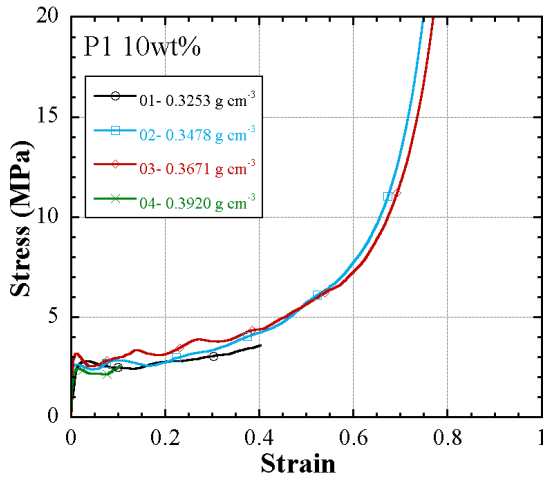
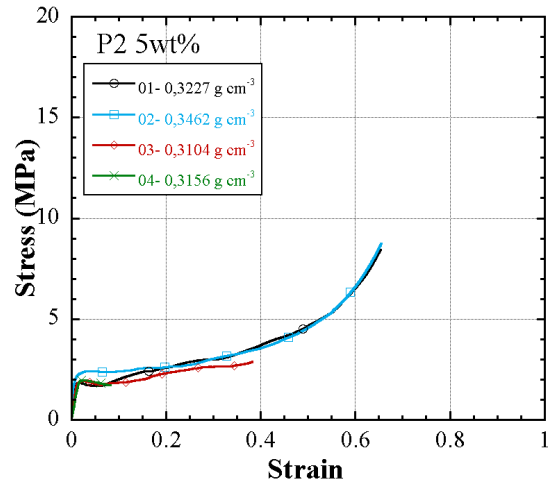


Figure 8.2. Stress-Strain curves of the foams with; (a) P0, (b) %5 P1 SiC, (c) %10 P1 SiC, (d) %5 P2 SiC, (e) %10 P2 SiC, (f) %5 P3 SiC, (g) %10 P3 SiC, (h) %5 P4 SiC, (i) %10 P4 SiC, (j) %5 P5 SiC, (k) %10 P5 SiC, and (l) %1 SiC whisker additions.

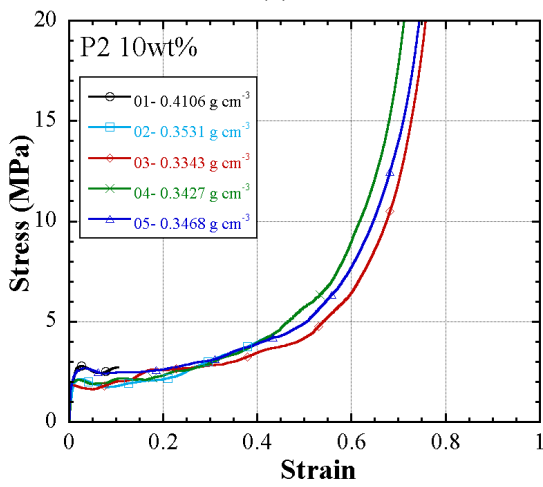
(cont. on next page)



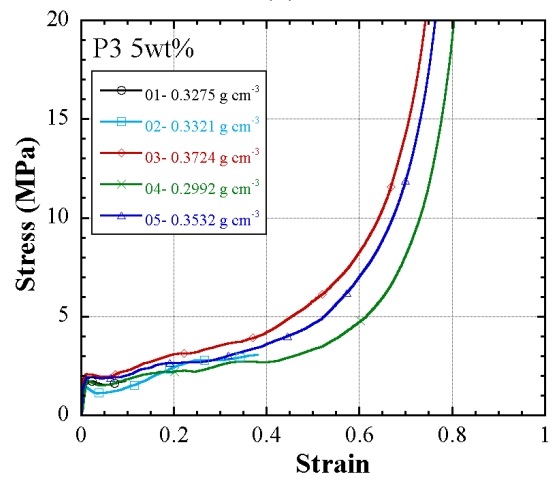
(c)



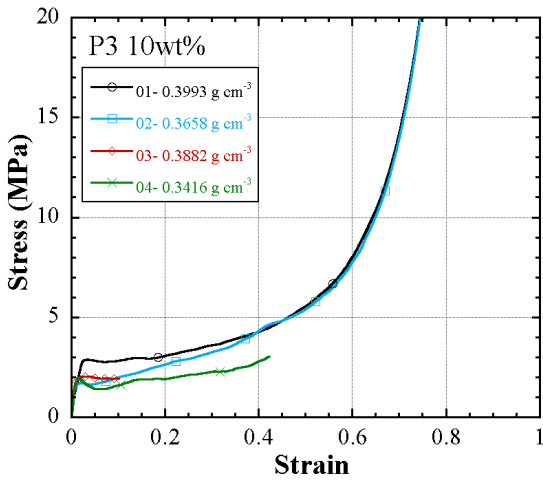
(d)



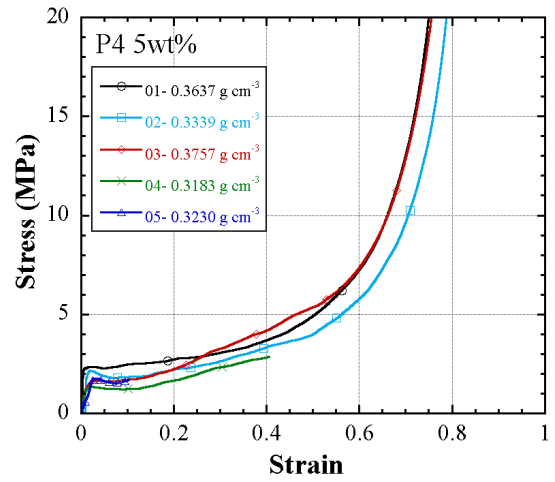
(e)



(f)

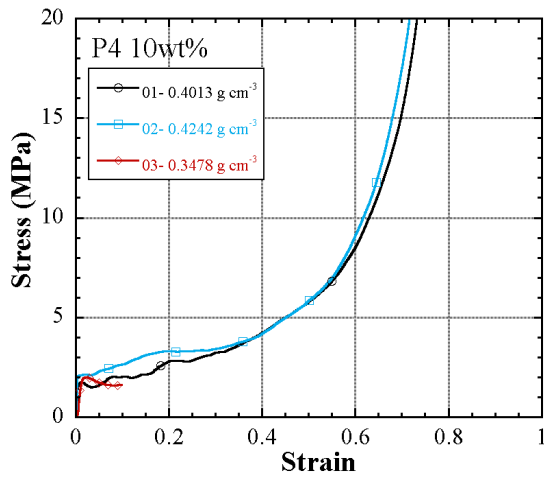


(g)

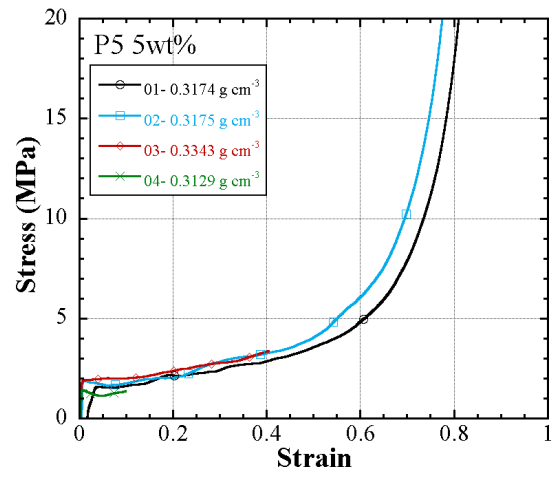


(h)

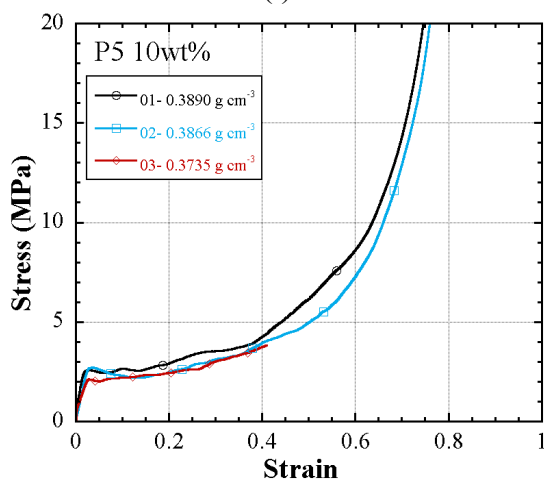
(cont. on next page)



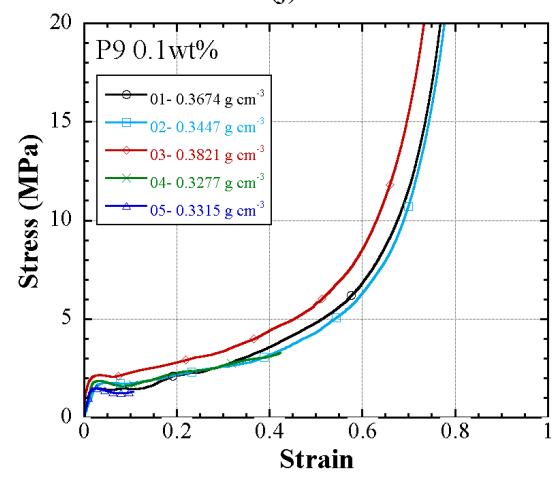
(i)



(j)

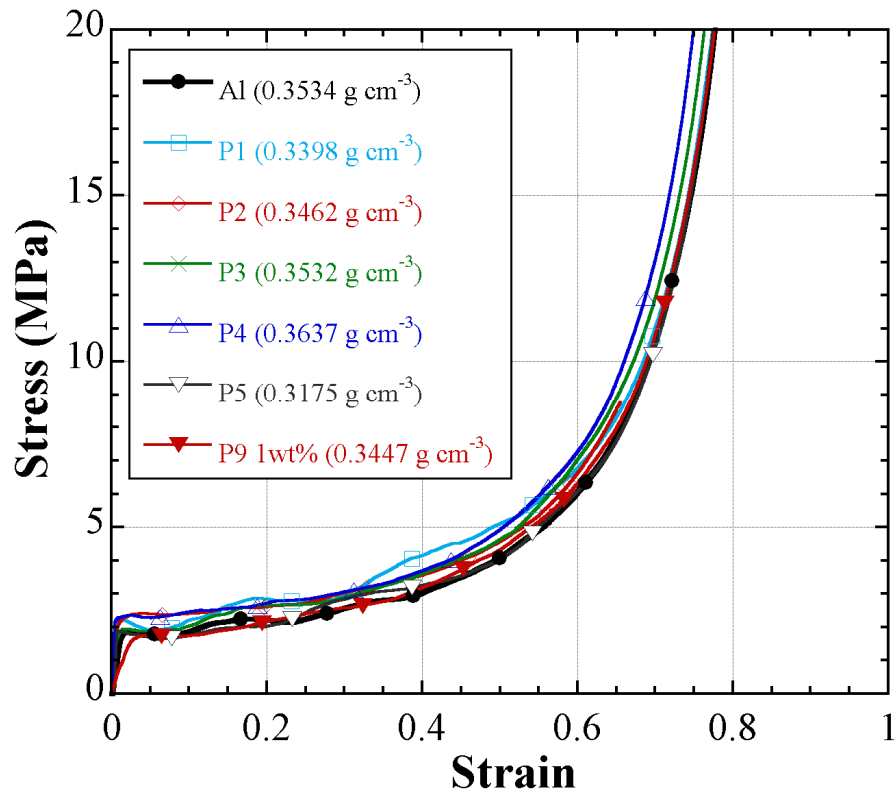


(k)

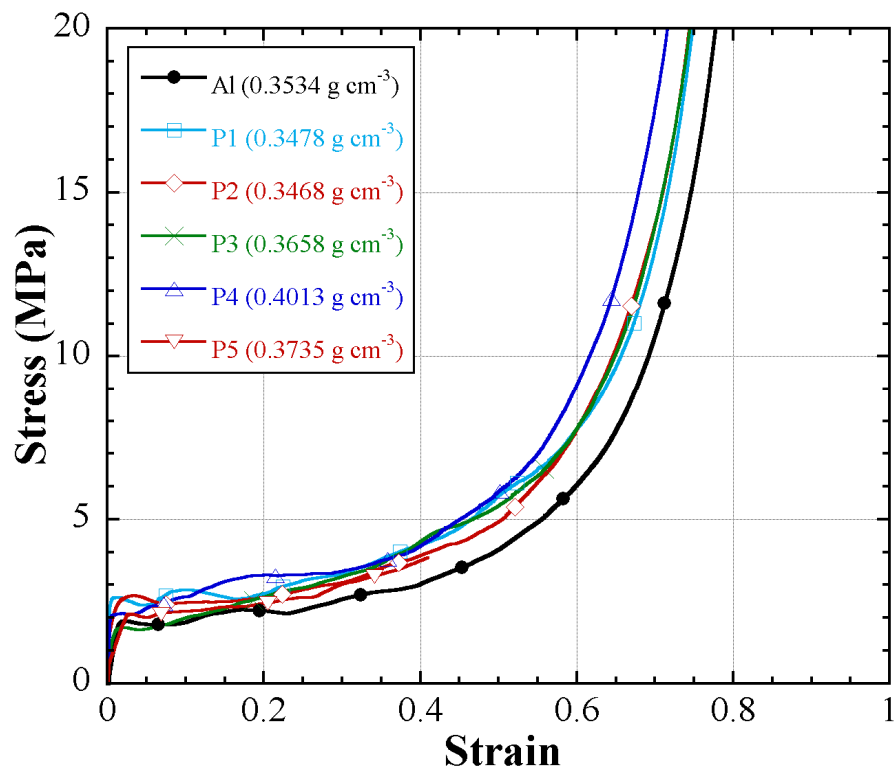


(l)

Figure 8.2. (cont.)



(a)



(b)

Figure 8.3. The stress-strain curves of the similar density foams: (a) 5 wt% P1-P5 SiC/Al and SiC whisker/Al and (b) 10 wt% P1-P5 SiC/Al foam.

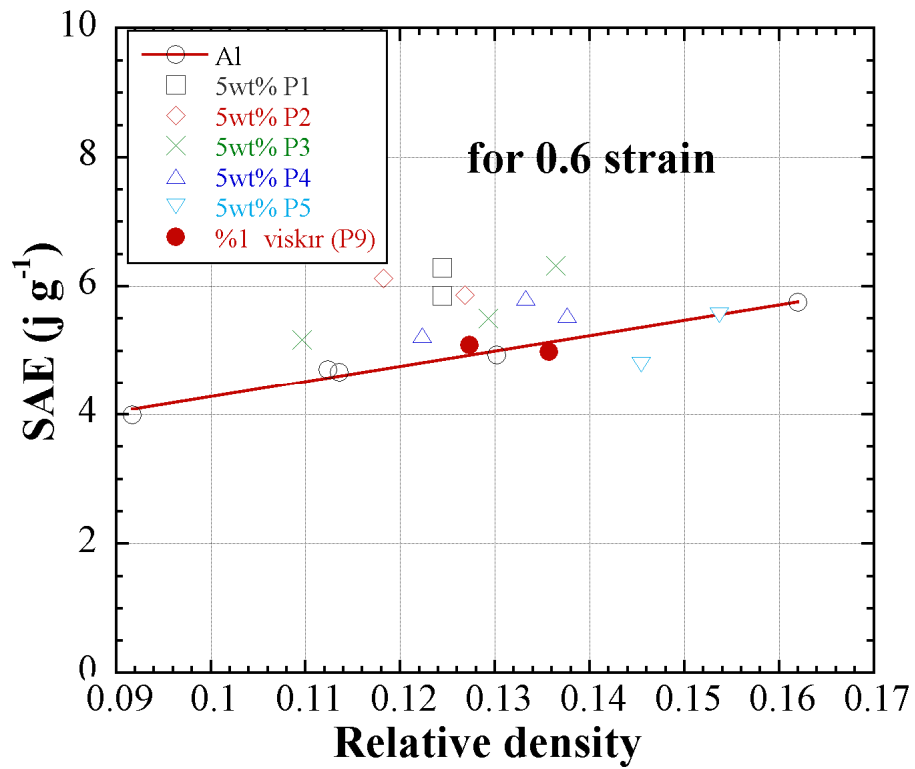
Table 8.1. Foam compression test samples and mechanical properties of foamed Al and 5 wt% SiC/Al compacts.

Specimen Code	Density (g.cm⁻³)	Relative Density	Maximum elastic stress (MPa)	0.1 strain stress (MPa)	Densification strain	0.6strain SAE (joule g⁻¹)
P0-01	0.3123	0.1151	1.8813	1.8610	-	-
P0-02	0.3534	0.1302	1.8915	1.8712	0.69	4.9313
P0-03	0.3212	0.1183	1.1797	1.2203	-	-
P0-04	0.3351	0.1235	1.9322	-	-	-
P0-05	0.3050	0.1124	1.5559	1.4847	0.72	4.7025
P1-05-01	0.3072	0.1125	1.8983	1.9322	-	-
P1-05-02	0.3545	0.1298	2.8305	2.6440	-	-
P1-05-03	0.3396	0.1244	2.6322	2.1813	0.69	5.8564
P1-05-04	0.3398	0.1244	2.2101	2.2051	0.74	6.2873
P2-05-01	0.3227	0.1182	1.8305	2.010	0.65	6.1274
P2-05-02	0.3462	0.1268	2.3932	2.4338	0.64	5.8595
P2-05-03	0.3104	0.1137	1.9322	1.8373	-	-
P2-05-04	0.3156	0.1156	1.9729	1.7407	-	-
P3-05-01	0.3275	0.1199	1.7372	1.7915	-	-
P3-05-02	0.3321	0.1216	1.4018	1.4117	-	-
P3-05-03	0.3724	0.1364	2.0745	2.2779	0.68	6.3244
P3-05-04	0.2992	0.1096	1.7220	1.8305	0.73	5.1716
P3-05-05	0.3532	0.1293	1.9254	2.0203	0.72	5.5073
P4-05-01	0.3637	0.1332	2.3593	2.4542	0.68	5.8299
P4-05-02	0.3339	0.1223	2.1338	1.8254	0.72	5.2416
P4-05-03	0.3757	0.1376	1.6593	1.6949	0.77	5.5563
P4-05-04	0.3183	0.1166	1.3153	1.2085	-	-
P4-05-05	0.3230	0.1183	1.7712	1.6610	-	-
P5-05-01	0.4013	0.1454	1.5661	1.6678	0.74	4.7916
P5-05-02	0.4242	0.1537	1.8813	1.7491	0.71	5.5489
P5-05-03	0.3478	0.1260	2.0084	1.9949	-	-
P5-05-04	0.3623	0.1313	1.3847	1.3576	-	-

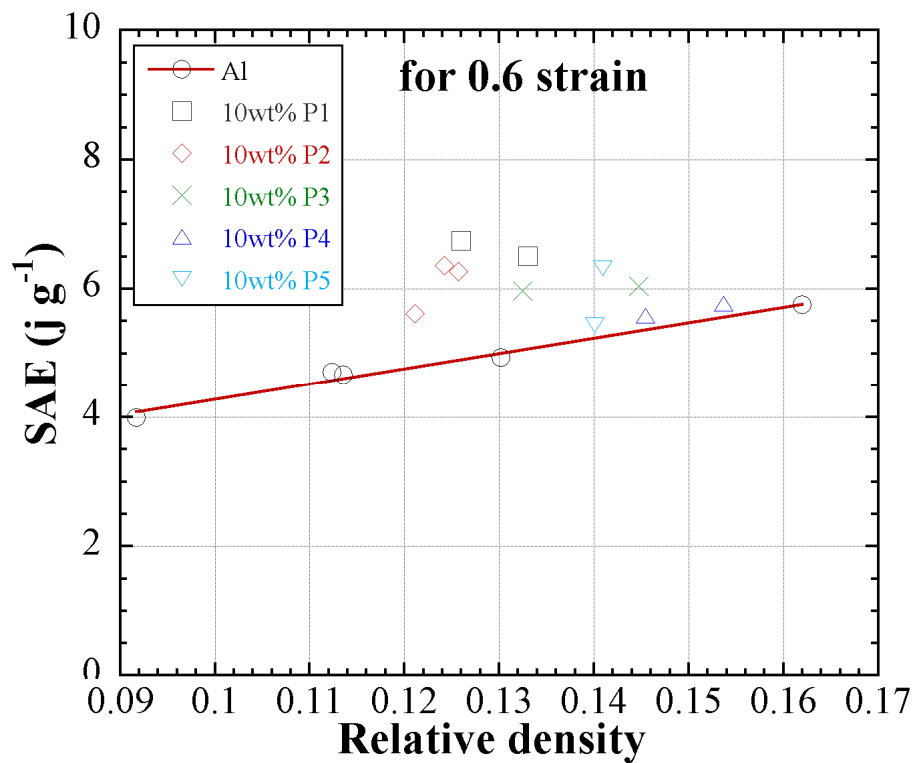
Table 8.2. Foam compression test samples and mechanical properties of foamed 10 wt% SiC/Al compacts.

Specimen Code	Density (g.cm ⁻³)	Relative Density	Maximum elastic stress (MPa)	0.1 strain stress (MPa)	Densification strain	0.6strain SAE (joule g ⁻¹)
P1-10-01	0.3253	0.1179	2.7983	2.4779	-	-
P1-10-02	0.3478	0.1260	2.6084	2.8338	0.73	6.7440
P1-10-03	0.3671	0.1330	3.1864	2.9830	0.71	6.5068
P1-10-04	0.3920	0.1420	2.4067	2.4746	-	-
P2-10-01	0.4106	0.1488	2.7831	2.7423	-	-
P2-10-02	0.3531	0.1279	2.1322	1.7661	-	-
P2-10-03	0.3343	0.1211	1.8169	1.6406	0.71	5.6164
P2-10-04	0.3427	0.1242	2.0881	1.8983	0.75	6.3601
P2-10-05	0.3468	0.1257	2.6644	2.4610	0.71	6.2725
P3-10-01	0.3993	0.1447	2.8881	2.8169	0.72	6.0447
P3-10-02	0.3658	0.1325	1.6983	1.9830	0.67	5.9710
P3-10-03	0.3882	0.1407	2.0356	1.9136	-	-
P3-10-04	0.3416	0.1238	1.9271	1.6017	-	-
P4-10-01	0.4013	0.1454	1.7356	2.0203	0.71	5.5885
P4-10-02	0.4242	0.1537	2.1288	2.6305	0.73	5.7695
P4-10-03	0.3478	0.1260	1.9796	1.6406	-	-
P5-10-01	0.3890	0.1409	2.5831	2.6542	0.70	6.3226
P5-10-02	0.3866	0.1401	2.7051	2.3186	0.69	5.4426
P5-10-03	0.3735	0.1353	2.1051	2.1864	-	-

The effect of SiC addition on SAE values are shown in Figures 8.4 (a) and (b) for 5 wt% SiC and 1wt% SiC whisker addition and 10 wt% SiC addition, respectively. The SAE values increases with increasing relative density of the foams, and except P5 SiC/Al and whisker/Al foams, SiC/Al foams show higher SAE values than those of Al foams for both 5 and 10 wt% addition.



(a)



(b)

Figure 8.4. The variation of SAE values of foams with relative density; (a) 5 wt% P1-P5 SiC and 1 w% SiC whisker and (b) 10 wt% P1-P5 SiC/Al foams.

In few experiments, relatively larger rectangular foam samples (5x2x3 cm) were compression tested and the deformations were video-recorded in order to observe the operative deformation mechanisms in-situ. The deformed micrographs of Al and 10 wt% P6 SiC/Al foam of large sample size as a function of percent strain are shown in Figures 8.5 and 8.6, respectively. Following the elastic region the deformation was localized in the regions marked with black arrows in Figures 8.5 and 8.6. It is also seen in the same figures that the deformation localization starts from the locations of the largest cell size or the lowest density (weakest link), marked with white arrows at 0% strains in Figures 8.5 and 8.6. The deformation localization then proceeded through the undeformed sections of the samples as the strain increased. Microscopic analysis of the localized regions have shown that the main deformation mechanism in both foams was the cell wall bending, i.e. cell edges buckled over cell walls (Figures 8.7(a) and (b)). It is also seen in Figure 8.7 (b) that the buckling of the cell walls in some occasions resulted in tearing of the cell walls (marked with white arrows). The effect of SiC particle on the cell wall tearing is clearly shown in Figures 8.8 (a) and (b). In Figure 8.8(a), the crack started on the cell wall surfaces is seen to follow the particle/metal interface and resulted in particle debonding (marked with arrow). Figure 8.8 (b) shows the particles on the locations of cracks on a bended cell wall. Microscopic observations of P1-P5 SiC foams also clearly show that thicker cell edges bent over the buckled thinner cell walls and tearing of the cell walls (Figures 8.9(a-d)). It was also found that whisker contained foams show the similar deformation mechanism as with Al foams.

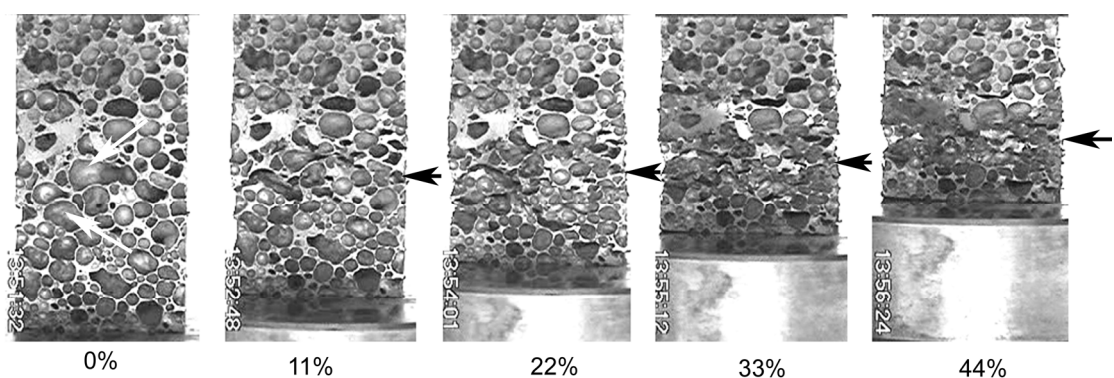


Figure 8.5. The deforming Al foam sample at various percent strains.

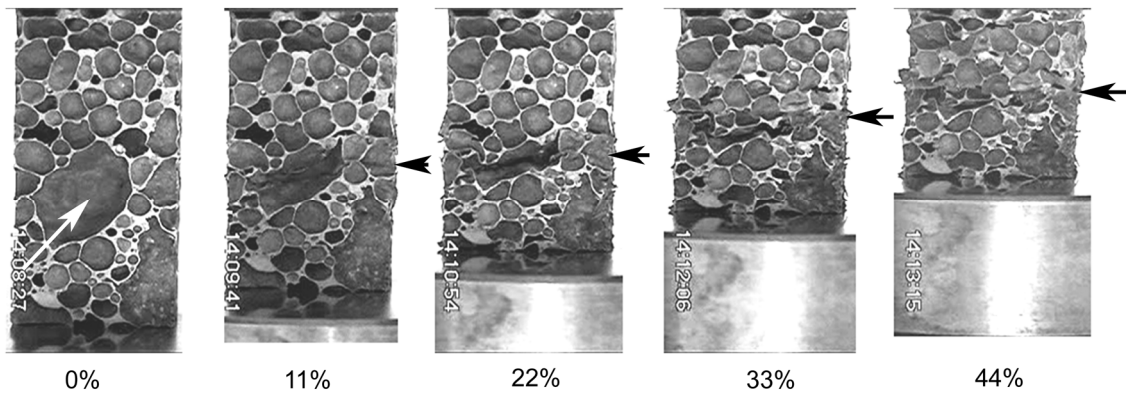


Figure 8.6. The deforming 10 wt% P6 SiC/Al foam sample at various percent strains.

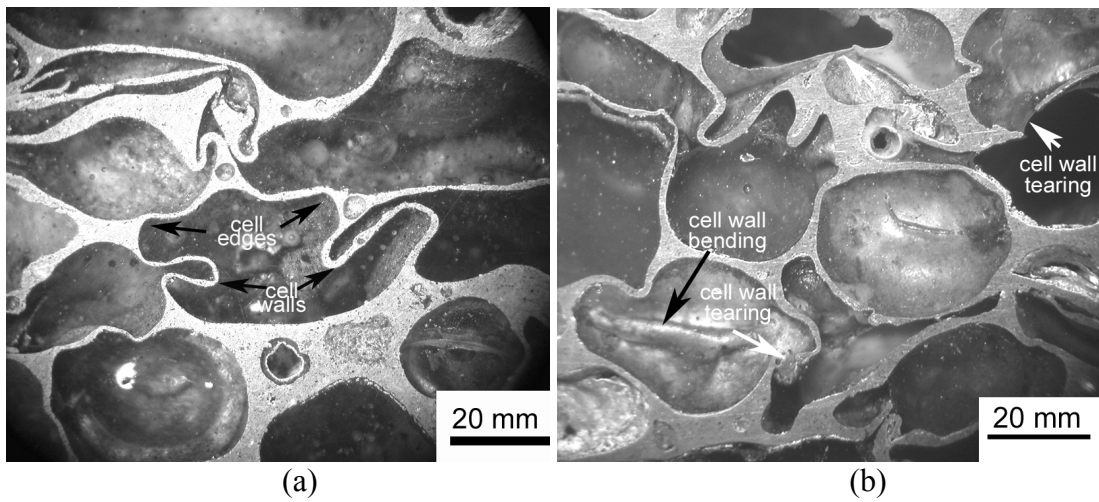


Figure 8.7. The deformed cell micrographs of (a) Al foam and (b) 10 wt% P6 SiC/Al foam samples showing cell wall bending and tearing.

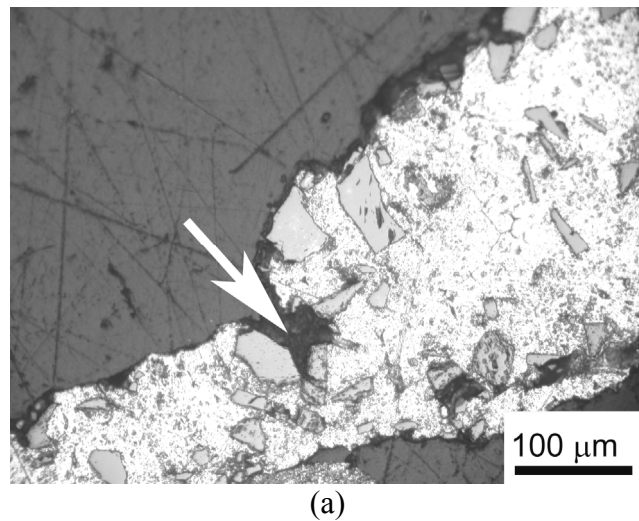


Figure 8.8. Development of cracks around the SiC particles (a) near to a cell edge and (b) on the bent cell walls of 10 wt% P6 SiC/Al foam tested until about 50% strains.

(cont. on next page)

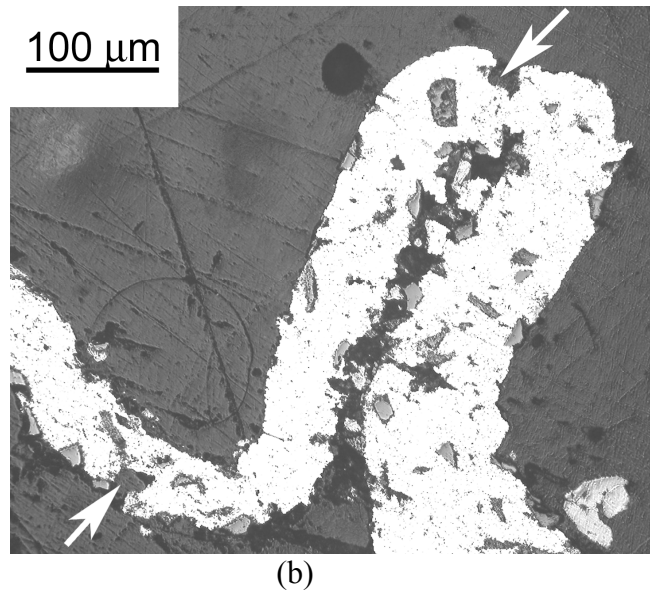


Figure 8.8. (cont.)

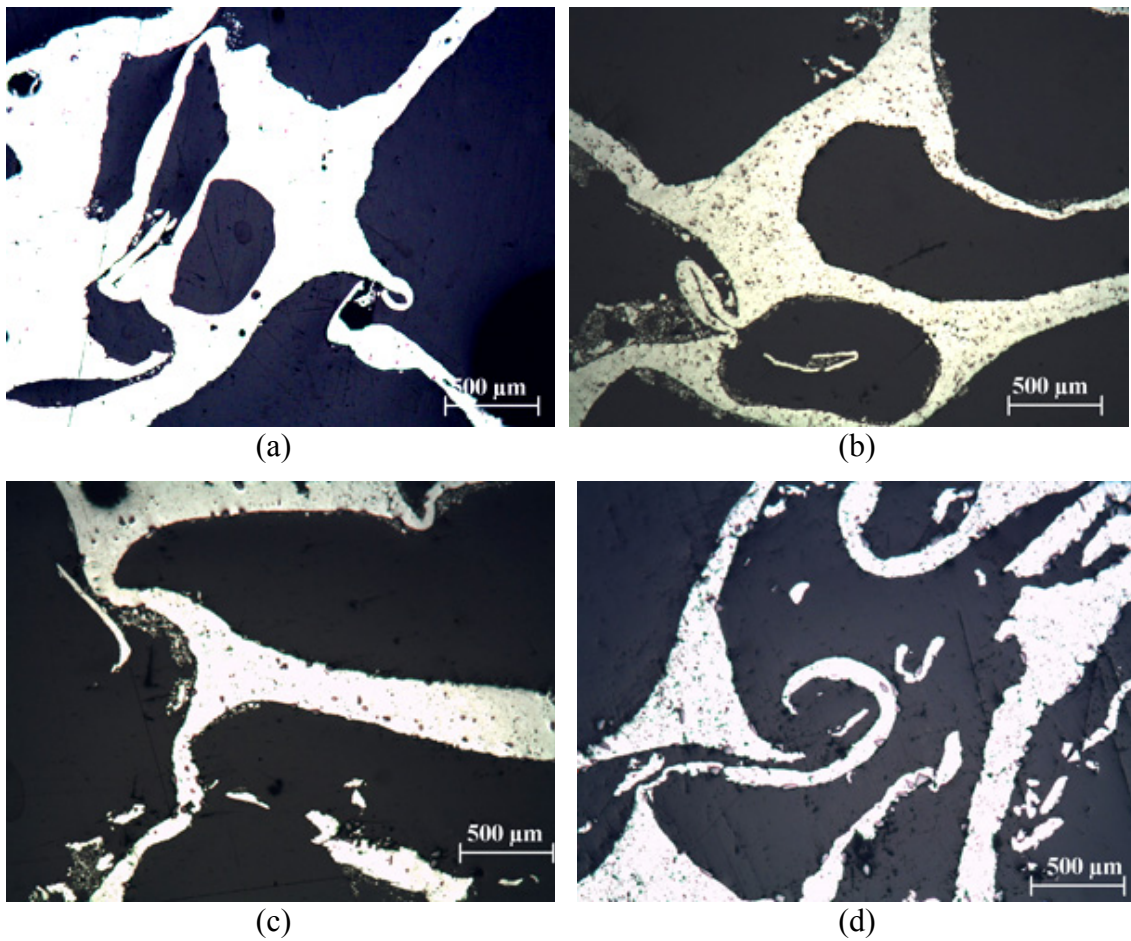


Figure 8.9. The pictures of the deformed (0.40 strain) cell walls of (a) Al (P0), (b) 5 wt% P1, (c) 5 wt% P3 and (d) 5 wt% P5 SiC/Al foams.

CHAPTER 9

DISCUSSION

9.1. The Effect of Particle Addition on the Compact Expansions

Several different factors affect the foamability of the powder compacts including compaction pressure and temperature, foaming temperature and heating rate and the microstructure of the compacts to be foamed. The effects of compaction and foaming conditions on the foaming behavior of AlSi7 and 6061 Al compacts were previously determined (Duarte and Banhart 2000, Duarte, et al. 2002). It was found that increasing foaming temperature increased the foam expansions in both compacts within the temperature range of 600-800 °C. Increasing temperature reduced the viscosity; hence, promoted the gas evolutions, leading to increased foam expansions. It was shown in the same study that the volume expansions were saturated at 750 °C for AlSi7 alloy compact, while the viscosity of 6061 Al alloy compact was not sufficient for efficient foaming until about 800 °C. For the studied Al compacts without particle addition, the foaming temperature is between 663-750 °C and the maximum expansions were found to vary between 3 and 4.5. The expansion values of the studied Al compacts without particle addition were also found to be comparable with those of previously studied AlSi7 and Al compacts (Asavavisithchai and Kennedy 2006a, Banhart 2000a).

The foam evolution in the foaming powder compact process may be considered composing of several stages. The foam formation starts in the solid state just before the melting of the compact (Region 1 of Figure 9.1). The low rate of the expansion at the beginning of the foaming process results from the fact that as the compact is in the mushy state with a relatively high viscosity and by the complete melting of the compact the expansion rate increases greatly, the compact reaching the maximum expansion in Region 2 of Figure 9.1. The observed maximum expansion in the expansion-time graph in Region 2 is attributed to the sudden hydrogen gas release (Duarte and Banhart 2000). As the foam expands after Region 2 in Region 3 and 4, the decaying processes become active with cell wall rupture and coarsening and drainage. The cell wall rupture results from the thinning of the cell walls: the liquid metal flows from the film surface (cell

wall) to the plateau borders (cell edges) under the action of gravity and the pressure difference between film and plateau border. The cell walls get thinner until about a minimum thickness and then collapse. Although the foam expansions in Region 4 of Figure 9.1 remain to be almost constant with increasing foaming duration after 300 s, the foam structure evolution continues.

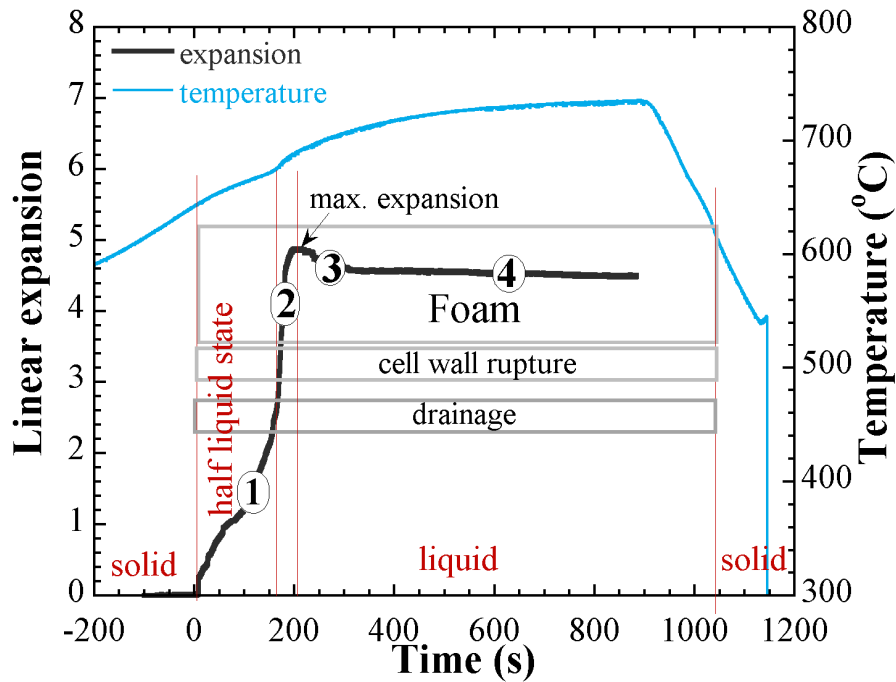


Figure 9.1. Typical linear expansion and temperature vs. time graph of an Al compact.

The drainage reduces the cell wall thickness and forms a dense layer at the bottom and the cell rupture induces larger cells at the top sections of the foam cylinder. Stanzick *et al.* (Stanzick, et al. 2002b) observed the expansions of compacted AlSi7 and thixocast AlSi6Cu4 precursors using real time X-ray radioscopy. The cell wall rupture time for both types of precursors was determined around 50 ms. The cell rupture occurred at cell wall thicknesses below 50 μm . It should be noted that whenever the cell wall thickness reaches this critical value, the cell rupture will occur. The cell rupture time (T) was further approximated using the following relation;

$$T = \frac{b}{2} \sqrt{\frac{c\rho}{\sigma}} \quad (9.1)$$

where, b , c , ρ and σ are the cell wall length, thickness, liquid metal density and surface tension, respectively. The cell rupture events were further determined as a function of foaming time and found to increase significantly with foaming time after an incubation time of 106 s. The incubation time was also found to be well in accord with the present study, corresponding to the maximum expansions at about 150 s. For the studied foams, therefore, the cell wall rupture is likely to be dominant decay process after the maximum expansion reached in the expansion-time graphs as elaborated below.

The number of cells decreases significantly in foamed Al compacts after the maximum expansion as shown in Figure 9.2(a) (77% decrease in cell size in 300 s, from 145 to 33). The foamed P6 SiC/Al compacts although having less number of cells show the similar number cell size reduction with the increasing foaming durations as shown in the same figure. The reduced number of cells at the beginning of foaming in SiC/Al compacts is likely to be due to the increased viscosity of the SiC/Al compacts, leading to the delayed incubation time of the bubble nucleation. With increasing foaming duration, the average cell size increases with the increased events of the cell wall rupture. As the foaming duration proceeds, thinner cells collapse and drainage intensifies, leading to increased cell wall thickness as shown in Figure 9.2(b). The average cell wall thickness of the Al foams increases about 60% in a foam duration of 400 s as depicted in Figure 9.2(b). As the cell wall thickness values were measured from the cross-sections of the foam cylinders, the thicker cell walls at the bottom of the cylinder resulting from the drainage increased the average cell wall thickness. The variation of the cell wall thickness for foamed Al compacts for 100 and 200 s is shown in Figure 9.3(a). It is seen in the same figure that the thicknesses of the cell walls are relatively thinner at the top than the bottom section of the foam cylinder. The minimum cell wall thickness as seen in Figure 9.3(a) is around 40 μm , which is in accord with the critical cell wall thickness measured previously in a similar Al compact (Stanzick, et al. 2002b). Figures 9.3(b) and (c) shows the variations of Al and P6/Al compact cell wall thickness after 100 and 200 s, respectively. The particle size of P6 varies between 3-40 μm . The minimum cell wall thickness of P6/Al foamed compacts is about 66 μm and 60 μm after 100 and 200 s, respectively. This proves the thicker cell wall thickness in SiC particle contained foams. As the drainage occurs through the bottom sections due to gravity, thicker cell walls with wider thickness ranges are observed at the bottom sections of the foams.

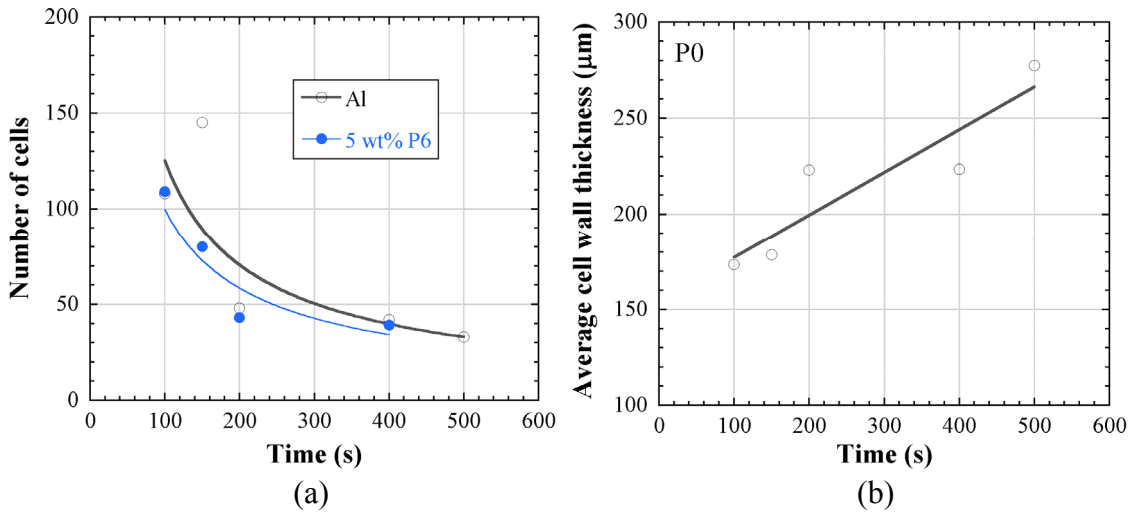


Figure 9.2. The variation of (a) number of cells and (b) average cell wall thickness with furnace folding time in foamed compacts.

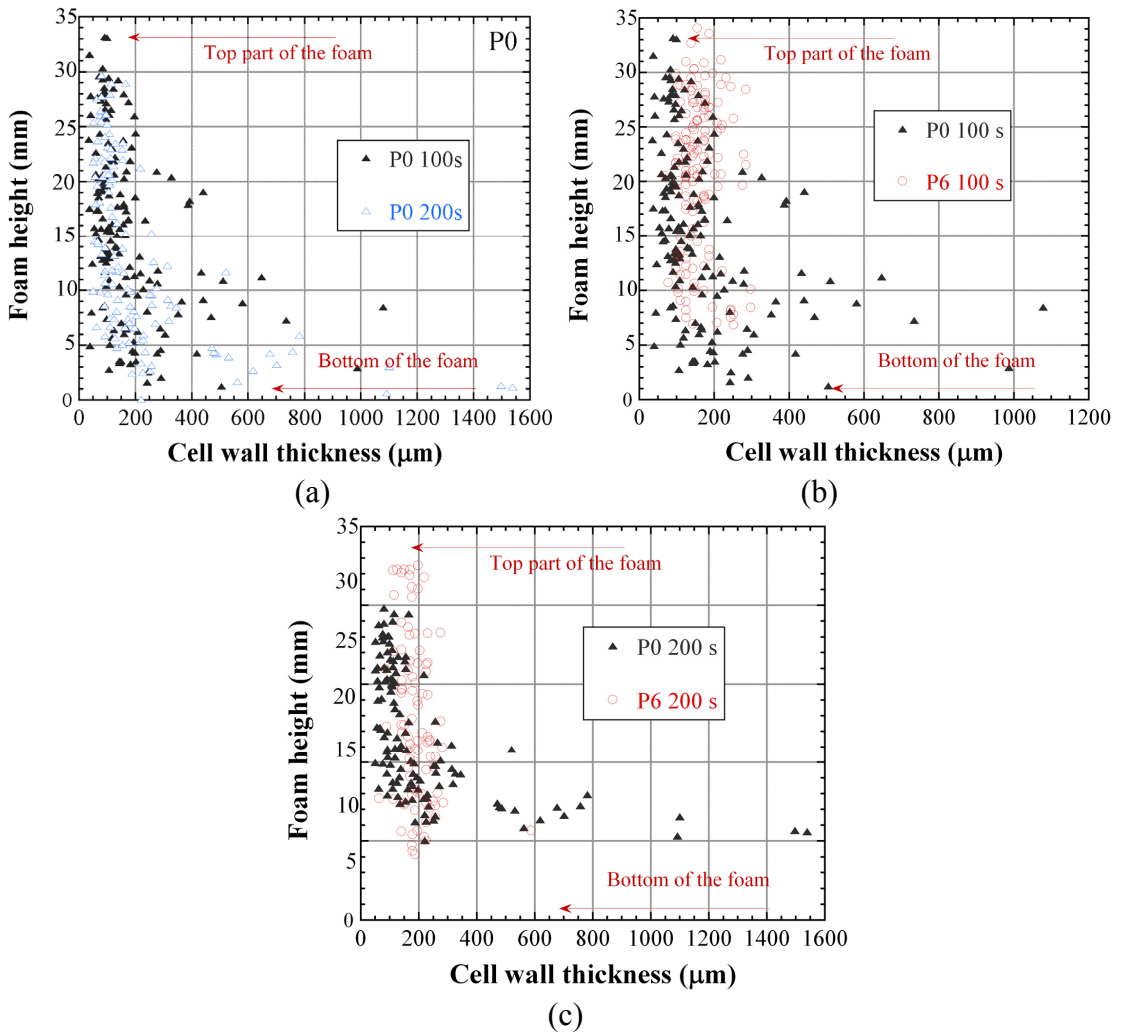


Figure 9.3. Cell wall thickness variation along the foam cylinder; (a) P0 after 100 and 200 s, (b) P0 and P6 after 100 s and (c) P0 and P6 after 200 s.

Haibel *et al.* (Haibel, et al. 2006) analyzed the possible stabilization mechanisms operative in the foaming powder compact process. In the case of no particles on plateau borders and cell walls, the liquid metal on a cell wall, under the effect of the pressure difference,

$$\Delta P = 2\sigma\left(\frac{1}{R_{PB}} - \frac{1}{R_F}\right) \quad (9.2)$$

flows from the cell walls to the plateau borders (R_{PB} and R_F are the radius of curvature of plateau border and cell face, respectively). The partially wetted particles on the cell wall form menisci of radius of $R_F \cong R_{PB}$, which reduces the pressure difference and capillary suction. The increased viscosity of the melt by the presence of small particles in the film may immobilize the liquid metal flow. Babcsan et. al. (Babcsan, et al. 2005, Babcsan, et al. 2007) further analyzed the stability of Al metal foaming processes ex-situ and in-situ. In foams with 13 μm SiC particle addition, the particles were observed to segregate to the cell surface, while in foams with 70 μm SiC particles, only small amount of particles observed on the cell surface. In the present study, both small and large particles were observed to predominantly accumulate on the cell wall surfaces. Deqing and Ziyuan (Wang and Shi 2003) investigated the effect of SiC (1, 7, 14 and 20 μm) and Al_2O_3 (3.5, 5 and 10 μm) particle addition on the foam expansion in Alcan foam processing route. It was noted that, low concentration of large particles could not form an adequate coverage of cell surface; hence, lead to unstable foam, while high concentration of small particles increased the viscosity of the melt significantly so that the air injection could not foam the composite melt. The results of present study are also noted to be in agreement with the above findings.

Figure 9.4(a) and (b) show sequentially the variations of maximum and linear expansions of 5 and 10 wt% SiC/Al compacts as a function of average particle size. On the same graphs, the expansions of Al compacts are also shown. The straight dotted lines in the graphs are the average expansion values of Al compacts and the circles on the data points show the average values. It is noted in Figure 9.4(a) that for 5 wt% SiC addition, the values of maximum and liner expansions are higher than those of Al compacts without particle addition except the largest size SiC addition (P5), while the highest expansion values were detected in compacts with small average particle size (14

and 21 μm). Increasing particle wt% from 5 to 10% decreases the LE_{max} and LE values of the compacts with smaller size SiC particle addition (Figure 9.4(b)). Although 5 wt% P7 powder (36 μm) addition shows similar LE and LE_{max} values with the similar average particle size P3 powder (34 μm) addition, 5 and 10 wt% P8 powder additions show higher LE and LE_{max} expansion values than P2 powder (24 μm) addition. Since, LE is measured in a longer foaming time period, the effect of SiC particle addition at 10 wt% is found to be less pronounced in LE than LE_{max} values. Nevertheless, these have confirmed that particle size, wt% and distribution are effective in the powder compact expansions.

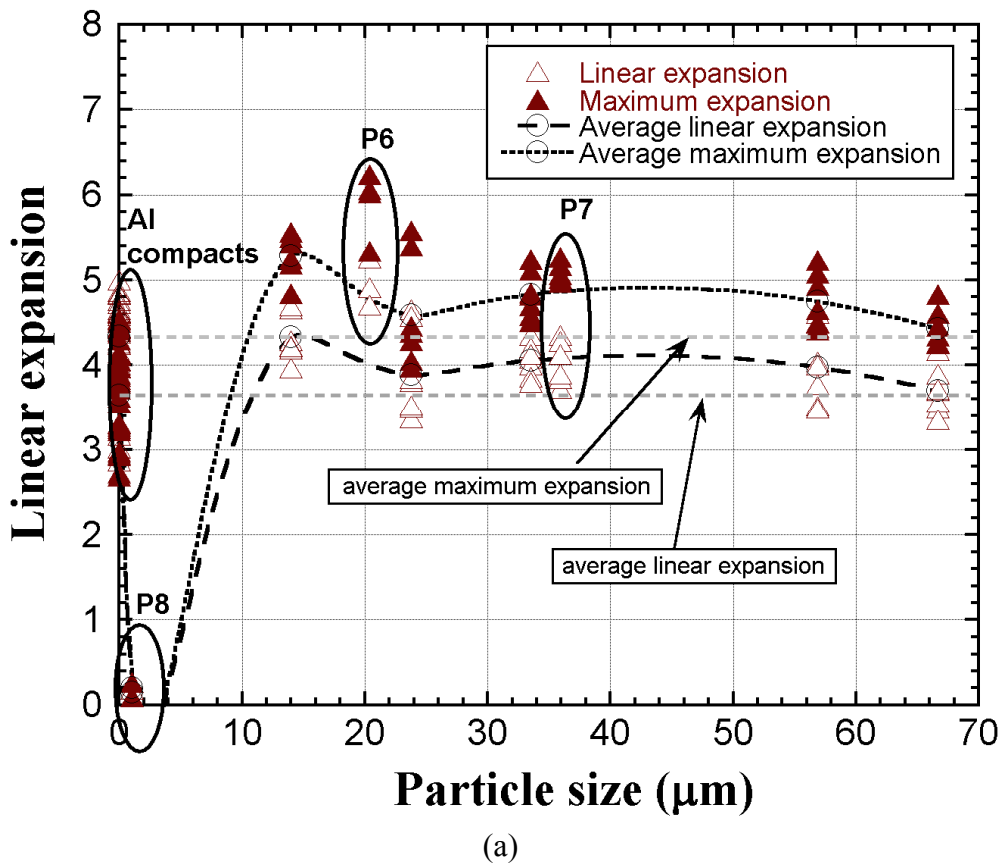


Figure 9.4. Linear and maximum expansion as function of particle size; (a) 5 and (b) 10 wt% particle added compacts.

(cont. on next page)

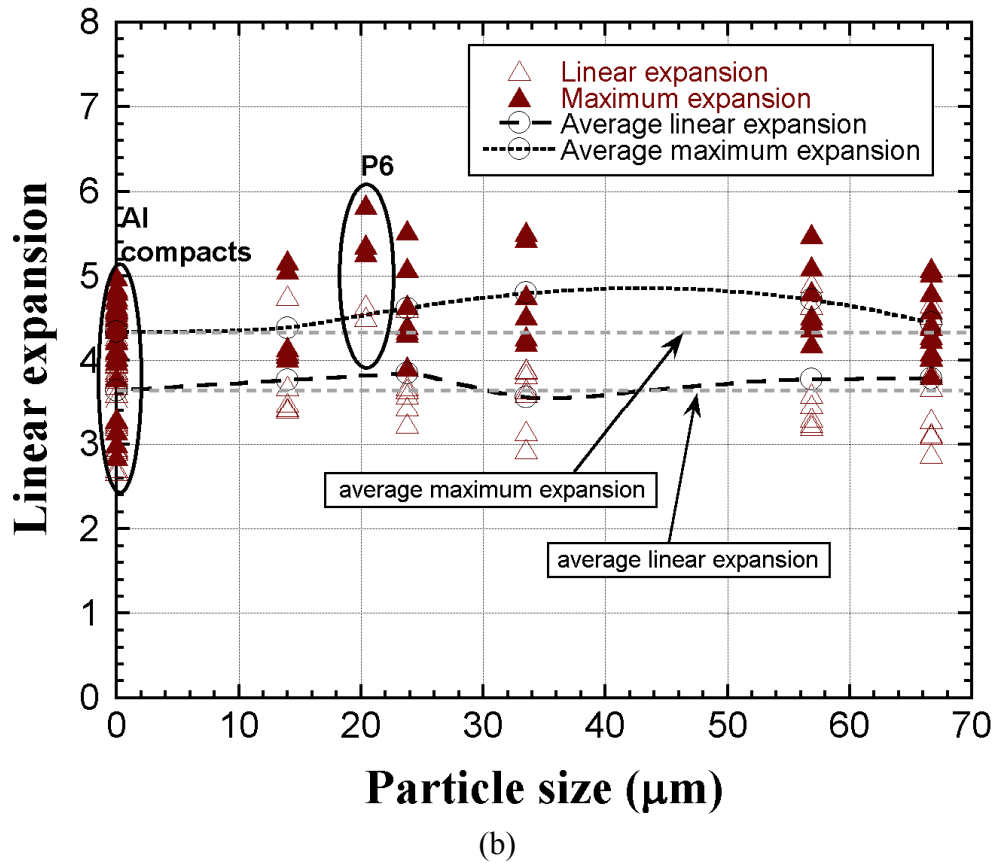


Figure 9.4. (cont.)

9.2. The Characteristics of the Compact Expansions

Expansion-temperature-time graphs of foamed SiC whisker/Al compacts are shown in Figure 9.5. Following characteristics parameters are extracted from the graphs in the same figure: the time between the start of foaming and the complete melting of the compact (t_1), the time between complete melting and maximum expansion (t_2) and time between start of the foaming and maximum expansion (t_3) and the expansion rate of the compact between t_1 and t_2 . The compact heating rate is calculated between the start of the foaming and t_1 . The effect of heating rate on the time of expansion of t_3 is shown in Figure 9.6(a); increasing heating rate reduces the t_3 . This is expected as the compact is heated quickly, it reaches the maximum expansion in shorter time. The variation of the expansion rate with heating rate is shown in Figure 9.6(b) for Al and 5wt% P2 SiC/Al and 0.5 and 1wt% SiC whisker/Al compacts. Increasing heating rate increases the compact expansion rate but the effect is more pronounced for SiC particle contained compacts. The increased expansion rate in SiC contained compacts shows the

effect of particles on the decay processes of the foam structure. The effects of SiC particulate and whisker addition on the foam LE_{max} and LE are shown in Figures 9.7(a) and (b), respectively. With increasing heating rate, LE_{max} values of compacts increases, while SiC particle and whisker contained compacts the expansion is higher at low heating rates. At increasingly high heating rates, the LE_{max} values of Al and SiC/Al compact become very similar. This proves the effect of SiC particles in increasing compact expansion at lower heating rates by increasing the viscosity of the compacts at the studied foam temperature. At increasing heating rates as the decay process rate is reduced, the effect particle addition vanishes. The high heating rates and SiC addition has similar effects on the compact expansions. At increasing foaming durations, the effect of SiC addition is less pronounced on the expansion values as shown in Figure 9.7(b). Finally it is noted the increased LE_{max} values lead to increase in LE values as depicted in Figure 9.8.

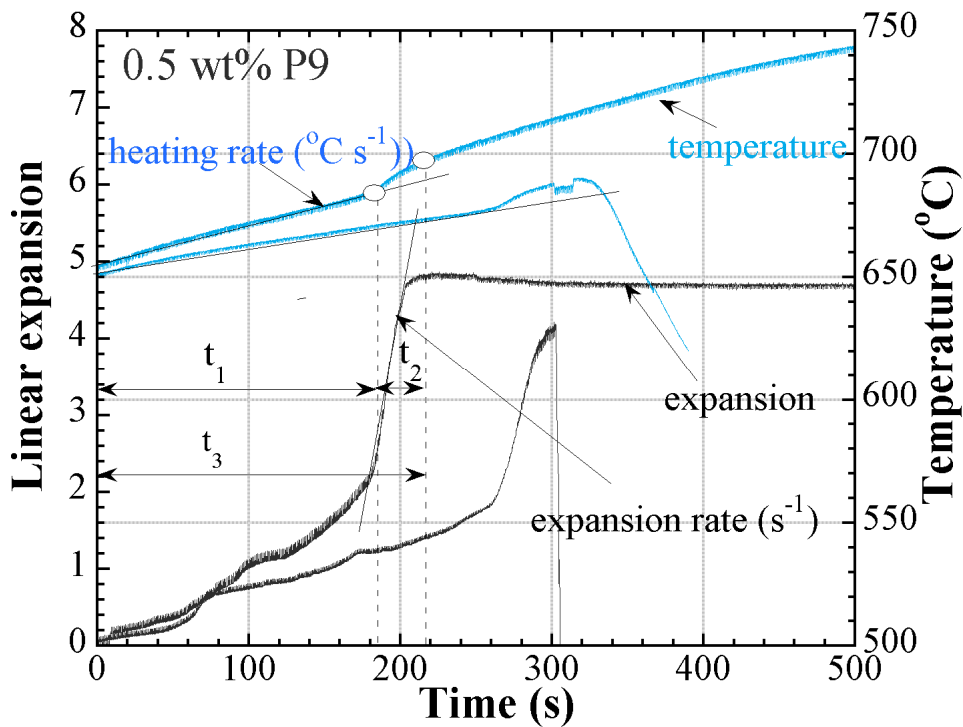


Figure 9.5. The characteristic behavior of the compact foaming (0.5 wt% P9).

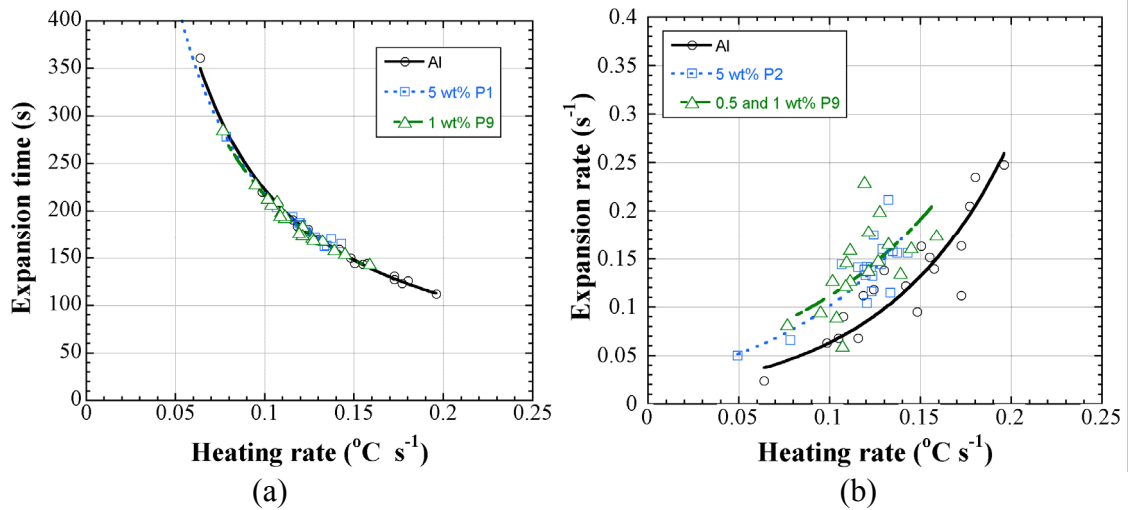


Figure 9.6. The effect of heating rate on the (a) expansion time (t_3) and (b) expansion rate of the foamed compacts.

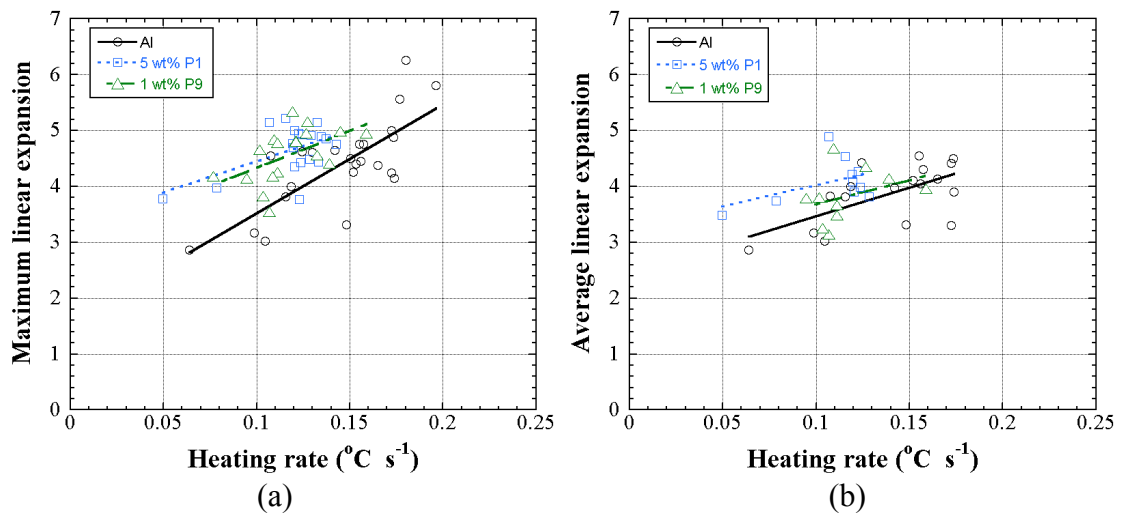


Figure 9.7. Effect of heating rate on (a) maximum and (b) average linear expansion for different foams.

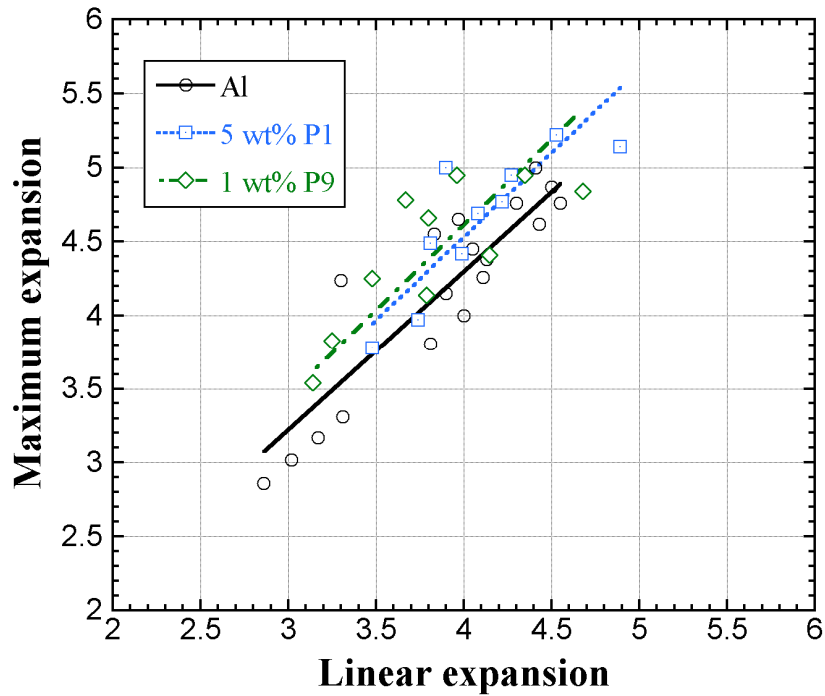


Figure 9.8. Relation between maximum and average linear expansion.

9.3. The Effect of Cumulative Surface Area

Figure 9.9 shows the variations of LE_{max} and LE values of the compacts as function of cumulative particle surface area of SiC particles. Although the expansion values scattered significantly for the same type of the compacts, the average linear and maximum expansion values of SiC added compacts are higher than those of Al compacts at relatively low cumulative particle surface area. The expansion values tend to reach a maximum at about $65 \times 10^3 \text{ mm}^2$ cumulative particle surface area. At increasingly high cumulative particle surface areas, for example 5wt% P8 SiC/Al compacts ($\sim 1350 \times 10^3 \text{ mm}^2$), almost no expansion occurs as depicted in Figure 9.4(a) due to the excessive increase in the compact viscosity. The wt% values of the particle added compacts corresponding to the critical cumulative surface area of the particles, taken as $65 \times 10^3 \text{ mm}^2$ on the average, are further drawn in Figure 9.10 as function of the particle size. The region above the linear curve shown in Figure 9.10 is the region of likely high compact viscosity and below the region of likely low compact viscosity. The optimum particle sizes corresponding to the maximum expansions are also shown in Figure 9.10 for 5, 10 and 15 wt% particle additions. For 56 μm particle size addition, the optimum percentage particle addition is relatively high, 14 wt%, while this value

decreases to about 3.5 wt% when the particle size decreases to 14 μm . For P7 particles (21 μm), the optimum wt% addition is about 5 wt%, which is in accord with the measured relatively high expansion values for 5 wt% addition and relatively low expansion values for 10 and 15 wt% addition (Figure 9.4(b)). Similarly, the expansion values of P7 SiC/Al compacts at 5 wt% addition is expected to be higher than those of P8 SiC/Al compacts, since the optimum wt% is about 9 for P8 powder. Figure 9.10 also shows that, the critical wt% of P8 powder is about 0.3 wt%, which is in accord with the reduced expansion values after about 1 wt% P8 SiC addition (Fig. 6.27). The slight increase of the foam average expansions with increasing particle wt% in large size SiC particles is attributed to the increased particle cell wall surface coverage, while the decrease in the foamability at increasing wt% of particles in P1 SiC/Al compacts is likely due to the increased viscosity of the melt (Figure 9.4(a) and (b)). The powder size distribution may also be effective; a wider particle size distribution would increase the cell wall surface particle coverage, leading to higher expansions. It should also be noted that above findings are only applicable to the studied Al powder compacts since Al powders may show different foaming behavior depending on the alloying element and the oxide content.

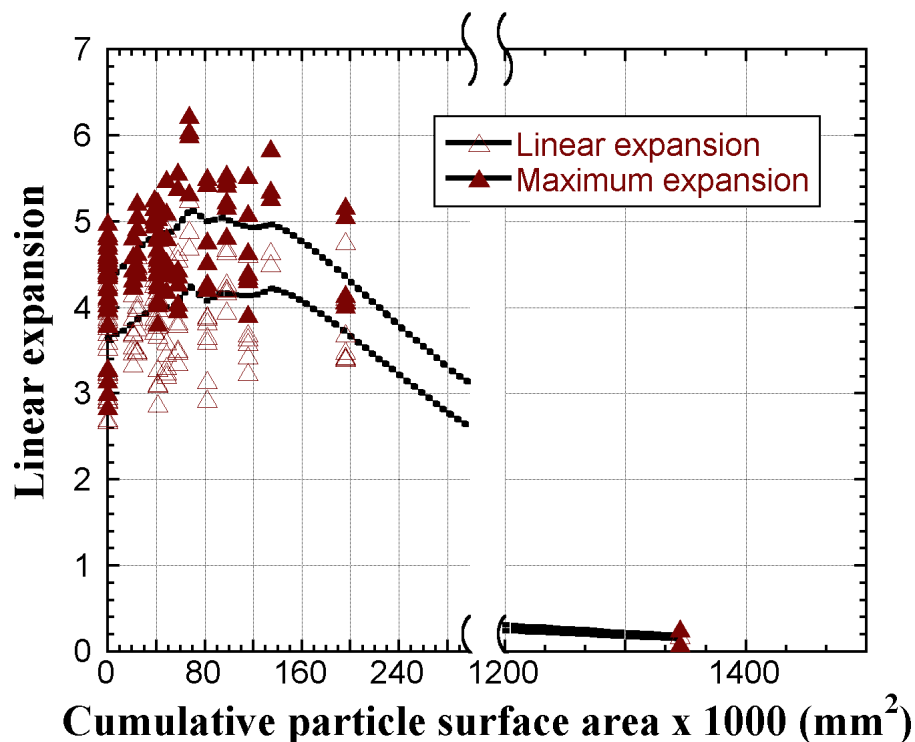


Figure 9.9. Variation of linear and maximum expansion with cumulative particle surface area of SiC particles.

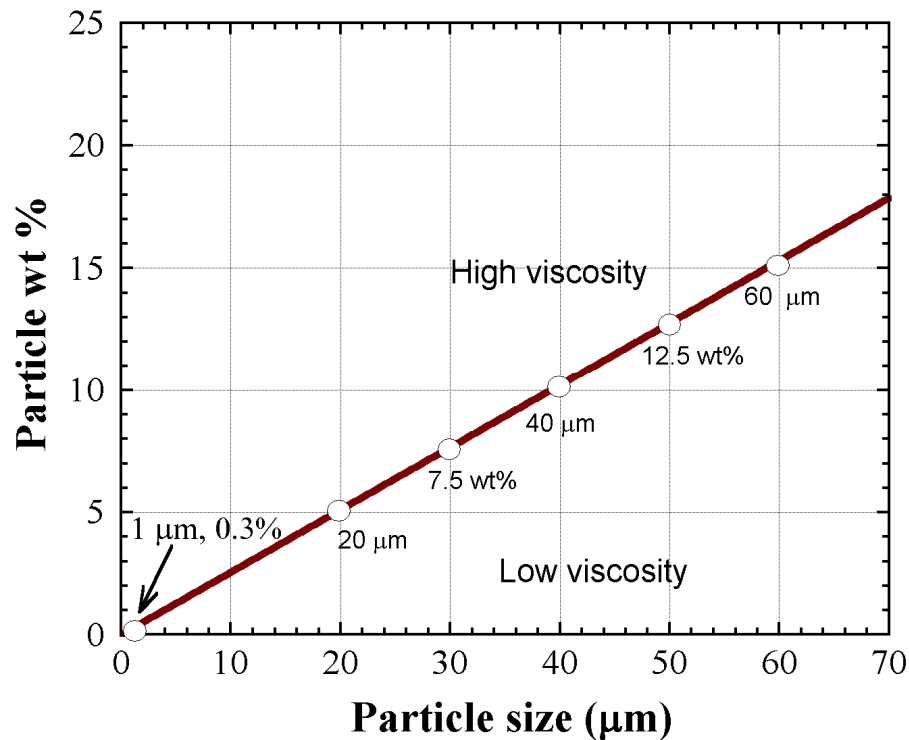


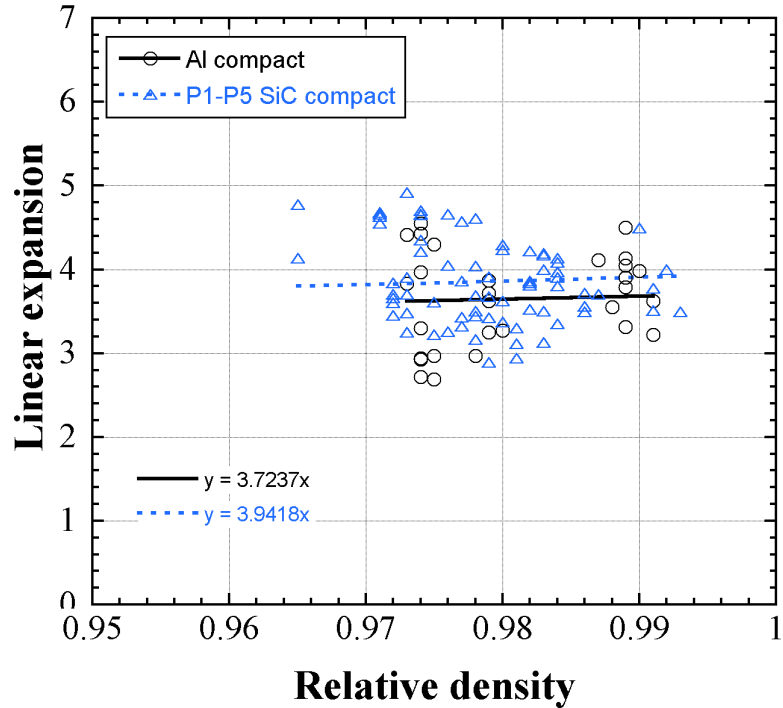
Figure 9.10. Optimum wt% of SiC particle addition as a function of particle size.

Deqing and Ziyuan (Wang and Shi 2003) investigated the effect of SiC (1, 7, 14 and 20 μm) and Al₂O₃ (3.5, 5 and 10 μm) particle addition on the foam expansion in Alcan foam processing route. It was noted that, low concentration of large particles could not form an adequate coverage of cell surface; hence, lead to unstable foam, while high concentration of small particles increased the viscosity of the melt significantly so that the air injection could not foam the composite melt. The results of present study are also noted to be in agreement with the above findings.

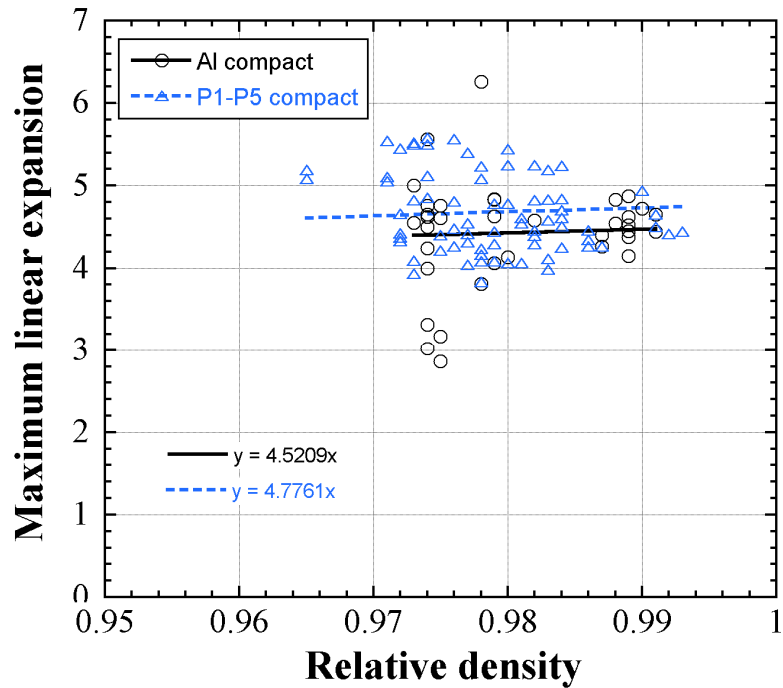
9.4. The Effect Compact Relative Density

The effect of relative density of the compacts on LE and LE_{max} for the Al and P1-P5 SiC/Al foamed compacts are shown in Figures 9.11(a) and (b), respectively. Relative density of the compacts varies between 0.965 and 0.993 within the studied compact relative densities, it is noted in Figures 9.11(a) and (b), the relative density slightly affects the expansions. As the relative densities increases both LE and LE_{max} increases. Therefore, the effect of variations of the relative density of the foamed compacts on the

expansion values may be ignored. On the other hand, Figure 9.11(a) and (b) clearly show that at the similar relative densities SiC/Al compacts experienced more than 10% increase in expansion values.



(a)



(b)

Figure 9.11. The effect of relative density on (a) LE and (b) LE_{max} values of Al and P1-P5 SiC/Al foamed compacts.

9.5. The Reaction Between SiC and Liquid Al

It is known that SiC reacts with molten Al, producing brittle Al_3C_4 and Si-rich Al phases based on the following reaction (Fan, et al. 1998, Sritharan, et al. 2001, Yang, et al. 2004).



The reaction rate depends on the temperature, chemical composition of both matrix and reinforcement and reaction area (surface area of particles). It is proposed that the reduced foamability of nano SiC contained foams is due to the reaction between liquid Al and nano SiC, leading to increase of Si in Al. The extent of the reaction increases with increasing temperature after melting temperature. The liquid metal X-ray diffraction showed that the initial high rate of the reaction kinetics slows down and saturates to a low rate (Fan, et al. 1998). With SiC particle dissolution, Al_4C_3 grows and Si diffuses into the melt. When time passes, a layer of Al_4C_3 may form around SiC particles and this layer may act as a diffusion barrier for the diffusion of Si, C and Al. It is also known that Al_4C_3 dissolves when exposed to aqueous environment. As the reaction proceed the silicon level increases, and the melting point of the composite decreases with time (Lloyd, 1994). It was concluded that the morphology of the interfacial reaction product, Al_4C_3 , plays a significant role in the fluidity of A356 Al–SiCp composites at pouring temperatures higher than 700 °C (Ravi, et al. 2007). It was also noted that during the interfacial reaction, SiC decomposes into Si and C and the Si increases the Si content of molten A356 Al alloy which results in the changes in thermophysical properties such as density, specific heat, critical solid fraction, and viscosity

9.6. Mechanical Behavior

The following general equation has been proposed for the collapse stress (σ_p) of open and closed cell foams (Gibson and Ashby 1997):

$$\frac{\sigma_p}{\sigma_{ys}} = 0.3(\phi\rho)^{3/2} + (1-\phi)\rho \quad (9.4)$$

where, ϕ is the volume fraction of the solids contained on the plateau borders, ρ is the relative density of the foam (foam density/foam metal density) and σ_{ys} is the yield strength of Al metal.

The yield strength of Al and SiC/Al foam metals were determined by the Vickers Hardness Tests on the relatively thick cell edges. At least 10 hardness tests were performed and the results were averaged. The yield strength of Al foam metal was determined 110 MPa on the average, while the yield strength of 5 wt% P1 and P2 SiC and 10 wt% contained P1 and P2 Al metals were found 132, 138 and 156 and 161 MPa, respectively. Note that Equation 9.4 predicts the collapse stress values of open-cell foams when ϕ equals to 1 and the collapse stresses of closed cell foams when ϕ equals to 0. Equation 9.4 is fitted with experimental collapse stress values of Al foams (Figure 9.12). As seen in Figure 9.12, Al foams plateau stress values are well fitted with those of open cell foams, while closed cell foam has relatively higher plateau stress values. Except 10wt% P2/Al foam, foamed SiC/Al compacts show higher plateau stresses than the plateau stress values predicted using Equation 9.4 and a ϕ value of 1 corresponding to open cell foam structure. Microscopic observations clearly show that thicker cell edges bent over the buckled thinner cell walls, reflecting typical crushing behavior of open cell foams. A similar cell crushing behavior is also observed in SiC/Al foams. Equation 9.4 is also fitted with the ϕ value of 0.8 foam SiC/Al foams and the results are shown in Figure 9.13. Except, 10% P2 foam, SiC contained foams plateau stresses show well agreements with the values predicted by Equation 9.4. The differences between the collapse stresses of Al and SiC/Al foams are attributed to the difference between the hardness and ϕ values. The determined values of ϕ are also well accord with that of an SiC particle contained Alcan foam (0.85) at the similar density (0.32 g cm⁻³) (Valente, et al. 2000).

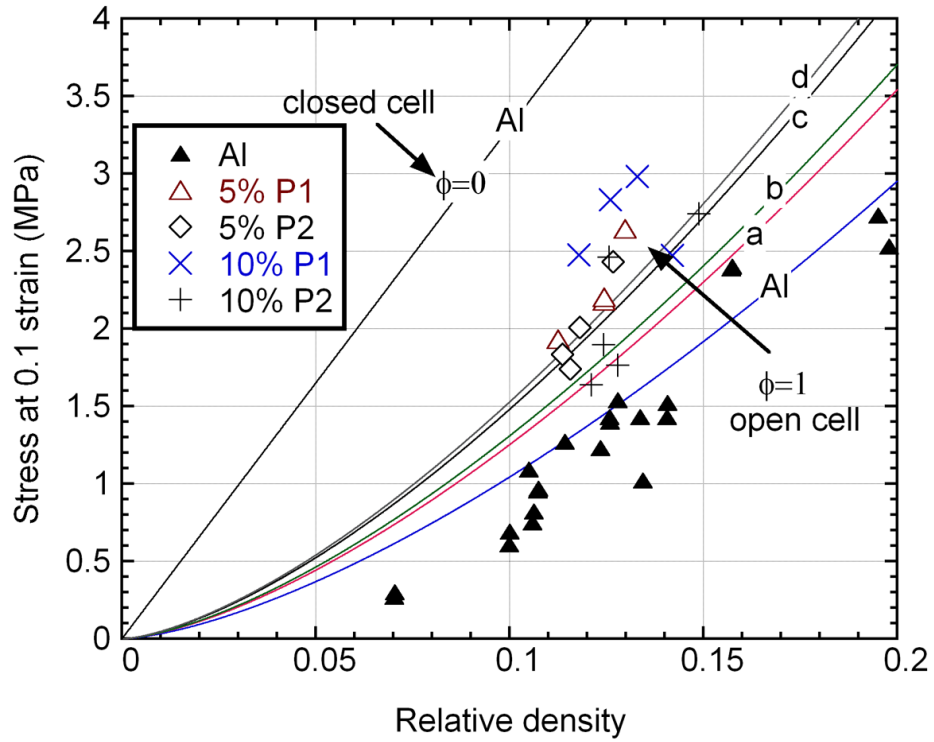


Figure 9.12. Stress vs. relative density of foamed Al and SiC/Al compacts based on the open cell foam structure (a) 5% P1, (b) 5% P2, (c) 10% P1 and (d) 10% P2.

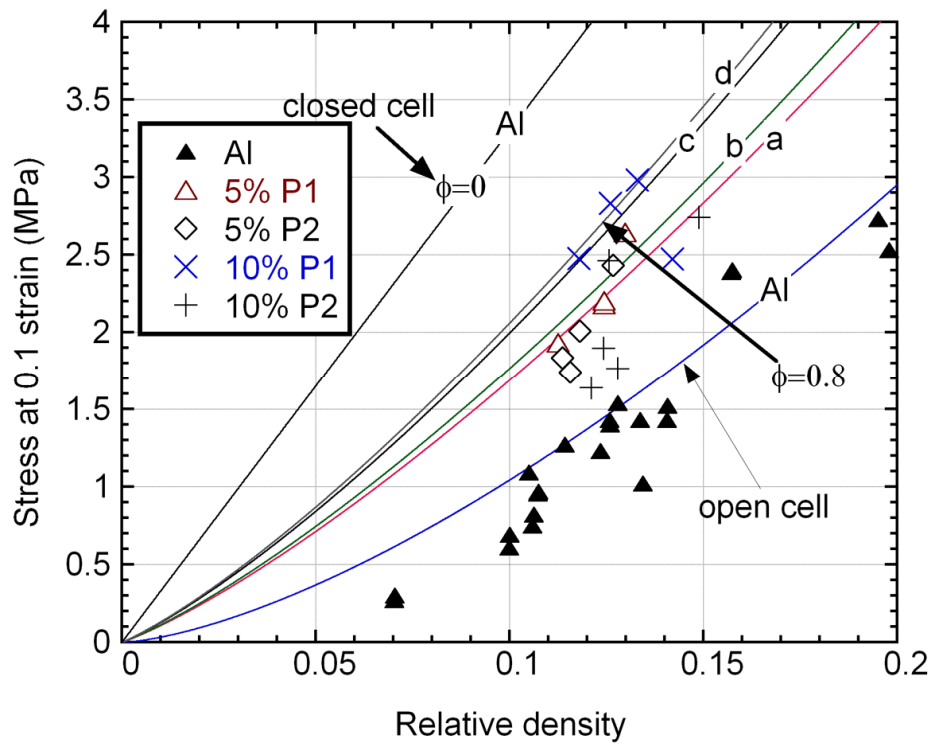


Figure 9.13. Stress vs. relative density of foamed Al and SiC/Al compacts based on ϕ value (a) 5% P1, (b) 5% P2, (c) 10% P1 and (d) 10% P2.

Stress-strain behavior of Al foam is strongly related with the density of the metal foam. Foams with higher densities show higher stresses under compression. Mechanical properties of foamed Al and SiC added compacts were adapted to Equation (9.4), and stress-strain behavior for the foams was determined analytically. Because of the plateau stress in Equation (9.4) is constant, the equation changes as follows.

$$\frac{\sigma_{pl}}{\sigma_{ys}} = \left[0.3(\phi\rho)^{3/2} + (1-\phi)\rho \right] \left[\frac{1}{D} \left(\frac{\varepsilon_d}{\varepsilon_d - \varepsilon} \right)^m \right] \quad (9.5)$$

where D and m are constants.. For Al foam at maximum expansion (0.25-0.3 g cm⁻³) ϕ is found as 1 from the equation (Equation (3.5)) and Equation (9.5) can be written as;

$$\sigma = \sigma_{ys} (0.3[1.0\rho]^{3/2}) \left[\frac{1}{D} \left(\frac{\varepsilon_d}{\varepsilon_d - \varepsilon} \right)^m \right] \quad (9.6)$$

The yield strength of Al foam metal was determined 110 MPa on the average according to the hardness test results. By interpolating these values at Equation (9.5) D and m values were found as 0.9 and 1 respectively. In Figure 9.14, stress-strain behaviors of experiments and calculated results are being compared for Al foams with different densities. Equation (9.4) was also used for 10wt% P6 and 5wt% P1 added foams. For these foams D and m values were similarly found as 2.2 and 0.85, respectively. In Figure 9.15 (a) and (b), comparison of calculated and experimental results for stress-strain values are presented. It is observed clearly from the graphs that, model and experimental results are very similar for the calculated D and m values.

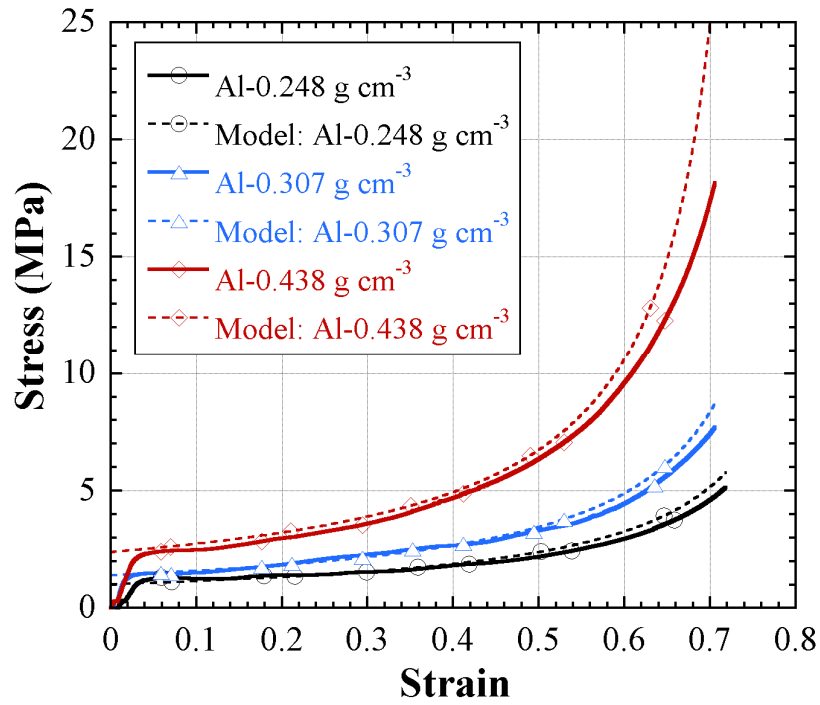
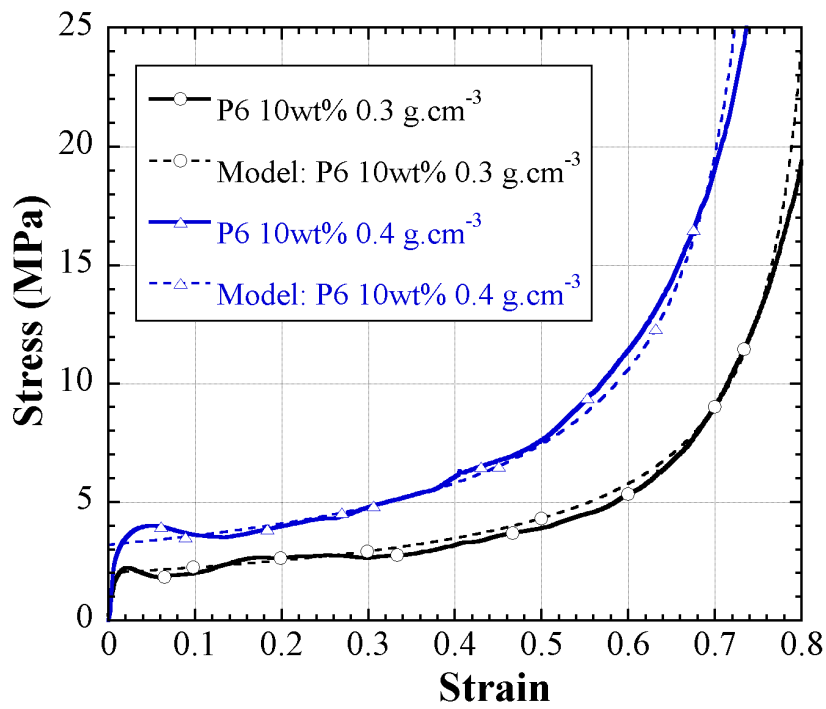


Figure 9.14. Stress-behavior of Al foams according to both experimental and analytical results.



(a)

Figure 9.15. Stress-strain behavior comparison of experimental and calculated results for (a) 10 wt% and (b) 5 wt% SiC added Al foams.

(cont. on next page)

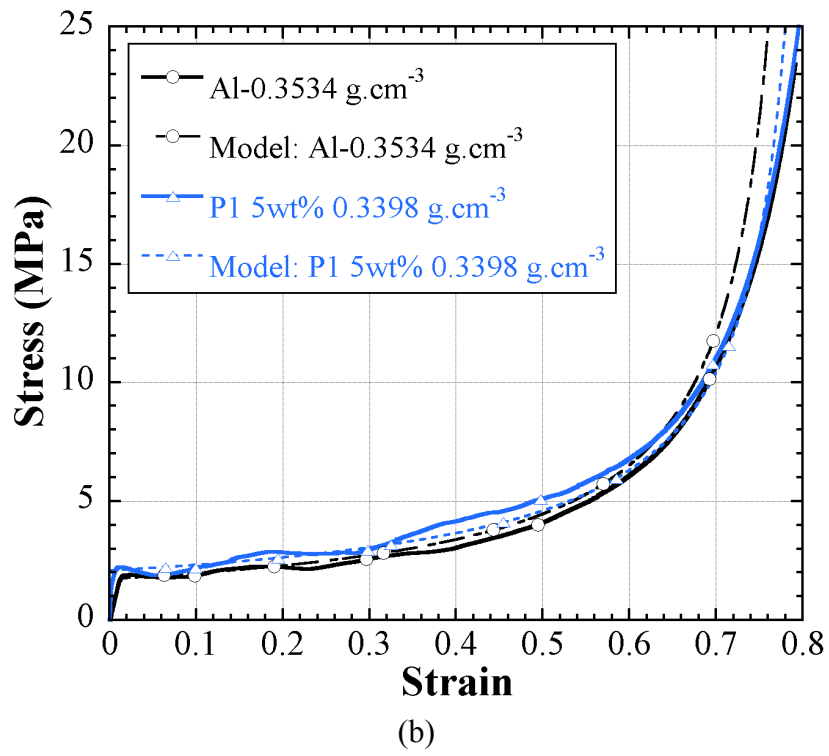


Figure 9.15. (cont.)

CHAPTER 10

CONCLUSIONS

The linear expansions of SiC/Al powder compacts with varying particle size, SiC content and size distribution were measured in order to determine the effect of particle addition on the foaming behavior of Al compacts. The size of the particles and whiskers ranged between 30 nm to 74 μm with the weight percentages between 0.1 and 15. For comparison, Al compacts without particle addition were also foamed. The effect of particle addition on the foam compression behavior was further assessed. A foaming set-up composing of a vertical split furnace and a linear expansion measurement system was used to measure linear expansion of the prepared compacts at a foaming temperature of 750 $^{\circ}\text{C}$. In addition, the variation of the compact temperature during the foaming experiments was also recorded.

For the studied Al compacts without particle addition, the foaming temperature was between 663-750 $^{\circ}\text{C}$ and the maximum expansions were found to vary between 3 and 4.5, which were found to be comparable with those of previously studied similar powder compacts. The low rate of the compact expansion detected at the beginning of the expansion-time graphs resulted from the compact mushy state, and it was followed by increased expansion rate due to the complete melting of the compact. The decaying processes were found operative during compact expansion in the form of cell wall rupture and coarsening and drainage after an incubation time of 150 s. The number of cells decreased significantly in foamed Al compacts after the maximum expansion, while foamed SiC/Al compacts had less number of cells. The minimum cell wall thickness was found to be around 40 μm for foamed Al compacts and 60 μm for foamed SiC/Al compacts, proving a higher cell wall thickness in SiC particle contained foams.

The linear and maximum expansions were found to be relatively high at relatively low particle weight percentages and decreased with increasing weight percentages of the particles for small size particle additions. The compacts with small average particle size but wider particle size distribution was shown to exhibit higher expansions than the compacts with similar average particle size but narrower particle size distribution, showing the importance of the particle size distribution on the

expansions of Al compacts. Microscopic analyses showed that particles were collectively located on the cell wall surfaces as they were partially wetted by liquid Al. The effect of particle size and wt%'s on the foam expansions was analyzed based on the cumulative surface area of the particles, which was presumed to be effective in increasing the surface viscosity of the cell walls. The foam expansions were shown to increase until about a critical cumulative particle surface area; thereafter decreased due to extensive increase in the compact viscosity at the studied foaming temperature.

The effect of SiC particles was to increase the compact expansion at relatively low heating rates by increasing the viscosity of the compacts at the studied foam temperature. At increasing heating rates as the decay process rate decreased, the effect of particle addition was found to vanish. The high heating rates and SiC addition were shown to have similar effects on the compact expansion. At increasing foaming times, the effect of SiC addition was found to be less pronounced on the expansion values, showing the reduced effect of SiC particle addition on the compact expansion/stability at increasing foaming times.

Compression tests showed that the density of the foam was the most effective parameter in increasing the plateau stresses. Microscopic analysis showed that the main deformation mechanism in Al and SiC/Al foams was the cell wall bending, i.e. cell edges buckled over cell walls. This resembled the deformation characteristics of the open cell foams. Buckling of the cell walls in some occasions resulted in tearing of the cell walls. It was also found that whisker contained foams showed similar deformation mechanism. Foams with 5 and 10 wt% SiC particle addition showed 15-100% higher plateau stresses than Al foams at the similar relative densities. The increased plateau stresses in foamed SiC/Al compacts was attributed to higher degree of Al metal located at the cell walls and increased foam material yield strength with Si inclusion into Al matrix.

10.1. Recommendations for Future Studies

Nano size SiC added compacts resulted in poor expansion compared with other particle additions. Increased reaction surface area due to small particle size and non homogeneous distribution of the particles in the compact can result in poor expansion. As it is very difficult to observe products of the reaction between Al and SiC in the

foam structure, investigating the reaction with liquid metal X-ray diffraction analyzer for different type of SiC additions can be one of the most recommended future works for the study. To disperse nano size ceramic particles uniformly in metal, ultrasonic dispersion during foaming of the compact can be investigated.

Viscosity measurements of the Al melts with different SiC additions would help in understanding the expansion behavior of the SiC added compacts. These measurements can be done by measuring the voltage of the stirring motor of the composite melt. By these viscosity measurements different reaction characteristics between the SiC types will be included in viscosity of the melt foams.

With the increased mechanical properties of the SiC added foams, stronger sandwich panels and components can be manufactured. Manufacturing a specific foam component with SiC addition can result in a better understanding of the foaming process. Using different and more common Al powders which are commercially available would also help to decrease the unit price of the foam. This would increase the application areas of the foams considerably.

REFERENCES

- Alexander, J.M. , 1960, An approximate analysis of collapse of thin-walled cylindrical shells under axial loading. *Q J Mech. Appl Math.* 13: p. 1-9.
- Allen, B.C., Mote, M.W. and Sabroff, A.M., 1963, Method of Making Foamed Metal Bodies, US Patent, 3.087.807.
- Andrews, E. W., Gioux, G., Onck, P. and Gibson, L. J., 2001, Size effects in ductile cellular solids. Part II: experimental results. *International Journal of Mechanical Sciences.* 43(3): p. 701-713.
- Asavavisithchai, S. and Kennedy, A. R., 2006a, The effect of compaction method on the expansion and stability of aluminium foams. *Advanced Engineering Materials.* 8(9): p. 810-815.
- Asavavisithchai, S. and Kennedy, A. R., 2006b, The effect of Mg addition on the stability of Al-Al₂O₃ foams made by a powder metallurgy route. *Scripta Materialia.* 54(7): p. 1331-1334.
- Asavavisithchai, S. and Kennedy, A. R., 2006c, Effect of powder oxide content on the expansion and stability of PM-route Al foams. *Journal of Colloid and Interface Science.* 297(2): p. 715-723.
- Ashby, M.F., Evans, A.G., Fleck, N.A., Gibson, L.J., Hutchinson, J.W. and Wadley, H.N.G., 2000, Metal Foams: A Design Guide, Butterworth-Heinemann
- Babcsan, N., Leitimeier, D. and Banhart, J. B., 2005, Metal foams - high temperature colloids - Part I. Ex situ analysis of metal foams. *Colloids and Surfaces a-Physicochemical and Engineering Aspects.* 261(1-3): p. 123-130.
- Babcsan, N., Leitlmeier, D., Degischer, H. P. and Banhart, J., 2004, The role of oxidation in blowing particle-stabilised aluminium foams. *Advanced Engineering Materials.* 6(6): p. 421-428.
- Babcsan, N., Moreno, F. G. and Banhart, J., 2007, Metal foams - High temperature colloids - Part II: In situ analysis of metal foams. *Colloids and Surfaces a-Physicochemical and Engineering Aspects.* 309(1-3): p. 254-263.

- Banhart, J., 2000a, Manufacturing routes for metallic foams. *Jom-Journal of the Minerals Metals & Materials Society*. 52(12): p. 22-27.
- Banhart, J., 2000b, Metallic foams: challenges and opportunities, Eurofoam 2000.
- Banhart, J., 2001, Manufacture, characterisation and application of cellular metals and metal foams. *Progress in Materials Science*. 46(6): p. 559-U3.
- Banhart, J., 2003, Aluminum foams: On the road to real applications. *Mrs Bulletin*. 28(4): p. 290-295.
- Banhart, J., 2006, Metal foams: Production and stability. *Advanced Engineering Materials*. 8(9): p. 781-794.
- Banhart, J. and Baumeister, J., 1998, Production Methods for Metallic Foams. *MSR Symposium Proceeding*. Vol.521: p. pp.121-132.
- Banhart, J., Stanzick, H., Helfen, L., Baumbach, T. and Nijhof, K., 2001, Real-time X-ray investigation of aluminum foam sandwich production. *Advanced Engineering Materials*. 3(6): p. 407-411.
- Baumeister, J. and Schrader, H., 1992, Methods for Manufacturing Foamable Metal Bodies, US patent, 5151246
- Baumgartner, F., Duarte, I. and Banhart, J., 2000, Industrialization of powder compact foaming process. *Advanced Engineering Materials*. 2(4): p. 168-174.
- Beals, J. T. and Thompson, M. S., 1997, Density gradient effects on aluminium foam compression behaviour. *Journal of Materials Science*. 32(13): p. 3595-3600.
- Calladine, C.R. and English, R.W., 1984, Strain-rate and inertia effects in the collapse of two types of energy-absorbing structure. *Int. J. Mech. Sci*. 26: p. 689-701.
- Chan, K. C. and Xie, L. S., 2003, Dependency of densification properties on cell topology of metal foams. *Scripta Materialia*. 48(8): p. 1147-1152.

- Chen, W. G., 2001, Experimental and numerical study on bending collapse of aluminum foam-filled hat profiles. *International Journal of Solids and Structures*. 38(44-45): p. 7919-7944.
- Deshpande, V. S. and Fleck, N. A., 2000, High strain rate compressive behaviour of aluminium alloy foams. *International Journal of Impact Engineering*. 24(3): p. 277-298.
- Duarte, I. and Banhart, J., 2000, A study of aluminium foam formation - Kinetics and microstructure. *Acta Materialia*. 48(9): p. 2349-2362.
- Duarte, I., Mascarenhas, J., Ferreira, A and Banhart, J, 2002, The evolution of morphology and kinetics during the foaming process of aluminium foams. *Advanced Materials Forum I*. 230-2: p. 96-101.
- Elmoutaouakkil, A., Salvo, L., Maire, E. and Peix, G., 2002, 2D and 3D characterization of metal foams using X-ray tomography. *Advanced Engineering Materials*. 4(10): p. 803-807.
- Fan, T., Shi, Z., Zhang, D. and Wu, R., 1998, The interfacial reaction characteristics in SiC/Al composite above liquidus during remelting. *Materials Science and Engineering*. A257: p. 281-286.
- Fuganti, A., Lorenzi, L., Hanssen, A. G. and Langseth, M., 2000, Aluminium foam for automotive applications. *Advanced Engineering Materials*. 2(4): p. 200-204.
- Gama, B. A., Bogetti, T. A., Fink, B. K., Yu, C. J., Claar, T. D., Eifert, H. H. and Gillespie, J. W., 2001, Aluminum foam integral armor: a new dimension in armor design. *Composite Structures*. 52(3-4): p. 381-395.
- Gergely, V. and Clyne, B., 2000, The FORMGRIP process: Foaming of reinforced metals by gas release in precursors. *Advanced Engineering Materials*. 2(4): p. 175-178.
- Gergely, V. and Clyne, T. W., 2004, Drainage in standing liquid metal foams: modelling and experimental observations. *Acta Materialia*. 52(10): p. 3047-3058.
- Gibson, L. J., 2000, Mechanical behavior of metallic foams. *Annual Review of Materials Science*. 30: p. 191-227.

- Gibson, L.J. and Ashby, M.F., 1997, Cellular Solids: Structures and Properties, Cambridge University Press
- Guden, M., Toksoy, A. K. and Kavi, H., 2006, Experimental investigation of interaction effects in foam-filled thin-walled aluminum tubes. *Journal of Materials Science*. 41(19): p. 6417-6424.
- Haibel, A., Rack, A. and Banhart, J., 2006, Why are metal foams stable? *Applied Physics Letters*. 89(15).
- Hall, I. W., Guden, M. and Yu, C. J., 2000, Crushing of aluminum closed cell foams: Density and strain rate effects. *Scripta Materialia*. 43(6): p. 515-521.
- Han, F. S., Zhu, Z. G. and Liu, C. S., 1998, Examination of acoustic absorption characteristics of foamed aluminum. *Acustica*. 84(3): p. 573-576.
- Hanssen, A. G., Langseth, M. and Hopperstad, O. S., 1999, Static crushing of square aluminium extrusions with aluminium foam filler. *International Journal of Mechanical Sciences*. 41(8): p. 967-993.
- Hanssen, A. G., Langseth, M. and Hopperstad, O. S., 2000, Static and dynamic crushing of square aluminium extrusions with aluminium foam filler. *International Journal of Impact Engineering*. 24(4): p. 347-383.
- Hanssen, A. G., Langseth, M. and Hopperstad, O. S., 2001, Optimum design for energy absorption of square aluminium columns with aluminium foam filler. *International Journal of Mechanical Sciences*. 43(1): p. 153-176.
- Helfen, L., Baumbach, T., Pernot, P., Cloetens, P., Stanzick, H., Schladitz, K. and Banhart, J., 2005, Investigation of pore initiation in metal foams by synchrotron-radiation tomography. *Applied Physics Letters*. 86(23).
- Iida, T. and Guthrie, R.I.L., 1988, The Physical Properties of Liquid Metals, Clarendon Press, Oxford.
- Kaptay, G., 2004, Interfacial criteria for stabilization of liquid foams by solid particles. *Colloids and Surfaces a-Physicochemical and Engineering Aspects*. 230(1-3): p. 67-80.

- Kathuria, Y. P., 2001a, Laser assisted aluminum foaming. *Surface & Coatings Technology*. 142: p. 56-60.
- Kathuria, Y. P., 2001b, Laser assisted foaming of aluminum. *Advanced Engineering Materials*. 3(9): p. 702-705.
- Kathuria, Y. P., 2001c, Physical processes in laser-assisted aluminum foaming. *Journal of Materials Engineering and Performance*. 10(4): p. 429-434.
- Kathuria, Y. P., 2003a, Nd-YAG laser assisted aluminum foaming. *Journal of Materials Processing Technology*. 142(2): p. 466-470.
- Kathuria, Y. P., 2003b, A preliminary study on laser assisted aluminum foaming. *Journal of Materials Science*. 38(13): p. 2875-2881.
- Kennedy, A. R., 2002, The effect of TiH₂ heat treatment on gas release and foaming in Al-TiH₂ preforms. *Scripta Materialia*. 47: p. 763-767.
- Kennedy, A. R. and Asavavisitchai, S., 2004, Effects of TiB₂ particle addition on the expansion, structure and mechanical properties of PM Al foams. *Scripta Materialia*. 50(1): p. 115-119.
- Kennedy, A. R. and Asavavisithchai, S., 2004, Effect of ceramic particle additions on foam expansion and stability in compacted Al-TiH₂ powder precursors. *Advanced Engineering Materials*. 6(6): p. 400-402.
- Kennedy, A. R. and Lopez, V. H., 2003, The decomposition behavior of as-received and oxidized TiH₂ foaming-agent powder. *Materials Science and Engineering a-Structural Materials Properties Microstructure and Processing*. 357(1-2): p. 258-263.
- Kenny, L. D., 1996, Mechanical properties of particle stabilized aluminum foam, ed. 1883-1889, Transtec Publications Ltd
- Kitazono, K., Sato, E. and Kuribayashi, K., 2004, Novel manufacturing process of closed-cell aluminum foam by accumulative roll-bonding. *Scripta Materialia*. 50(4): p. 495-498.

- Korner, C. and Singer, R. F., 2000, Processing of metal foams - Challenges and opportunities. *Advanced Engineering Materials*. 2(4): p. 159-165.
- Kumar, P. S., Ramachandra, S. and Ramamurty, U., 2003, Effect of displacement-rate on the indentation behavior of an aluminum foam. *Materials Science and Engineering a-Structural Materials Properties Microstructure and Processing*. 347(1-2): p. 330-337.
- Langseth, M. and Hopperstad, O. S., 1996, Static and dynamic axial crushing of square thin-walled aluminium extrusions. *International Journal of Impact Engineering*. 18(7-8): p. 949-968.
- Lee, S., Barthelat, F., Moldovan, N., Espinosa, H. D. and Wadley, H. N. G., 2006, Deformation rate effects on failure modes of open-cell Al foams and textile cellular materials. *International Journal of Solids and Structures*. 43(1): p. 53-73.
- Leitlmeier, D., Degischer, H. P. and Flankl, H. J., 2002, Development of a foaming process for particulate reinforced aluminum melts. *Advanced Engineering Materials*. 4(10): p. 735-740.
- Lloyd, D.J., 1994, Particle reinforced aluminum and magnesium matrix composites, *International Materials Reviews*, 39(1): p. 1-23.
- Lu, T. J., Hess, A. and Ashby, M. F., 1999, Sound absorption in metallic foams. *Journal of Applied Physics*. 85(11): p. 7528-7539.
- Maiti, S.K., Gibson, L. J. and Ashby, M. F., 1984, Deformation and energy absorption diagrams for cellular solids. *Acta Materialia*. 32: p. 1963-1975.
- Miyoshi, T., Itoh, M., Akiyama, S. and Kitahara, A., 2000, ALPORAS aluminum foam: Production process, properties, and applications. *Advanced Engineering Materials*. 2(4): p. 179-183.
- Mukai, T., Kanahashi, H., Miyoshi, T., Mabuchi, M., Nieh, T. G. and Higashi, K., 1999, Experimental study of energy absorption in a close-celled aluminum foam under dynamic loading. *Scripta Materialia*. 40(8): p. 921-927.

- Mukai, T., Miyoshi, T., Nakano, S., Somekawa, H. and Higashi, K., 2006, Compressive response of a closed-cell aluminum foam at high strain rate. *Scripta Materialia*. 54(4): p. 533-537.
- Onck, P. R., Andrews, E. W. and Gibson, L. J., 2001, Size effects in ductile cellular solids. Part I: modeling. *International Journal of Mechanical Sciences*. 43(3): p. 681-699.
- Paul, A. and Ramamurty, U., 2000, Strain rate sensitivity of a closed-cell aluminum foam. *Materials Science and Engineering a-Structural Materials Properties Microstructure and Processing*. 281(1-2): p. 1-7.
- Peroni, L., Avalle, M. and Peroni, M., 2008, The mechanical behaviour of aluminium foam structures in different loading conditions. *International Journal of Impact Engineering*. 35(7): p. 644-658.
- Raj, R. E. and Daniel, B. S. S., 2007, Aluminum melt foam processing for light-weight structures. *Materials and Manufacturing Processes*. 22(4): p. 525-530.
- Rakow, J. F. and Waas, A. M., 2005, Size effects and the shear response of aluminum foam. *Mechanics of Materials*. 37(1): p. 69-82.
- Ramakrishna, S. and Hamada, H., 1998, Energy absorption characteristics of crash worthy structural composite materials, ed. 585-619.
- Ravi, K.R., Pillai, R.M., Amaranathan, K.R., Pai, B.C. and Chakraborty, M. 2008, Fluidity of aluminum alloys and composites: A review. *Journal of Alloys and Compounds*, 456: p. 201-210.
- Ravi, K.R., Pillai, R.M., Pai, B.C. and Chakraborty, M., 2007, Influence of Interfacial Reaction on the Fluidity of A356 Al-SiC_p Composites-A Theoretical Approach, *Metallurgical and Materials Transactions A*, 38A: p. 2531-2539.
- Reid, S. R. and Peng, C., 1997, Dynamic uniaxial crushing of wood. *International Journal of Impact Engineering*. 19(5-6): p. 531-570.
- Santosa, S., Banhart, J. and Wierzbicki, T., 2000a, Bending crush resistance of partially foam-filled sections. *Advanced Engineering Materials*. 2(4): p. 223-227.

- Santosa, S., Banhart, J. and Wierzbicki, T., 2001, Experimental and numerical analyses of bending of foam-filled sections. *Acta Mechanica*. 148(1-4): p. 199-213.
- Santosa, S. P., Wierzbicki, T., Hanssen, A. G. and Langseth, M., 2000b, Experimental and numerical studies of foam-filled sections. *International Journal of Impact Engineering*. 24(5): p. 509-534.
- Santosa, S. and Wierzbicki, T., 1998, Crash behavior of box columns filled with aluminum honeycomb or foam. *Computers & Structures*. 68(4): p. 343-367.
- Schwingel, D., Seeliger, H. W., Vecchionacci, C., Alwes, D. and Dittrich, J., 2007, Aluminium foam sandwich structures for space applications. *Acta Astronautica*. 61(1-6): p. 326-330.
- Seitzberger, M., Rammerstorfer, F. G., Degischer, H. P. and Gradinger, R., 1997, Crushing of axially compressed steel tubes filled with aluminium foam. *Acta Mechanica*. 125(1-4): p. 93-105.
- Seitzberger, M., Rammerstorfer, F. G., Gradinger, R., Degischer, H. P., Blaimschein, M. and Walch, C., 2000, Experimental studies on the quasi-static axial crushing of steel columns filled with aluminium foam. *International Journal of Solids and Structures*. 37(30): p. 4125-4147.
- Simone, A. E. and Gibson, L. J., 1998, Effects of solid distribution on the stiffness and strength of metallic foams. *Acta Materialia*. 46(6): p. 2139-2150.
- Song, H. W., Fan, Z. H., Yu, G., Wang, Q. C. and Tobota, A., 2005, Partition energy absorption of axially crushed aluminum foam-filled hat sections. *International Journal of Solids and Structures*. 42(9-10): p. 2575-2600.
- Song, Z. L., Ma, L. Q., Wu, Z. J. and He, D. P., 2000, Effects of viscosity on cellular structure of foamed aluminum in foaming process. *Journal of Materials Science*. 35(1): p. 15-20.
- Song, Z. L. and Nutt, S. R., 2007, Rheology of foaming aluminum melts. *Materials Science and Engineering a-Structural Materials Properties Microstructure and Processing*. 458(1-2): p. 108-115.

- Song, Z. L., Zhu, J. S., Ma, L. Q. and He, D. P., 2001, Evolution of foamed aluminum structure in foaming process. *Materials Science and Engineering a-Structural Materials Properties Microstructure and Processing*. 298(1-2): p. 137-143.
- Sosnick, B., 1948, Process for Making Foamlike Mass of Metal, US Patent, 2,434,775
- Sritharan, T., Chan, L.S., Tan, L.K. and Hung, N.P., 2001, A feature of the reaction between Al and SiC particles in an MMC. *Materials Characterization*,(47): p. 75-77.
- Stanzick, H., Klenke, J., Danilkin, S. and Banhart, J., 2002a, Material flow in metal foams studied by neutron radiography. *Applied Physics a-Materials Science & Processing*. 74: p. S1118-S1120.
- Stanzick, H., Wichmann, M., Weise, J., Helfen, L., Baumbach, T. and Banhart, J., 2002b, Process control in aluminum foam production using real-time X-ray radiography. *Advanced Engineering Materials*. 4(10): p. 814-823.
- Su, X. Y., Yu, T. X. and Reid, S. R., 1995a, Inertia-sensitive impact energy-absorbing Structures. 1. Effects of inertia and elasticity *International Journal of Impact Engineering*. 16(4): p. 651-672.
- Su, X. Y., Yu, T. X. and Reid, S. R., 1995b, Inertia-sensitive impact energy-absorbing structures. 2. Effect of strain rate. *International Journal of Impact Engineering*. 16(4): p. 673-689.
- Tagarielli, V. L., Deshpande, V. S. and Fleck, N. A., 2008, The high strain rate response of PVC foams and end-grain balsa wood. *Composites Part B-Engineering*. 39(1): p. 83-91.
- Valente, M., Parisi, M. and Nani, F., 2000, Image analysis of millistructure for mechanical characterization of aluminum foam. *Advanced Engineering Materials*. 2(11): p. 748-750.
- Wang, D. Q. and Shi, Z. Y., 2003, Effect of ceramic particles on cell size and wall thickness of aluminum foam. *Materials Science and Engineering a-Structural Materials Properties Microstructure and Processing*. 361(1-2): p. 45-49.

- Wang, J., Guo, Q., Nishio, M., Ogawa, H., Shu, D., Li, K., He, S. and Sun, B., 2003, The apparent viscosity of fine particle reinforced composite melt, *Journal of Materials Processing Technology*, 136, p. 60-63.
- Wang, Q., Fan, Z., Song, H. and Gui, L., 2005, Experimental and numerical analyses of the axial crushing behaviour of hat sections partially filled with aluminum foam. *International Journal of Crashworthiness*. 10(5): p. 535-543.
- Weaire, D and Hutzler, S, 1999, The Physics of Foams. *Oxford University Press*.
- Wubben, Th and Odenbach, S, 2004, On the stabilization mechanisms in liquid metallic foams. *Proceedings in Applied Mathematics and Mechanics*. 4: p. 270-271.
- Yang, C. C. and Nakae, H., 2000, Foaming characteristics control during production of aluminum alloy foam. *Journal of Alloys and Compounds*. 313: p. 188-191.
- Yang, G., Fan, T. and Zhang, D., 2004, Interfacial reaction of Al matrix composites reinforced with TiO₂-coated SiC particles during remelting. *Materials Letters*,(58): p. 1546-1552.
- Yu, C. J., Eifert, H. H., Banhart, J. and Baumeister, J., 1998, Metal foaming by a powder metallurgy method: Production, properties and applications. *Materials Research Innovations*. 2(3): p. 181-188.
- Zhao, H., Elnasri, I. and Abdennadher, S., 2005, An experimental study on the behaviour under impact loading of metallic cellular materials. *International Journal of Mechanical Sciences*. 47(4-5): p. 757-774.
- Zhao, H., Elnasri, I. and Li, H. J., 2006, The mechanism of strength enhancement under impact loading of cellular materials. *Advanced Engineering Materials*. 8(9): p. 877-883.

APPENDIX A

HARDNESS TEST RESULTS

Micro-hardness test results of foams with different SiC percentages with different particle sizes.

Foams without SiC									
P0	L1	L2	HV						
01	56.74	58.76	27.7						
02	60.03	60.03	25.7						
03	55.34	54.92	30.4						
04	54.01	53.86	31.8						
05	47.97	50.17	38.4						
5 % SiC addition					10 % SiC addition				
P1-05	L1	L2	HV		P1-10	L1	L2	HV	
01	54.37	55.74	30.5		01	42.7	38.05	57.7	
02	45.72	43.27	46.8		02	45.64	47.22	42.9	
03	46.72	47.78	41.5		03	54.03	52.03	32.9	
04	55.11	55.45	30.3		04	55.27	56.39	29.7	
05	48.15	47.98	40.1		05	43.38	44.35	48.1	
P2-05	L1	L2	HV		P2-10	L1	L2	HV	
01	50.99	50.04	36.03		01	58.25	55.37	28.7	
02	51.54	51.10	35.01		02	49.44	50.02	37.4	
03	50.63	51.12	35.98		03	50.38	49.31	37.3	
04	48.64	52.03	36.5		04	52.80	54.55	32.1	
05	43.68	46.29	46.0		05	55.86	55.00	30.1	
P3-05	L1	L2	HV		P3-10	L1	L2	HV	
01	51.24	49.95	36.2		01	57.43	57.43	28.1	
02	48.88	49.61	38.2		02	53.16	54.18	32.1	
03	54.43	55.74	30.5		03	49.22	50.75	37.0	
04	50.66	50.27	36.4		04	52.81	54.76	32.0	
05	47.12	48.14	40.8		05	52.53	54.20	32.5	
P4-05	L1	L2	HV		P4-10	L1	L2	HV	
01	54.09	54.86	31.2		01	47.35	50.18	39.8	
02	45.96	45.51	44.3		02	44.67	45.50	45.6	
03	53.75	52.73	32.6		03	50.06	51.36	36.0	
04	47.23	46.86	41.8		04	52.77	51.58	34.0	
05	52.10	51.92	34.2		05	44.50	44.81	46.2	
P5-05	L1	L2	HV		P5-10	L1	L2	HV	
01	47.69	45.72	42.4		01	46.31	45.21	44.2	
02	55.17	53.19	31.5		02	44.75	45.58	45.4	
03	52.83	50.47	34.7		03	44.27	44.88	46.6	
04	49.81	50.26	37.0		04	44.99	44.56	46.2	
05	48.98	49.49	38.2		05	48.64	49.94	38.1	